

Dissertation

submitted to the

Combined Faculty of Mathematics, Engineering and Natural Sciences
of Heidelberg University, Germany

for the degree of

Doctor of Natural Sciences

Put forward by

Vanessa Lydia Franke

born in Essen, Germany

Oral examination: February 16th, 2023

**In vivo determination of pH and magnesium ion concentration
by means of ^{31}P MRSI:
A multi-parametric look-up approach**

Referees: Prof. Dr. Peter Bachert
Prof. Dr. Michael Hausmann

**In vivo determination of pH and magnesium ion concentration by means of
³¹P MRSI: A multi-parametric look-up approach**

Phosphorus (³¹P) magnetic resonance spectroscopic imaging (MRSI) enables non-invasive imaging of pH value and magnesium ion concentration, [Mg²⁺], in living tissue. Typically, the chemical shifts of ³¹P metabolites are translated to pH and [Mg²⁺] via calibration equations, which, however, are well-defined only for physiological conditions, thus limiting their reliability in pathologies.

In this thesis, a novel approach for the in vivo determination of pH and [Mg²⁺] applicable for various chemical conditions, utilizing multiple ³¹P spectral properties in form of a look-up table, is proposed. To this end, the variability of spectral properties in vivo was investigated in high-quality human ³¹P MRSI data acquired at $B_0 = 7\text{ T}$, and reproduced in measurements of 114 model solutions prepared with physiologically relevant pH, [Mg²⁺] and ionic strengths, at $B_0 = 9.4\text{ T}$. The identified chemical shift changes of the adenosine-5'-triphosphate (ATP) resonances were translated into a multi-dimensional model, which was used for the implementation of a look-up algorithm, accounting also for measurement uncertainties. Application to in vivo data resulted in successful assignments of plausible pH and [Mg²⁺] values in healthy and tumorous tissue. The proposed approach is extendable by including further spectral properties, potentially allowing for more profound tissue characterizations, being particularly important for the application in pathologies.

In-vivo-Bestimmung des pH-Wertes und der Magnesiumionenkonzentration mittels ^{31}P MRSI: Ein Ansatz anhand einer multiparametrischen Look-Up-Tabelle

Phosphor-Magnetresonanzspektroskopische Bildgebung (^{31}P MRSI) ermöglicht die nicht-invasive Bildgebung des pH-Wertes und der Magnesiumionenkonzentration, $[\text{Mg}^{2+}]$, in lebendem Gewebe. Hierzu werden in der Regel die chemischen Verschiebungen der ^{31}P -Metaboliten über Kalibrierungsgleichungen in pH und $[\text{Mg}^{2+}]$ umgerechnet, die jedoch nur für physiologische Bedingungen wohldefiniert sind, was ihre Zuverlässigkeit in Pathologien einschränkt.

In dieser Arbeit wird ein neuer Ansatz für die In-vivo-Bestimmung von pH und $[\text{Mg}^{2+}]$ unter verschiedenen chemischen Bedingungen vorgestellt, der mehrere Eigenschaften in ^{31}P -Spektren in Form einer Look-Up-Tabelle nutzt. Zu diesem Zweck wurde die Variabilität der spektralen Eigenschaften in vivo anhand von hochwertigen ^{31}P MRSI-Daten, aufgenommen bei $B_0 = 7\text{ T}$, untersucht und in Messungen von 114 Modelllösungen mit physiologisch relevanten pH, $[\text{Mg}^{2+}]$ und Ionenstärken bei $B_0 = 9.4\text{ T}$ reproduziert. Die identifizierten Änderungen der chemischen Verschiebungen der Adenosin-5'-Triphosphat (ATP) Resonanzen wurden in ein mehrdimensionales Modell überführt, das für die Implementierung des Look-Up-Algorithmus verwendet wurde, der auch experimentelle Unsicherheiten berücksichtigt. Die Anwendung auf In-vivo-Daten führte zur erfolgreichen Zuordnung plausibler pH- und $[\text{Mg}^{2+}]$ -Werte in gesundem und tumorösem Gewebe. Der vorgeschlagene Ansatz ist durch die Einbeziehung weiterer spektraler Eigenschaften beliebig erweiterbar, was potentiell eine umfassendere Gewebecharakterisierung ermöglicht, die insbesondere für die Anwendung in Pathologien von Bedeutung ist.

Contents

List of abbreviations	v
1 Introduction	1
2 Fundamentals	5
2.1 Nuclear magnetic resonance (NMR)	5
2.1.1 Atomic nuclei in an external magnetic field	5
2.1.2 Macroscopic magnetization	6
2.1.3 Time evolution of the macroscopic magnetization	8
2.1.4 Magnetic resonance	8
2.1.5 Relaxation and Bloch equations	10
2.1.6 MR signal	10
2.2 Magnetic resonance spectroscopy (MRS)	12
2.2.1 Chemical shift	12
2.2.2 Scalar coupling	13
2.2.3 Influence of chemical exchange on MR spectra	14
2.2.4 Signal processing	17
2.3 Magnetic resonance spectroscopic imaging (MRSI)	19
2.3.1 Spatial encoding	19
2.3.2 Spatial zerofilling	20
2.4 Biochemical fundamentals	21
2.4.1 pH value	21
2.4.2 Main phosphorus compounds in this work	22
2.4.3 Intra- and extracellular concentrations of ions in vivo	23
2.5 Phosphorus (^{31}P) MRS	26
2.5.1 Determination of intracellular pH	26
2.5.2 Determination of intracellular magnesium ion concentration	29
3 Functions for modelling the ATP chemical shifts in dependence on the magnesium ion concentration	33
3.1 Model with heuristic ansatz	33
3.2 Model based on the London equation	34

3.3	Model based on the Hill equation	35
4	Materials and Methods	37
4.1	MR imaging systems	37
4.1.1	7-T whole-body MR system	37
4.1.2	9.4-T small animal PET-MR system	37
4.2	MR sequences	40
4.2.1	FID sequence	40
4.2.2	3D MRSI sequence	40
4.3	Preparation of model solutions	43
4.4	Experimental and Data Processing Protocols	46
4.4.1	General data processing steps	46
4.4.2	Measurements in vivo	46
4.4.3	Measurements on model solutions	50
4.5	Implementation of the look-up algorithm	53
4.5.1	Basic principle of the look-up algorithm	53
4.5.2	Calculation of three-dimensional probability distributions	54
4.5.3	Determination of output values (pH, Mg, K)	57
4.5.4	Choice of the sampling grid	59
5	Results	61
5.1	Identification of the relevant ranges of pH and magnesium ion concentration in vivo	61
5.1.1	³¹ P MRSI data from the human lower leg muscle of healthy volunteers	61
5.1.2	³¹ P MRSI human brain data from patients with glioblastoma	67
5.1.3	Summary of value ranges obtained in the analyzed in vivo data	73
5.2	Characterization of ³¹ P spectral properties in varying chemical environments	75
5.2.1	Overview of spectral changes with changing chemical environment	75
5.2.2	Quantified chemical shifts in dependence on the chemical environment	80
5.3	Modelling of the ATP chemical shifts	84
5.3.1	Model with heuristic ansatz	85
5.3.2	Model based on the London equation	90
5.3.3	Model based on the Hill equation	95
5.3.4	Evaluation of the models	102

5.4	Application of the implemented approach to in vivo ^{31}P MRSI data	104
5.4.1	Preceding considerations	104
5.4.2	Data from the human lower leg muscle of healthy volunteers . . .	105
5.4.3	Data from patients with glioblastoma	110
6	Discussion	115
6.1	Challenges of the existing methods for the determination of pH and $[\text{Mg}^{2+}]$ via ^{31}P MRS	115
6.1.1	Dependence on accurate calibration equations	115
6.1.2	Inorganic phosphate (P_i) as a measure for intracellular pH	115
6.2	Influences on the ^{31}P spectra acquired in model solutions	118
6.2.1	Temperature of the model solutions during the ^{31}P MRS measurement	118
6.2.2	Chemical composition of the prepared model solutions	120
6.3	Assessment of the proposed approach	122
6.4	Considerations concerning the implemented look-up algorithm	124
6.5	Large variation of δ_α measured in vivo	125
6.6	Applicability to in vivo ^{31}P MRSI data	126
6.6.1	Missing compatibility of the look-up values for α -ATP with the look-up values for γ - and β -ATP	126
6.6.2	Comparison with conventional methods	128
6.6.3	Different patterns in the glioblastoma datasets	129
6.7	Future steps	129
6.7.1	Further investigating the influences on the α -ATP chemical shift .	129
6.7.2	Incorporating the linewidths and J-coupling constants of ATP . .	130
6.7.3	Combining the proposed approach with other methods besides ^{31}P MRS	131
7	Summary and Conclusion	133
	Appendices	I
A	Derivation of a modified form of the Hill equation for NMR	I
B	Quantified linewidths and J-coupling constants in dependence on the chemical environment	III
C	Modelling of the α - and β -ATP chemical shifts	VIII
D	Test of functionality of the implemented look-up algorithm on model solution measurements	XVI

Contents

E	Application of the look-up algorithm to in vivo ³¹ P MRSI datasets using all three ATP chemical shifts	XX
	List of Figures	XX
	List of Tables	XXVI
	List of Scientific Publications	XXIX
	Bibliography	XXXIII
	Acknowledgments	XLI

List of abbreviations

ADP adenosine-5'-diphosphate

ATP adenosine-5'-triphosphate

BSA Bovine Serum Albumin

CEST Chemical Exchange Saturation Transfer

CK creatine kinase

Cr creatine

CRLBs Cramér-Rao lower bounds

DPG 2,3-Diphosphoglycerate

FID free induction decay

FT Fourier transform

GM *gastrocnemius medialis*

GPC glycerophosphocholine

GPE glycerophosphoethanolamine

HHE Henderson Hasselbalch equation

HP hyperpolarized

MPL mobile phospholipids

MR magnetic resonance

MRI magnetic resonance imaging

MRS magnetic resonance spectroscopy

List of abbreviations

MRSI magnetic resonance spectroscopic imaging

NAD nicotinamide adenine dinucleotide

NMR nuclear magnetic resonance

NOE nuclear Overhauser effect

P_i inorganic phosphate

PC phosphocholine

PCr phosphocreatine

PE phosphoethanolamine

RF radiofrequency

ROI region-of-interest

ROIs regions-of-interest

SNR signal-to-noise ratio

Sol *soleus*

TA *tibialis anterior*

UDPG Uridine Diphosphoglucose

VE demineralized

WHT whole tumor volume

WM white matter

1 Introduction

Following the postulation of the existence of a nuclear spin in the 1920s, the phenomenon of nuclear magnetic resonance (NMR) was experimentally proven by Rabi et al. in 1938 [1]. In 1946, the groups of Bloch and Purcell, independently from each other, demonstrated NMR in condensed matter [2, 3]. With the discovery of the dependence of nuclear resonance frequencies on their chemical environment by Proctor et al. and Dickinson et al. in 1950, the importance of NMR increased significantly [4, 5]. NMR spectroscopy developed into an essential technique in analytical chemistry and biochemistry.

Magnetic resonance (MR) paved its way into medical diagnostics in 1973, when Lauterbur and Mansfield discovered that the spatial distribution of nuclear spins can be determined by the use of magnetic field gradients [6, 7]. Based on this finding, magnetic resonance imaging (MRI) evolved, which uses the strong MR signal of hydrogen (^1H) nuclei in tissue to image anatomical structures. MRI provides images with excellent soft tissue contrast, and does not require ionizing radiation. Thus, the development of MRI revolutionized medical imaging.

In contrast to MRI, which has become an indispensable part of medical diagnostics, *in vivo* MR spectroscopy (MRS) has so far not made its way into daily clinical routine. However, it is a powerful tool for biomedical research, as it allows for the non-invasive investigation of specific biochemical properties and processes in healthy as well as in diseased tissue. Besides the widely used ^1H MRS, phosphorus (^{31}P) MRS is of particular interest for investigations on the energy metabolism. It enables the detection of metabolites involved e.g. in energy storage (adenosine-5'-triphosphate (ATP)), buffering (phosphocreatine (PCr)), and supply (nicotinamide adenine dinucleotide (NAD), ATP). Since the first biological and medical applications of ^{31}P MRS in the 1970s [8], technological developments, e.g. the development of MR systems with higher field strengths, resulted in a continuous improvement of ^{31}P MRS data quality, and thus opened the door for numerous *in vivo* applications. Higher magnetic field strengths are an important advantage for *in vivo* ^{31}P MRS, due to its low sensitivity, which translates to long measurement times not being feasible in the clinical routine. This might change in the near future with the increasing availability of ultra-high field MR systems ($B_0 \geq 7\text{T}$).

1 Introduction

The combination of MR spectroscopy with MR imaging methods, called magnetic resonance spectroscopic imaging (MRSI), is of particular interest for biomedical research and potential clinical applications, as it allows for the spatially resolved measurement of biochemical parameters in the entire investigated volume. ^{31}P MRSI allows for example for the non-invasive imaging of physiological parameters such as the pH value and the magnesium ion concentration, $[\text{Mg}^{2+}]$, which are both biochemical parameters playing key roles in metabolic and enzymatic processes of living tissue. Hence, they are of interest in research on different diseases, e.g. cancer [9–13], diabetes [14], muscular [15], psychiatric [16, 17] and neurodegenerative diseases [18, 19], to name a few.

The determination of pH and $[\text{Mg}^{2+}]$ via ^{31}P MRS is feasible due to (i) the strong sensitivity of ^{31}P resonance frequencies to changes of the chemical environment, and (ii) the large chemical shift dispersion, allowing for a reliable quantification of individual resonances. Thus, chemical parameters, e.g. pH and $[\text{Mg}^{2+}]$, can be indirectly assessed via the chemical shift quantification of specific ^{31}P metabolites. Conventionally, the chemical shifts of inorganic phosphate (P_i) and ATP are translated to pH and $[\text{Mg}^{2+}]$ via defined calibration equations acquired in model solutions. For the determination of pH, typically, a modified form of the Henderson Hasselbalch equation for the chemical shift of P_i is used, which was first reported by Moon and Richards in 1973 [20]. The determination of free $[\text{Mg}^{2+}]$ is typically assessed via the chemical shifts of ATP, which was first reported by Gupta et al. in 1978 [21].

The necessity of accurate calibration equations for a reliable determination of pH and $[\text{Mg}^{2+}]$ was already discussed in detail in the 1980s and early 1990s [22–25]. However, until today, standardized constants are typically used in the calibration equations, even for the application to pathologies. The use of constant parameters, which are well-defined only for normal physiological conditions, limits the reliability of the determined pH and $[\text{Mg}^{2+}]$ values particularly for the application to pathophysiological conditions, where the chemical environment is altered significantly. For the case of the determination of $[\text{Mg}^{2+}]$ via the ATP chemical shifts, this challenge has already been partly addressed. Several approaches have been proposed, which account for the concomitant effect of the pH value on the ATP chemical shifts [26–29]. Moreover, methods for the simultaneous determination of pH and $[\text{Mg}^{2+}]$ based on the ATP resonances were demonstrated [30]. However, the proposed approaches, so far, do not account for other influences, besides pH and magnesium ions, e.g. varying ionic strength, and work with parameters for their calibration equations, which are only well-defined for normal physiological conditions.

In this thesis, a novel approach for the in vivo determination of pH and $[\text{Mg}^{2+}]$ by means of ^{31}P MRS applicable for various chemical conditions, is proposed. The basic idea of this approach is the utilization of multiple quantities of an acquired ^{31}P spectrum to determine pH and $[\text{Mg}^{2+}]$, and is realized in the form of a look-up algorithm. In contrast to earlier approaches, the herein proposed look-up algorithm has the advantage of (i) being applicable to various chemical conditions, (ii) reducing the complexity of the look-up based assignment by solely focusing on conditions relevant in vivo, and (iii) increasing the robustness for the application in vivo by incorporating measurement uncertainties. As first proof-of-principle, a look-up algorithm is implemented, which determines pH and $[\text{Mg}^{2+}]$ for different ionic strengths based on the measured chemical shifts of the three resonances of ATP. The use of the ATP resonances for the determination of pH is advantageous regarding the measurement time due to its typically higher signal-to-noise ratio, compared to the resonance of P_i , which is used in the conventional modified Henderson Hasselbalch equation. A potential reduction of measurement time is of particular interest for applications in vivo.

For the development of this novel approach, first, high-quality in vivo ^{31}P MRSI data acquired from different tissue types at $B_0 = 7\text{ T}$ were investigated, in order to identify ranges for pH and $[\text{Mg}^{2+}]$, which are expected to be relevant in vivo. Second, a detailed characterization of ^{31}P spectral changes due to varying chemical conditions was performed on measurements in suitable model solutions. In total, 114 model solutions prepared with physiologically relevant pH, $[\text{Mg}^{2+}]$ and ionic strengths were measured at $B_0 = 9.4\text{ T}$, in order to reproduce the variability of ^{31}P chemical shifts obtained in vivo. Third, multi-dimensional models were developed, which describe the observed changes of the ATP chemical shifts with varying chemical conditions. Based on the developed models, the proof-of-principle look-up algorithm was implemented, which determines the physiological parameters pH, $[\text{Mg}^{2+}]$ and ionic strength, based on the three measured chemical shifts of ATP. Finally, the implemented look-up algorithm was applied to in vivo ^{31}P MRSI data from the lower leg muscle of healthy volunteers, and from the human brain of patients with glioblastoma, and compared to pH and $[\text{Mg}^{2+}]$ maps calculated with the conventional methods.

2 Fundamentals

2.1 Nuclear magnetic resonance (NMR)

2.1.1 Atomic nuclei in an external magnetic field

Atomic nuclei with an odd number of nucleons have a nuclear spin $\vec{I} \neq 0$, for which the quantum mechanical rules for angular momentum apply.

The commutator relations for the nuclear spin operator $\hat{\vec{I}} = (\hat{I}_x, \hat{I}_y, \hat{I}_z)$ are as follows:

$$[\hat{I}_i, \hat{I}_j] = i\hbar\epsilon_{ijk}\hat{I}_k \quad (2.1)$$

$$[\hat{I}^2, \hat{I}_i] = 0, \quad (2.2)$$

where $i, j, k \in x, y, z$.

The spin system is characterized by its angular momentum quantum number I , and the magnetic quantum number $m = (-I, -I+1, \dots, I-1, I)$. Applying the operators \hat{I}^2 and \hat{I}_z on the spin eigenstates $|I, m\rangle$ yield the following eigenvalue equations:

$$\hat{I}^2|I, m\rangle = I(I+1)\hbar^2|I, m\rangle \quad (2.3)$$

$$\hat{I}_z|I, m\rangle = m\hbar|I, m\rangle, \quad (2.4)$$

with \hbar as the reduced Planck constant. The nuclear spin is associated with a magnetic moment $\vec{\mu}$:

$$\vec{\mu} = \gamma\vec{I}, \quad (2.5)$$

where γ is the nucleus-specific gyromagnetic ratio. For the hydrogen (^1H) nucleus, $\gamma_{\text{H}} \approx 2.675 \times 10^8 \frac{\text{rad}}{\text{sT}}$ and respectively $\frac{\gamma_{\text{H}}}{2\pi} \approx 42.576 \frac{\text{MHz}}{\text{T}}$. For the phosphorus nucleus (^{31}P), the gyromagnetic ratio is $\gamma_{\text{31P}} \approx 1.083 \times 10^8 \frac{\text{rad}}{\text{sT}}$ and respectively $\frac{\gamma_{\text{31P}}}{2\pi} \approx 17.235 \frac{\text{MHz}}{\text{T}}$.

The interaction of a magnetic moment in an external magnetic field \vec{B}_0 is described by the Hamiltonian $\hat{H} = -\hat{\vec{\mu}} \cdot \vec{B}$. For a static magnetic field of $\vec{B} = (0, 0, B_0)$,

$$\hat{H} = -\hat{\vec{\mu}} \cdot \vec{B} = -\gamma\hat{I}_z B_0, \quad (2.6)$$

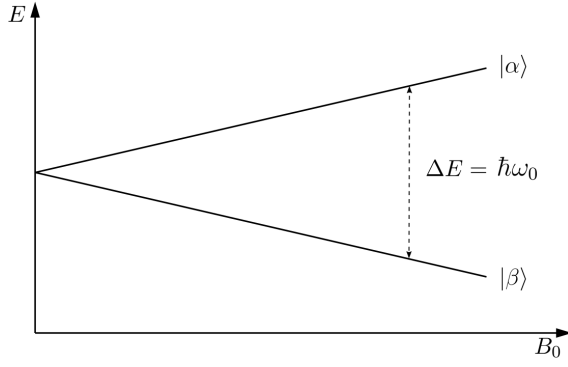


Figure 2.1: Zeeman splitting of energy levels for a nucleus with spin $I = \frac{1}{2}$ in dependence of the external static magnetic field B_0 . The energy difference ΔE between the two possible states $|\alpha\rangle$ and $|\beta\rangle$ is $\hbar\omega_0$.

and the time-invariant Schrödinger equation $\hat{H}|I, m\rangle = E|I, m\rangle$ yields the energy eigenvalues E_m :

$$E_m = -\gamma\hbar m B_0. \quad (2.7)$$

The splitting into $2I + 1$ equidistant energy levels due to an external magnetic field is called Zeeman effect. For spins with $I = \frac{1}{2}$, the energy difference between the two possible eigenstates $|\alpha\rangle = |\frac{1}{2}, -\frac{1}{2}\rangle$, and $|\beta\rangle = |\frac{1}{2}, +\frac{1}{2}\rangle$ is

$$\Delta E = E_\alpha - E_\beta = \gamma\hbar B_0 = \hbar\omega_0. \quad (2.8)$$

The Larmor frequency

$$\omega_0 = \gamma B_0 \quad (2.9)$$

is of central importance for nuclear magnetic resonance and is dependent on the gyromagnetic ratio γ and the magnetic field strength B_0 .

The experiments of this work are performed at static magnetic field strengths of $B_0 = 7\text{ T}$ and 9.4 T , resulting in Larmor frequencies of $f_{1\text{H}} = \frac{\omega_0}{2\pi} \approx 298\text{ MHz}$ and 400 MHz for ^1H , and $f_{31\text{P}} = 120\text{ MHz}$ and 162 MHz for ^{31}P .

2.1.2 Macroscopic magnetization

In the following, not only one isolated spin is considered, but an ensemble of N nuclei in a macroscopic sample of volume V in thermal equilibrium. As previously described, in the external static magnetic field, the $2I + 1$ energy levels will be occupied following the Boltzmann statistics. The occupation probability for energy level m is:

$$p_m = \frac{1}{Z} \cdot e^{-E_m/k_B T}, \quad (2.10)$$

2.1 Nuclear magnetic resonance (NMR)

with the canonical partition function $Z = \sum_{m=-I}^I (e^{-E_m/(k_B T)})$, the Boltzmann constant k_B , and the equilibrium temperature T .

For nuclei with spin $I = \frac{1}{2}$, the expectation value of the z component of the magnetic moment is given by

$$\begin{aligned} \langle \hat{\mu}_z \rangle &= \gamma \langle \hat{I}_z \rangle = \gamma \left[p_{-\frac{1}{2}} \langle \alpha | \hat{I}_z | \alpha \rangle + p_{+\frac{1}{2}} \langle \beta | \hat{I}_z | \beta \rangle \right] \\ &= \gamma \frac{\hbar}{2} \left[p_{+\frac{1}{2}} - p_{-\frac{1}{2}} \right] \\ &= \gamma \frac{\hbar}{2} P, \end{aligned} \quad (2.11)$$

where the difference in the population probabilities of the two possible states is also defined as the polarization P , representing the normalized difference in population. Inserting the energy eigenvalues E_m (2.7) into the population probability (2.10) yields

$$P = \frac{e^{\frac{\gamma B_0 \hbar}{2k_B T}} - e^{-\frac{\gamma B_0 \hbar}{2k_B T}}}{e^{\frac{\gamma B_0 \hbar}{2k_B T}} + e^{-\frac{\gamma B_0 \hbar}{2k_B T}}} = \tanh \left(\frac{\gamma \hbar B_0}{2k_B T} \right). \quad (2.12)$$

For room and body temperature, $\gamma \hbar B_0 \ll k_B T$, hence $\tanh(x)$ can be approximated by a Taylor expansion for $x = 0$ (high temperature approximation), yielding in the first order

$$P \approx \frac{\gamma \hbar B_0}{2k_B T}. \quad (2.13)$$

For a magnetic field strength of $B_0 = 7\text{ T}$ and body temperature of $T \approx 310.15\text{ K}$, the polarization is in the order of $P \approx 3.5 \times 10^{-6}$ for ^1H and $P \approx 1.4 \times 10^{-6}$ for ^{31}P .

The macroscopic magnetization \vec{M} of the spin ensemble is given by the sum of all magnetic moments per volume V :

$$\vec{M} = \frac{1}{V} \sum_{i=1}^N \langle \hat{\mu}_i \rangle = \frac{N}{V} \langle \hat{\mu} \rangle. \quad (2.14)$$

With $\vec{B}_0 = (0, 0, B_0)$ and equation (2.11), this yields

$$M_0 = \frac{N}{V} \langle \hat{\mu}_z \rangle = \frac{N}{V} \gamma \frac{\hbar}{2} P \approx \frac{1}{4} \frac{N}{V} \frac{\gamma^2 \hbar^2}{k_B T} B_0. \quad (2.15)$$

Equation (2.15) shows, that the macroscopic magnetization increases with $\frac{N}{V}$, B_0 , γ^2 and $\frac{1}{T}$. For in vivo experiments, the temperature is fixed by the body temperature and $\frac{N}{V}$ by the tissue density. Thus, only the choice of the nucleus (e.g. ^1H , ^{31}P) or the magnetic field strength can increase M_0 .

2.1.3 Time evolution of the macroscopic magnetization

For nuclear spins in a time-varying magnetic field $\vec{B}(t)$, the time-dependent Schrödinger equation holds:

$$i\hbar \frac{\partial}{\partial t} |I, m\rangle = \hat{H}(t) |I, m\rangle, \quad (2.16)$$

with $\hat{H}(t) = -\hat{\mu} \cdot \vec{B}(t)$ being the time-dependent Hamiltonian. Using the *Ehrenfest theorem*, the time dependence of the expectation value of the magnetic moment can be calculated by

$$\frac{d}{dt} \langle \hat{\mu}_j \rangle = \frac{i}{\hbar} \langle [\hat{H}, \hat{\mu}_j] \rangle + \left\langle \frac{\partial \hat{\mu}_j}{\partial t} \right\rangle. \quad (2.17)$$

Using the commutator relations (2.1), this yields

$$\frac{d}{dt} \langle \hat{\mu} \rangle = \langle \hat{\mu} \rangle \times \gamma \vec{B}(t). \quad (2.18)$$

Due to the *correspondence principle*, a transition from a quantum mechanical description $\langle \hat{\mu} \rangle$ to a classical description of the macroscopic magnetization \vec{M} is justified. The equation of motion for \vec{M} is therefore:

$$\frac{d}{dt} \vec{M}(t) = \vec{M}(t) \times \gamma \vec{B}(t). \quad (2.19)$$

In a static magnetic field $\vec{B}_0 = (0, 0, B_0)$, this means that the macroscopic magnetization vector precesses around the z-axis with the Larmor frequency $\omega_0 = \gamma B_0$.

2.1.4 Magnetic resonance

The static magnetic field alone is not enough to observe magnetic resonance. A time-dependent radio frequency (RF) excitation field $\vec{B}_1(t)$ of frequency ω_{RF} is applied, which is polarized perpendicular to the main magnetic field \vec{B} :

$$\vec{B}_1 = B_1 \begin{pmatrix} \cos(\omega_{\text{RF}} t) \\ \sin(\omega_{\text{RF}} t) \\ 0 \end{pmatrix} \quad (2.20)$$

resulting in a total magnetic field of $\vec{B}(t) = \vec{B}_0 + \vec{B}_1(t)$.

In order to simplify the equation of motion (2.19), a transformation into the coordinate system rotating with frequency ω_{RF} around the z axis (*rotating frame*, $(x', y', z' = z)$) is performed. This yields a simplified equation of motion:

$$\frac{d}{dt} \vec{M}'(t) = \vec{M}'(t) \times \gamma \vec{B}_{\text{eff}}, \quad (2.21)$$

with the effective magnetic field

$$\vec{B}_{\text{eff}} = \begin{pmatrix} B_1 \\ 0 \\ B_0 - \frac{\omega_{\text{RF}}}{\gamma} \end{pmatrix}. \quad (2.22)$$

If the resonance condition $\omega_{\text{RF}} = -\gamma B_0$ is met, the effective field in the rotating frame \vec{B}_{eff} reduces to $B_1 \cdot \vec{e}'_x$ and the magnetization vector \vec{M}' rotates around the x' -axis with the frequency $\omega_1 = \gamma B_1$. The magnetization vector \vec{M} rotates towards the transverse x' - y' plane by the angle

$$\theta = \int_0^{t_p} \omega_1(t) dt = \int_0^{t_p} \gamma B_1(t) dt, \quad (2.23)$$

with t_p being the pulse length of the RF pulse. In the case of a constant amplitude B_1 , equation (2.23) simplifies to

$$\theta = \gamma B_1 \cdot t_p. \quad (2.24)$$

The so-called flip angle θ can be increased by increasing the amplitude B_1 or the pulse length t_p .

The picture of the magnetization vector being tipped out of its equilibrium state due to the application of an RF field B_1 of frequency ω_0 is the basis of the classical description of magnetic resonance and can be used to explain many of its phenomena.

In a quantum mechanical picture, the irradiation of the RF field with the Larmor frequency ω_0 causes a rearrangement of the occupation of the energy levels of the spin system.

2.1.5 Relaxation and Bloch equations

When the RF irradiation is switched off, the excited magnetization vector strives back to its equilibrium state due to the interactions of the nuclei with their environment. The transversal magnetization decays to $M_{xy} = 0$ and the longitudinal magnetization increases to the initial magnetization $M_z = M_0$. To describe these processes, Felix Bloch introduced two time constants T_1 and T_2 , which extend the equations of motion (2.19) to the fundamental Bloch equations [2]:

$$\frac{d}{dt}M_x = \gamma(\vec{M} \times \vec{B})_x - \frac{M_x}{T_2}, \quad (2.25)$$

$$\frac{d}{dt}M_y = \gamma(\vec{M} \times \vec{B})_y - \frac{M_y}{T_2}, \quad (2.26)$$

$$\frac{d}{dt}M_z = \gamma(\vec{M} \times \vec{B})_z - \frac{M_z - M_0}{T_1}. \quad (2.27)$$

The time constant T_1 is also called the spin-lattice relaxation time and is described by the interaction of the spin system with its environment. Due to energy transfer between the spin energy levels and the thermal reservoir (lattice), the longitudinal component of the magnetization returns to its equilibrium state.

The transverse relaxation time T_2 can be described by the interaction between the individual spins and is therefore also called the spin-spin relaxation time. The dephasing of the individual spin packages results in the decay of the transversal component of the magnetization vector.

In a real NMR experiment, an additional dephasing of the spin packages is caused by local inhomogeneities of the magnetic field B_0 , which is described by the time constant $T_2' = \gamma\Delta B_0$. The apparent transverse relaxation is described by the time constant T_2^* :

$$\frac{1}{T_2^*} = \frac{1}{T_2} + \frac{1}{T_2'}. \quad (2.28)$$

2.1.6 MR signal

The Bloch equations (2.25) can be solved under the assumption that the relaxation during the RF pulse is negligible, i.e. $t_p \ll T_{1,2}$. Combining the transverse components of the magnetization to $M_{xy} = M_x + iM_y$, this yields

$$M_{xy}(t) = M_{xy}(0)e^{i\omega_0 t} e^{-\frac{t}{T_2^*}} \quad (2.29)$$

$$M_z(t) = M_0 - (M_0 - M_z(0))e^{-\frac{t}{T_1}}, \quad (2.30)$$

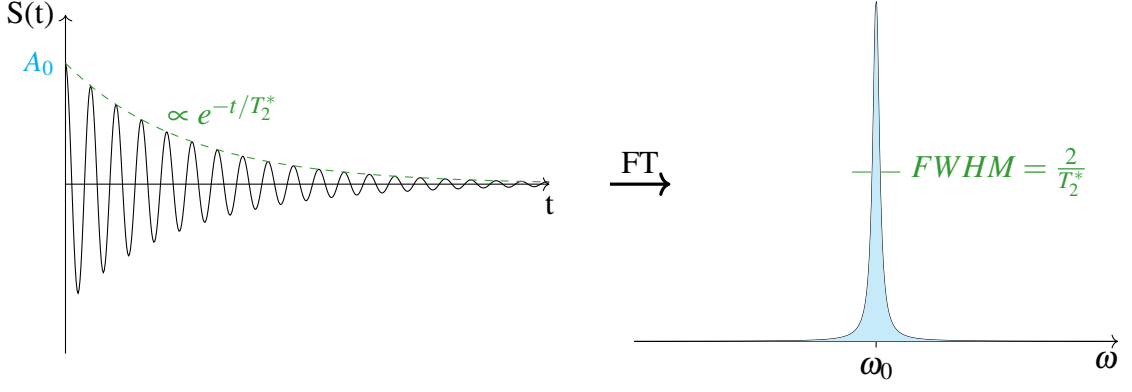


Figure 2.2: Time course of the measured MR signal $S(t)$, also called the *free induction decay* (FID), and the resulting spectrum $F(\omega)$ after application of a Fourier Transform (FT). The signal amplitude A_0 corresponds to the area under the Lorentzian shaped curve $F(\omega)$ (indicated in blue), and is in principle directly proportional to the concentration of nuclei contributing to the measured MR signal. The linewidth of the Lorentzian is given by $2/T_2^*$.

where $M_{xy}(0)$ and $M_z(0)$ are the transverse and longitudinal components of \vec{M} at the beginning of the relaxation process, i.e. at the end of the RF irradiation.

In an NMR experiment, the precession of the transverse magnetization causes a time-varying magnetic flux inducing a voltage $U_{ind}(t)$ in a receiver coil positioned perpendicular to the static magnetic field \vec{B}_0 . The induced voltage is the measured MR signal $S(t)$ which is directly proportional to the magnitude of the transverse component of the magnetization M_{xy} in the measured volume V :

$$S(t) = U_{ind}(t) \propto \int \rho(\vec{r}) e^{i\omega_0 t} dV. \quad (2.31)$$

Hereby, $\rho(\vec{r})$ is the spatial density distribution of the individual spins. Because the transverse magnetization decays with the T_2^* relaxation time (eq. (2.29)), the measured MR signal is given by

$$S(t) = A_0 e^{i\omega_0 t} e^{-\frac{t}{T_2^*}}. \quad (2.32)$$

The MR signal $S(t)$ (2.32) is also called the *free induction decay*, or shortly FID.

Applying the Fourier Transform (FT) to the signal $S(t)$, yields the MR spectrum, which reveals information about the resonances contained in the MR signal (see figure 2.2). The resonance peaks have Lorentzian line shapes with a width given by $FWHM = 2/T_2^*$. The area under the peak corresponds to the signal amplitude A_0 .

2.2 Magnetic resonance spectroscopy (MRS)

In the following, the most important fundamental aspects of MR spectroscopy (MRS), which are of relevance for this work, are summarized. For a detailed description the textbooks [31–33] are recommended.

2.2.1 Chemical shift

In all previous considerations, a sample containing identical spins characterized by the same Larmor frequency ω_0 were considered, which results in only one resonance peak at the position ω_0 . This situation changes for nuclear spins situated in atoms and molecules, due to the shielding of the different electron clouds from the external magnetic field B_0 . The local magnetic field changes to

$$\vec{B}_{\text{loc}} = \vec{B}_0(1 - \sigma), \quad (2.33)$$

where σ is the molecule specific shielding constant, which is dependent on the chemical environment of the nucleus. Therefore, the value of σ changes for different molecules and chemical groups. In general, σ is a tensor, because the shielding is dependent on the relative orientation of the entire electron shell of the molecule to the external magnetic field. However, the case of isotropic shielding (and therewith σ being a scalar) is assumed in the following.

The shielding of the magnetic field results in a shift of the local resonance frequency

$$\vec{\omega}_{\text{loc}} = \gamma \vec{B}_0(1 - \sigma). \quad (2.34)$$

The difference between the local frequency of a resonance from a reference frequency ω_{ref} is referred to as the chemical shift, which is a measure that is independent of the magnetic field strength B_0 and is given in parts per million (ppm):

$$\delta_i = \frac{\omega_i - \omega_{\text{ref}}}{\omega_{\text{ref}}} \times 10^6. \quad (2.35)$$

The choice of the reference frequency depends on the application. For ^{31}P MRS, phosphocreatine (PCr) is conventionally used as reference compound. From equation (2.34) it follows, that the spectral dispersion of resonances increases linearly with increasing magnetic field strength B_0 . The chemical shift provides direct information about the chemical environment of nuclei, and thus can be used for the detection and assignment of chemical compounds characterized by their unique resonance frequency (Figure 2.3).

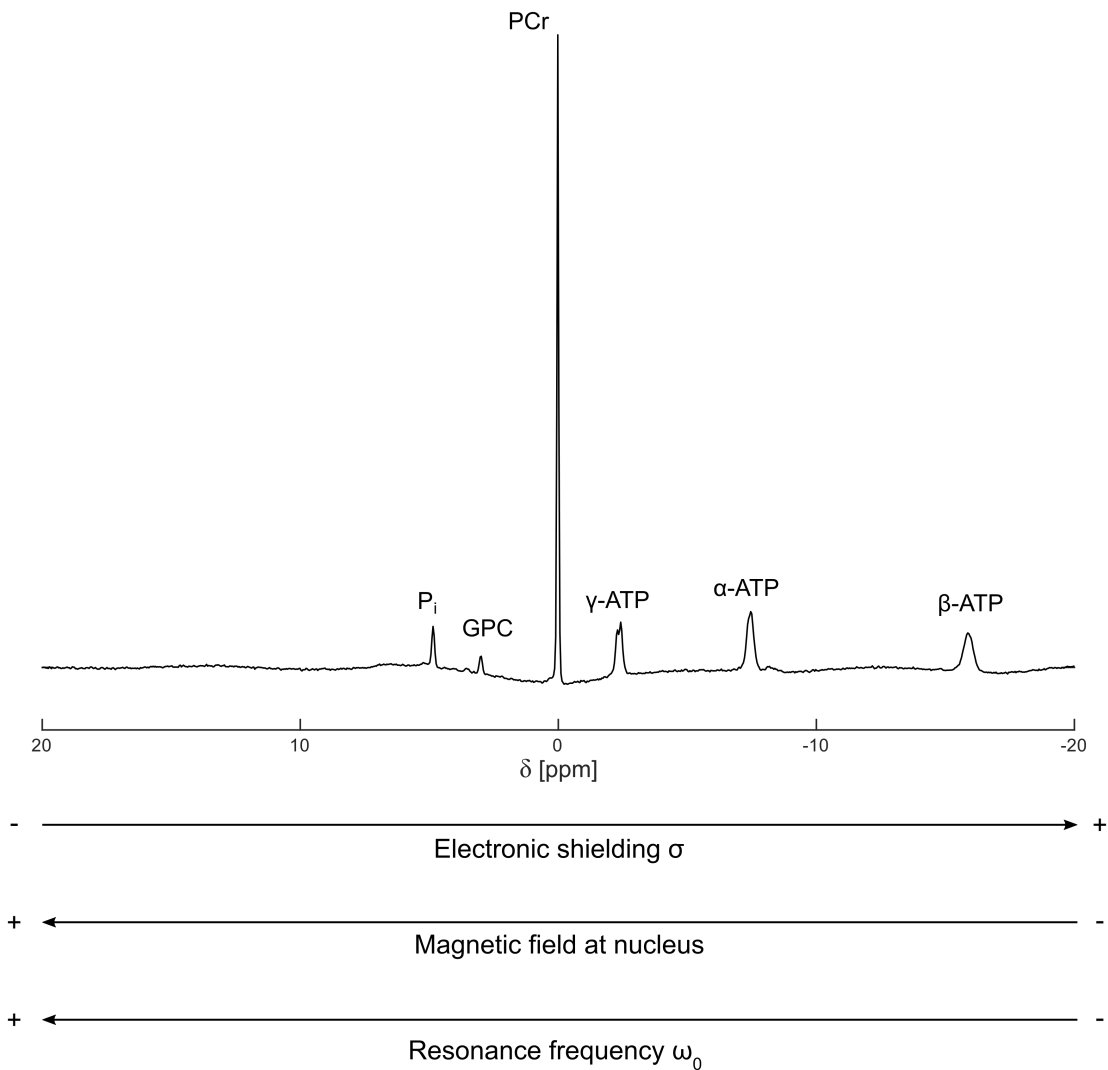


Figure 2.3: Representative ^{31}P MR spectrum acquired from muscle tissue from a human lower leg at $B_0 = 7\text{T}$. Based on their different resonance frequencies, different compounds can be distinguished (from left to right): inorganic phosphate (P_i), glycerophosphocholine (GPC), phosphocreatine (PCr), and the three resonances of adenosine-5'-triphosphate (ATP). Out of convention, in MRS, the chemical shift axis is plotted from positive to negative values.

2.2.2 Scalar coupling

An additional property that can be observed in MR spectra is the splitting of resonance lines into several smaller lines (*multiplets*). This phenomenon is referred to as scalar coupling, J coupling or spin-spin coupling [31]. Scalar coupling originates from the indirect interaction between neighboring spins in chemical bonds through their shell electrons, underlying the Pauli exclusion principle. These interactions lead to changes of the energy levels, which can be described by the J coupling constants. The scalar coupling

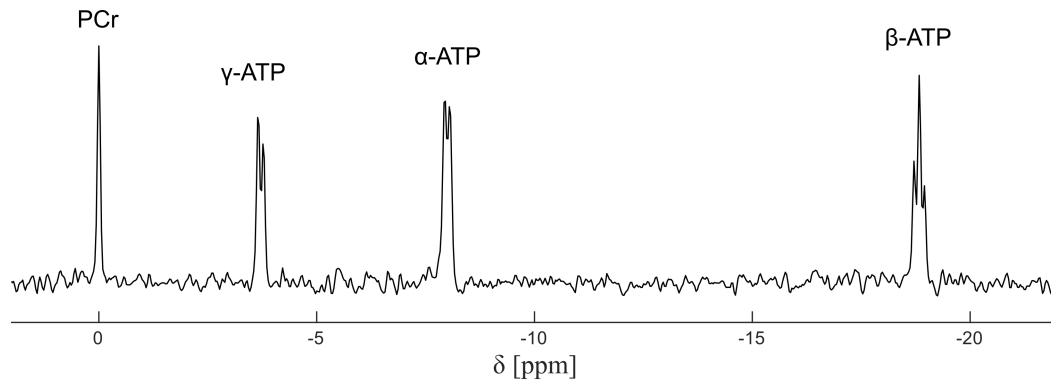


Figure 2.4: ^{31}P MR spectrum of a model solution containing phosphocreatine (PCr) and adenosine-5'-triphosphate (ATP), acquired at $B_0 = 9.4\text{ T}$, demonstrating the multiplet splitting of ATP. The resonances of γ - and α -ATP split into doublets, whereas the β -ATP resonance is a doublet-of-doublets, appearing as pseudo-triplet.

constant is independent on the external magnetic field strength B_0 , but depends on the number of bonds between the coupled spins. The J coupling constant rapidly decreases with increasing number of bonds, and can typically be ignored for more than three bonds. For the ^{31}P -O- ^{31}P bond, which is of relevance for ^{31}P MRS, the J coupling constants are typically between 15 – 20 Hz [31].

Of relevance for this work, is the multiplet splitting of adenosine-5'-triphosphate (ATP) due to the ^{31}P -O- ^{31}P bonds between the γ -, β - and α -nuclei (cf. chemical structure of ATP in Figure 2.8). A detailed description about the line splitting of ATP can be found in [34]. The γ - and α -resonances are so called doublets, i.e. they split into two separate lines, due the respective coupling with the ^{31}P nucleus at the β position, and are described by the coupling constants $J_{\gamma\beta}$ and $J_{\alpha\beta}$. The resonance signal of β -ATP is a so-called doublet-of-doublets, i.e. a doublet splitting of two doublets resulting in four resonance lines. Because $J_{\gamma\beta} \approx J_{\alpha\beta}$, the two middle resonances coincide and typically cannot be resolved. Thus, the β -ATP multiplet is observed as pseudo-triplet (Figure 2.4).

2.2.3 Influence of chemical exchange on MR spectra

Chemical exchange between two MR visible species has influences on their corresponding measured MR signals. A detailed description of the effects of chemical exchange on MR spectra can be found in [32, 33]. In the following, processes in the *intermediate exchange regime* are briefly summarized, which are important for this work.

A two-site exchange process between species A and B with populations $p_A = \frac{[A]}{[A]+[B]}$ and

$p_B = \frac{[B]}{[A]+[B]}$ will be considered:



The exchange process is characterized by the rate constant $k_{ex} = \frac{1}{\tau_{ex}} = k + k'$. The resonance frequencies of the two species A and B are different, which are defined via the chemical shifts δ_A and δ_B . When the exchange rate k_{ex} has approximately the same magnitude as the chemical shift difference $\Delta\delta = \delta_A - \delta_B$, the system is considered to be in the *intermediate exchange regime*, where the MR lineshapes are most sensitive to chemical exchange processes. It is further distinguished between *slow intermediate exchange* and *fast intermediate exchange*:

$$k_{ex} < |\Delta\delta/2| \quad (\text{slow intermediate exchange}) \quad (2.37)$$

$$k_{ex} > |\Delta\delta/2| \quad (\text{fast intermediate exchange}). \quad (2.38)$$

The case $k_{ex} = \Delta\delta/2$ is called the *coalescence point*. The effect of chemical exchange on the MR spectrum of species A and B in the different mentioned regimes is visualized in Figure 2.5.

In the fast exchange limit $k_{ex} \gg |\Delta\delta/2|$, the two resonance lines of species A and B collapse into a sharp, single peak. The position of this resonance peak is given by the mean of the two chemical shifts δ_A and δ_B , weighted by the concentrations of the two species in equilibrium:

$$\delta_{\text{obs}} = p_A \cdot \delta_A + p_B \cdot \delta_B. \quad (2.39)$$

In equilibrium, the ratio of the species concentrations is called the equilibrium constant K , and is equal to the ratio of the rate constants, i.e. $K = [B]_{\text{equ}}/[A]_{\text{equ}} = k/k'$. The equilibrium constant K can be derived from the position δ_{obs} , when the chemical shifts of the species A and B are known:

$$\delta_{\text{obs}} = p_A \cdot \delta_A + p_B \cdot \delta_B = \frac{\delta_A + K \cdot \delta_B}{1 + K}. \quad (2.40)$$

The effect of chemical exchange on the longitudinal relaxation rates can be described with the so called Bloch-McConnell equations, which can be found e.g. in [31, 32], or in the original publication from 1958 [35].

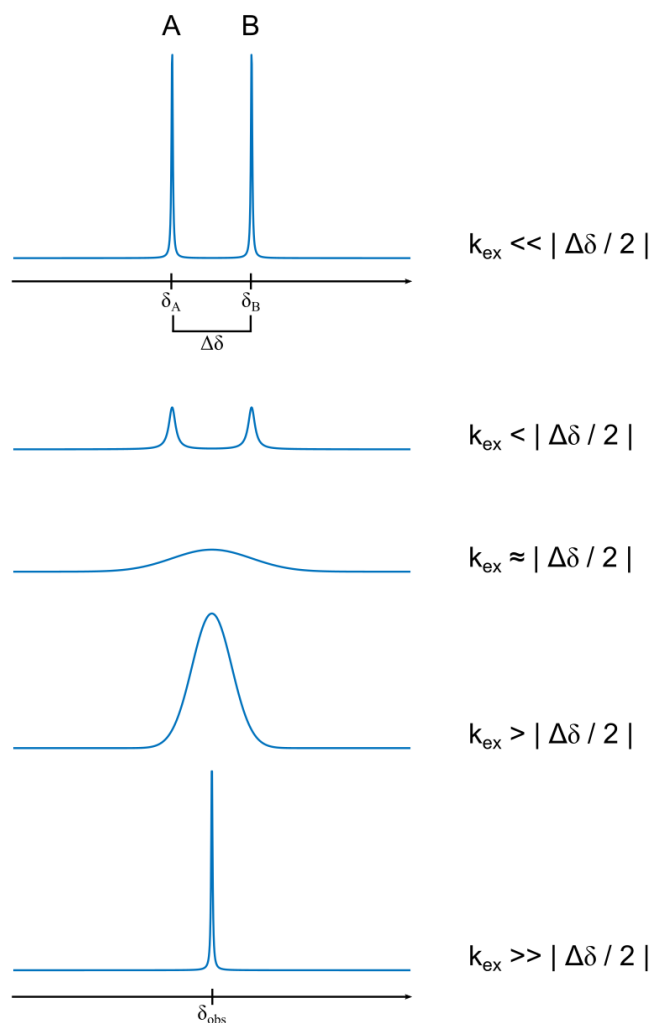


Figure 2.5: Schematic representation of NMR lineshapes in presence of chemical exchange. Chemical exchange between the two equally populated species A and B, with the corresponding chemical shifts δ_A and δ_B , is assumed. Dependent on the magnitude of the exchange rate k_{ex} relative to the chemical shift difference $\Delta\delta = \delta_A - \delta_B$, the lineshape changes. In the *slow exchange* regime ($k_{ex} \ll |\Delta\delta/2|$), two separate, sharp resonance lines are observed, whose lineshapes become broader, for the case of *slow intermediate exchange* ($k_{ex} < |\Delta\delta/2|$). At the coalescence point ($k_{ex} \approx |\Delta\delta/2|$), one extremely broad resonance line is observed. In the *fast exchange* limit ($k_{ex} \gg |\Delta\delta/2|$) one sharp resonance line is observed with the chemical shift δ_{obs} , given by the mean of the two chemical shifts δ_A and δ_B , weighted by the populations of species A and B (cf. equation (2.40)).

2.2.4 Signal processing

The quality and information content of the MR spectrum is directly related to the quality of the FID. In this section, it will be shortly demonstrated how the appearance of the MR spectrum can be improved by specific processing of the FID. For a more detailed description the reader is referred to [31]. It should be noted, that some equations are expressed in terms of frequency f , others in terms of angular frequency $\omega = 2\pi f$.

Multi-scan principle

One way to improve the signal-to-noise ratio (SNR) of a spectrum is averaging, which means the adding of the FIDs of n consecutive, identical experiments. This leads to an improvement in SNR of the factor \sqrt{n} .

For in vivo experiments, the possibility of improving the SNR by time-averaging is limited, because an improvement in SNR of factor 10 requires a factor of $10^2 = 100$ more acquisitions, meaning a factor of 100 in the measurement time.

Time-domain filtering

Time-domain filtering or apodization is commonly used to attenuate the noisy data points at the end of the FID, and therewith artificially improving the SNR of the spectrum. Prior to Fourier transformation, the time domain signal $S(t)$ is multiplied with a filter function $S_{\text{filter}}(t)$:

$$S_{\text{filtered}}(t) = S(t) \cdot S_{\text{filter}}(t). \quad (2.41)$$

Two commonly used filter functions are:

1. Exponential filter: $S_{\text{filter}}(t) = e^{-bt}$
2. Gaussian-shaped filter: $S_{\text{filter}}(t) = e^{-(bt)^2}$

Analog-to-digital conversion

In all previous sections, the NMR signal was described as a continuous, analog signal. However, in a real NMR experiment, the received signal can only be sampled discretely. This is done with an analog-to-digital converter (ADC), sampling the FID over N time-points with the *dwell time* Δt . The maximal reconstructable frequency is limited by the *Nyquist frequency* f_{Nyquist} , defined by the Nyquist-Shannon sampling theorem. Signals with a frequency greater than the Nyquist frequency, will still be digitized, but at an incorrect frequency, which is also called *aliasing* of resonances.

2 Fundamentals

The **spectral bandwidth** SW equals $2f_{\text{Nyquist}}$ and can also be expressed in terms of the dwell time Δt :

$$SW = \frac{1}{\Delta t}. \quad (2.42)$$

The **spectral resolution** $\Delta\nu$ is given by the spectral bandwidth SW divided by the sampled timepoints N , which is equivalent to 1 over the total acquisition (sampling) time T_{acq} :

$$\Delta\nu = \frac{1}{T_{\text{acq}}} = \frac{1}{N\Delta t}. \quad (2.43)$$

Thus, the spectral resolution can be improved by decreasing the spectral bandwidth or increasing the acquisition time. However, the possibility of decreasing the spectral bandwidth is limited due to aliasing, and increasing the acquisition time leads to an increase of the relative noise contributions. Alternatively, the extension of acquisition time can be simulated by adding points with zero amplitude to the acquired FID. This procedure is called time-domain **zero-filling**, and can improve the spectral appearance significantly.

B_0 shift correction

Due to B_0 inhomogeneities, the reference frequency can be different from the adjusted transmitter frequency, leading to a shift of the acquired spectrum. In order to position the reference peak to exactly 0 ppm, a B_0 shift correction can be performed, shifting the entire spectrum by a specific amount. This is simply done by multiplying the acquired FID with a phase factor:

$$S_{\text{cor}}(t) = S(t) \cdot e^{-2\pi i \cdot \Delta f \cdot t}, \quad (2.44)$$

where Δf is the frequency difference between the adjusted transmitter and actual resonance frequency of the reference substance. Δf is in general determined by a first reference fit, only quantifying the signal of the reference substance (see section 4.4.1).

2.3 Magnetic resonance spectroscopic imaging (MRSI)

So far, the basic principles of MRS were introduced. In general, MRS refers to the acquisition of non-localized MR signals coming from the entire measured sample. Methods enabling the acquisition of localized MR spectra of the entire measured volume are referred to as magnetic resonance spectroscopic imaging (MRSI). In the scope of this work, 3D MRSI sequences will be used for the acquisition of in vivo data. Therefore, the basic principles of spatial encoding relevant to this specific sequence will be introduced. For a full and more detailed description of the spatial encoding in the field of MR, the reader is referred to [31, 36].

2.3.1 Spatial encoding

In order to perform localized MR measurements, the spatial information has to be encoded in the MR signal. This can be realized by the use of magnetic field gradients $\vec{G} = (G_x, G_y, G_z)$ yielding a spatial variation of the main magnetic field:

$$\vec{B}_0(\vec{r}) = \vec{B}_0 + \vec{G} \cdot \vec{r}. \quad (2.45)$$

Hereby, $\vec{G} \parallel \vec{B}_0$ in order to maintain the quantization axis of the nuclear spins. Due to the spatially varying magnetic field $\vec{B}(\vec{r})$, the Larmor frequency also becomes location-dependent:

$$\omega_0(\vec{r}) = \gamma(B_0 + \vec{G} \cdot \vec{r}) = \omega_0 + \gamma\vec{G} \cdot \vec{r}. \quad (2.46)$$

Under the assumption that only nuclear spin packets with the same Larmor frequency ω_0 are present in the sample and by neglecting the relaxation effects, the MR signal equation (2.32) changes to

$$S(t) \propto \int \rho(\vec{r}) e^{i\omega_0 t} e^{i\gamma\vec{G} \cdot \vec{r} t} d\vec{r}. \quad (2.47)$$

By introducing a spatial frequency variable $\vec{k}(t)$:

$$\vec{k}(t) = \gamma \int_0^t \vec{G}(\tau) d\tau \quad (2.48)$$

and considering the general case of spin packets with different Larmor frequencies being present in the sample, the acquired MR signal from the macroscopic sample can be

written as

$$S(\vec{k}, t) = \int_{\vec{r}} \int_{\omega} S(\vec{r}, \omega) e^{i\omega t} e^{i\vec{k} \cdot \vec{r}} d\omega d\vec{r}. \quad (2.49)$$

By using a 4D Fourier transformation, localized MR spectra $S(\vec{r}, \omega)$ can be obtained. For the spatial encoding of the three spatial dimensions, different techniques can be used, for which a detailed description can be found in [31, 36]. For the 3D MRSI sequence used in this work, only *phase encoding* is used, and will be shortly introduced in the following.

Phase encoding

In order to encode the spatial information in the phase of the MR signal, a phase-encoding gradient is switched on for the time t_{PE} inbetween RF excitation and start of the signal acquisition. While the Gradient is switched on, the spin packets at different spatial locations accumulate a different phase according to equation (2.48). During the signal read-out the spatial information is then phase-encoded. By repeating this procedure with varying gradient strengths, the entire k-space (and the position-space which is linked via Fourier transform) can be successively sampled.

This procedure can be done for all 3 spatial dimensions, leading to a 4D dataset with one acquired FID (and respective spectrum) at each point of the 3D volume.

2.3.2 Spatial zerofilling

Spatial zerofilling refers to the extension of the k-space by adding zeros at the edges of the k-space, and therewith fictively improving the spatial resolution. Mathematically, the added zeros lead simply to an interpolation between the actual acquired data points, but the physical information content is not increased. Nevertheless, spatial zerofilling is a common technique used in MRSI as it results in smoother spectroscopic maps.

The zerofilling factor describes the factor of zeros being added to the k-space. A zero-filling factor of 2, which is also referred to as 'one-fold spatial zerofilling', means the doubling of the spatial resolution by adding the same number of zeros as number of acquired k-space points.

2.4 Biochemical fundamentals

In this section, biochemical and physiological fundamentals being of importance for this work, are briefly summarized. For a more detailed description, the interested reader is referred to [37–39].

2.4.1 pH value

The pH value of a solution is a measure of its concentration of H^+ and is defined as

$$pH = \log \frac{1}{[H^+]} = -\log [H^+]. \quad (2.50)$$

Hereby, it should be noted that in aqueous solutions H^+ is present as protonated water H_3O^+ , but is often denoted as H^+ for simplicity.

The ionization equilibrium of a weak acid is given by



where HA is the acid and A^- its conjugate base. With the acid dissociation constant

$$K_a = \frac{[H^+][A^-]}{[HA]} \quad (2.52)$$

the pK_a value of the acid can be defined as

$$pK_a = \log \frac{1}{K_a} = -\log K_a. \quad (2.53)$$

A conjugate acid base pair has the fundamental property of being able to partly compensate for changes of the pH value in a solution, or in other words to *buffer*. In general, a weak acid has the highest buffer capacity around its pK_a value.

Henderson Hasselbalch equation

Starting from equation (2.52) and the use of equations (2.50) and (2.53), the following useful expression can be derived:

$$pH = pK_a + \log \frac{[A^-]}{[HA]}. \quad (2.54)$$

This relation is commonly known as the **Henderson Hasselbalch equation**. Thus, the pH value of a solution can be calculated when the molar ratio of A^- to HA and the pK_a

2 Fundamentals

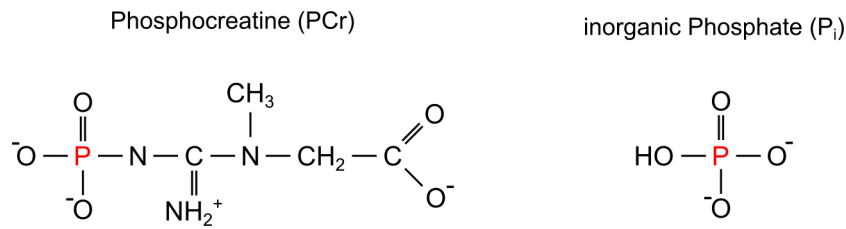


Figure 2.6: Chemical structures of phosphocreatine (PCr) and inorganic phosphate (P_i) in its form HPO₄²⁻.

of the acid is known.

pH gradient in vivo

In living tissue, the pH value plays a key role in cellular metabolism and is linked with the regulation of physiological processes. Under physiological conditions, the pH value inside the cell (intracellular pH) is around $\text{pH}_i = 7.0 - 7.2$, whereas the pH value in the extracellular space (extracellular pH) is around $\text{pH}_e = 7.3 - 7.6$ [37, 40]. In some diseases, pH_i and/or pH_e are altered. In cancer, the pH gradient of intra- and extracellular space is known to be reversed, i.e. pH_i is increased, whereas pH_e is decreased [40–44].

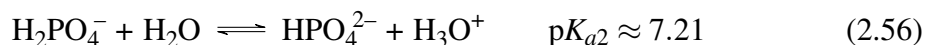
2.4.2 Main phosphorus compounds in this work

Phosphorus compounds are of interest for biomedical research, because they are associated with key roles in the energy metabolism.

Phosphocreatine (PCr) is the phosphorylated form of creatine (Cr) and can function as buffer for the universal energy carrier adenosine-5'-triphosphate (ATP) (see below). With the help of the enzyme creatine kinase (CK), the phosphate group of PCr can be transferred to adenosine-5'-diphosphate (ADP), in order to generate ATP, which can then be utilized again.

When free energy is needed, it can be provided by the hydrolysis of ATP to ADP + P_i.

The **inorganic phosphate (P_i)** formed by the dissociation of phosphate groups, plays an important role in the cell, due to its function as a buffer in the physiological range. In aqueous solution, phosphate ions are present in different forms dependent on the pH value of the solution. There are three equilibrium reactions:



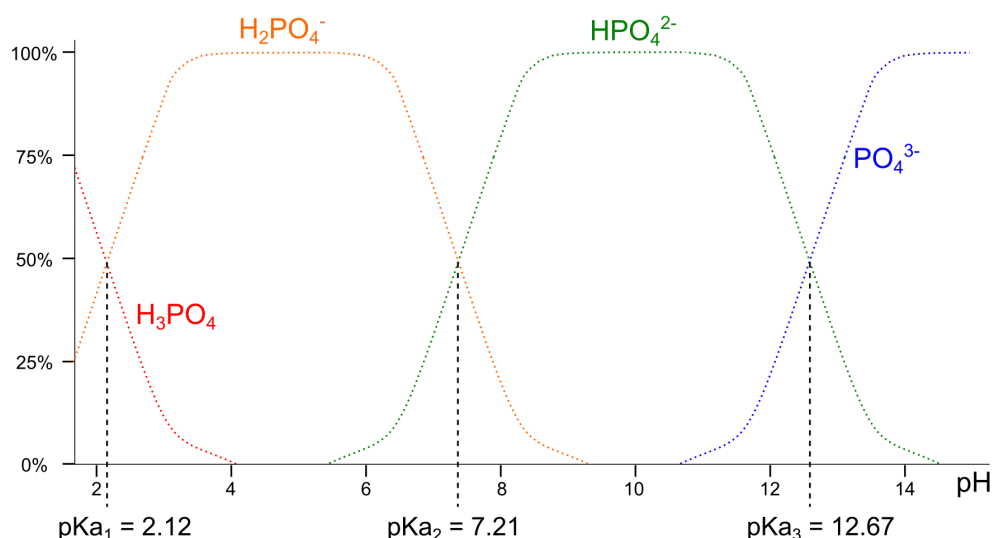


Figure 2.7: Schematic diagram of the dissociation of phosphoric acid, which is present in three different forms dependent on the pH value. In the physiological relevant range around pH 7, the two species H_2PO_4^- and HPO_4^{2-} are present. At $\text{pH} = \text{p}K_{a2} = 7.21$, the proportion of the two species is the same. The $\text{p}K_a$ values are taken from [38].

The $\text{p}K_a$ values are given for the temperature of 25°C and are taken from [38].

In the physiological range, only the species H_2PO_4^- and HPO_4^{2-} are present (cf. Figure 2.7), hence the equilibrium reaction (2.56) is relevant. Dependent on the pH value of the solution, the proportions of these two species change (Figure 2.7), enabling the determination of pH value by means of ^{31}P MRS (see section 2.5.1).

As already mentioned above, **adenosine-5'-triphosphate** (ATP) is the universal energy carrier in biological systems. In vivo, ATP is mainly present in its biologically active form, where it is complexed with a magnesium ion, i.e. $[\text{Mg}(\text{ATP})]^{4-}$. The two possible conformations of MgATP complexes are shown in Figure 2.8B. The change of the electron configuration due to the complex-formation leads to changes of the observed chemical shift and of the J-coupling constant of the ATP resonances.

2.4.3 Intra- and extracellular concentrations of ions in vivo

Besides being required for ATP to be biological active, the magnesium cation Mg^{2+} has numerous other regulatory functions in living tissue, e.g. in enzymatic reactions and in the stabilisation of DNA and RNA. Therefore, it is of interest in biomedical research. The intracellular concentration of free magnesium ions $[\text{Mg}_{\text{free}}^{2+}]$ is reported to be altered in numerous pathologies, e.g. diabetes and Alzheimer's disease [14, 19]. Moreover, it is

2 Fundamentals

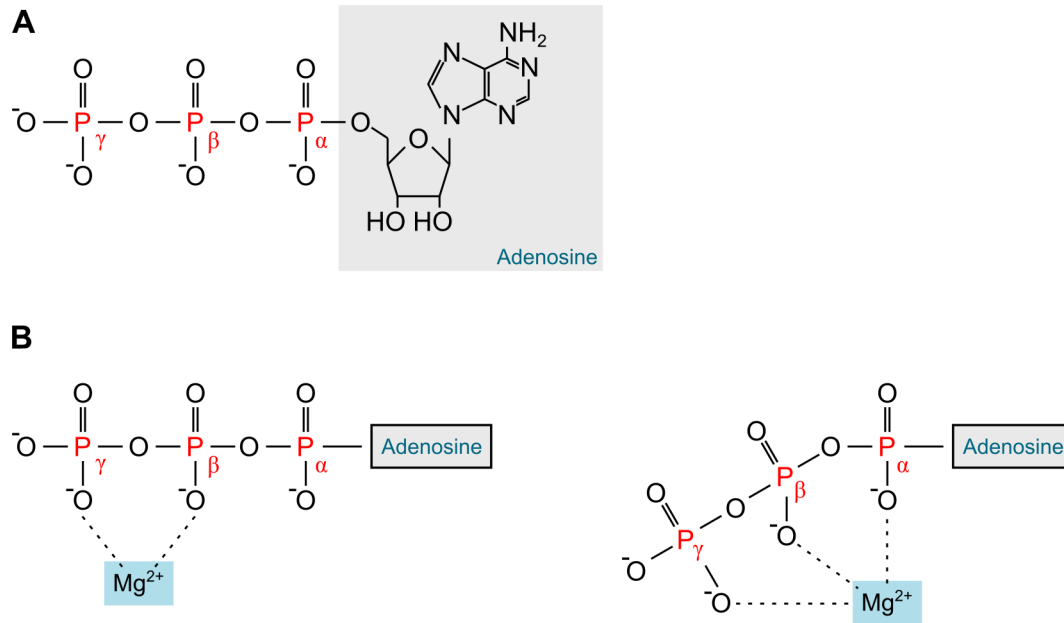


Figure 2.8: (A) Chemical structures of adenosine-5'-triphosphate (ATP) and (B) the two possible forms of the Mg-ATP complex $[Mg(ATP)]^{4-}$.

also object of research in other diseases, e.g. migraine, Duchenne muscular dystrophy and cancer [11, 15, 45].

Also the concentration of other ions, e.g. sodium (Na^{2+}) and potassium (K^{+}) are of interest in the research on different diseases, where the gradient of sodium and potassium concentration from intra- to extracellular space is altered [46]. In the following table, typical concentrations of Mg^{2+} , Na^{2+} and K^{+} are given for the extra- and intracellular space. Additionally, also the concentration of calcium (Ca^{2+}) and chloride (Cl^{-}) are given, because they may also be of relevance.

Table 2.1: Intra- and extracellular concentration of most abundant ions in vivo. The values are taken from [37] and are rounded.

ion	intracellular [mM]	extracellular [mM]
Mg ²⁺	15*	1
Na ²⁺	15	143
K ⁺	140	4
Ca ²⁺	$1 \cdot 10^{-4}$	1
Cl ⁻	8	115

*Reported to be 30mM in [47]

2.5 Phosphorus (^{31}P) MRS

Compared to hydrogen, phosphorus (^{31}P) has a 2.47-fold lower gyromagnetic ratio ($\gamma_{\text{H}} = 42.6 \text{ MHz T}^{-1}$ vs. $\gamma_{^{31}\text{P}} = 17.25 \text{ MHz T}^{-1}$), resulting in a lower SNR. However, it has a 100% natural abundance and a relatively large chemical shift dispersion in vivo ($\approx 30 \text{ ppm}$), leading to a high spectral resolution even at clinical magnetic field strengths. ^{31}P MRS is a powerful tool due to its capability to detect metabolites playing key roles in the energy metabolism (cf. section 2.4.2). Furthermore, physiological parameters such as intracellular pH and intracellular concentration of free magnesium ions $[\text{Mg}_{\text{free}}^{2+}]$ can be indirectly assessed. A representative ^{31}P MR spectrum acquired of the human calf muscle of a healthy volunteer is shown in Figure 2.3.

2.5.1 Determination of intracellular pH

As already mentioned in section 2.4.2, the pH value can be assessed by ^{31}P MRS due to the fact, that the proportion of the two present phosphate species, i.e. H_2PO_4^- and HPO_4^{2-} , changes depending on the pH value of the surrounding tissue. For the relevant equilibrium reaction (equation (2.56)), fast exchange can be assumed (see section 2.2.3), meaning that the observed chemical shift δ_{obs} of P_i is given as the mean of δ_{A} and δ_{HA} weighted by the relative populations of H_2PO_4^- and HPO_4^{2-} (see Figure 2.9).

The reason for the higher resonance frequency of HPO_4^{2-} can be explained by considering the chemical structures of HPO_4^{2-} and H_2PO_4^- (Figure 2.10). For HPO_4^{2-} , the oxygen atom at position 3 is present in its unprotonated form, leading to a longer P–O bond. Due to this difference in bond length, the electronic shielding of the ^{31}P atom is decreased for HPO_4^{2-} , and thus its resonance frequency is increased (cf. Figure 2.9).

In order to calculate the pH value by means of ^{31}P MRS, the Henderson Hasselbalch equation (equation (2.54)) can be adapted for the equilibrium reaction of phosphoric acid which is relevant for the physiological pH range (equation (2.56)):

$$\text{pH} = \text{p}K_a + \log \frac{[\text{H}_2\text{PO}_4^-]}{[\text{HPO}_4^{2-}]}, \quad (2.58)$$

with

$$\text{p}K_a = \frac{[\text{H}_3\text{O}^+][\text{H}_2\text{PO}_4^-]}{[\text{HPO}_4^{2-}]}. \quad (2.59)$$

The ratio $\frac{[\text{H}_2\text{PO}_4^-]}{[\text{HPO}_4^{2-}]}$ in equation (2.58) can be rewritten in terms of chemical shift ratios. Starting from the general assumption, that the observed chemical shift δ_{obs} of P_i is given

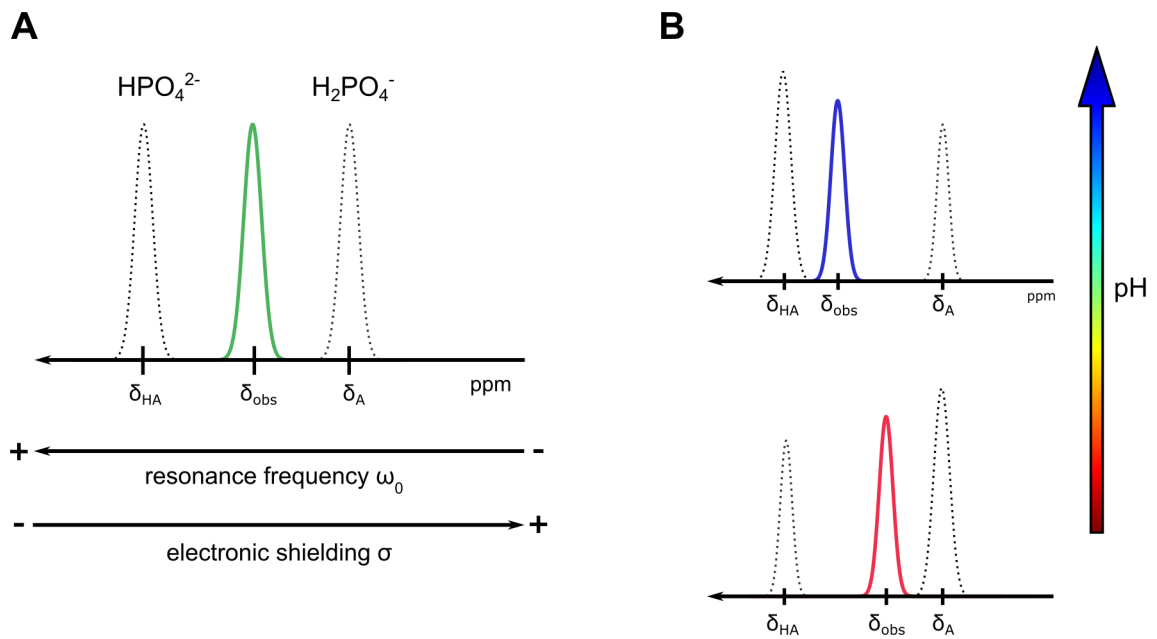


Figure 2.9: Schematic representation of the chemical shift changes of inorganic phosphate (P_i) due to a change in the pH value. (A) In the fast exchange regime, one resonance signal is observed for P_i , i.e. δ_{obs} , with the weighted average frequency of the protonated species H_2PO_4^- with the chemical shift δ_{HA} and the unprotonated species HPO_4^{2-} with the chemical shift δ_A . The resonance frequency is higher for HPO_4^{2-} than for H_2PO_4^- , because the electronic shielding is decreased. (B) Depending on the pH value of the solution, the proportion of protonated and unprotonated species changes, resulting in a down- or up-field shift of δ_{obs} .

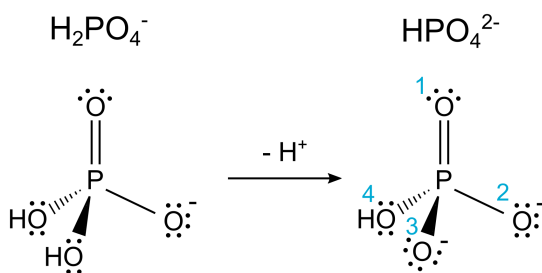


Figure 2.10: Chemical structures of the two phosphate species relevant in the physiological pH range, i.e. H_2PO_4^- (left) and HPO_4^{2-} (right). For HPO_4^{2-} , the oxygen at position 3 is present in its unprotonated form. This leads to a longer P-O bond than for H_2PO_4^- . Due to this difference in bond length, the electronic shielding of the ^{31}P atom is decreased for HPO_4^{2-} , and thus its resonance frequency increased (cf. Figure 2.9).

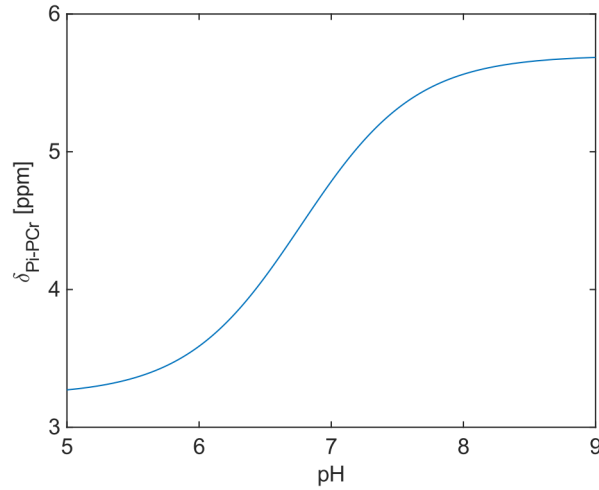


Figure 2.11: Visualization of the modified Henderson Hasselbalch equation (equation (2.64)) for $pK_a = 6.77$, $\delta_{HA} = 3.23$ ppm and $\delta_A = 5.7$ ppm. This calibration curve is used to translate the measured chemical shift of P_i relative to PCr (δ_{P_i-PCr}) to the underlying intracellular pH value.

as the weighted mean of the two chemical shifts of the protonated and unprotonated species, i.e. δ_{HA} and δ_A (see section 2.2.3, equation (2.40)):

$$\delta_{obs} = p_A \cdot \delta_A + p_{HA} \cdot \delta_{HA} \quad (2.60)$$

with

$$p_A = \frac{[H_2PO_4^-]}{[HPO_4^{2-}] + [H_2PO_4^-]} \quad (2.61)$$

$$p_{HA} = \frac{[HPO_4^{2-}]}{[HPO_4^{2-}] + [H_2PO_4^-]}, \quad (2.62)$$

it follows that

$$\frac{[H_2PO_4^-]}{[HPO_4^{2-}]} = \frac{\delta_{obs} - \delta_{HA}}{\delta_A - \delta_{obs}}, \quad (2.63)$$

which leads to a **modified Henderson Hasselbalch equation** of the following form:

$$pH = pK_a + \log \frac{\delta_{obs} - \delta_{HA}}{\delta_A - \delta_{obs}}. \quad (2.64)$$

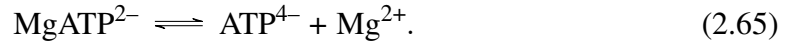
This relation is used to translate the observed chemical shift of P_i to the pH value of the solution and was first reported by Moon and Richards in 1973 [20]. As commonly done in ^{31}P MRS, the chemical shifts are given relative to the chemical shift of PCr. The

relation $\delta_{P_i-PCr}(pH)$ is visualized in Figure 2.11. The buffer system phosphoric acid is very suitable for the pH determination in vivo, as the gradient $\frac{\Delta\delta_{P_i}}{\Delta pH}$ is (i) approximately linear in the physiological range around pH 7, and (ii) large enough to yield a measurable change of δ_{P_i} for small changes in pH (≈ 0.13 ppm per 0.1 pH units).

Whenever the modified Henderson Hasselbalch equation is used in this work, the values reported in the standard NMR spectroscopy book by Robin de Graaff [31] will be used: $pK_a = 6.77$, $\delta_{HA} = 3.23$ ppm and $\delta_A = 5.7$ ppm.

2.5.2 Determination of intracellular magnesium ion concentration

Due to the fact, that ATP is mostly present in its biologically active form. i.e. complexed to a magnesium ion, it is possible to indirectly determine the concentration of free magnesium ions in a solution through the chemical shifts of ATP. Similar to the considerations of the two phosphate species being in chemical exchange (see section 2.5.1) enabling the determination of pH value based on the chemical shift of P_i , the determination of the magnesium ion concentration by means of ^{31}P MRS can be explained. To this end, the following reaction is considered:



Depending on the ratio of the two species, i.e. free $[\text{ATP}^{4-}]$ and the complex $[\text{Mg}(\text{ATP})^{4-}]$, the observed chemical shift δ_{obs} will be shifted further towards δ_{ATP} or δ_{MgATP} :

$$\delta_{obs} = p_{\text{ATP}} \cdot \delta_{\text{ATP}} + p_{\text{MgATP}} \cdot \delta_{\text{MgATP}}. \quad (2.66)$$

By using the definition of the dissociation constant K_D for this reaction:

$$K_D = \frac{[\text{Mg}^{2+}] [\text{ATP}^{4-}]}{[\text{MgATP}^{2-}]}, \quad (2.67)$$

equation (2.66) can be rearranged as follows:

$$[\text{Mg}^{2+}] = K_D \cdot \frac{\delta_{obs} - \delta_{\text{ATP}}}{\delta_{\text{MgATP}} - \delta_{obs}}. \quad (2.68)$$

Due to the strong dependency of the β -ATP chemical shift on the magnesium concentration, conventionally, δ_β is used as δ_{obs} in equation (2.68). More specifically, as first done by Gupta et al. in 1978 [21], the chemical shift of β -ATP relative to the chemical shift of

2 Fundamentals

α -ATP, i.e. as $\delta_{\alpha\beta}$. is used.

Following this rather simple approach, numerous other approaches for the determination of $[\text{Mg}^{2+}]$ were proposed, either by extending the approach from Gupta et al., or by proposing differently developed ones. For example, London et al. [26] considered not only the complexation of free magnesium with free ATP (equation (2.65)), but also the protonation of ATP and MgATP, introducing two additional dissociation constants:

$$K_H = \frac{[\text{H}^+][\text{ATP}^{4-}]}{[\text{ATPH}^{3-}]} \quad (2.69)$$

$$K_{D'} = \frac{[\text{Mg}^{2+}][\text{ATPH}^{3-}]}{[\text{MgATPH}^-]} \quad (2.70)$$

Thus, four different species are considered in equation (2.66), yielding

$$[\text{Mg}^{2+}] = K_D \cdot \frac{\delta_{\text{obs}}(1 + 10^{pK-pH}) - \delta_1 - \delta_2 \cdot 10^{pK-pH}}{\delta_3 + \delta_4 \left(\frac{K_D}{K_{D'}}\right) 10^{pK-pH} - \delta_{\text{obs}}(1 + \left(\frac{K_D}{K_{D'}}\right) 10^{pK-pH})}. \quad (2.71)$$

Hereby, the expression for pH (equation (2.50)), and the expression for pK_a (equation (2.53)) now adapted for the protonation of ATP, i.e. $pK_a^{\text{ATP}} = \frac{[\text{H}_3\text{O}^+][\text{ATP}^{4-}]}{[\text{ATPH}^{3-}]}$ are used to replace $[\text{H}^+]$ and K_D . Hence, pK in equation (2.71) is the pK_a value of ATP. For the detailed derivation of equation (2.71), it is referred to [26].

A further developed approach is given by Golding and Golding [27], who considered another additional equilibrium, i.e. $\text{ATPMg}^{2-} + \text{Mg}^{2+} \rightleftharpoons \text{Mg}_2\text{ATP}$, with the dissociation constant

$$K_{2D} = \frac{[\text{Mg}^{2+}][\text{MgATP}^{2-}]}{[\text{Mg}_2\text{ATP}]}, \quad (2.72)$$

leading to a rather long expression for $[\text{Mg}^{2+}]$. Barker et al. [48] applied the formula from Golding and Golding for ^{31}P MRSI measurements in the human brain, and presented the formula in the following form:

$$[\text{Mg}^{2+}] = -0.5 \cdot K_{2D} \cdot \frac{\delta_3 - \delta_{\text{obs}} + \beta \cdot (\delta_4 - \delta_{\text{obs}}) + \sqrt{t}}{\delta_5 - \delta_{\text{obs}}}, \quad (2.73)$$

where

$$\beta = 10^{-pH} \cdot \frac{K_D \cdot K_{1D}}{K_H} \quad (2.74)$$

$$t = (\delta_{\text{obs}} - \delta_3 + \beta \cdot (\delta_{\text{obs}} - \delta_4))^2 + \left(4 \frac{K_D}{K_{2D}} \cdot (\delta_5 - \delta_{\text{obs}})\right) + \left(10^{-pH} \cdot \frac{\delta_{\text{obs}} - \delta_2}{K_H} + \delta_{\text{obs}} - \delta_1\right). \quad (2.75)$$

In this representation $K_{1D} = K_{D'}$ (like in equation (2.70)). δ_i with $i \in [1;5]$ are the chemical shifts of the 5 different ATP species considered in this approach:

- ATP: $\delta_1 = 10.60$ ppm
- ATPH: $\delta_2 = 11.66$ ppm and $K_H = 0.34$ μM
- MgATP: $\delta_3 = 8.16$ ppm and $K_D = 90$ μM
- MgATPH: $\delta_4 = 8.52$ ppm and $K_{1D} = 720$ μM
- Mg₂ATP: $\delta_5 = 9.25$ ppm and $K_{2D} = 0.2$ M

3 Functions for modelling the ATP chemical shifts in dependence on the magnesium ion concentration

In order to implement the look-up algorithm of this work, an interpolation of the value space is necessary, because only a limited number of data points i.e. MR spectra from model solutions prepared with different chemical conditions, can be acquired. Based on literature [21, 23, 27] and results of initial experiments of this work, it is known, that in the herein investigated value range, the change of the ATP chemical shifts is non-linear with varying magnesium ion concentration. Based on this knowledge, the dependency $\delta(Mg)$ will be the starting point for the development of the final multi-dimensional models, i.e. $\delta(Mg, pH, K)$, whereby Mg shortly denotes the magnesium ion concentration and K denotes the potassium ion concentration $[K^+]$.

For the interpolation of $\delta(Mg)$, three different model functions will be applied and compared. These model functions will be introduced in this section. First, a heuristically developed function based on initial experimental results will be presented. Second, the formula given by London et al. for the calculation of the free magnesium ion concentration will be rearranged and adapted to develop a suitable model. And third, a function will be derived, which is based on the Hill equation used in chemistry.

3.1 Model with heuristic ansatz

An heuristic ansatz was developed to describe the dependence of the measured ATP chemical shifts on the relative magnesium ion concentration, denoted as $R = \frac{[Mg_{tot}]}{[ATP_{tot}]}$. The measured chemical shifts $\delta(R)$ appear to follow a sigmoidal course (cf. Figure 5.18 in section 5.2). Therefore, the following parameterized sigmoid function is assumed:

$$\delta^{Heur}(R) = A \cdot \frac{1}{1 + e^{-d \cdot R}} + C, \quad (3.1)$$

where A describes the amplitude of the chemical shift, d the strength of the bend, and C being the chemical shift offset (lower limiting chemical shift).

3.2 Model based on the London equation

The expression for the calculation of the free magnesium ion concentration proposed by London et al. [26] (introduced in section 2.5.2), considers the influence of the pH value on the ATP limiting chemical shifts. The expression given in [26] (equation 2.71) can be rearranged as follows:

$$\delta_{\text{obs}} \left([\text{Mg}^{2+}], pH \right) = \frac{\delta_1 + \delta_2 \cdot 10^{pK-pH} + \frac{[\text{Mg}^{2+}]}{K_D} \cdot (\delta_3 + \delta_4 \cdot \frac{K_D}{K_{D'}} \cdot 10^{pK-pH})}{1 + 10^{pK-pH} + \frac{[\text{Mg}^{2+}]}{K_D} \cdot (1 + \frac{K_D}{K_{D'}} \cdot 10^{pK-pH})}. \quad (3.2)$$

In the experiments of this work, the concentration of the free magnesium ions $[\text{Mg}^{2+}]$ is not known a priori and needs to be replaced by an expression including only the total magnesium and the total ATP concentration, which are known. All expressions used for the derivation of the equation given by London et al. (equation 2.71, see section 2.5.2, equations (2.67), (2.69), (2.70)), and the following expressions for the total magnesium and total ATP concentration, shortly denoted as Mg_{tot} and ATP_{tot} :

$$\text{Mg}_{\text{tot}} = [\text{Mg}^{2+}] + [\text{MgATP}^{2-}] \quad (3.3)$$

$$\text{ATP}_{\text{tot}} = [\text{ATP}^{4-}] + [\text{MgATP}^{2-}], \quad (3.4)$$

yield a system of non-linear equations which cannot be solved analytically. Hence, $[\text{Mg}^{2+}]$ cannot be easily replaced by an expression including only Mg_{tot} and ATP_{tot} .

To obtain an approximated solution, the fraction $\frac{[\text{Mg}^{2+}]}{K_D}$ will be replaced by the oversimplification

$$\frac{[\text{Mg}^{2+}]}{K_D} \approx f_1 \cdot \frac{\text{Mg}_{\text{tot}}}{\text{ATP}_{\text{tot}}} = f_1 \cdot R, \quad (3.5)$$

which expresses the ratio $\frac{[\text{Mg}^{2+}]}{K_D}$ as a specific proportion f_1 of the total relative magnesium ion concentration R . Note, that f_1 does change depending on the total magnesium concentration. Hence it has to be kept in mind, that the model developed based on the London equation with a constant value for f_1 is an oversimplification describing the relation $\delta(R)$ not correctly for all magnesium concentrations. In the following, the ratio $\frac{K_D}{K_{D'}}$ will be denoted as f_2 , yielding the following expression for $\delta^{\text{London}}(R, pH)$:

$$\delta^{\text{London}}(R, pH) = \frac{\delta_1 + \delta_2 \cdot 10^{pK-pH} + f_1 \cdot R \cdot (\delta_3 + \delta_4 \cdot f_2 \cdot 10^{pK-pH})}{1 + 10^{pK-pH} + f_1 \cdot R \cdot (1 + f_2 \cdot 10^{pK-pH})}. \quad (3.6)$$

3.3 Model based on the Hill equation

In section 2.5.1, the modified Henderson Hasselbalch equation was introduced as the standard calibration equation for the determination of pH by means of ^{31}P MRS. An equation, which is more general than the modified Henderson Hasselbalch equation, was used in the work of Pettegrew et al. [23]. The model function to describe the dependency of the chemical shift δ_{obs} on the pH value, used in [23], has the following general form:

$$\delta_{\text{obs}} = \frac{\delta_{\text{HA}} \cdot [\text{H}^+]^n + \delta_{\text{A}} \cdot (K_{\text{A}})^n}{[\text{H}^+]^n + (K_{\text{A}})^n}. \quad (3.7)$$

Here, n is the so-called Hill coefficient describing the cooperativity of the underlying binding. Equation (3.7) is a modified form of the Hill equation, which is used in chemistry to describe the binding of a ligand to a receptor. A more detailed description and the derivation of these modified form of the Hill equation can be found in Appendix A.

For the case of $n = 1$, equation (3.7) can be easily rearranged to yield the modified Henderson Hasselbalch equation in the well-known form of equation (2.64). For the gold-standard method to determine pH (using the chemical shift of P_i), it was shown in experiments, that $n \approx 1$ [23].

For other binding reactions however, e.g. (i) the protonation of ATP, or (ii) the binding of magnesium ions to ATP (see section 2.5.2), the assumption $n = 1$ might be invalid. This is supported by results from experiments of Pettegrew et al. [23], where the Hill coefficients for the titration curves $\delta(\text{pH})$ for the three resonances of ATP were determined. The determined Hill coefficients n showed a strong dependence on the chemical conditions, i.e. Mg_{tot} , and were found to be in the range between $n \approx (0.6 - 1.2)$. Although the investigations from Pettegrew et al. addressed only the influence of the pH value, it can be assumed that also the Hill coefficients for the binding of magnesium ions to ATP might be different from 1. This is further supported by assumptions in the work from Golding and Golding [27], where also double-binding reactions (cf. equation (2.72)) are considered, which would result in a Hill coefficient $n \neq 1$.

By drawing an analogy between the protonation of HPO_4^- (equation (2.58)) and the complexation of magnesium ions to ATP molecules (equation (2.65)), the general expression given by equation (3.7) can be used as follows:

$$\delta_{\text{obs}}^{\text{ATP}} = \frac{\delta_{\text{MgATP}} \cdot [\text{Mg}^{2+}]^n + \delta_{\text{ATP}} \cdot (K_{\text{D}})^n}{[\text{Mg}^{2+}]^n + (K_{\text{D}})^n} = \frac{\delta_{\text{MgATP}} \cdot [\text{MgATP}^{2-}]^n + \delta_{\text{ATP}} \cdot [\text{ATP}^{4-}]^n}{[\text{MgATP}^{2-}]^n + [\text{ATP}^{4-}]^n}, \quad (3.8)$$

3 Functions for modelling the ATP chemical shifts in dependence on the magnesium ion concentration

whereby the expression for K_D (equation (2.67)) was used. By using the expressions for the total magnesium and total ATP concentration (equations (3.3) and (3.4)) and for the dissociation constant (equation (2.67)), the expression for the observed chemical shift of ATP, can be rewritten in a way, that only the known variables Mg_{tot} and ATP_{tot} , as well as the dissociation constant K_D occur in the equation. The unknown concentrations $[MgATP^{2-}]$ and $[ATP^{4-}]$ will be eliminated. To improve readability of the function $\delta(Mg_{tot})$, the following auxiliary variables will be used:

$$p = K_D + Mg_{tot} - ATP_{tot} \quad (3.9)$$

$$q = -K_D \cdot ATP_{tot}. \quad (3.10)$$

With these variables, the following expressions result for $[ATP^{4-}]$ and $[MgATP^{2-}]$:

$$[ATP^{4-}] = -\frac{p}{2} \pm \sqrt{\left(\frac{p}{2}\right)^2 - q} := A_{\pm} \quad (3.11)$$

$$[MgATP^{2-}] = Mg_{tot} \cdot \frac{A_{\pm}}{A_{\pm} + K_D} \quad (3.12)$$

The expressions (3.11) and (3.12) can be inserted in equation (3.8) to yield $\delta(Mg_{tot})$. Because there are two expressions for $[ATP^{4-}]$ (equation (3.11)) with different signs, there are also two solutions for $\delta(Mg_{tot})$. Analysis of the expressions for the concentrations of ATP and MgATP (equations (3.11) and (3.12)) shows that keeping the solution with negative sign can result in value ranges for the concentration of MgATP that are negative, which is unphysical. Hence, the solution with negative sign is discarded, and only the solution with positive sign used:

$$\delta^{Hill}(Mg_{tot}) = \frac{\delta_{MgATP} \cdot \left(Mg_{tot} \cdot \frac{A_{+}}{A_{+} + K_D}\right)^n + \delta_{ATP} \cdot (A_{+})^n}{\left(Mg_{tot} \cdot \frac{A_{+}}{A_{+} + K_D}\right)^n + (A_{+})^n}. \quad (3.13)$$

4 Materials and Methods

4.1 MR imaging systems

All measurements were conducted on MR systems at the German Cancer Research Center (DKFZ) in Heidelberg. The in vivo measurements of healthy volunteers and patients were performed on the whole-body 7-T MR scanner (MAGNETOM, Siemens Healthineers, Erlangen, Germany). The measurements on model solutions were performed on the 9.4-T small animal PET-MR scanner (BioSpec 94/20 USR, Bruker Biospin MRI GmbH, Ettlingen, Germany).

4.1.1 7-T whole-body MR system

The 7-T MR scanner has a static magnetic field strength of $B_0 \approx 6.98\text{ T}$ and is equipped with an additional coil system for B_0 homogenization (*shimming*) (Figure 4.1A). The high-frequency broadband system allows for measuring the MR signal of different nuclei (e.g. $f_{31\text{P}} = 120.29\text{ MHz}$ or $f_{1\text{H}} = 297.15\text{ MHz}$).

For the measurements of the lower leg muscles of healthy volunteers, a double-resonant ^{31}P - ^1H volume coil with birdcage design (Rapid Biomedical, Rimpar, Germany) was used (Figure 4.1B). The brain measurements of patients with glioblastoma were performed using the double-resonant ^{31}P - ^1H head coil (Rapid Biomedical, Rimpar, Germany) having 32 receiver channels for ^{31}P (Figure 4.1C).

4.1.2 9.4-T small animal PET-MR system

The 9.4-T small animal PET-MR scanner is designed for measurements of mice and rat, and has a static magnetic field strength of $B_0 \approx 9.403\text{ T}$, which is actively shielded (Figure 4.2A).

All measurements on the 9.4-T small animal scanner were conducted using a double-resonant ^{31}P - ^1H volume resonator with an inner diameter of 35 mm (Figure 4.2B) tuned to the resonance frequencies of ^{31}P and ^1H nuclei at 9.4T: $f_{31\text{P}} = 162.07\text{ MHz}$ and $f_{1\text{H}} = 400.35\text{ MHz}$. The small animal scanner enables temperature controlled measurements and is therefore equipped with a heating and temperature monitoring system. Distilled

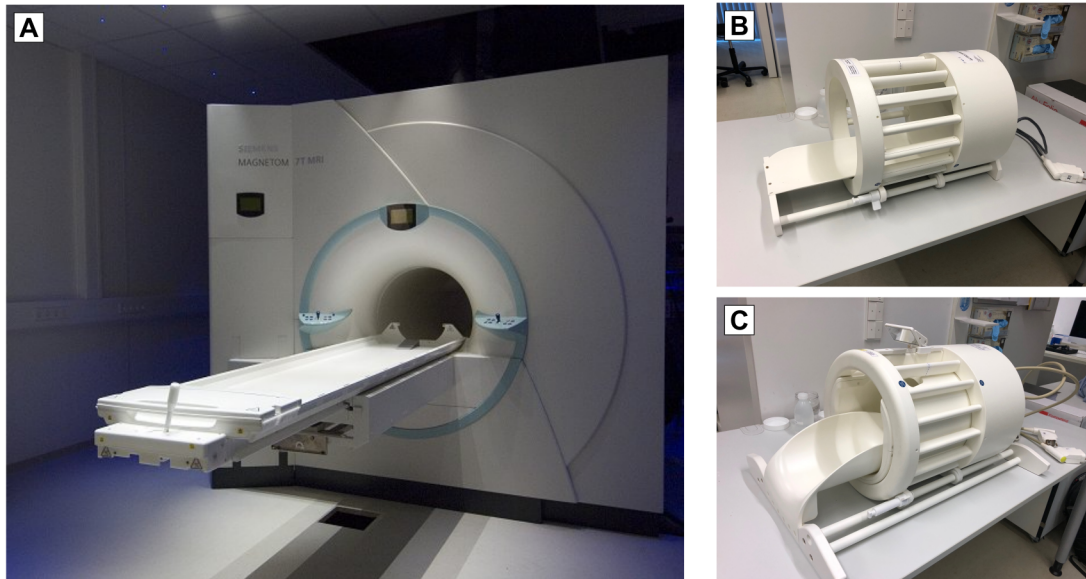


Figure 4.1: (A) The 7-T MR scanner (MAGNETOM 7T, Siemens Healthineers, Erlangen, Germany) at the German Cancer Research Center (DKFZ) on which the in vivo measurements of healthy volunteers and patients were conducted. The image is taken from [49]. (B) The double-resonant ^{31}P - ^1H volume coil with birdcage design used for the measurements of the lower leg, and (C) the double-resonant ^{31}P - ^1H head coil with 32 receiver channels for ^{31}P . Both coils are manufactured by Rapid Biomedical, Rimpar, Germany.

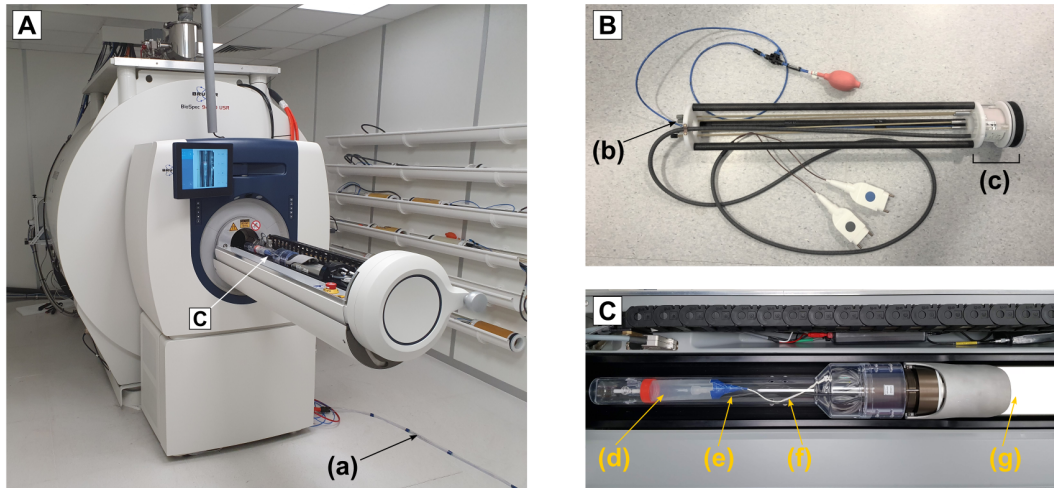


Figure 4.2: (A) The 9.4-T small animal PET-MR scanner (Biospec 94/20 USR, Bruker Biospin MRI GmbH, Ettlingen, Germany) at the German Cancer Research Center (DKFZ), on which the measurements on model solutions were conducted with the (B) double-resonant ^{31}P - ^1H volume resonator with an inner diameter of 35 mm. The RF coil (c) can be tuned and matched with the corresponding knobs (b). (C) The chamber of the small animal bed can be heated with warm air by the use of a heating system. Distilled water is heated and pumped via tubes into the scanner room (a) to the heat exchanger behind the small animal bed (g). The heated air from the heat exchanger is then streamed via a perforated tube (e) into the phantom chamber. The phantom tube (d) is additionally equipped with a thermometer (f) measuring the temperature of the water inside the outer tube. The pictures for Figures A and C were taken by Dr. Philip Boyd and Justyna Platek from the Division of Medical Physics in Radiology at the DKFZ.

water is heated in a water bath in the console room and pumped to a heat exchanger behind the small animal bed (Figure 4.2C). Compressed air is heated by streaming to the heat exchanger and afterwards warming the small animal bed via a perforated tube. With a thermometer attached to the small animal bed, the temperature can be tracked. By adjusting the temperature of the water bath and the pressure of the air stream, the temperature can be adjusted and stabilized during the measurement. In this work, all measurements on model solutions were performed at a temperature of $T \approx 37^\circ\text{C}$.

4.2 MR sequences

4.2.1 FID sequence

For the acquisition of ^{31}P spectra in model solutions, a simple excite-acquire FID sequence was used (Figure 4.3). All spectra from model solutions acquired in this work were obtained with the same measurement parameters. After an excitation with a sinc-shaped RF pulse with flip angle $\text{FA} = 45^\circ$, 2048 time points are acquired with a dwell time of $\Delta t = 0.1$ ms corresponding to a spectral bandwidth of $\text{BW} = 10\text{kHz}$. In total, 1024 signal averages are acquired resulting in a total acquisition time of 5 minutes and 7 seconds.

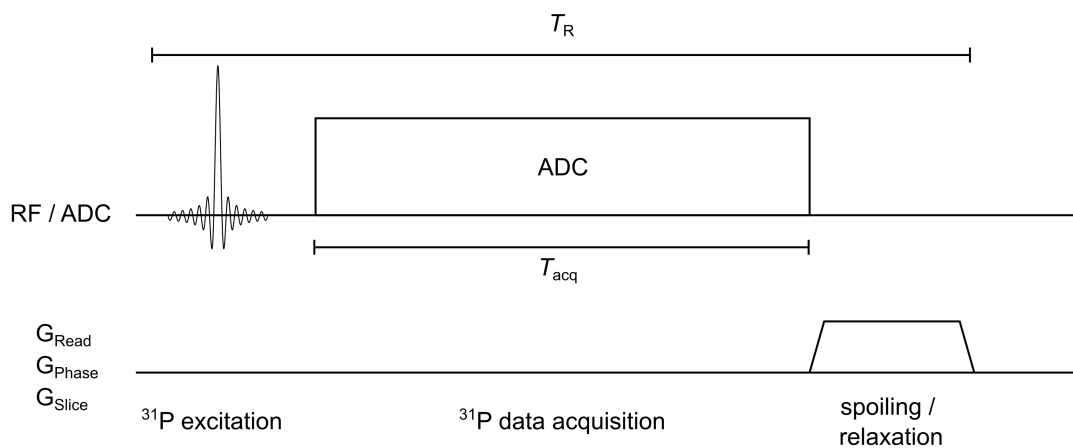


Figure 4.3: Schematic sequence diagram of a ^{31}P FID sequence for the unlocalized acquisition of ^{31}P MR spectra, comparable to the used sequence at the 9.4-T scanner. After a sinc-shaped excitation pulse, the data is acquired via an analog-to-digital converter (ADC) for the time T_{acq} . Prior to the next excitation, the residual transverse magnetization is destroyed with spoiler gradients. The time between two consecutive excitations is called repetition time T_{R} .

4.2.2 3D MRSI sequence

For the acquisition of spatially resolved ^{31}P spectra in the measurements of volunteers and patients, a 3D FID-MRSI sequence was used (Figure 4.4). In between excitation and data acquisition, the signal is spatially encoded in all three spatial dimensions by the use of phase encoding gradients (cf. section 2.3.1). The succession of excitation, spatial encoding with varying gradient strength and data acquisition is repeated $N_x \times N_y \times N_z$ times to acquire the complete k-space matrix. Consequently, the total acquisition time

for one average is

$$T_{\text{total}} = N_x \times N_y \times N_z \times T_R. \quad (4.1)$$

For an improvement of the SNR, usually, multiple averages are acquired, increasing the measurement time by the factor N_{Averages} .

In the used MRSI sequence, the k-space points are not acquired in a uniformly distributed manner, i.e. acquisition of the same number of averages at each point in k-space. The acquisition is performed following a Hamming-weighted sampling scheme, meaning that the k-space center is acquired with the highest number of averages, and the k-space points towards the edge with less averages, in the form of a Hamming filter. Therewith, the k-space center, which holds the information of the basic contrast, is weighted stronger than the k-space edges.

Additionally, in order to enhance the ^{31}P signal in each acquisition, a nuclear Overhauser effect (NOE) preparation can be applied prior to the ^{31}P excitation pulse. The NOE preparation consists of an adiabatic ^1H inversion pulse with succeeding spoiler gradients. The nuclear Overhauser effect was not explicitly introduced in the fundamentals, hence the reader is referred to Chapter 3 of [31] for a detailed explanation. The NOE preparation was applied for the measurements in the brain, but not in the lower leg muscle.

The parameters of the 3D MRSI sequence were different for the different applications (lower leg muscle / brain) and can be found in the corresponding sections describing the Measurement Protocols (section 4.4.2).

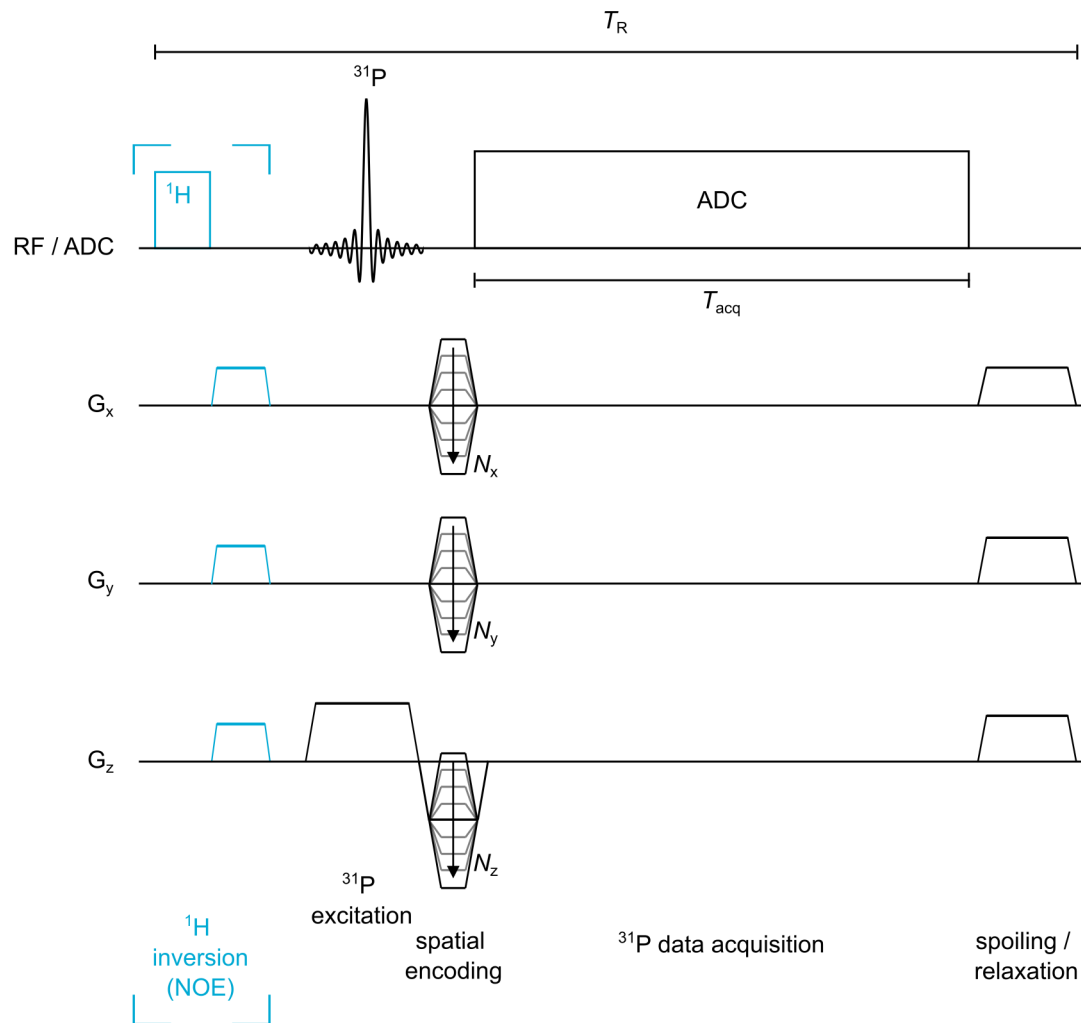


Figure 4.4: Sequence diagram of the used 3D ^{31}P FID-MRSI sequence for the acquisition of localized ^{31}P spectra. In between ^{31}P excitation and data acquisition, spatial encoding is realized with phase encoding gradients in all three dimensions (G_x , G_y , G_z). In order to enhance the ^{31}P signal, a nuclear Overhauser effect (NOE) preparation can be applied prior to ^{31}P excitation, which consists of an adiabatic ^1H inversion pulse with succeeding spoiler gradients. NOE enhancement was applied for the measurements in the brain of patients with glioblastoma, but not for the measurements in the lower leg muscles of healthy volunteers.

4.3 Preparation of model solutions

The characterization of the ^{31}P MR spectral properties was performed on suitable model solutions trying to mimic *in vivo* conditions. As the main focus of this work was the determination of the pH value and the magnesium ion concentration, the used model solutions contained only P_i and ATP, as the resonance signals of these metabolites are the most sensitive to changing pH and $[\text{Mg}^{2+}]$. As reference substance also PCr was added.

All sets of model solutions were prepared in a standardized way. All chemicals were solved in imidazole buffer which was prepared by using demineralized (VE) water. The final concentration of P_i , ATP and PCr was 5 mM in all solutions, for which sodium based salts were used. The standard preparation procedure was as follows:

1. Imidazole buffer solution (0.2M^1) was prepared with a pH value of approximately (8 – 9) (higher than the target pH values).
2. The P_i solution was prepared by solving disodium phosphate (Na_2HPO_4) and sodium dihydrogen phosphate (NaH_2PO_4) in a ratio of 3:1 in imidazole.
3. By solving disodium PCr ($\text{C}_4\text{H}_8\text{N}_3\text{O}_5\text{PNa}_2 \cdot x\text{H}_2\text{O}$) and disodium ATP ($\text{C}_{10}\text{H}_{14}\text{N}_5\text{O}_{13}\text{P}_3\text{Na}_2 \cdot x\text{H}_2\text{O}$) in imidazole and adding both to the P_i solution, the base solution for all model solutions was prepared.
4. Stock solutions for magnesium and potassium were prepared by solving MgCl and KCl in imidazole.
5. The base solution from step 3 was distributed in different tubes and the defined volumes of the magnesium and potassium stock solution were added, in order to achieve the respective target $[\text{K}^+]$ and $[\text{Mg}^{2+}]$.
6. This final solution was again distributed into different tubes for the pH titration. The target pH was titrated while the tubes were inside a water bath stabilizing the temperature of the solution at 37°C , using the pH-meter “Five Easy” (Mettler Toledo) with the electrode LF438 for pH measurement.

The pH titration was done in two steps. First, a coarse adjustment of the target pH value by using HCl with a concentration of 1 M was performed, and the volume of the solution was filled up with imidazole to a volume of 9.95 ml. Second, the pH was readjusted with only a small amount of 1 M HCl. The volume was then filled up with a small amount of

¹4.9 g imidazole + 360 ml VE water + 3 ml 0.1 M HCl

Table 4.1: Ion concentrations and target pH values of the six model solution sets used in this work. All concentrations are given in [mM]. All solutions contain 5 mM of PCr, P_i, and ATP. Note, that the exact titrated pH value of each model solution is slightly deviating from the target pH value listed here.

Set #	[Na ²⁺]	[K ⁺]	[Mg ²⁺]	pH
1	29	29	0, 1.25, 2.5, 3.75, 5, 10	6.8, 7.0, 7.2, 7.4
2	29	120	0, 1.25, 2.5, 3.75, 5, 10	6.8, 7.0, 7.2, 7.4
3	29	160	0, 1.25, 2.5, 3.75, 5, 10	6.8, 7.0, 7.2, 7.4
4	29	0, 50, 75, 100, 150, 200	0.625, 2.5	7.0, 7.4
5	29	0, 100, 200	0, 5, 10	6.8, 7.4
6*	96	29	0, 1.25, 2.5, 3.75, 5, 10	6.8, 7.0, 7.2, 7.4

*Not used for the model development

imidazole to the final volume of 10mM. The final pH value and the exact temperature of the solution were documented for later temperature correction of the pH value (see section 4.4.3). The final solutions were filled into 2 ml Eppendorf tubes and closed without entrapment of air bubbles.

With the described procedure, various sets of model solutions were prepared with different magnesium, potassium and sodium ion concentrations, and titrated to different pH values. The chemical composition of the six model solution sets, which are used in this work, can be found in Table 4.1. Typically one set consisted of 24 different model solutions (maximum number of model solutions, which could be prepared during one working day). The preparation was done by Renate Bangert from the Division of Medical Physics in Radiology at the DKFZ. The model solutions were measured within 24 hours after preparation.

Due to the use of sodium salts for the metabolites, the base concentration of sodium was 29 mM in all model solutions. In the solution set #6, 67 mM NaCl was added to achieve a

sodium concentration of $[\text{Na}^{2+}] = 96 \text{ mM}$. For the development of the multi-dimensional model $\delta(pH, Mg, K)$ (cf. section 5.3), solely datasets 1-5, i.e. a total number 114 model solutions, are used.²

²In the framework of this thesis, a total of 222 model solutions were prepared and measured, but not all of them are listed here, as they were prepared under slightly different conditions (particularly in the initial experiments). However, they were also used as test datasets for the sanity check of the algorithm (cf. Appendix D)

4.4 Experimental and Data Processing Protocols

4.4.1 General data processing steps

The reconstruction, post-processing, quantification and evaluation steps of all acquired datasets were performed in MATLAB (version 2020a, The MathWorks Inc., Natick, USA). For the reconstruction of the acquired raw data of both used MR systems, different algorithms customized for Siemens and Bruker raw data formats were used. The postprocessing, as well as the quantification steps were adapted to the respective application, i.e. in vivo measurements (muscle / brain) or model solutions.

For the quantification of all spectra, a home-built implementation of the AMARES algorithm [50] for MATLAB was used. A more detailed description of the implementation of this algorithm can be found in [9]. For all cases, the quantification protocol started with a *reference fit*, only quantifying the reference signal PCr modelled as singlet with Gaussian (in vivo data) or Lorentzian (model solution data) lineshape. The quantified phase of PCr was used for phase correction of zeroth order. Also the B_0 shifts were corrected by using the quantified frequency of PCr. The main fitting step quantifying the amplitudes, frequencies and linewidths of all contained metabolites was then performed on the phase- and B_0 -shift corrected spectra. As a quantity for quantification uncertainties, the Cramér-Rao lower bounds (CRLBs) were utilized throughout the study [51].

The fit models of this main step were different for each application and are described in the corresponding sections 4.4.2 and 4.4.3.

4.4.2 Measurements in vivo

All in vivo measurements were approved by the local ethics committee of the Medical Faculty of the University of Heidelberg. Written consent was received from all subjects. The measurements of healthy volunteers and of patients were both performed at the 7-T whole body MR scanner (section 4.1.1) using the 3D ^{31}P MRSI sequence described in section 4.2.2. The most important sequence parameters for both applications can be found in Table 4.2. Additionally to the ^{31}P MRSI, also 3D morphological ^1H images were acquired.

Measurements of the human lower leg muscle

The lower legs of three healthy volunteers were measured using the double-resonant ^{31}P - ^1H volume coil with birdcage design (Figure 4.1B in section 4.1.1). A detailed description of the complete measurement and processing protocol can be found in [52]. The

Table 4.2: Sequence parameters of the used 3D ^{31}P MRSI sequences for the in vivo measurements of the lower leg muscles of healthy volunteers and of the human brain of patients with glioblastoma. Δx denotes the voxel size.

Parameter	Lower leg muscle	Brain
Matrix size	$(24 \times 24 \times 16)$	$(20 \times 24 \times 16)$
Nominal Δx	$(8 \times 8 \times 16) \text{ mm}^3$	$(12.5 \times 12.5 \times 12.5) \text{ mm}^3$
T_R	240ms	250ms
FA	20°	20°
Spectral BW	5 kHz	5 kHz
Time points	1024	1024
Averages	16	18
T_{total}	56 min	52 min
NOE preparation	no	yes

most important sequence parameters are summarized in Table 4.2. After reconstruction of the raw data, the 3D datasets of all three volunteers were processed by one-fold spatial zero-filling resulting in an image size of $(48 \times 48 \times 32)$, and application of a 10-Hz Gaussian filter in the time domain. The quantification of spectra was performed voxelwise as described in section 4.4.1. In the B_0 -shift- and phase-corrected signals, the frequencies, linewidths and amplitudes of all visible metabolites, i.e. PCr, P_i , GPC, and the three resonances of ATP, were quantified. All of these metabolites were modelled as singlets with Gaussian lineshape.

Measurements of patients with glioblastoma

For the purpose of this work, 3D ^{31}P MRSI datasets from patients with glioblastoma were retrospectively analyzed. The patient measurements were conducted using the double-resonant ^{31}P - ^1H head-coil (Figure 4.1C in section 4.1.1). A summary of the sequence parameters are listed in Table 4.2. The complete measurement protocol can be found in [9].

In order to enhance the SNR of the ^{31}P MRSI datasets, a low-rank denoising approach was applied prior to the conventional postprocessing steps. For a detailed description of this low-rank denoising, as well as details about the coil combination of the 32 receiver channels, the reader is also referred to [9]. After low-rank denoising, the datasets were

4 Materials and Methods

further processed by one-fold spatial zero-filling resulting in a image size of $(40 \times 48 \times 32)$, and time domain filtering with a 15-Hz Gaussian filter. After B_0 -shift- and phase-correction of zeroth order, amplitudes, frequencies and linewidths of all observed ^{31}P metabolites were quantified following the fitting scheme described in [10]. The following metabolites were quantified: phosphoethanolamine (PE), phosphocholine (PC), intracellular inorganic phosphate (P_i), extracellular eP_i , glycerophosphoethanolamine (GPE), glycerophosphocholine (GPC), phosphocreatine (PCr), nicotinamide adenine dinucleotide (NAD), the three resonances of ATP, 2,3-Diphosphoglycerate (DPG), mobile phospholipids (MPL), and Uridine Diphosphoglucose (UDPG).

Calculation of pH and magnesium maps

For all datasets, i.e. from lower leg muscles and brain, 3D pH and magnesium maps were calculated. pH maps were generated by voxelwise calculation of the pH via the standard version of the modified Henderson-Hasselbalch equation (equation (2.64)) using the quantified chemical shift difference between P_i and PCr, i.e. $\delta_{\text{obs}} = \delta_{\text{P}_i-\text{PCr}}$. For the modified HHE, the parameters given in [31] are used (cf. 2.5.1).

For the calculation of the 3D maps showing the concentration of free magnesium ions $[\text{Mg}_{\text{free}}^{2+}]$, the equation given by Golding and Golding [27] for the chemical shift difference between the α - and β -resonance of ATP was used (equation (2.73) with $\delta_{\text{obs}} = \delta_{\alpha\beta}$). The pH value required in this formula was calculated as described above.

Region-of-interest analysis

In order to compare the calculated physiological values e.g. pH value and $[\text{Mg}_{\text{free}}^{2+}]$, from different regions in the measured volumes, 3D regions-of-interest (ROIs) were defined in the Medical Imaging Interaction Toolkit (MITK) [53] using the corresponding morphological ^1H images.

For the lower leg datasets, ROIs for three different muscle groups, i.e. *tibialis anterior* (TA), *soleus* (Sol), and *gastrocnemius medialis* (GM), were defined, which are representatively shown for volunteer 1 in Figure 4.5.

The ROIs in the datasets of patients with glioblastoma were defined by Nina Weckesser from the Division of Radiology at the DKFZ. In this work, only two different regions will be compared, i.e. the ROI covering the whole tumor volume (WHT), and a ROI covering white matter (WM) on the contralateral side. The ROI selection is representatively shown for patient 1 in Figure 4.6. Note, that the WM ROI is not visible in the presented slice.

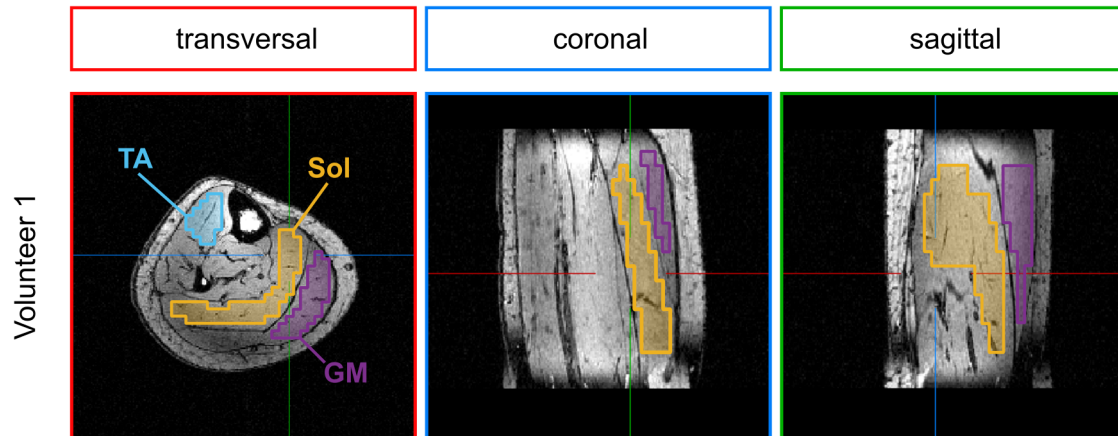


Figure 4.5: The definition of 3D regions-of-interest (ROIs) for the lower leg muscle datasets, representatively shown for volunteer 1. ROIs for the following three muscle groups were define: *tibialis anterior* (TA), *soleus* (Sol), *gastrocnemius medialis* (GM).

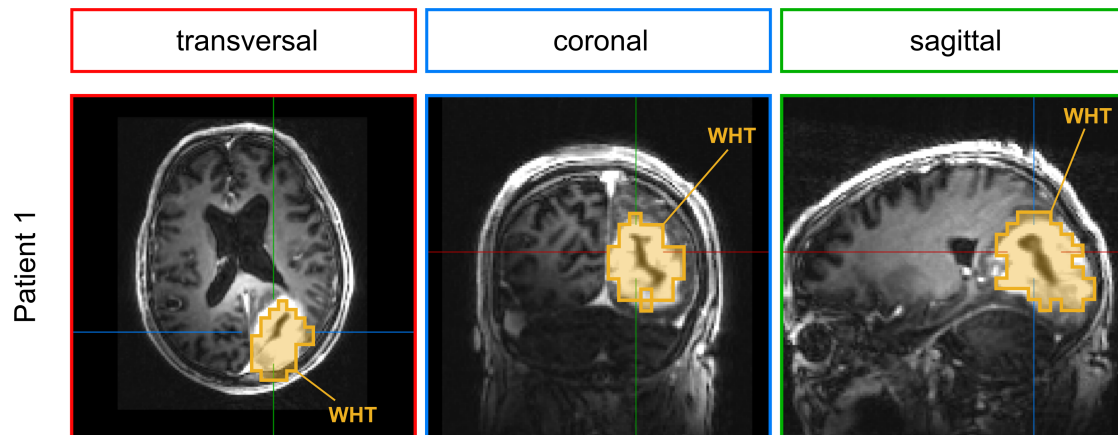


Figure 4.6: The definition of the ROI covering the whole tumor volume (WHT) representatively shown for patient 1. The defined ROI covering healthy white matter located on the contralateral side of the tumor lies in different slices than the tumor slices, and are hence not visible in this illustration. The ROIs in the datasets from all patients were defined by Nina Weckesser from the Division of Radiology at the DKFZ.

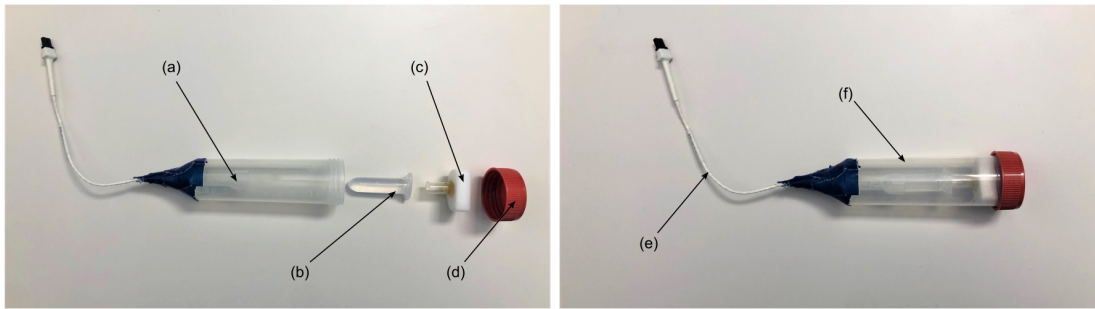


Figure 4.7: Self-built phantom-mount used for the measurements of model solutions. Into the conventional 50-ml tube, a mounting was glued to the bottom (a), which can hold a 2 ml Eppendorf tube filled with the model solution (b). The Eppendorf tube is additionally fixed in the center of the outer tube with the help of a bubble trap (c), to which also a mounting is glued, keeping the Eppendorf tube at a certain distance from the bubble trap. The outer tube can be closed with the conventional lid (d). The sensor of the thermometer (e) was inserted at the bottom of the outer tube, in order to measure the water temperature inside the tube. Prior to the measurement, the outer tube (f) is filled with pre-heated water in order to reach the required temperature of 37°C in the small Eppendorf tube more quickly.

4.4.3 Measurements on model solutions

Data acquisition

The ^{31}P spectra of model solutions were acquired at the 9.4-T small animal scanner using a FID sequence as described in section 4.2.1. For the measurement, the 2 ml Eppendorf tubes were placed into a self-built phantom-mount and fixed with a bubble trap (Figure 4.7). This self-built phantom-mount can be filled with water enabling a more robust B_0 homogenization (*shimming*) due to the reduced susceptibility changes at the edges of the Eppendorf tube. Additionally, a thermometer was built into the outer tube enabling the tracking of the water temperature inside the phantom mount during the MR measurements. In order to reach the required temperature of 37°C in the sample more quickly, the water filled into the outer falcon was pre-heated to a temperature of about 40°C. After placing the sample in the phantom-mount and filling with pre-heated water, the phantom-mount was put into the small animal bed and the thermometer connected to the control panel. The small animal bed was then moved into the iso-center of the magnet. After the standard adjustments of the MR scanner (i.e. tune and match, shimming) and stabilization of the temperature, the ^{31}P spectra were acquired. The temperature of the water surrounding the measured sample at the beginning and at the end of the FID acquisition was documented. The mean temperature during the individual measurements was $\bar{T} = (37.1 \pm 0.3)$.

The described procedure was repeated for all samples (typically 24 model solutions per subset, cf. Table 4.1). At the end, the raw data was exported for each acquired FID individually.

Data processing and evaluation

The raw data of each acquired FID was reconstructed individually. No additional filter or time-domain zero-filling was applied to the data. After zero-phase and B_0 -shift correction (as described earlier), the frequencies, amplitudes and linewidths of all contained metabolites, i.e. PCr, P_i , and the three resonances of ATP, were quantified in the main fitting step. Because the multiplet splitting of ATP is resolvable in the measurements of model solutions, the fit model includes now also the multiplet pattern of ATP using prior knowledge for the J-coupling constants. For a robust quantification, the main fitting step consisted of two consecutive fits:

1. All resonances were modelled as singlets with Lorentzian lineshape.
2. The quantified frequency of β -ATP from step 1 is used as prior knowledge for the frequency of the central peak of the β -ATP pseudo triplet in the second fit.

In the fit model of the second fit, the J-coupling constant was modelled with the starting value and boundaries $J = (18 \pm 3)\text{Hz}$, based on J-coupling constants typically observed [54–56]. For spectra of model solutions with an intermediate magnesium ion concentration, i.e. $0.25 \leq R \leq 0.75$, the quantification of the ATP resonances did not work reliably in all cases. When a resonance was not fitted reasonably after visual inspection, an additional fitting step with prior knowledge for the frequency, which was visually determined, was performed. At the end, the difference of fitted to acquired spectra was visually checked for significant residual signal.

Temperature correction

Although imidazole buffer solution was used for the model solutions, the pH value changes with different temperature, which was observed in initial experiments. An experiment was conducted to investigate the pH(T) dependence. To this end, imidazole buffer solution was prepared (cf. section 4.3), and heated in a water bath. Between $T = [33 - 39]^\circ\text{C}$, 39 pairs of (pH-T) were measured. Based on a linear fit to these datapoints, the correction factor $-0.04 \frac{\text{pH}}{^\circ\text{C}}$ was determined. During the data evaluation, the measured, titrated pH

4 Materials and Methods

value pH_{titr} was corrected as follows:

$$\text{pH}_{\text{cor}} = \text{pH}_{\text{titr}} - 0.04 \frac{\text{pH}}{^{\circ}\text{C}} \cdot (T_{\text{meas}} - T_{\text{titr}}), \quad (4.2)$$

where T_{meas} is the measured mean temperature of the model solution during the acquisition of the FID. The corrected pH value pH_{cor} is used in further evaluation steps.

4.5 Implementation of the look-up algorithm

The basic idea of the developed look-up approach is to use the information from multiple spectral properties obtained in a measured ^{31}P spectrum to deduce multiple parameters describing the underlying biochemical conditions of the investigated sample. As first proof-of-principle, an approach will be implemented for the determination of the parameters pH value, magnesium ion concentration $[\text{Mg}^{2+}]$ and potassium ion concentration $[\text{K}^+]$, by using the chemical shifts of the three resonances of ATP, i.e. δ_γ , δ_α and δ_β . In this implementation, the potassium ion concentration $[\text{K}^+]$ is used as a surrogate for the ionic strength in general. For better readability, the magnesium and potassium ion concentrations will be hereafter simply denoted as Mg and K .

As described earlier, the chemical shift of each ATP resonance is influenced by several biochemical parameters. Thus, there is no unique parameter set (pH, Mg, K) for one specific measured chemical shift δ_i^{meas} . However, one can make use of three different parameters, i.e. $(\delta_\gamma, \delta_\alpha, \delta_\beta)$, whose functional relation to (pH, Mg, K) is assumed to be known by the developed model functions $\delta_i^{\text{model}}(pH, Mg, K)$ with $i \in (\gamma, \alpha, \beta)$. The determination of the three unknown parameters (pH, Mg, K) by the combined use of the three measured parameters $(\delta_\gamma, \delta_\alpha, \delta_\beta)$ is assumed to be possible due to the fact, that each chemical shift changes to a different degree with varying (pH, Mg, K) . This varying degree of change of the γ -, α - and β chemical shifts will be assessed in detail in section 5.2.2 of the results.

4.5.1 Basic principle of the look-up algorithm

As already described above, the purpose of the look-up algorithm is the assignment of the three measured parameters $(\delta_\gamma, \delta_\alpha, \delta_\beta)$ to the unknown parameters (pH, Mg, K) . In principle, this assignment is given by the model functions $\delta_i^{\text{model}}(pH, Mg, K)$, $i \in (\gamma, \alpha, \beta)$. However, the non-linearity of $\delta_i^{\text{model}}(pH, Mg, K)$ makes its inversion challenging. Thus, a search algorithm is implemented to find possible solution triples (pH, Mg, K) for a given δ_i^{meas} in a numerical manner.

For each possible value pair of Mg and K values, i.e. (Mg_k, K_k) with k being one point in the two-dimensional $(Mg-K)$ value space, the pH value is determined, which corresponds to the given measured chemical shift, defined by the model function $\delta_i^{\text{model}}(pH)|_{(Mg_k, K_k)}$. This yields one pH value solution for each of the possible (Mg_k, K_k) pairs i.e. $(\delta_{\text{meas}}) \rightarrow (pH_k, Mg_k, K_k)$. This assignment is done separately for δ_γ , δ_α , δ_β , yielding the solution sets $(pH_k, Mg_k, K_k)_\gamma$, $(pH_k, Mg_k, K_k)_\alpha$, $(pH_k, Mg_k, K_k)_\beta$.

Due to the fact that the measured chemical shifts $(\delta_\gamma, \delta_\alpha, \delta_\beta)$ are resulting from the same

^{31}P spectrum, only the specific solution triple, for which the condition

$$(pH, Mg, K)_\gamma \stackrel{!}{=} (pH, Mg, K)_\alpha \stackrel{!}{=} (pH, Mg, K)_\beta \quad (4.3)$$

holds, should provide the correct solution triple.

4.5.2 Calculation of three-dimensional probability distributions

Typically, the condition in equation (4.3) cannot be found due to uncertainties in the developed model functions as well as measurement uncertainties. Therefore the described principle will be extended by incorporating an error margin on the measured chemical shift. The assignment of possible solutions as described above, will be done not only for δ^{meas} , but also for a specific range $\delta = \delta^{\text{meas}} \pm \Delta\delta^{\text{meas}}$. Hereby, a Gaussian distribution with $\sigma = 0.01$ ppm is assumed for $P(\delta)$ (Figure 4.8A).

The assignment of $\delta \rightarrow (pH, Mg, K)$ is realized in the following steps:

1. For each point (Mg_k, K_k) and for each element in $\delta = (\delta_{\text{meas}} \pm 5\sigma)$, the pH value is found, for which the chemical shift defined by the model function $\delta^{\text{model}}(pH)|_{(Mg_k, K_k)}$ is closest to the measured chemical shift. In other words, the probability distribution $P(\delta)$ is projected onto the pH axis, which is defined by the model function $\delta^{\text{model}}(pH)|_{(Mg_k, K_k)}$ (Figure 4.8 B1 and B2). This projection means, that the probability P of each $\delta_j \in (\delta_{\text{meas}} \pm 5\sigma)$ is assigned to the point on the pH axis, which corresponds to the smallest distance between δ_j and $\delta_{\text{model}}(pH)|_{(Mg_k, K_k)}$. Note, that the probability distribution $P(pH)$ is no longer Gaussian, due to the non-linearity of the model function.
2. $P(pH)$ is interpolated (using a Hermite spline) and assigned to the corresponding point (Mg_k, K_k) (Figure 4.8 C1 and C2).
3. This projection is repeated for each point in the sampling grid $(Mg-K)$, yielding the final three-dimensional probability distribution $P(pH, Mg, K)$ (Figure 4.8D), which assigns each point in the grid $(pH-Mg-K)$ a specific probability, that the measured chemical shift corresponds to that point.
4. The probability distribution $P(pH, Mg, K)$ is normalized.

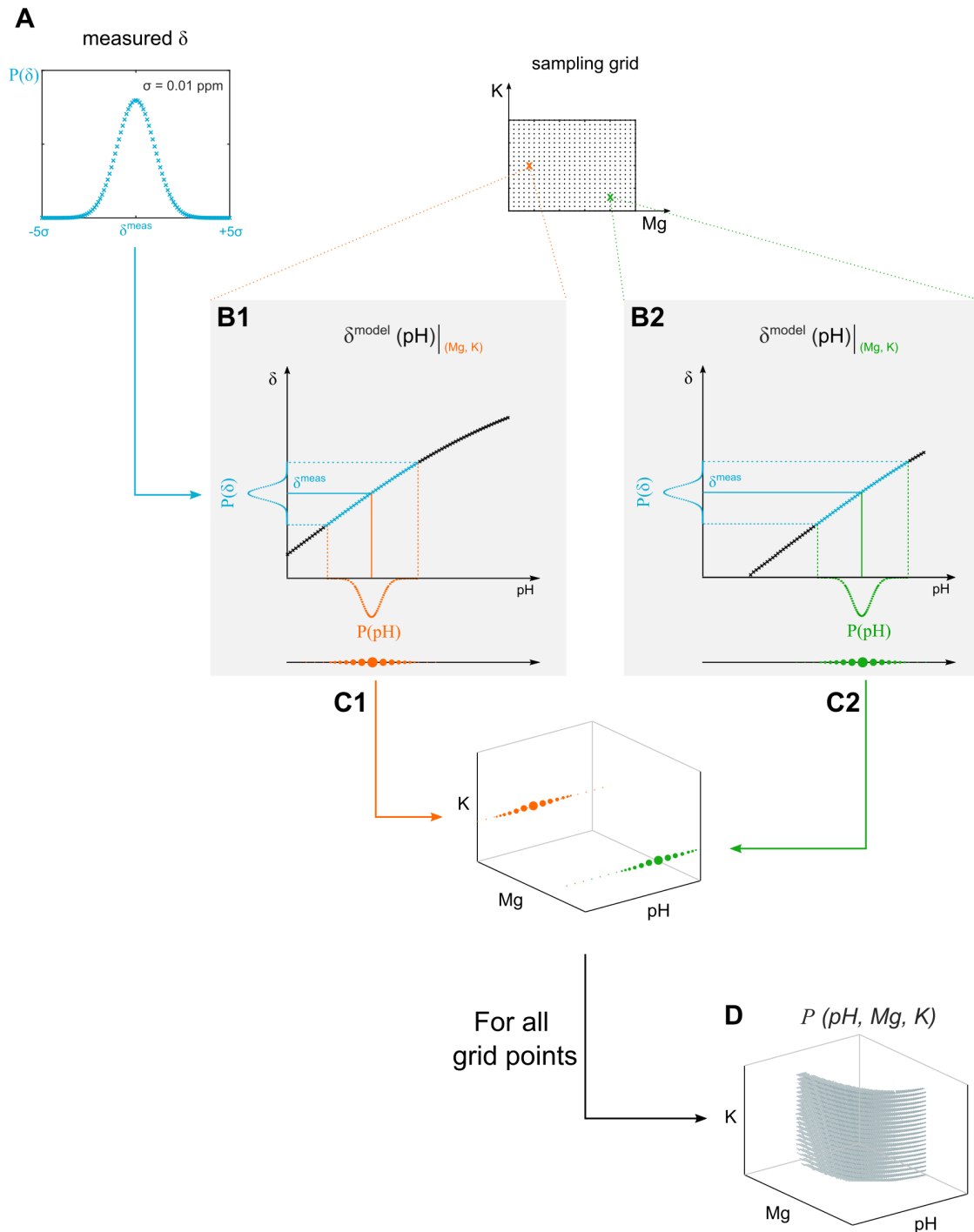
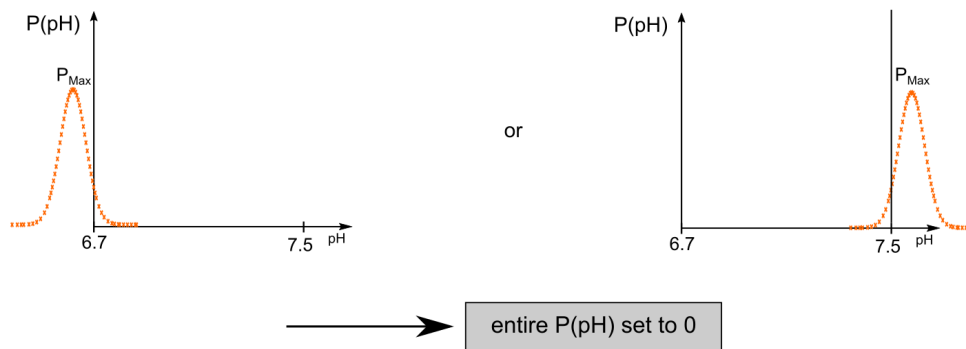


Figure 4.8: Schematic representation of the workflow for the calculation of the three-dimensional probability distributions $P(pH, Mg, K)$. (A) For the measured chemical shift δ_{meas} , a Gaussian distribution $P(\delta)$ is assumed with $\sigma = 0.01$ ppm. (B1, B2) For each point in the sampling grid defined by the 2D subspace (Mg, K) , the distribution $P(\delta_{meas} \pm 5\sigma)$ is projected onto the pH axis as defined by the model function $\delta_{model}(pH)|_{(Mg, K)}$. (C1, C2) For each point in the sampling grid, the probability distribution $P(pH)$ is interpolated and assigned to the corresponding point (Mg, K) . In the illustration, the dot size corresponds to the value for P . (D) This assignment is done for all grid points resulting in a three-dimensional probability distribution $P(pH, Mg, K)$, assigning each point in the sampling grid $(pH-Mg-K)$ a specific probability.

Case 1: $P_{\text{Max}}(\text{pH})$ outside of valid range



Case 2: $P(\text{pH})$ not entirely in valid range

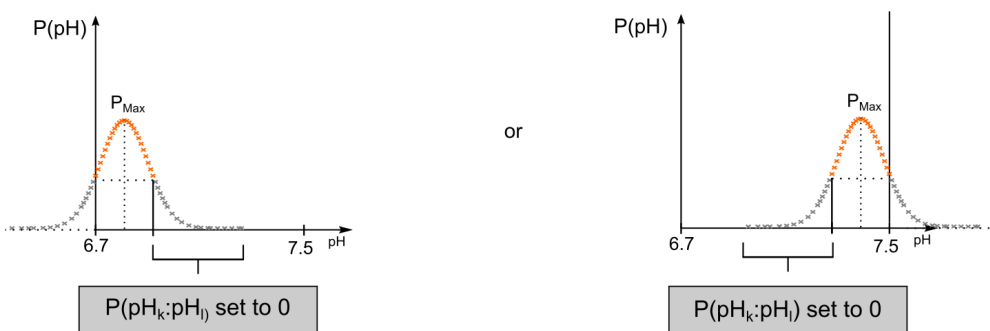


Figure 4.9: Special cases for the determination of the probability distributions. Case 1: The maximum of the determined distribution $P(\text{pH})$ is outside of the valid range. $P(\text{pH})$ is set to 0. Case 2: $P(\text{pH})$ is not entirely in the valid range. The probability of the points $\text{pH}_k : \text{pH}_l$ inside the valid range, which represent the “mirrored” part of $P(\text{pH})$ being outside the valid range, is set to 0. This is done in order to keep the center of mass of the distribution as uninfluenced as possible.

Due to the fact, that the determined probability distribution $P(\text{pH}, Mg, K)$ might yield pH values not covered by the value space (cf. section 4.5.4), the following cases require special handling within the look-up algorithm (Figure 4.9):

- Case 1: The measured chemical shift δ^{meas} is assigned to a pH value outside of the pH range, i.e. $\delta^{\text{meas}} \rightarrow (\text{pH} < 6.7 \mid \text{pH} > 7.5)$.
 \implies The output value $P(\text{pH})|_{(Mg_k, K_k)}$ is set to 0.
- Case 2: The projected distribution $P(\text{pH})$ has probabilities outside the defined pH range, i.e. $P(\text{pH})$ at the edges $\neq 0$
 \implies The distance between $P_{\text{max}}(\text{pH})$ to the edge of $P(\text{pH})$ is determined, and for the pH points lying on the other side of P_{max} (i.e. inside the valid range) which

are further away from maximal point than the edge, i.e. $\text{pH}_k:\text{pH}_l$ in Figure 4.9, the value P is set to 0.

The implementation of the second case follows the rationale to keep the center of mass of the distribution as uninfluenced as possible.

4.5.3 Determination of output values (pH, Mg, K)

For specific input chemical shifts δ_i^{meas} , the probability density functions are calculated separately for γ -, α - and β -ATP, yielding $P_\gamma(\text{pH}, \text{Mg}, K)$, $P_\alpha(\text{pH}, \text{Mg}, K)$ and $P_\beta(\text{pH}, \text{Mg}, K)$ (Figure 4.10). The joint probability function $P_{\text{joint}}(\text{pH}, \text{Mg}, K)$ is determined by multiplying $P_i(\text{pH}, \text{Mg}, K), i \in (\gamma, \alpha, \beta)$. The final output values of the look-up algorithm pH_{Out} , Mg_{Out} , and K_{Out} are determined as the weighted mean of all possible solutions:

$$\text{pH}_{\text{Out}} = \frac{\sum_{i_{\text{grid}}=1}^{N_{\text{grid}}} \left(P_{i_{\text{grid}}}^{\text{joint}} \cdot \text{pH}_{i_{\text{grid}}} \right)}{\sum_{i_{\text{grid}}=1}^{N_{\text{grid}}} P_{i_{\text{grid}}}^{\text{joint}}} \quad (4.4)$$

$$\text{Mg}_{\text{Out}} = \frac{\sum_{i_{\text{grid}}=1}^{N_{\text{grid}}} \left(P_{i_{\text{grid}}}^{\text{joint}} \cdot \text{Mg}_{i_{\text{grid}}} \right)}{\sum_{i_{\text{grid}}=1}^{N_{\text{grid}}} P_{i_{\text{grid}}}^{\text{joint}}} \quad (4.5)$$

$$\text{K}_{\text{Out}} = \frac{\sum_{i_{\text{grid}}=1}^{N_{\text{grid}}} \left(P_{i_{\text{grid}}}^{\text{joint}} \cdot \text{K}_{i_{\text{grid}}} \right)}{\sum_{i_{\text{grid}}=1}^{N_{\text{grid}}} P_{i_{\text{grid}}}^{\text{joint}}}. \quad (4.6)$$

Hereby, i_{grid} is one point in the three-dimensional sampling grid ($\text{pH}-\text{Mg}-\text{K}$), and N_{grid} the total number of these grid points.

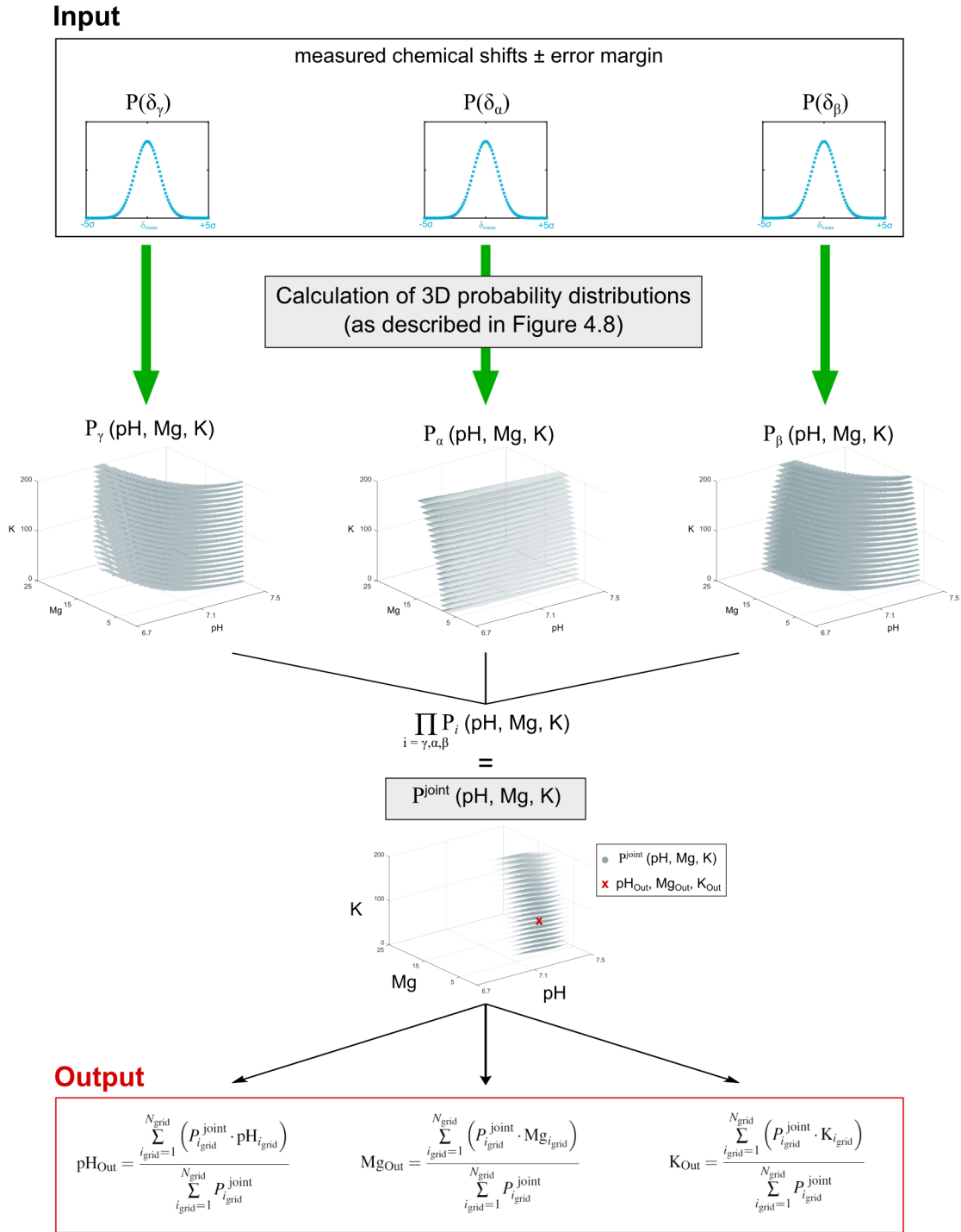


Figure 4.10: Schematic representation of the workflow for the determination of (pH, Mg, K) using the proposed look-up algorithm. For the measured chemical shifts $\delta_\gamma^{\text{meas}}$, $\delta_\alpha^{\text{meas}}$, $\delta_\beta^{\text{meas}}$, the probability distributions $P_\gamma(pH, Mg, K)$, $P_\alpha(pH, Mg, K)$ and $P_\beta(pH, Mg, K)$ are calculated separately as described in Figure 4.8. The product $\prod_{i=\gamma,\alpha,\beta} P_i(pH, Mg, K)$ yields the joint probability $P_{\text{joint}}(pH, Mg, K)$, which is used to calculate the output values pH_{Out} , Mg_{Out} , K_{Out} as the weighted mean values of all possible values.

4.5.4 Choice of the sampling grid

The identification of the value ranges for $(pH-Mg-K)$, which are assumed to be relevant in vivo, will be addressed in detail in section 5.1, but are preempted here in order to provide a correct description of the implemented algorithm.

For the sampling grid spanning the three-dimensional value space $(pH-Mg-K)$, the following value ranges and spacings were used:

- $pH = (6.7 : 0.01 : 7.5)$
- $Mg = (0 : 0.1 : 25)$ in [mM]
- $K = (0 : 10 : 200)$ in [mM]

Hence, the look-up table has the total number of entries $N_{\text{grid}} = N_{pH} \times N_{Mg} \times N_K = 81 \times 251 \times 21 = 426,951$.

For pH and Mg , not only values within the experimental acquired value ranges, i.e. $pH = (6.8 - 7.4)$ and $Mg = (0 - 10)$ mM (compare Table 4.1 in section 4.3) were interpolated, but were extrapolated also to values outside this ranges. Hereby, the pH value range was only slightly increased by 0.1 pH units at the lower and upper edge of the obtained range. This increase by 0.1 pH units was motivated by the fact that the assignment of measured chemical shifts to the underlying parameters is done by also incorporating a certain error margin for the measured chemical shifts, i.e. $(\delta_{\text{meas}} \pm \Delta\delta_{\text{meas}})$ (cf. section 4.5.2). Consequently, the error margins of chemical shifts corresponding to pH values at the edges of the range, i.e. $pH = 6.8$ or 7.4 , would need to be assigned to pH values outside the range of $(6.8 - 7.4)$. The range for Mg was increased because the comparison of the ATP chemical shifts measured in vivo and in model solutions indicated, that some in vivo chemical shifts seem to translate to magnesium values larger than 10 mM (cf. Figure 5.18; $R = 2$ corresponds to $[Mg^{2+}] = 10$ mM; in particular for α -ATP). Supported by literature values reporting values of up to $(15 - 30)$ mM for intracellular $[Mg^{2+}]$ [37, 47], the range for the look-up table was increased to $(0 - 25)$ mM.

Due to the fact, that the change of δ^{meas} with varying K is the lowest of all three parameters, a coarse grid was chosen for K , which is assumed to be sufficient for a reliable assignment of values. This is done in order to reduce the computational complexity.

5 Results

5.1 Identification of the relevant ranges of pH and magnesium ion concentration in vivo

In this section, in vivo ^{31}P MRSI data are analyzed in order to identify relevant value ranges of pH and magnesium ion concentration, as well as the chemical shift ranges of the corresponding metabolites. To cover a large range of conditions, different tissue types were analyzed, i.e. muscle and brain tissue, and also the comparison between healthy and diseased tissue was addressed on the example of data from patients with glioblastoma. The used datasets were acquired with MR sequences of current highest standards. The human lower leg muscle data are published in [52], and the pH maps of the patients with glioblastoma are published in [9, 10].

5.1.1 ^{31}P MRSI data from the human lower leg muscle of healthy volunteers

In all volunteers, the 3D ^{31}P MRSI datasets from the lower legs yielded spectra of high quality, enabling a robust quantification of all detectable metabolites, i.e. inorganic phosphate (P_i), glycerophosphocholine (GPC), phosphocreatine (PCr), and the three resonances of ATP, in the entire measured volume (representatively shown for three voxels from the dataset of volunteer 2; Figure 5.1). The B_0 -shift corrected spectra revealed spatial variations of the quantified chemical shifts of P_i and β -ATP (see Figure 5.1, dashed lines). The largest difference is observed when comparing the muscle groups TA and Sol (indicated as blue-shaded area in Figure 5.1).

The local variation of δ_{P_i} and δ_{β} translates to local differences of the calculated values in the 3D maps of pH and $[\text{Mg}_{\text{free}}^{2+}]$ (Figures 5.2 and 5.3). For all volunteers, the pH values calculated by the modified Henderson Hasselbalch equation (2.64) as given in [31], range between 6.98 and 7.08 pH units. The calculated $[\text{Mg}_{\text{free}}^{2+}]$ based on the equation by Golding and Golding [27, 48] range between 0.7 and 1.3 mM.

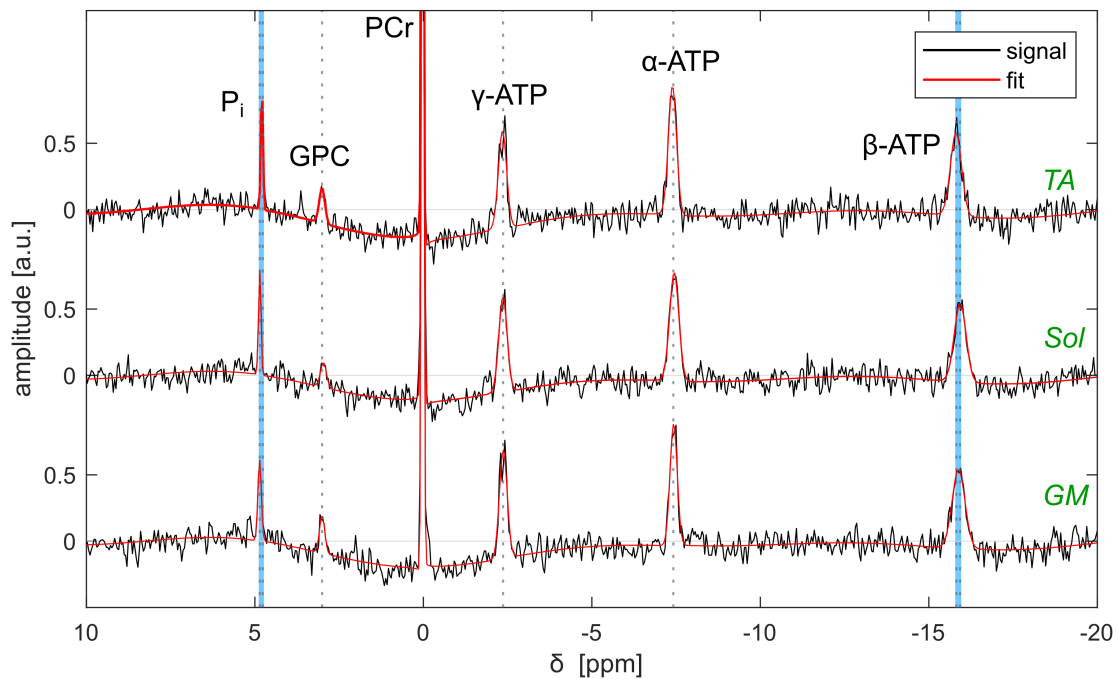


Figure 5.1: Representative ^{31}P MR spectra localized in the lower leg muscles *tibialis anterior* (TA; top), *soleus* (Sol; middle), and *gastrocnemius medialis* (GM; bottom) of volunteer 2. Locations of the selected voxels are displayed in Figure 5.2. Signals (black) and corresponding fits (red) are corrected for zero- and first-order phases, and B_0 -shifts. The following metabolites were quantified (from left to right): inorganic phosphate (P_i), glycerophosphocholine (GPC), phosphocreatine (PCr), and the three resonances of adenosine-5'-triphosphate (ATP). The chemical shifts of P_i and β -ATP vary depending on the location, whereas the chemical shifts of the other metabolites do not show any visible difference. The maximal chemical shift difference between the spectra from TA and Sol is indicated in blue. Figure is reproduced with permission from [52].

5.1 Identification of the relevant ranges of pH and magnesium ion concentration in vivo

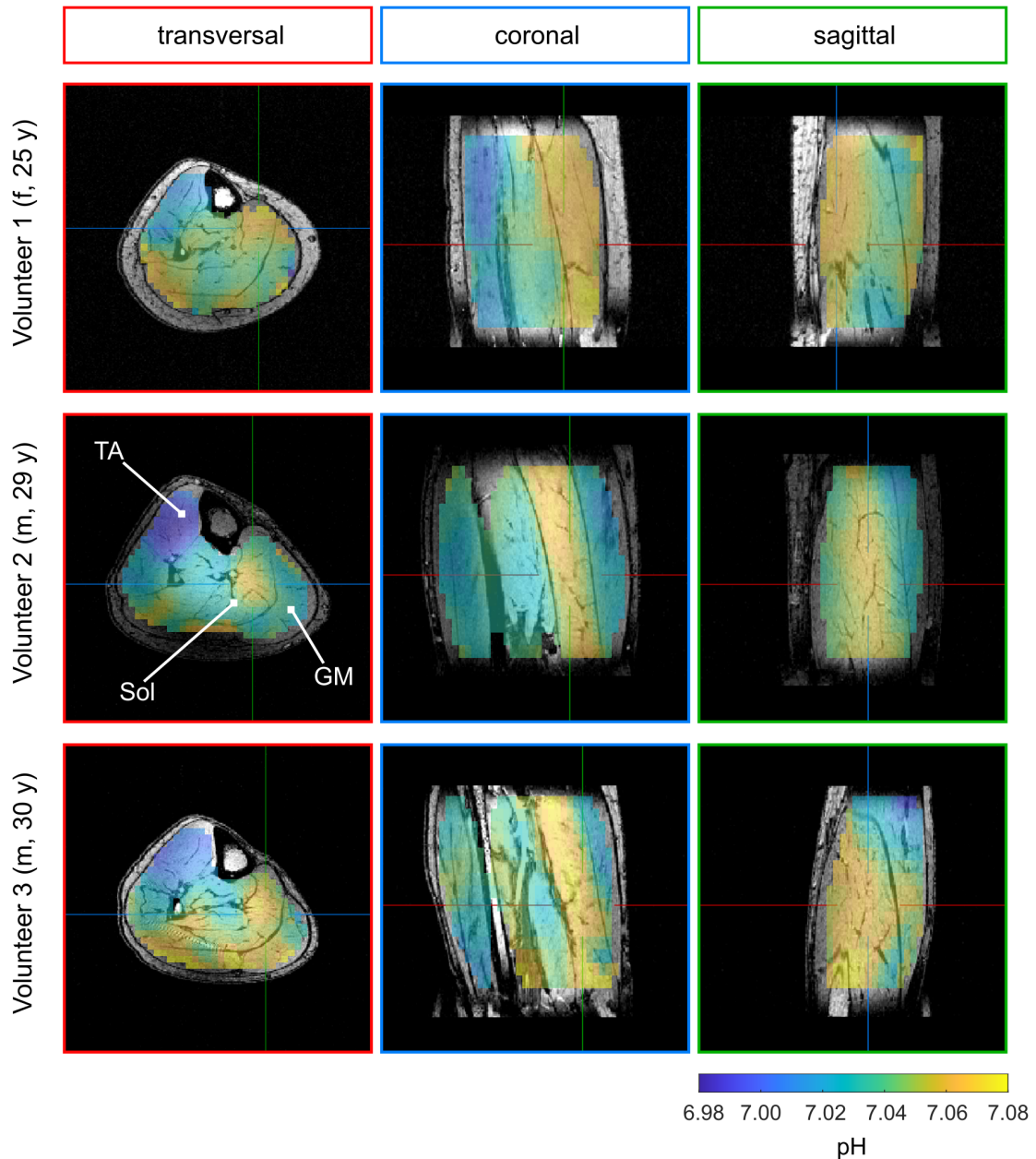


Figure 5.2: 3D maps of pH values in the lower leg muscles calculated using the modified Henderson-Hasselbalch equation (2.64) as given in [31]. The transversal, coronal and sagittal views (indicated as colored lines) of the maps from all three volunteers are overlaid with the morphological ^1H images. Locations of the representative voxels from the *tibialis anterior* (TA), *soleus* (Sol) and *gastrocnemius medialis* (GM) shown in Figure 5.1 are marked in the transversal slice of the dataset from volunteer 2. The maps of all volunteers show local differences of the calculated pH values with comparable patterns. In the TA, the lowest pH values are observed, followed by the GM and the Sol with the highest pH values, resulting in a visible contrast along the muscle strands, in particular in the coronal view of the maps. Figure is reproduced with permission from [52].

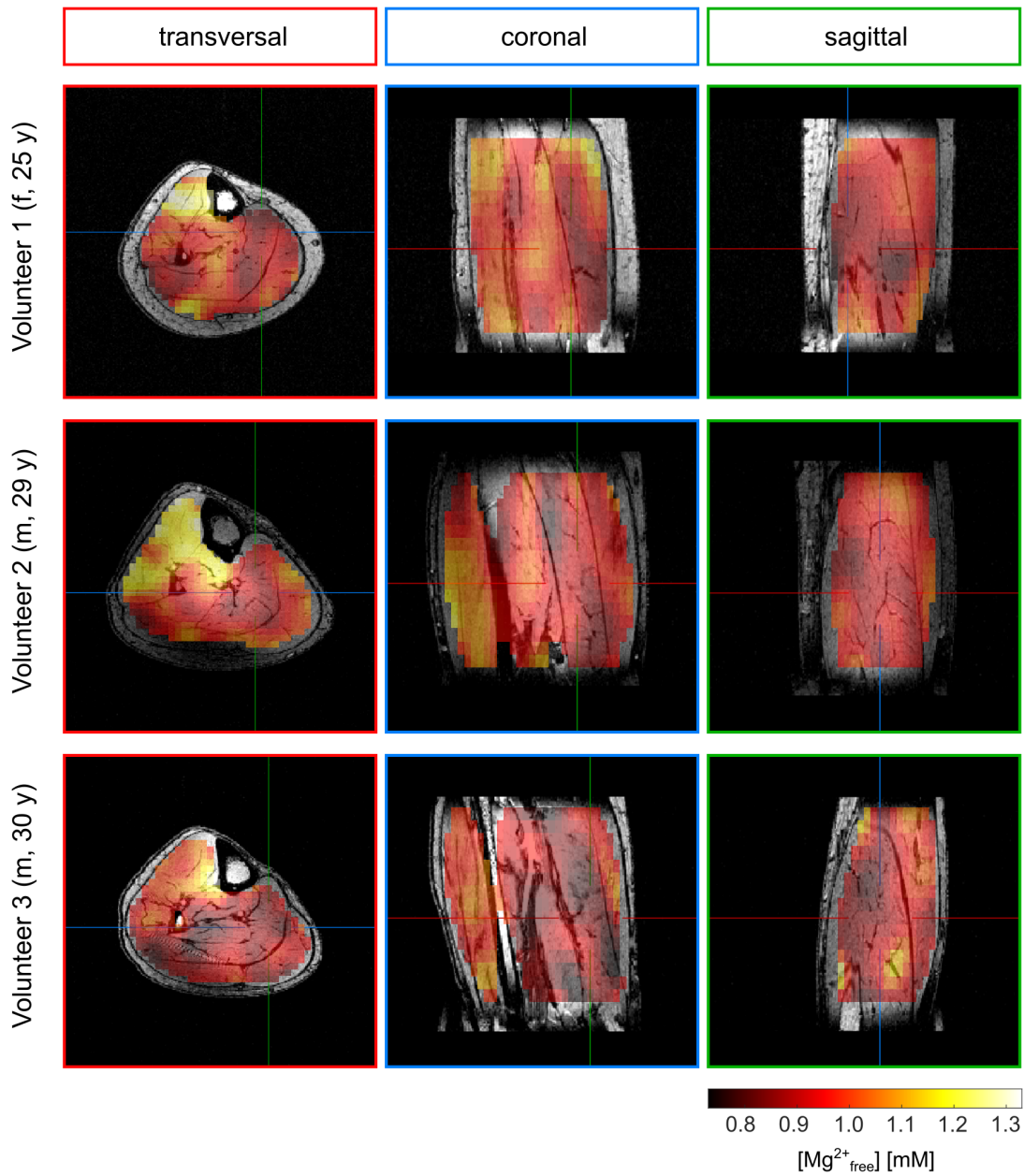


Figure 5.3: 3D maps of $[\text{Mg}_{\text{free}}^{2+}]$ values of the lower leg muscles calculated using the formula from Golding and Golding [27, 48]. The transversal, coronal and sagittal views (indicated as colored lines) of the maps from all three volunteers are overlaid with the morphological ^1H images. In the maps from all volunteers, local differences of the calculated $[\text{Mg}_{\text{free}}^{2+}]$ values can be observed. The patterns are comparable between the volunteers, but show more inter-subject variability than the pH maps. Figure is reproduced with permission from [52].

5.1 Identification of the relevant ranges of pH and magnesium ion concentration in vivo

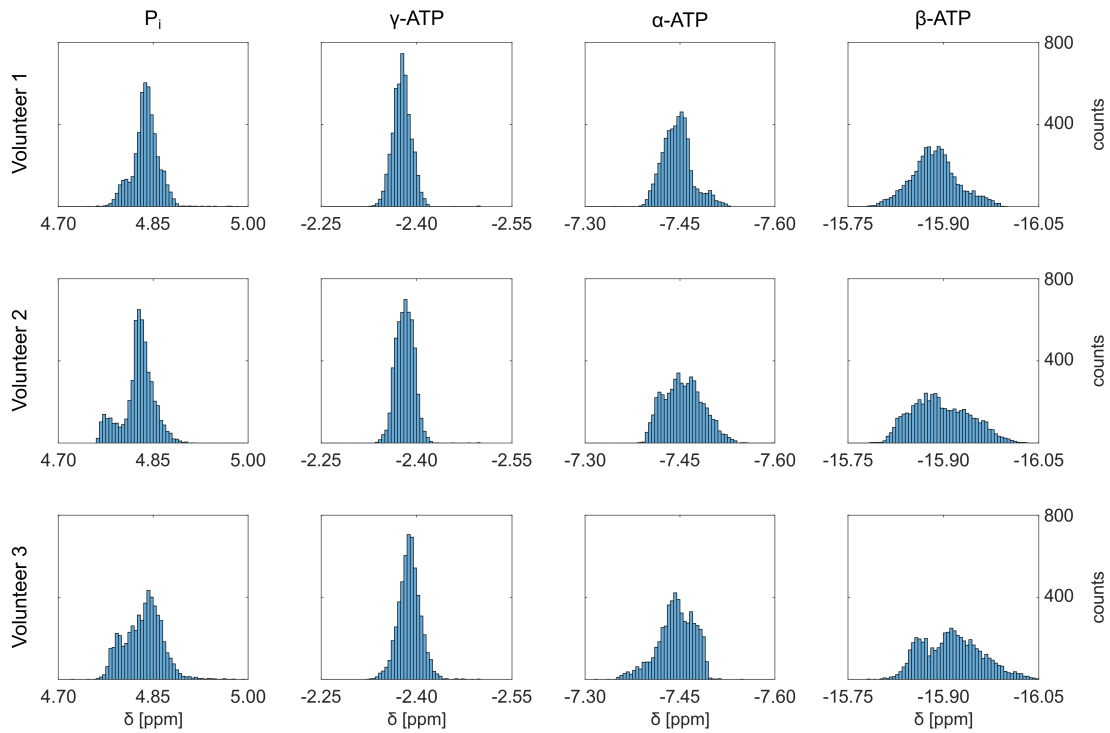


Figure 5.4: Distributions of the chemical shifts of P_i, γ-, α- and β-ATP (columns) obtained from the 3D ³¹P MRSI lower leg muscle datasets shown for each volunteer individually (rows). The range for the counts is the same for all histograms and is shown on the right side of the figure. The medians of the chemical shifts is approximately the same for all volunteers, i.e. 4.84 ppm for P_i, -2.38 ppm for γ-ATP, -7.45 ppm for α-ATP, and -15.9 ppm for β-ATP. The total number of voxels in muscle tissue is 4,781 for volunteer 1, 5,233 for volunteer 2, and 5,362 for volunteer 3. The number of outliers, i.e. voxels with values being outside of the shown range, is maximal 8.

In order to quantify the variation of pH and magnesium values as well as the corresponding chemical shifts across the lower leg muscles, the data is also presented in histograms for each volunteer separately (Figures 5.4 and 5.5). The overall value ranges of the observed chemical shifts are comparable for all volunteers, but the distributions show some differences between the individuals, in particular for P_i, α- and β-ATP (Figure 5.4). The high count of voxels with $\delta_{P_i} \approx 4.8$ ppm (Figure 5.4), and correspondingly with $\text{pH} \approx 7.0$ (Figure 5.5), result from the muscle TA (see pH maps in Figure 5.2).

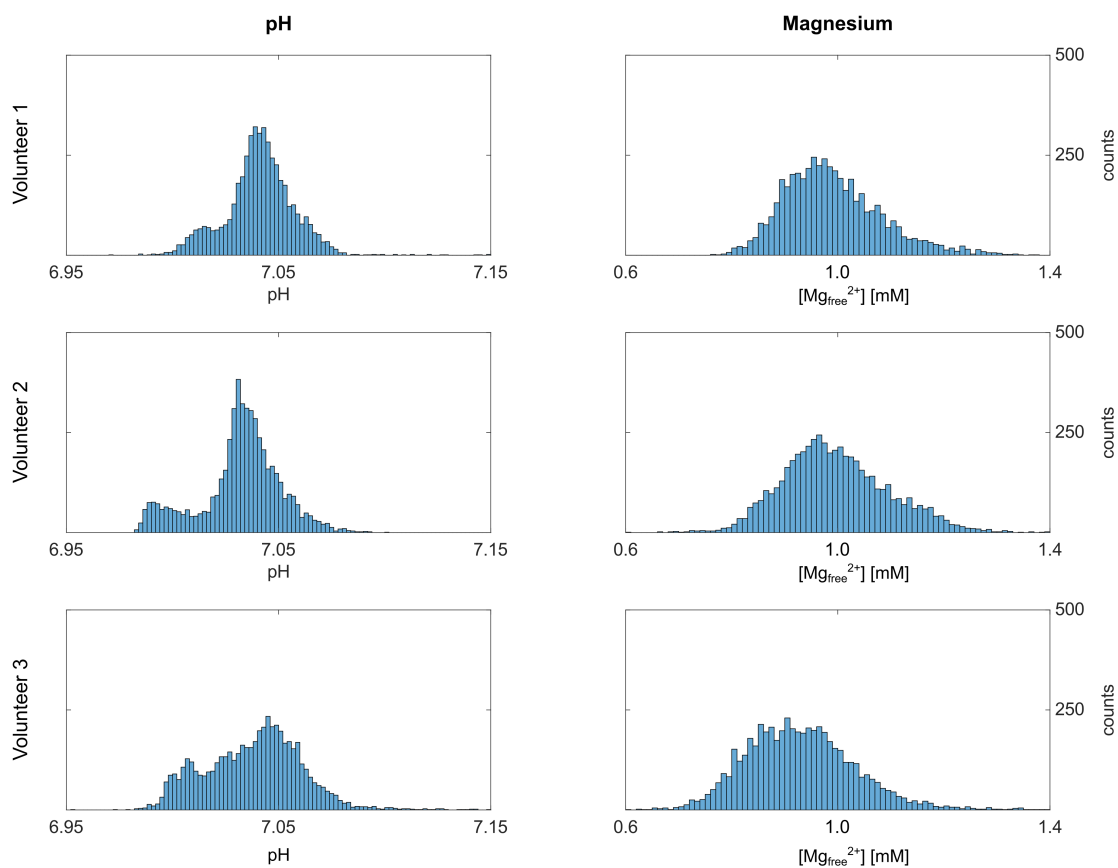


Figure 5.5: Distribution of the calculated pH (left column) and magnesium values (right column) from the 3D ^{31}P MRSI lower leg muscle data shown for each volunteer individually (rows). The range for the counts is the same for all histograms and shown on the right side of the figure. The number of outliers is maximal 5. The accumulation of counts around $\text{pH} \approx (7.00 - 7.02)$ can be associated with voxels from the TA muscle, where the lowest pH values were observed (compare Figure 5.2). The distribution of $[\text{Mg}_{\text{free}}^{2+}]$ values is more uniform, as already seen in Figure 5.3.

5.1.2 ^{31}P MRSI human brain data from patients with glioblastoma

The acquired spectra from brain tissue are of good quality, showing the expected spectral pattern (Figure 5.6). The following metabolites can be reliably quantified in the voxels covering healthy tissue: phosphoethanolamine (PE), phosphocholine (PC), extracellular inorganic Phosphate ($e\text{P}_i$), intracellular inorganic phosphate (P_i), glycerophosphoethanolamine (GPE), glycerophosphocholine (GPC), phosphocreatine (PCr), nicotinamide adenine dinucleotide (NAD), and the three resonances of ATP. In the representative spectrum from the tumor region additionally the resonances of 2,3-Diphosphoglycerate (DPG), mobile phospholipids (MPL), and Uridine Diphosphoglucose (UDPG) can be observed. The amplitudes of PCr, ATP, GPE and GPC are decreased, and the linewidth of the PC resonance is decreased. Particularly interesting for this work are the changes for P_i and ATP. The P_i resonance is broadened and shifted upfield (see Figure 5.6 blue shading), indicating an increase of the pH value. Most importantly, also the resonances of ATP are shifted upfield. The acquired tumor spectra from all patients show both intra- and intersubject variation of the spectral patterns to some extent.

The calculated intracellular pH maps of all three patients show an elevated pH value in the tumor region, even revealing a heterogeneity within the tumor (Figure 5.7). The calculated pH values in healthy tissue are around (6.95 – 7.0), and in the tumor region between (7.1 – 7.25). The calculated $[\text{Mg}_{\text{free}}^{2+}]$ maps (Figure 5.8) also show local differences, although not having such a clear trend in all of the investigated patients. However, in all patients, the areas of high muscle content, i.e. the temples and the neck region, show $[\text{Mg}_{\text{free}}^{2+}]$ values > 0.75 mM, which is in agreement with data from the lower leg muscle (cf. Figure 5.3). Due to the relatively large value range in Figure 5.8 (in order to visualize also the muscle tissue correctly), the tumor region cannot be distinguished as clearly as in the pH maps. In the regions-of-interest (ROIs) analysis at the end of this chapter (5.4), the local differences between healthy and diseased tissue will become more apparent. Nevertheless, also in the maps shown here, trends towards slightly elevated $[\text{Mg}_{\text{free}}^{2+}]$ values in the periphery of the tumor region are visible in the transversal and sagittal slice of patient 1. The map of patient 2 suffers from a high heterogeneity of calculated $[\text{Mg}_{\text{free}}^{2+}]$ values, presumably due to poor spectral quality resulting from a high B_0 heterogeneity due to the caudal position of the tumor. This point will be discussed further in section 6.6.3 of the discussion.

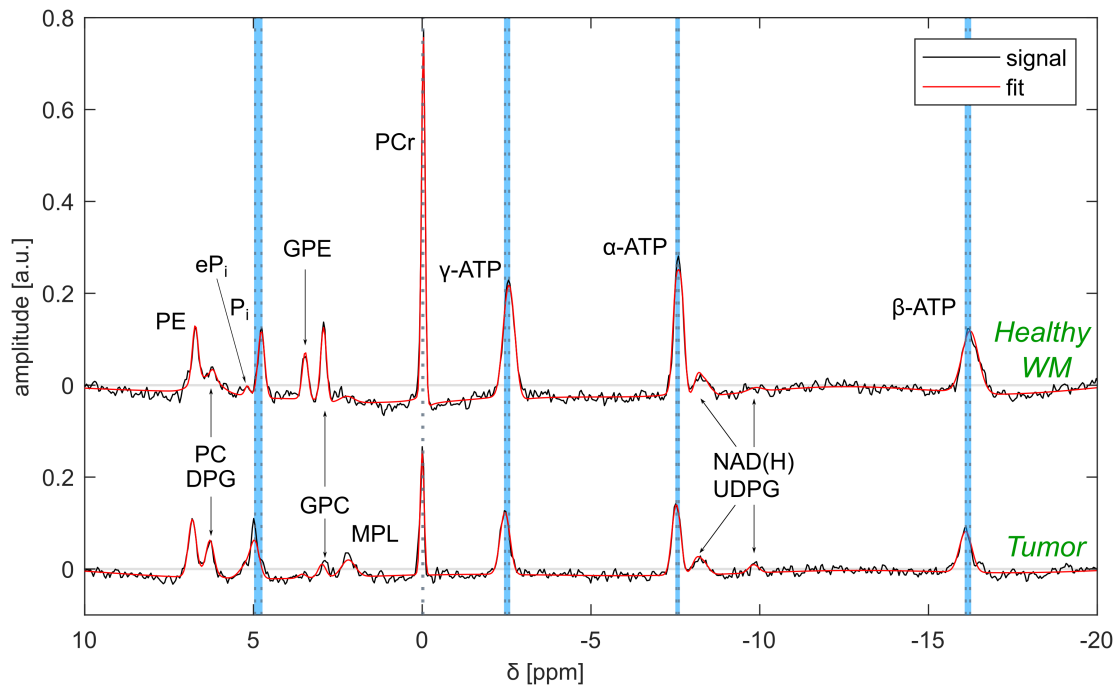


Figure 5.6: Representative ^{31}P spectra from patient 1. Locations of the selected voxels are shown in the pH maps (Figure 5.7, first row). In the spectrum from healthy white matter (WM), the resonances from the typical brain metabolites can be seen (from left to right): phosphoethanolamine (PE), phosphocholine (PC), extracellular inorganic Phosphate (eP_i), intracellular inorganic phosphate (P_i), glycerophosphoethanolamine (GPE), glycerophosphocholine (GPC), phosphocreatine (PCr), and the three resonances of adenosine-5'-triphosphate (ATP). Downfield from α -ATP, the resonance of nicotinamide adenine dinucleotide (NAD) can be observed. In the spectrum from tumor tissue, the amplitudes of PCr, ATP, GPC and GPE are reduced. The P_i peak is broadened and shifted upfield, presumably due to a higher pH value. Moreover, also the resonances of ATP are shifted upfield.

5.1 Identification of the relevant ranges of pH and magnesium ion concentration in vivo

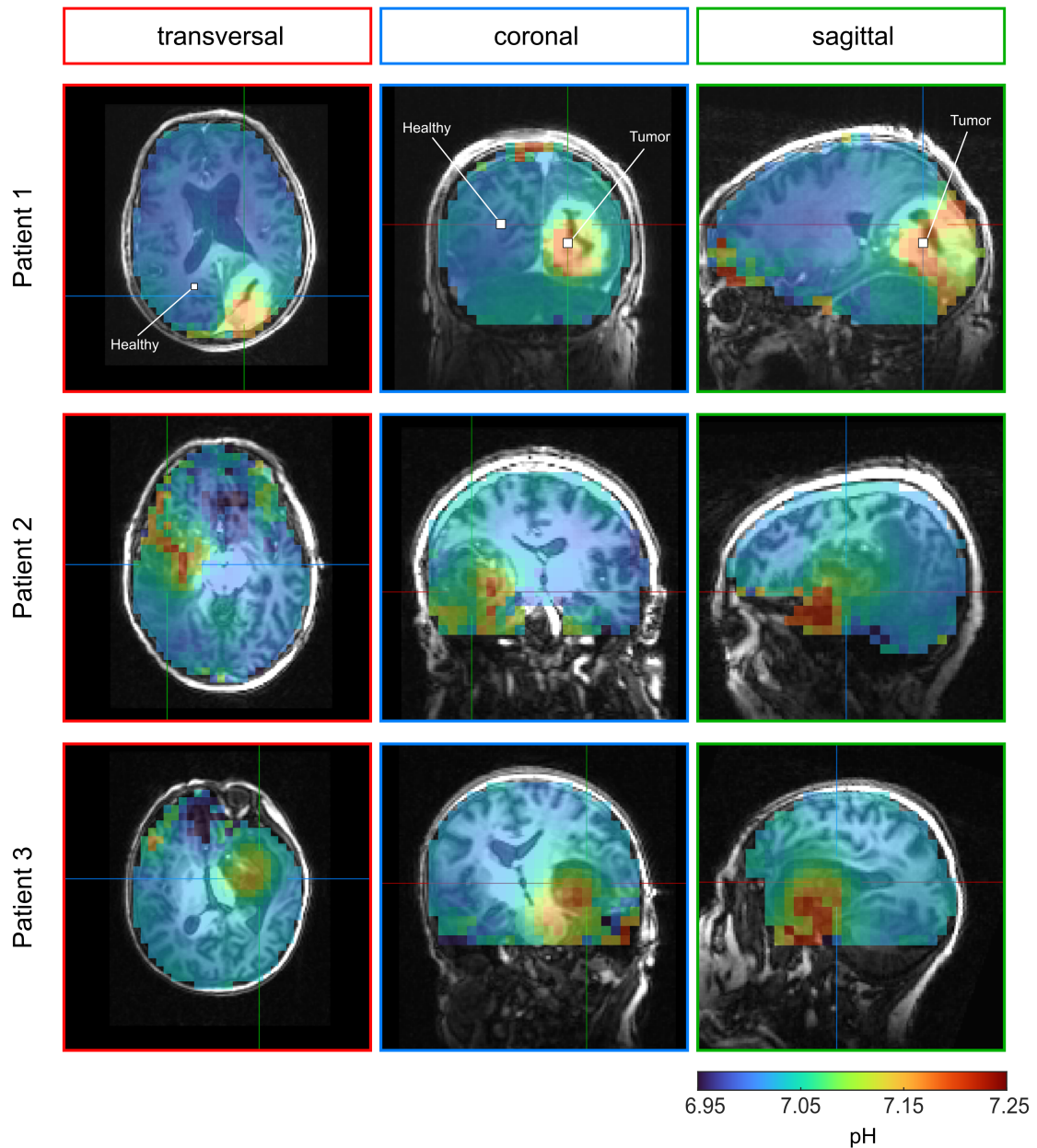


Figure 5.7: 3D maps of intracellular pH values calculated using the the modified Henderson Hasselbalch equation (2.64) as given in [31]. The transversal, coronal and sagittal view (colored lines) of the maps from all three patients are overlaid with the morphological ^1H images. Locations of the voxels from healthy white matter and tumor shown in Figure 5.6 are marked in the maps from patient 1 (first row). For all patients, the calculated pH values are elevated in the tumor region with values in the range of (7.1 – 7.25) compared to the surrounding healthy tissue, where the $\text{pH} \approx 7.0$ for the entire brain. In the tumor region, also a heterogeneity of calculated pH values can be observed.

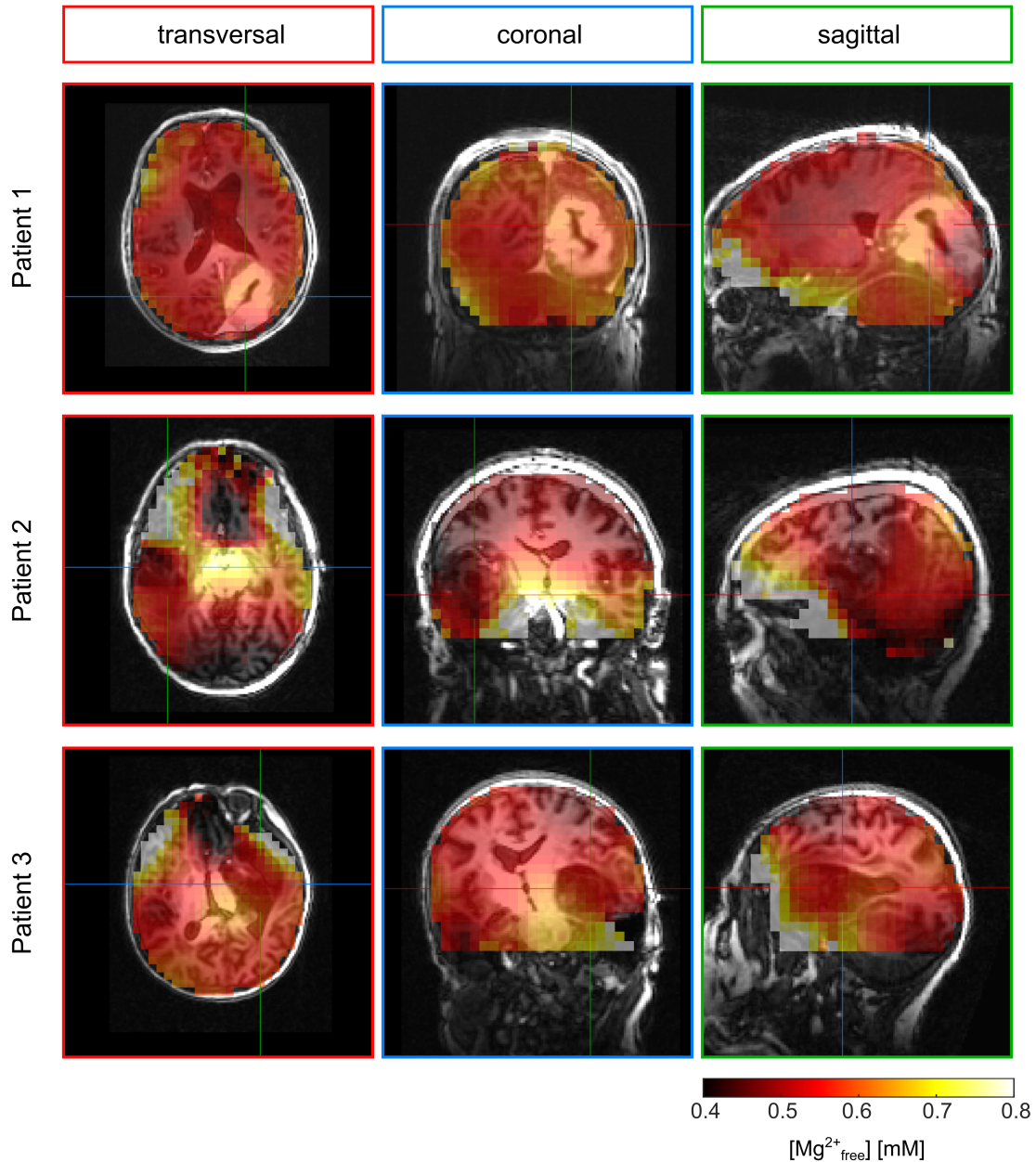


Figure 5.8: 3D maps of $[\text{Mg}_{\text{free}}^{2+}]$ in patients with glioblastoma calculated using the formula from Golding and Golding [27, 48]. The transversal, coronal and sagittal view (colored lines) of the maps from all three patients are overlaid with the morphological ^1H images. The maps from patients 1 and 3 show values of $[\text{Mg}_{\text{free}}^{2+}] \approx 0.5 \text{ mM}$ for the entire brain, except for areas with a high muscle content, i.e. around the temples and in the neck area, where the $[\text{Mg}_{\text{free}}^{2+}]$ value is increased. Moreover, for patient 1, a slightly higher $[\text{Mg}_{\text{free}}^{2+}]$ value is obtained in the periphery of the tumor. A better comparison between healthy and diseased tissue will be given in the regions-of-interest (ROIs) analysis at the end of the chapter (section 5.4). It should be noted, that the displayed map from patient 2 suffers from a high heterogeneity, presumably due to poor spectral quality resulting from a high B_0 heterogeneity due to the caudal position of the tumor.

5.1 Identification of the relevant ranges of pH and magnesium ion concentration in vivo

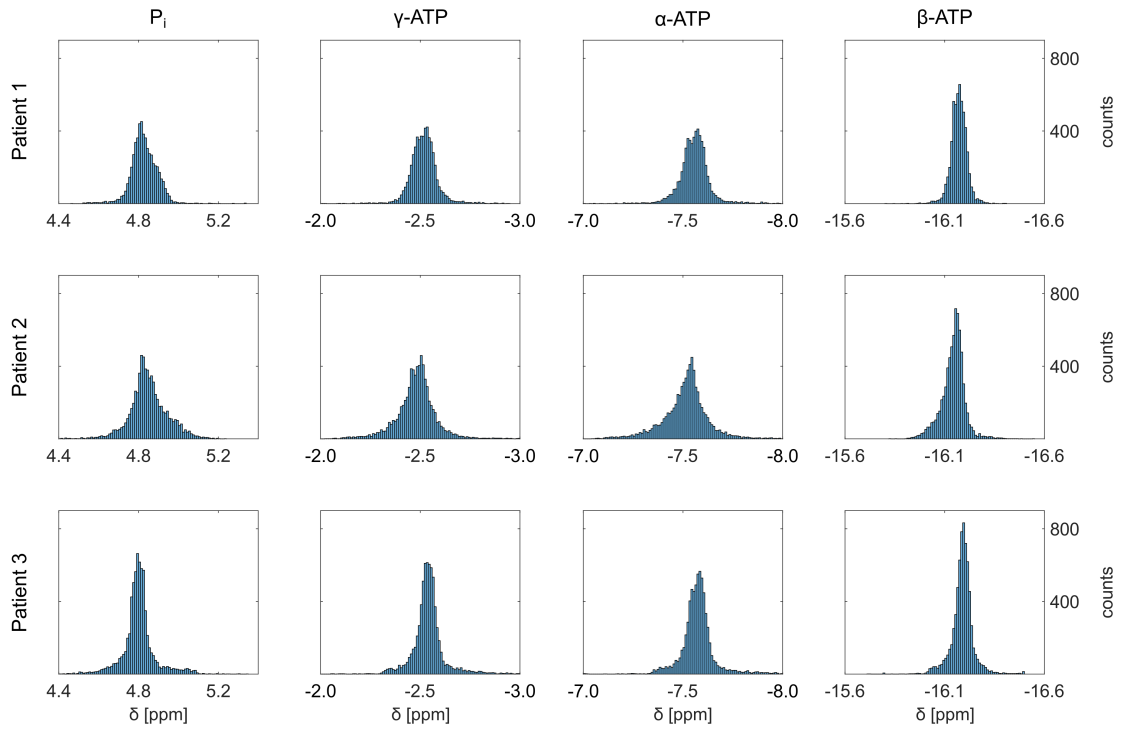


Figure 5.9: Distribution of chemical shifts for P_i , γ -, α - and β -ATP (columns) obtained from the 3D ^{31}P MRSI brain data shown for each patient individually (rows). The range for the counts is the same for all histograms and is shown on the right side of the figure. The median values of the chemical shifts differ for each patient, and range from $[4.80; 4.84]$ ppm for P_i , $[-2.54; -2.48]$ ppm for γ -ATP, $[-7.57; -7.52]$ ppm for α -ATP, and $[-16.19; -16.15]$ ppm for β -ATP. The total number of voxels in brain tissue is 6,933 for patient 1, 7,044 for patient 2, and 5,570 for patient 3. The number of outliers, i.e. voxels with values being outside of the shown range, is maximal 75.

The distributions of the observed chemical shifts (Figure 5.9) and calculated pH and $[\text{Mg}_{\text{free}}^{2+}]$ values (Figure 5.10) are comparable between the patients, but show some difference between patients, for P_i , γ - and α -ATP. The sideband of the right side of the histogram for P_i , i.e. values ≥ 4.9 ppm (particularly seen for patient 3) correspond to pH values ≥ 7.1 resulting from voxels in tumor tissue (compare Figure 5.8), which is also reflected in the pH histogram (Figure 5.10). The sideband in the magnesium histograms, i.e. voxels with $[\text{Mg}_{\text{free}}^{2+}] \geq 0.75$ mM, can be associated with voxels from muscle tissue, i.e. neck and temples, as well as partly from tumor tissue.

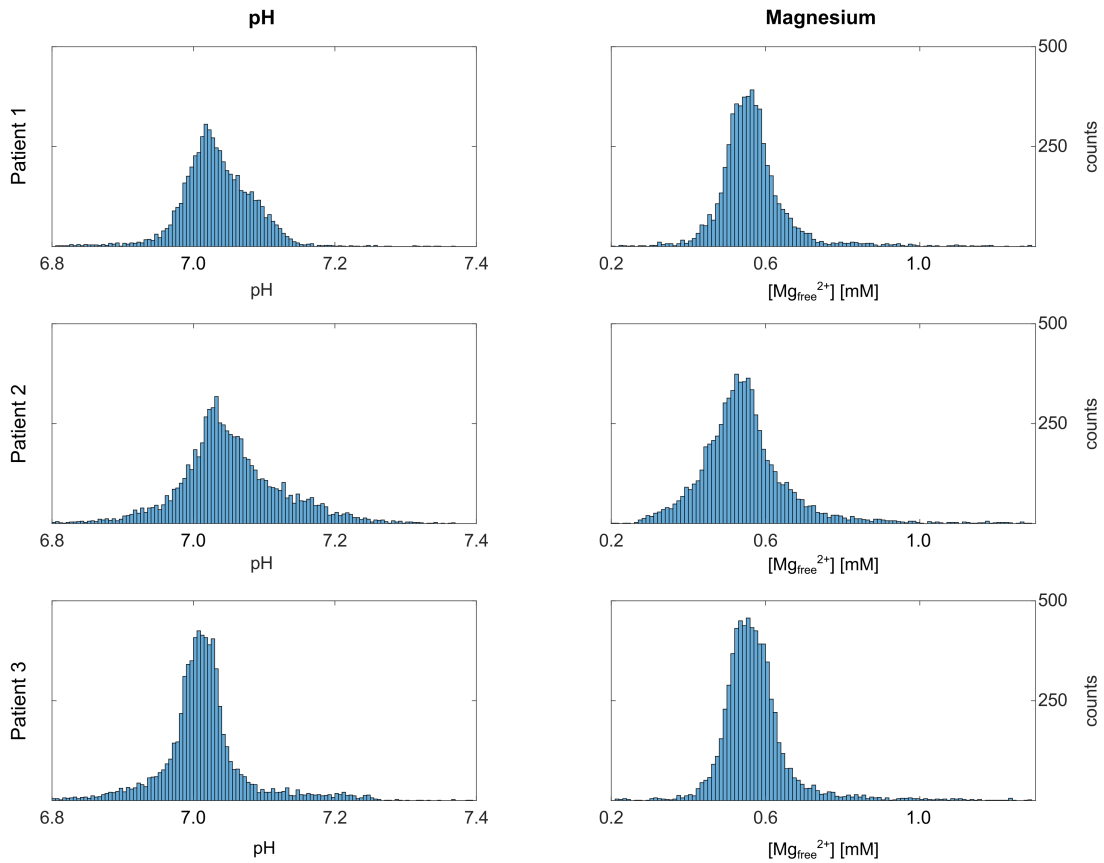


Figure 5.10: Distribution of the calculated pH (left column) and magnesium values (right column) from the 3D ^{31}P MRSI brain data shown for each patient individually (rows). The range for the counts is the same for all histograms and is shown on the right side of the figure. The number of outliers is maximal 133. The sideband on the right side of the pH histograms, i.e. $\text{pH} \geq 7.1$ are associated with voxels from tumor tissue, where higher values were observed (compare Figure 5.7). The right sideband in the magnesium histogram ($[\text{Mg}_{\text{free}}^{2+}] \geq 0.75 \text{ mM}$) can be associated with a mix of voxels from muscle tissue (neck and temples) and from the tumor region.

5.1.3 Summary of value ranges obtained in the analyzed in vivo data

The presented 3D maps from the healthy muscle tissue, as well as from brain tissue of patients with glioblastoma, demonstrate the variability of pH and $[\text{Mg}_{\text{free}}^{2+}]$ values in vivo. First, between different tissue types, and second, between healthy and diseased tissue.

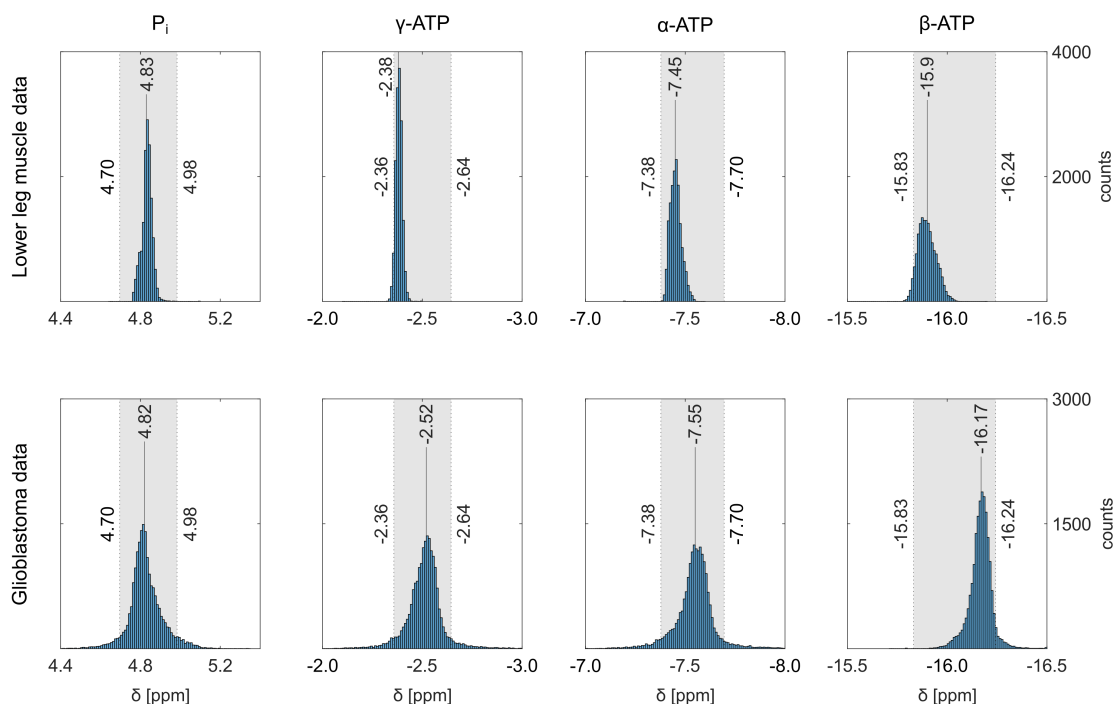


Figure 5.11: Chemical shift ranges obtained in vivo. The distributions of obtained chemical shifts for P_i , γ -, α - and β -ATP (columns) combined for all volunteers of the lower leg muscle measurements (top row) and for all patients from the brain measurements (bottom row) are shown. The respective chemical shift ranges are the same for top and bottom row, in order to show the difference of values between leg muscle tissue and brain tissue. The range for the counts is different and shown on the right side. The median value of the individual distribution is given in each histogram, also indicating the differences between the chemical shifts obtained from muscle and brain tissue. Based on the 5% and 95% percentiles calculated separately for muscle and glioblastoma data, chemical shift ranges were defined for all metabolites, which are assumed to sufficiently reflect all values typically obtained in vivo. For the lower boundary, the lowest 5% percentile was chosen either from muscle or brain data, and for the upper boundary, the highest 95% percentile. The resulting defined ranges are indicated as gray shading.

The overall distributions of the observed chemical shifts of all volunteers combined and all patients combined (Figure 5.11) gives an overview of the chemical shift ranges which are typically obtained in vivo. These ranges, which were defined based on the lowest 5%

5 Results

and highest 95% percentiles of all datasets, are indicated as gray shading, and will be used as reference for expected in vivo ranges in the following sections.

Additionally, an estimation of the value ranges for pH and $[\text{Mg}_{\text{free}}^{2+}]$ calculated with the conventional approaches, is made. For the pH value, values between (6.9 – 7.3), are assumed to be relevant in vivo. For the free magnesium ion concentration $[\text{Mg}_{\text{free}}^{2+}]$ values between (0.2 – 1.3) mM in the brain, and between (0.6 – 1.4) mM in muscle tissue are defined as relevant ranges.

Due to the fact, that in this thesis, the focus will be on the concentration of total magnesium ions $[\text{Mg}_{\text{tot}}]$, and not the concentration of free magnesium ions, an estimation for $[\text{Mg}_{\text{tot}}]$ will be given. Assuming a dissociation constant of $K_D \approx 90 \mu\text{M}$ [27, 48], and a total ATP concentration of 5 mM in muscle [37, 57], and 5 mM in brain tissue [58], the concentration of free magnesium ions can be translated to a concentration of total magnesium of $[\text{Mg}_{\text{total}}] \approx (2.3 - 4.1)$ mM in the brain, and (5.0 – 6.1) mM in muscle (see equation (2.68) in section 2.5.2). In the following sections, the magnesium ion concentration will be often given as the relative magnesium ion concentration $R = \frac{[\text{Mg}_{\text{total}}]}{[\text{ATP}_{\text{total}}]}$, as ratio of total magnesium to total ATP concentration. Not the concentration of free magnesium ions, but the ratio of magnesium to ATP is assumed to be a more suitable quantity considering spectral changes of the ATP resonances. The assumptions above, result in values for R of (1.0 – 1.2) in muscle, and (0.8 – 1.4) in brain, which are assumed to be relevant in vivo. When a different dissociation constant, e.g. $K_D \approx 35 \mu\text{M}$ (from [59]), is assumed, the above calculated values change as follows: $\text{Mg}_{\text{total}} = (5.3 - 6.3)$ mM (muscle), $\text{Mg}_{\text{total}} = (2.8 - 4.2)$ mM (brain) and correspondingly $R = (0.9 - 1.4)$ (brain) and $R = (1.1 - 1.3)$ (muscle).

The approximated values for the total magnesium ion concentration in brain are in line with measurements of [58] reporting $[\text{Mg}_{\text{total}}] \approx 3.5$ mM in brain. For muscle tissue, Seo et al. [60] discussed a value of $\text{Mg}_{\text{total}} \approx 12.6$ mM in muscle, which is higher than the herein estimated values.

Because not only the pH value and the magnesium ion concentration are varying in vivo, but also other physiological parameters, like concentration of other ions (e.g. sodium [46]), which are influencing K_D and pK_a values, the pH range assumed to be relevant is extended to $\text{pH} = (6.8 - 7.4)$ for the investigations in the following. Moreover, the magnesium range assumed to be relevant is extended to $R = (0 - 2)$, because (i) other salts, e.g. sodium and potassium, are assumed to mainly influence the ^{31}P MR signal of ATP, which is the indirect indicator for changes in the magnesium ion concentration, and (ii) some works [60] reported higher magnesium values.

5.2 Characterization of ^{31}P spectral properties in varying chemical environments

With the knowledge of the value ranges for pH and magnesium ion concentration being relevant in vivo, the spectral properties in this value range were investigated. To this end, ^{31}P spectra were acquired from model solutions with different chemical compositions, and the spectral properties investigated, in particular the changes of the chemical shifts. First, an overview of the spectral changes with changing pH value, magnesium ion concentration and potassium ion concentration (as surrogate for the ionic strength in general) will be given. In the second part, the dependencies of the quantified chemical shifts are examined. The detailed description of the changes in linewidths and J-coupling constants are beyond the scope of this work, but an excerpt is presented in Appendix B. Furthermore, it will be assessed in section 6.7.2 of the discussion.

5.2.1 Overview of spectral changes with changing chemical environment

The acquired spectra in model solutions were of high quality, enabling in general a robust quantification of all metabolites contained in the solutions, i.e. P_i , PCr, and the three resonances of ATP (representatively shown for two spectra in Figure 5.12). In the spectrum from the model solution with a high magnesium ion concentration, i.e. $R = 2$ (Figure 5.12A), the multiplets of ATP are well resolved. For the case of a lower magnesium ion concentration, i.e. $R = 0.75$ (Figure 5.12B), only the doublet of α -ATP is visibly resolved. The linewidths of the γ - and β -ATP resonances are very broad resulting in an overlap of the multiplets appearing as one broad peak, which hints towards the system being in the intermediate exchange regime (see section 2.2.3).

The spectral changes with changing pH and changing magnesium ion concentration are visualized for representative subsets in Figures 5.13 and 5.14. With increasing pH value (Figure 5.13), the chemical shifts of P_i and ATP shift upfield, meaning towards higher resonance frequency. Hereby, the δ_{P_i} and δ_γ show the largest change from pH 6.8 to 7.4, followed by δ_β . The chemical shift of α -ATP, δ_α , shows only minor changes with changing pH.

For increasing magnesium ion concentration from $R = 0$ to 2 (Figure 5.14), the chemical shifts of P_i and ATP also shift upfield. Hereby, the resonance of β -ATP shifts the most, followed by γ - and α -ATP. The resonance of P_i shows only a visible change when the magnesium ion concentration is increased to $R = 2$. With changing R , not only the chemical shifts, but also the linewidths of the resonances of ATP change. For the case

5 Results

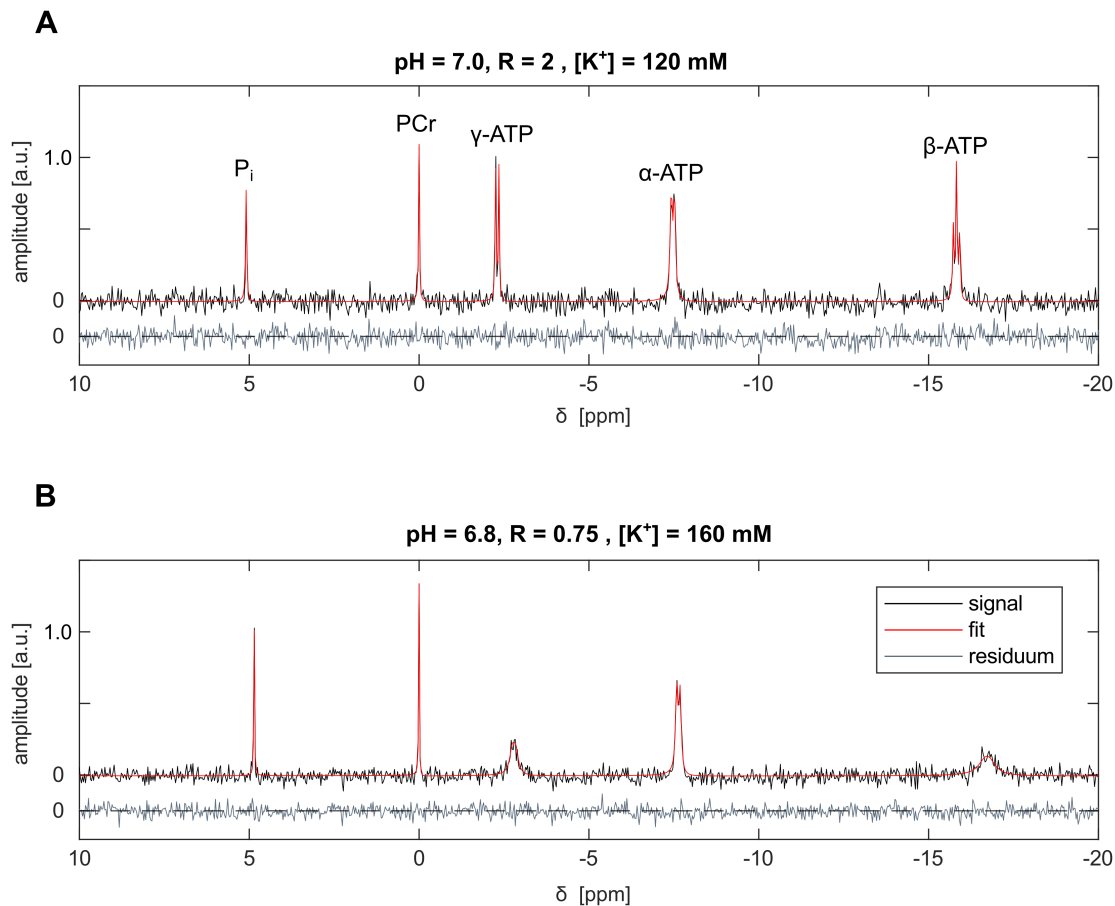


Figure 5.12: Representative ³¹P MR spectra acquired from two different model solutions at $B_0 = 9.4$ T: (A) model solution with pH = 7.0, $R = 2$, and $[K^+] = 120$ mM, (B) model solution with pH = 6.8, $R = 0.75$, and $[K^+] = 160$ mM. The fitted signal (red) is overlaid with the acquired signal (black), and the fit residuum is shown below (grey). All metabolites contained in the solutions could be quantified by the fit, resulting in a noise-like residuum. From left to right: inorganic phosphate (P_i), phosphocreatine (PCr), and the three resonances of adenosine-5'-triphosphate (ATP). Depending on the chemical environment, not only the chemical shifts, but also the linewidths change.

of no magnesium, i.e. $R = 0$, the linewidths of the ATP resonances are narrow enough to visually distinguish the multiplets. When the ratio of $[Mg_{tot}]$ to $[ATP_{tot}]$ is around one half, i.e. $R = 0.5$, the resonance lines of ATP are very broad, especially for β -ATP. With an further increase in R , the linewidths narrow again, and the multiplets are visually resolvable for a high magnesium ion concentration, e.g. $R = 2$.

The spectral changes with varying ionic strength, here investigated by means of changes of the concentrations of potassium and sodium ions are shown in Figure 5.15. With increasing $[K^+]$ and $[Na^{2+}]$, the resonances of P_i and ATP shift upfield, whereby γ - and β -ATP show the strongest change.

5.2 Characterization of ^{31}P spectral properties in varying chemical environments

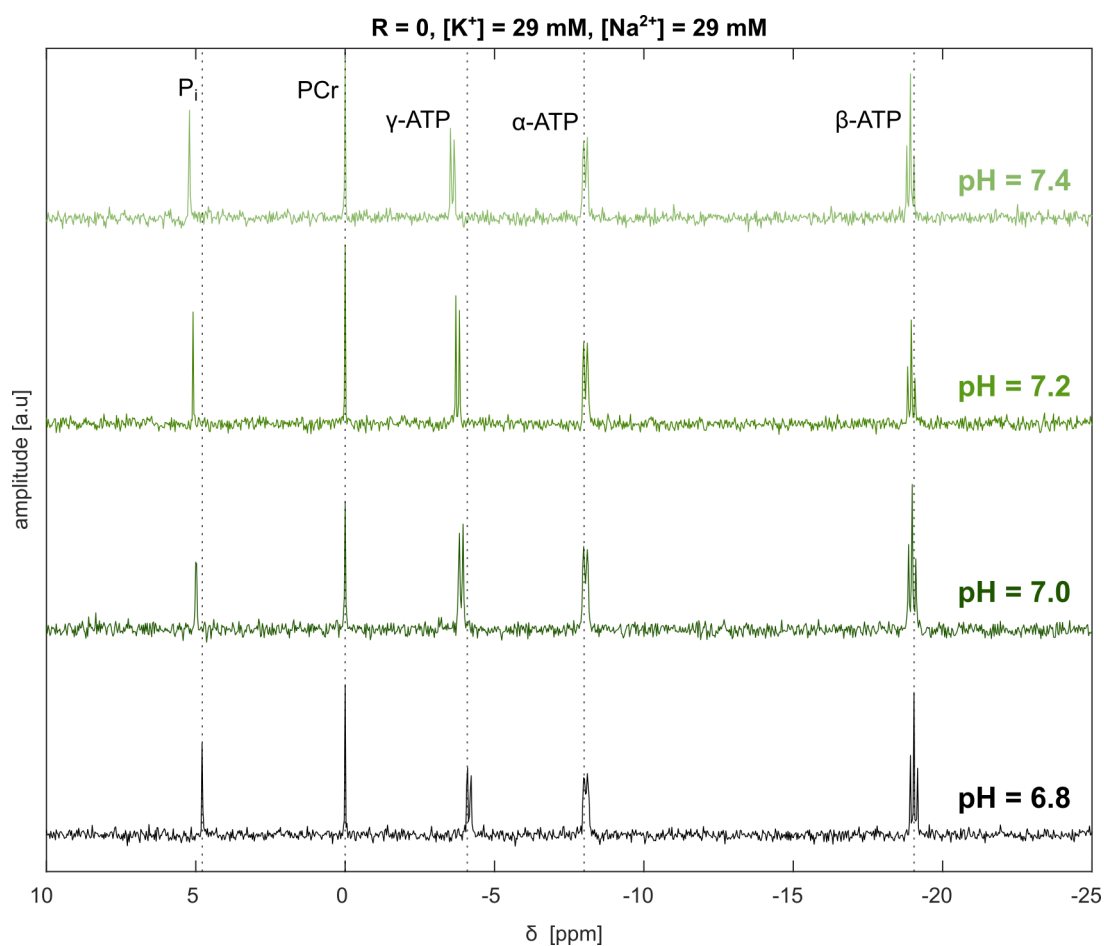


Figure 5.13: Spectral changes with changing pH value, shown representatively for the subset of model solutions with $R = 0$, $[\text{K}^+] = 29 \text{ mM}$, and $[\text{Na}^{2+}] = 29 \text{ mM}$. With increasing pH value, the chemical shifts of P_i and ATP shift upfield, i.e. to higher resonance frequencies. Hereby, the δ_{P_i} and δ_{γ} change the most, followed by δ_{α} . The resonance of $\alpha\text{-ATP}$ shows only minor shifts due to the changing pH value.

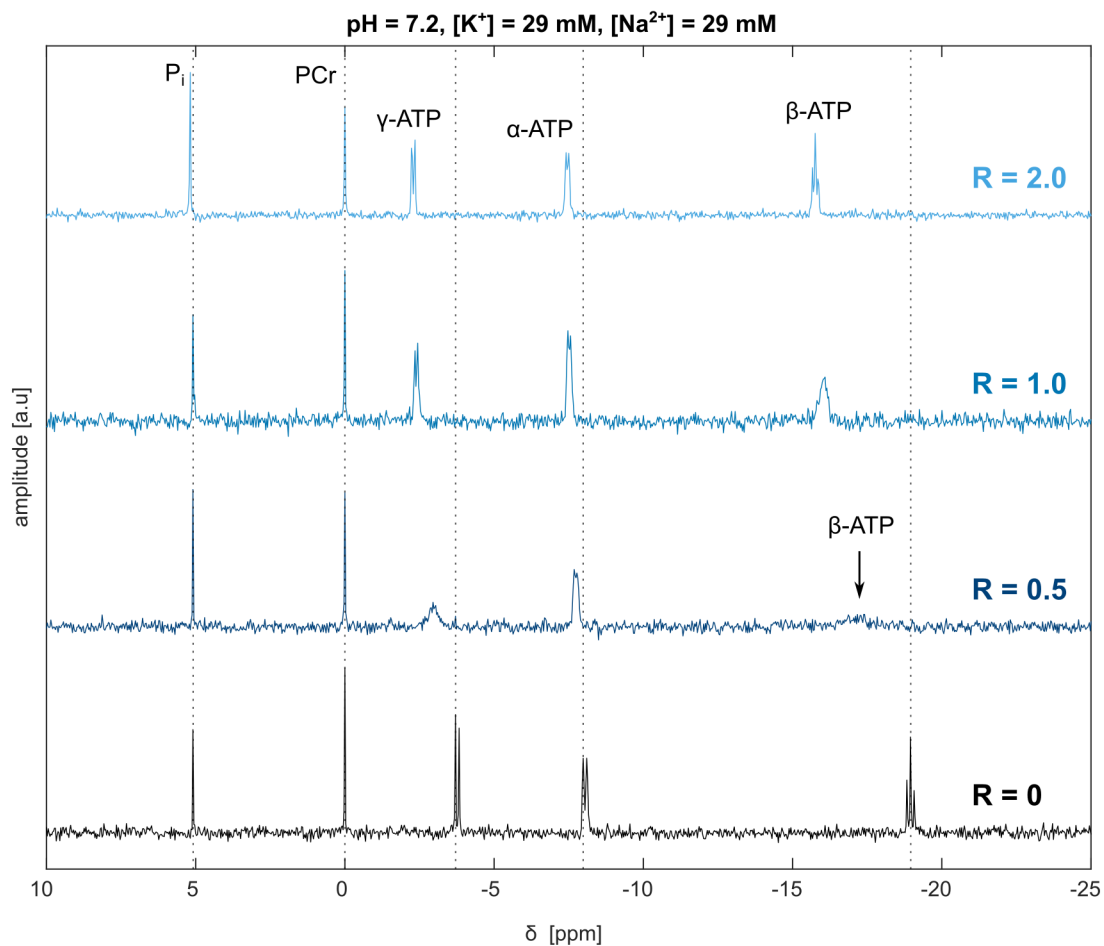


Figure 5.14: Spectral changes with changing magnesium ion concentration R , shown for the subset of model solutions with $\text{pH} = 7.2$, $[\text{K}^+] = 29 \text{ mM}$, and $[\text{Na}^{2+}] = 29 \text{ mM}$. With increasing R , the chemical shifts of P_i and ATP shift upfield, i.e. to higher resonance frequencies. Also the spectral lineshape changes with changing R . For the case of no magnesium, i.e. $R = 0$, and the case of high magnesium ion concentration, i.e. $R = 2$, the multiplets of ATP are well resolved. For intermediate magnesium ion concentrations, i.e. $R = 0.5$, the resonances of ATP are very broad resulting in an overlap of the multiplet signals appearing as singlets.

5.2 Characterization of ^{31}P spectral properties in varying chemical environments

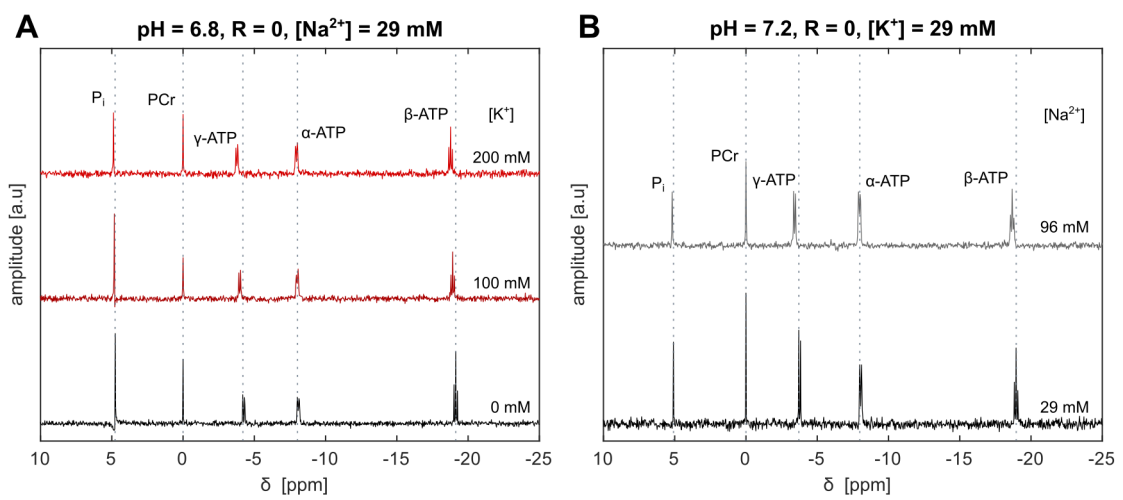


Figure 5.15: Spectral changes with changing potassium (A) and sodium (B) concentration. The resonances of P_i and ATP shift upfield with increasing $[\text{K}^+]$ and $[\text{Na}^{2+}]$, whereby γ - and β -ATP show the largest changes.

5.2.2 Quantified chemical shifts in dependence on the chemical environment

After this overview of the spectral changes due to different chemical environments, the dependencies of the quantified chemical shifts on the pH value, the magnesium ion concentration and the potassium ion concentration will be investigated for the value ranges covered with the model solution experiments. It should be noted, that all following considerations refer only to the resonances of P_i and ATP. As described in 2.2.1, PCr is used as reference substance.

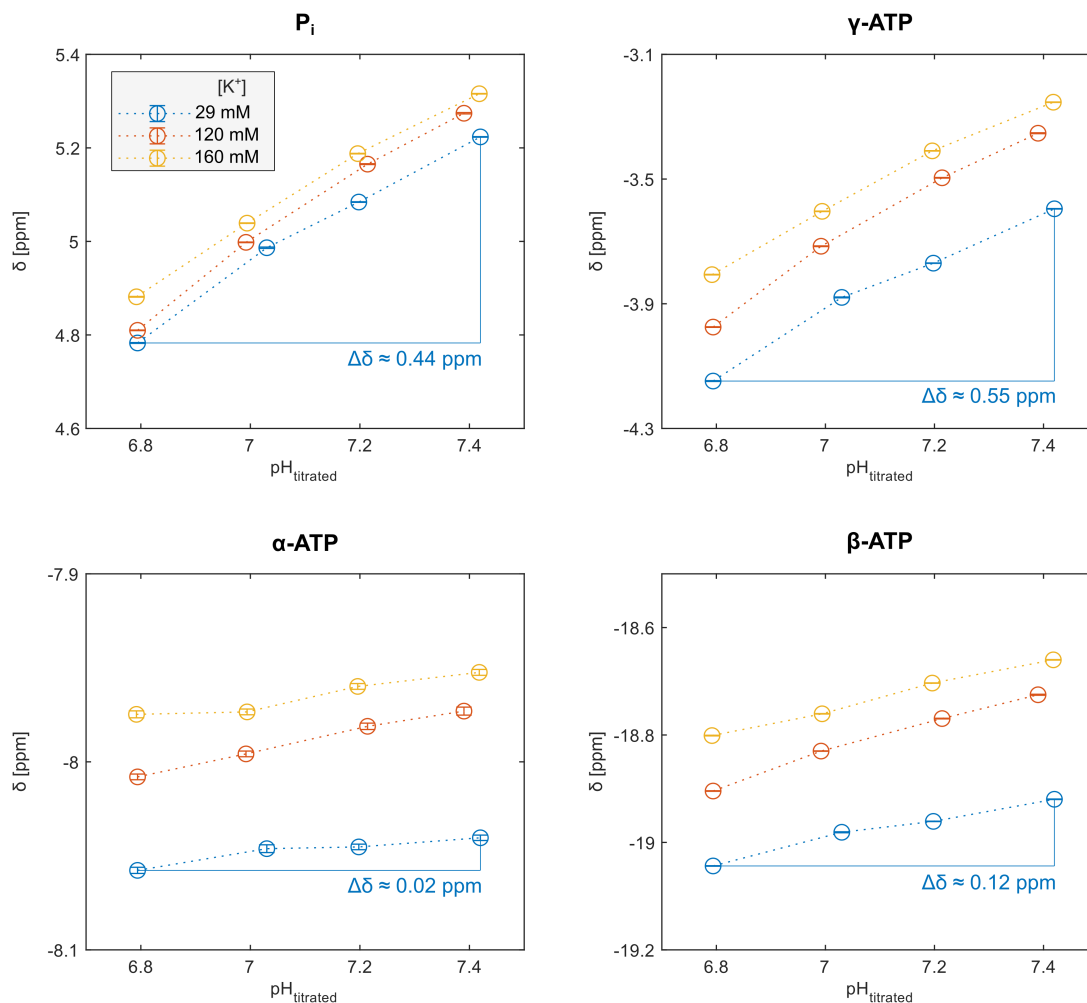


Figure 5.16: Quantified chemical shifts δ measured in the subsets with $R = 0$ and $[Na^{2+}] = 29$ mM, in dependency on the titrated pH value of the respective model solution. The chemical shifts of P_i and ATP are shown for the different subsets with $[K^+] = 29$ mM (blue), 120 mM (red), 160 mM (yellow). For all shown metabolites, δ increases approximately linearly with increasing pH in the investigated value range, whereby δ_γ and δ_{P_i} show the largest change from $pH = 6.8$ to 7.4.

5.2 Characterization of ^{31}P spectral properties in varying chemical environments

With increasing pH value and increasing potassium ion concentration, an approximately linear increase can be observed for all resonances for the investigated pH range of $\text{pH} = (6.8 - 7.4)$ (Figure 5.16) and potassium ion range of $[\text{K}^+] = (29 - 160)$ mM (Figure 5.17). For the representative subset shown here, i.e. $R = 0$, the strongest change over the investigated pH range was found for δ_γ with about $+0.55$ ppm, followed by δ_{P_i} with about $+0.44$ ppm. δ_β changes by about $+0.12$ ppm, and δ_α by about $+0.02$ ppm. With changing potassium ion concentration (Figure 5.17), δ_γ shows the strongest change with about $+0.34$ ppm over the range of $[\text{K}^+] = (29 - 160)$ mM, followed by δ_β . δ_α and δ_{P_i} change by about $+0.1$ ppm.

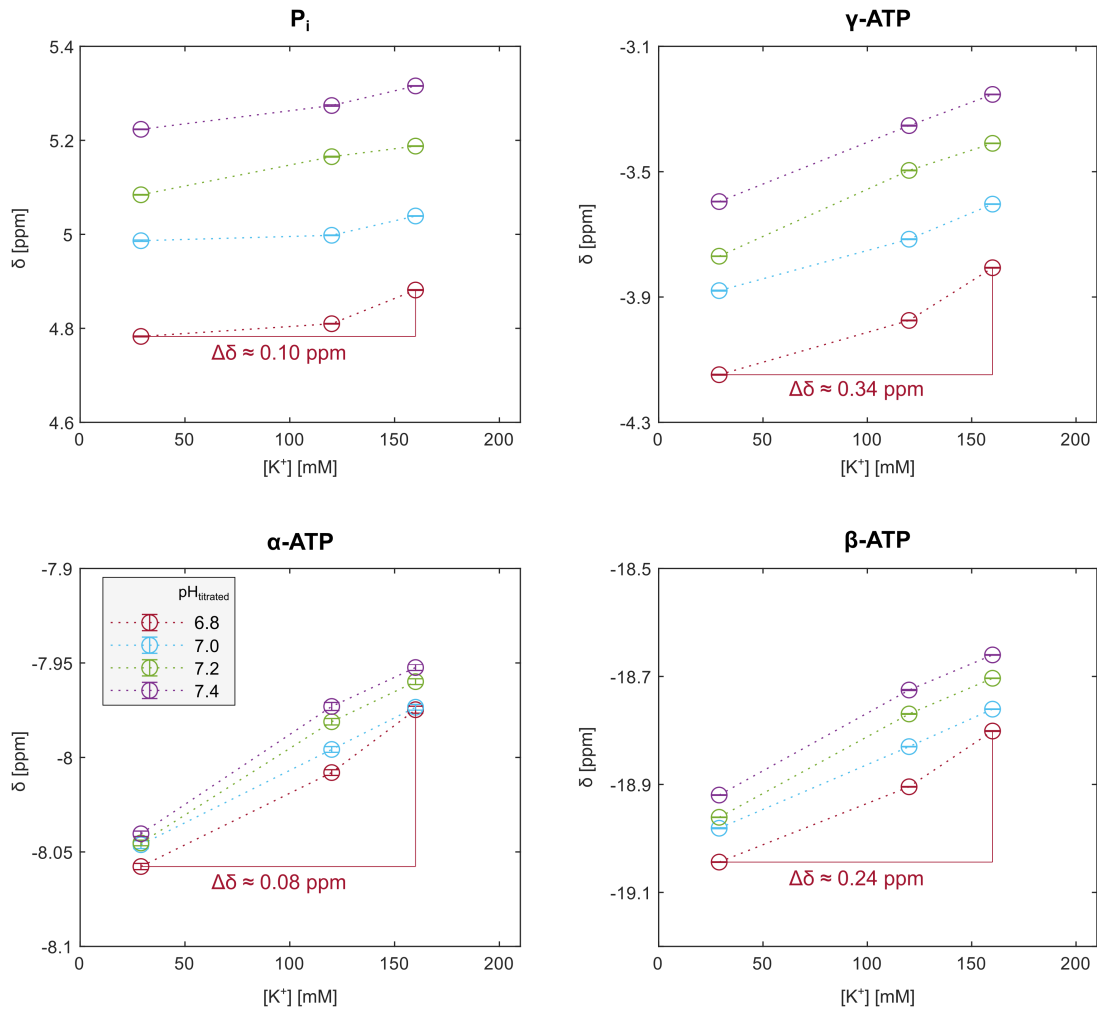


Figure 5.17: Quantified chemical shifts δ measured in the subsets with $R = 0$ and $[\text{Na}^{2+}] = 29$ mM, in dependency on the potassium concentration $[\text{K}^+]$. The chemical shifts of P_i and ATP are shown for the different subsets with $\text{pH} = 6.8$ (red), 7.0 (blue), 7.2 (green) and 7.4 (purple). For all shown metabolites, δ increases approximately linearly with increasing $[\text{K}^+]$, whereby δ_γ and δ_β show the largest increase from $[\text{K}^+] = 29$ to 160 mM.

5 Results

The dependence of the chemical shifts on the magnesium ion concentration R shows a non-linear relationship for the three resonances of ATP (Figure 5.18). For low and intermediate magnesium ion concentrations, i.e. $R = (0 - 0.75)$, δ_γ , δ_α and δ_β strongly increases with increasing R . This increase becomes smaller for higher R , until the chemical shifts reach a plateau around $R \geq 2$. The strongest change of the chemical shift over the range of $R = (0 - 2)$, shows β -ATP with about +3 ppm for pH = 6.8, followed by γ -ATP with about +2 ppm and α -ATP with about +0.7 ppm.

The measured chemical shifts of P_i do not show a strong change between $R = 0$ and 1. Only for a high magnesium ion concentration of $R = 2$, the quantified chemical shifts are about +0.05 ppm higher compared to those at $R = 1$.

The chemical shift ranges, which were determined to be relevant in vivo (see section 5.1.3), are indicated as dashed lines in Figure 5.18. For the ATP resonances, these chemical shift ranges translate to values of $R \geq 0.5$. Interestingly, the corresponding ranges for R are different for the three ATP resonances. Based on the obtained chemical shifts from the model solutions, for δ_α , the chemical shift range obtained in vivo corresponds to a rather broad range of $R \approx 0.5$ to values larger than $R = 2$. In contrast to that, for δ_γ and δ_β , the corresponding ranges for R are narrower, covering values from $R \approx (1 - 2)$ (for pH = 6.8). Another important observation is that the chemical shifts of P_i obtained from the model solutions are only in the range relevant in vivo for the subset with pH = 6.8. For the subset with pH = 7.4, the measured chemical shifts are higher than the chemical shifts obtained in vivo.

Due to the fact, that the $\delta(pH)$ and $\delta(K)$ dependency in the investigated range can be assumed to be linear, whereas $\delta(R)$ shows a non-linear relation, the modelling of $\delta(R)$ will be the starting point for the multi-dimensional models in the next section.

5.2 Characterization of ^{31}P spectral properties in varying chemical environments

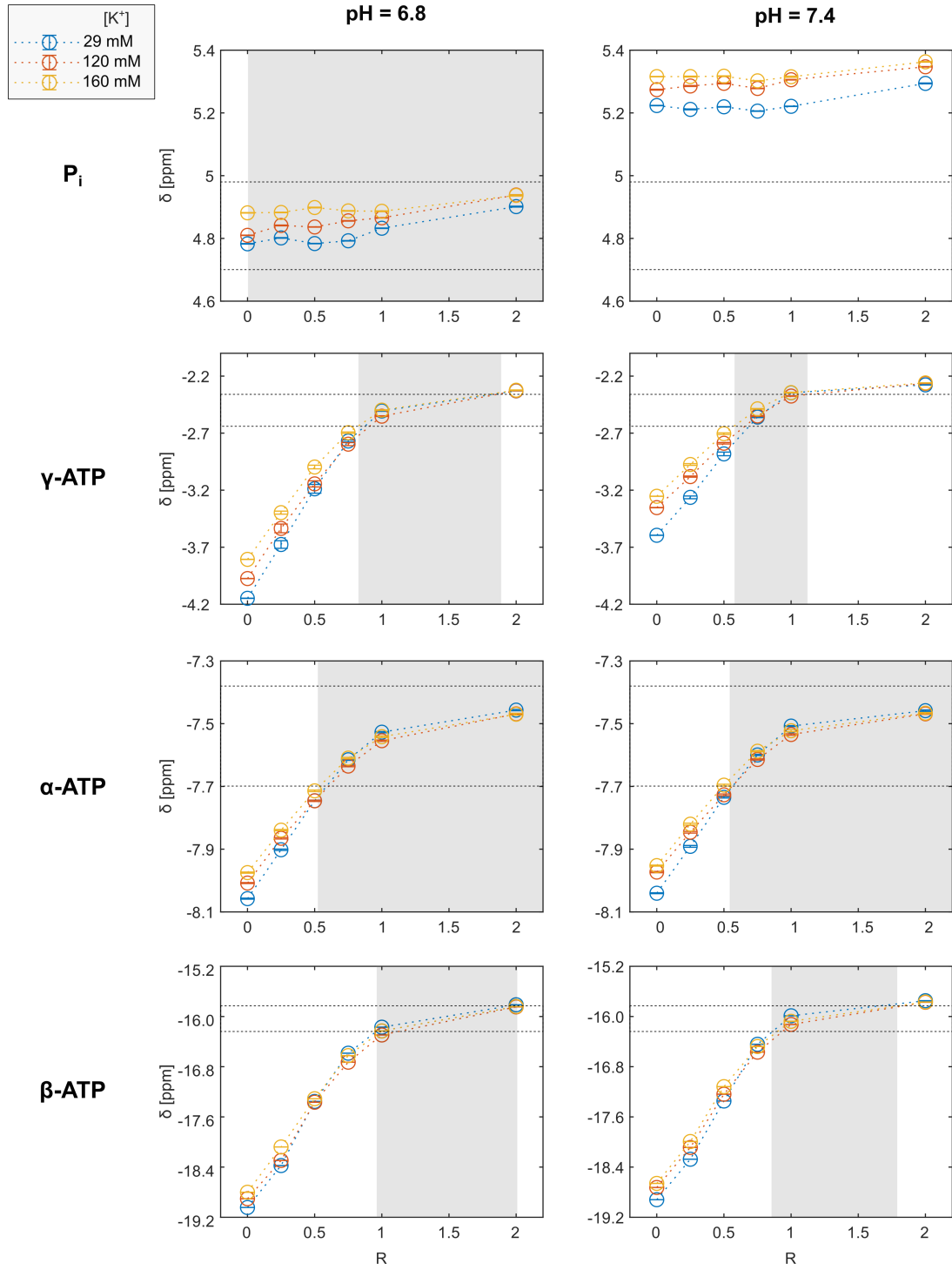


Figure 5.18: Quantified chemical shifts δ measured in the subsets with $\text{pH} = 6.8$ (left column) and $\text{pH} = 7.4$ (right column) in dependence on R . The chemical shifts of P_i and ATP are shown for the different subsets with $[\text{K}^+] = 29 \text{ mM}$ (blue), 120 mM (red), 160 mM (yellow), and $[\text{Na}^{2+}] = 29 \text{ mM}$. The chemical shift ranges, which were determined to be relevant in vivo (see section 5.1.3), are indicated as dashed lines. For the ATP resonances, these chemical shift ranges translate to values for R in the range of $(0.5 - 2)$ (gray shading), for both shown pH values. For P_i , only the subset with $\text{pH} = 6.8$ lies within the chemical shift range observed in vivo.

5.3 Modelling of the ATP chemical shifts

For a first proof-of-principle of the proposed look-up approach, the focus will be on the chemical shift dependencies of the three resonances of ATP. In principle, the implemented algorithm can be extended by further parameters, i.e. chemical shifts of other metabolites and/or linewidths and J-coupling constants. However, for the first proof-of-principle, only the chemical shifts ($\delta_\gamma, \delta_\alpha, \delta_\beta$) will be used. The use of the ATP resonances for the determination of pH is also beneficial in regard of the measurement time, compared to the use of the P_i resonance in the conventional modified Henderson Hasselbalch equation. A potentially reduced measurement time is of importance for the application in vivo.

In order to achieve an accurate assignment of input parameters to quantities describing the chemical environment via a look-up table, first of all, a sufficient number of entries, i.e. data points describing the relation between chemical shift and pH, magnesium ion concentration, and potassium ion concentration, are required. Due to the fact, that only a limited number of model solutions with different chemical properties can be prepared and measured, the additional entries will be generated by interpolating the entire value space. Moreover, an interpolation has the benefit of suppressing the noise on the measured chemical shifts, which fluctuate due to experimental influences, e.g. temperature. For this interpolation, a model is required describing the functional relation $\delta(pH, Mg, K)$.

The qualitative investigations of the chemical shift dependencies on pH, relative magnesium ion concentration R , and potassium ion concentration $[K^+]$ of the previous section (5.2), will be used as the basis for the development of such a model. Hereby, three different approaches to develop this functional relation will be shown. To improve the convergence of the final multi-dimensional fit functions, one-dimensional models are the starting point of the model development. The non-linear dependence of δ on the magnesium ion concentration (cf. section 5.2.2), will be the starting point for all three models, but the model function is however different (cf. Chapter 3). In the second step of the model development, the parameters in the model equations $\delta^{\text{model}}(Mg)$ which show a dependency on pH and $[K^+]$ are linearized, which is based on findings from section 5.2.

The comparison of the three different models with different number of parameters and underlying assumptions (cf. Chapter 3) will be assessed briefly at the end of the chapter on the basis of different metrics. Hereby, the focus lies not on finding the model describing the exact chemical environment, but more on finding a model that provides a sufficient description of the dependencies in the entire required value range, and hence being suitable for the application in vivo.

Important to mention is the use of different quantities describing the magnesium ion concentration in the different models. In the heuristic model (section 5.3.1) as well as in the London model (section 5.3.2), the quantity $R = \frac{[Mg_{total}]}{[ATP_{total}]}$ is used. For the Hill model (section 5.3.3), the absolute total magnesium ion concentration $[Mg_{total}]$ is used. Moreover, it should be noted, that in the following, the potassium ion concentration $[K^+]$ will be denoted simply as K , and the total magnesium ion concentration $[Mg_{tot}]$ as Mg_{tot} , whenever used in a function, e.g. $\delta(Mg_{tot}, pH, K)$. For all models, the results are shown graphically only for γ -ATP. The plots for α - and β -ATP for the model based on the Hill equation can be found in Appendix C.

5.3.1 Model with heuristic ansatz

The heuristically developed one-dimensional function for $\delta(R)$ (equation (3.1) in section 3.1) describes the slope of the measured chemical shifts sufficiently (Figure 5.19). The adjusted R^2 is > 0.99 for all shown subsets. For an intermediate magnesium ion concentration, i.e. $R = 1$, a systematic deviation between the fitted function and the measured chemical shifts can be observed. For all shown subsets, the data points for $R = 1$ lie above the fitted curves.

For α - and β -ATP, the fitted curves look similar to the ones for γ -ATP, but with a smaller dispersion for different pH values (as already seen in section 5.2.2). The adjusted R^2 for β -ATP are > 0.96 , and for α -ATP > 0.99 . Also for α - and β -ATP, the measured chemical shifts for $R = 1$ lie systematically above the fitted curves.

By investigating the determined parameters concerning their dependencies on pH and $[K^+]$ (Figure 5.20), the following assumptions can be made:

- Linear dependency of A on pH and $[K^+]$
- Linear dependency of C on pH and $[K^+]$
- No clear trend of d in dependency on pH and $[K^+]$ \longrightarrow d modelled as constant

Based on these observations, in the next step, the parameters A and C in equation (3.1) are changed as follows:

$$A = m_{A1} \cdot (pH - 7.1) + m_{A2} \cdot K + b_A \quad (5.1)$$

$$C = m_{C1} \cdot (pH - 7.1) + m_{C2} \cdot K + b_C \quad (5.2)$$

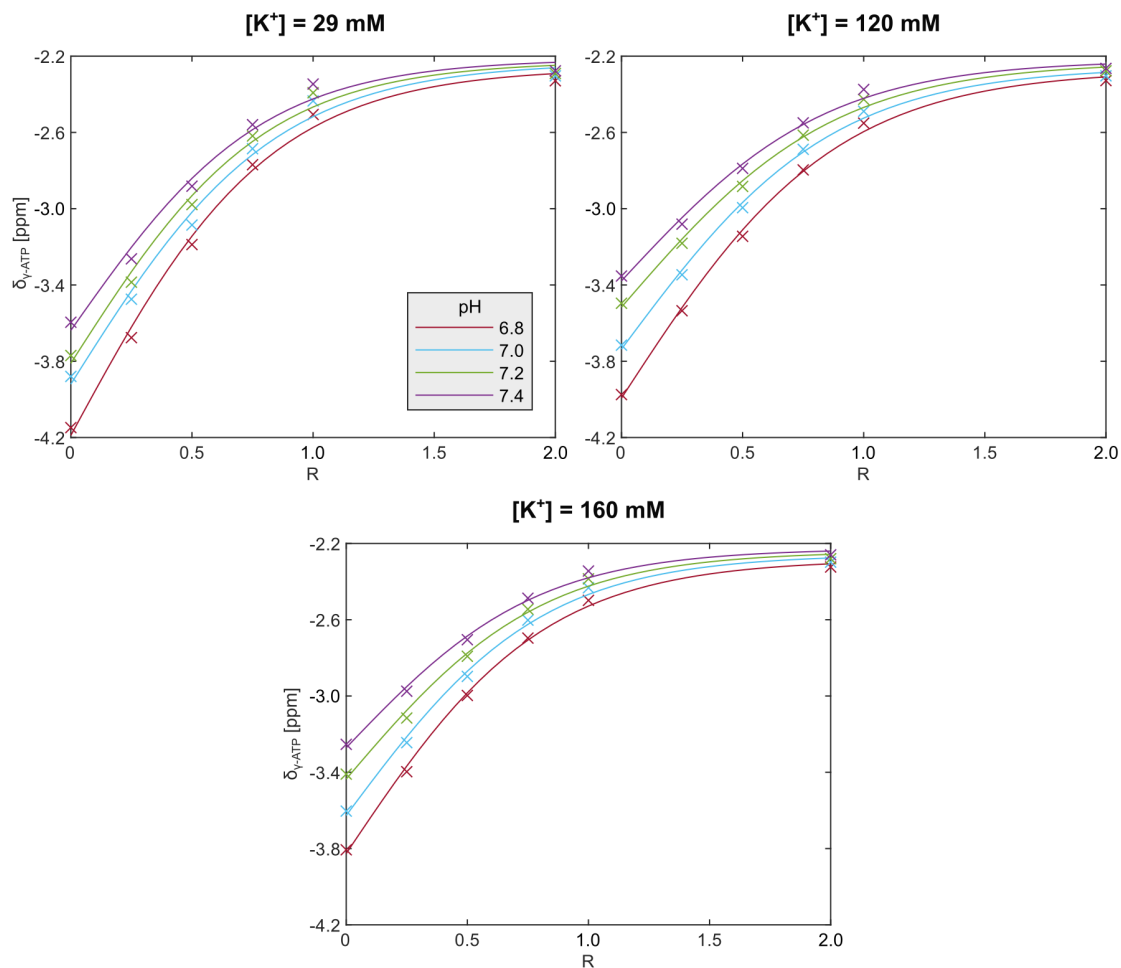


Figure 5.19: One-dimensional function $\delta_{\gamma}^{\text{Heur}}(R)$ fitted according to equation (3.1) (cf. section 3.1) for the subsets with $[K^+] = 29, 120, 160 \text{ mM}$, and for the pH values (6.8 – 7.4) (colors). The function $\delta_{\gamma}^{\text{Heur}}(R)$ describes the course of the measured chemical shifts adequately, but shows a systematic deviation for values with $R = 1$, for which the measured chemical shifts lie above the fitted curves.

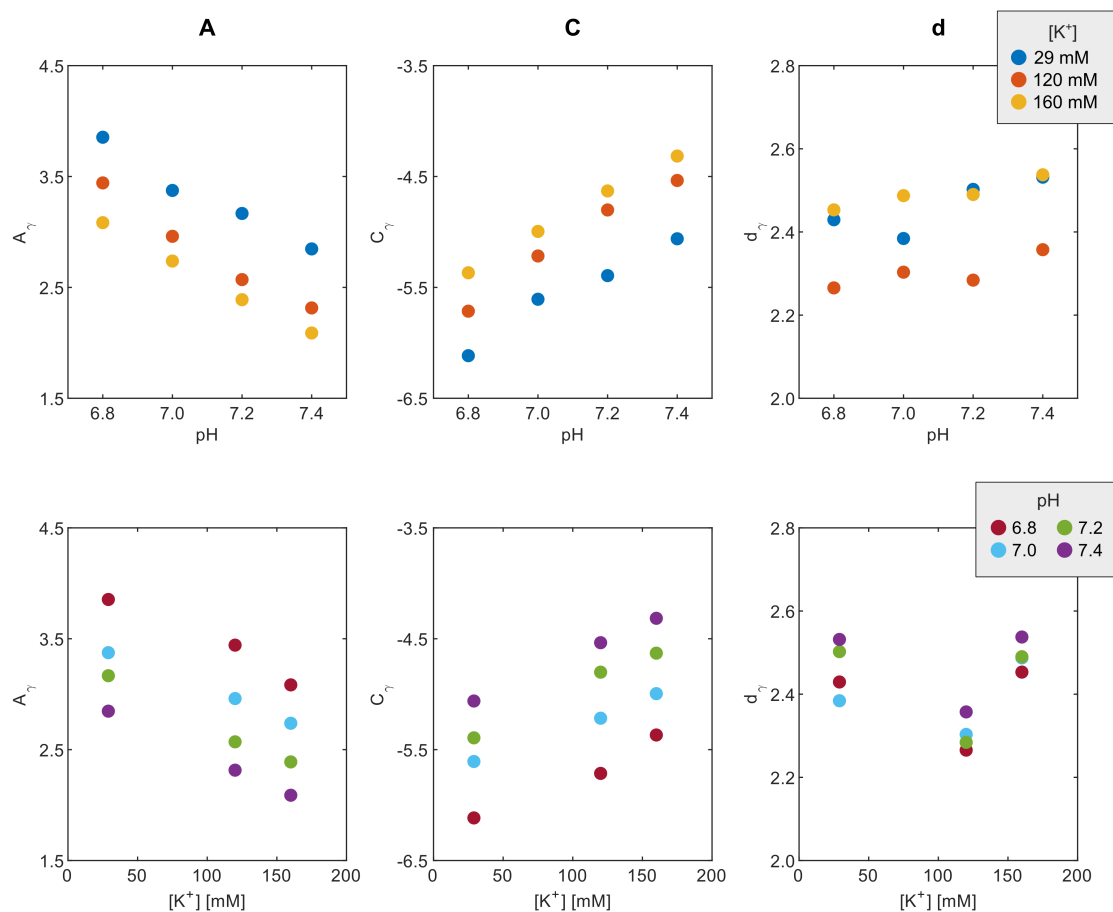


Figure 5.20: Fit parameters of the heuristically developed function $\delta^{\text{Heur}}(R)$ (equation (3.1) in section 3.1) for γ -ATP determined from the individual one-dimensional fits of the subsets with $[K^+] = (29, 120, 160)$ mM, plotted against the pH value (top row) and the potassium ion concentration (bottom row). The following parameters were determined by the fit: A , describing the chemical shift range; C , describing the offset; and d , describing the bend of the sigmoid curve. For parameters A and C , an approximately linear dependency on pH and $[K^+]$ can be observed. Parameter d is assumed to fluctuate around the mean value of $\bar{d}_\gamma \approx 2.4$ in the investigated pH and $[K^+]$ range.

5 Results

With this extended version of equation (3.1) a multi-dimensional fit $\delta(R, pH, K)$ was performed for γ -, α - and β -ATP (representatively shown for γ -ATP in Figure 5.21). The resulting fit parameters are given in Table 5.1. The values for the adjusted R^2 and the mean and maximal absolute deviations will be given at the end of this chapter and compared to the values from the other two models (Table 5.4).

The findings from section 5.2.2 are reflected in the resulting fit parameters (Table 5.1):

- Strongest pH dependency for γ -ATP, only a slight one for α - and β -ATP (see parameters m_{A1} and m_{C1})
- Strongest K dependency for β -ATP, followed by γ - and α -ATP (see parameters m_{A2} and m_{C2})

The parameter d describing the bend of the sigmoid curve is approximately the same for γ -, α - and β -ATP.

Table 5.1: Fit parameters of the multi-dimensional function $\delta^{\text{Heur}}(R, pH, K)$ (equation (3.1) with equations (5.1) and (5.2)) determined for the γ -, α - and β -ATP resonance. Parameters m_{A1} and m_{C1} describe the linear dependency on pH, m_{A2} and m_{C2} the linear dependency on $[K^+]$, b_A and b_C the chemical shift offsets, and d the slope of the sigmoid curve.

parameter	unit	γ -ATP	α -ATP	β -ATP
m_{A1}	$\left[\frac{\text{ppm}}{(\text{pH}-7.1)} \right]$	-1.58	-0.05	0
m_{C1}	$\left[\frac{\text{ppm}}{(\text{pH}-7.1)} \right]$	1.71	0.06	0.20
m_{A2}	$10^{-3} \left[\frac{\text{ppm}}{\text{mM}} \right]$	-5.7	-1.8	-6.5
m_{C2}	$10^{-3} \left[\frac{\text{ppm}}{\text{mM}} \right]$	4	1.6	5.6
b_A	[ppm]	3.51	1.31	7.27
b_C	[ppm]	-5.74	-8.74	-22.82
d	-	2.5	2.4	2.3

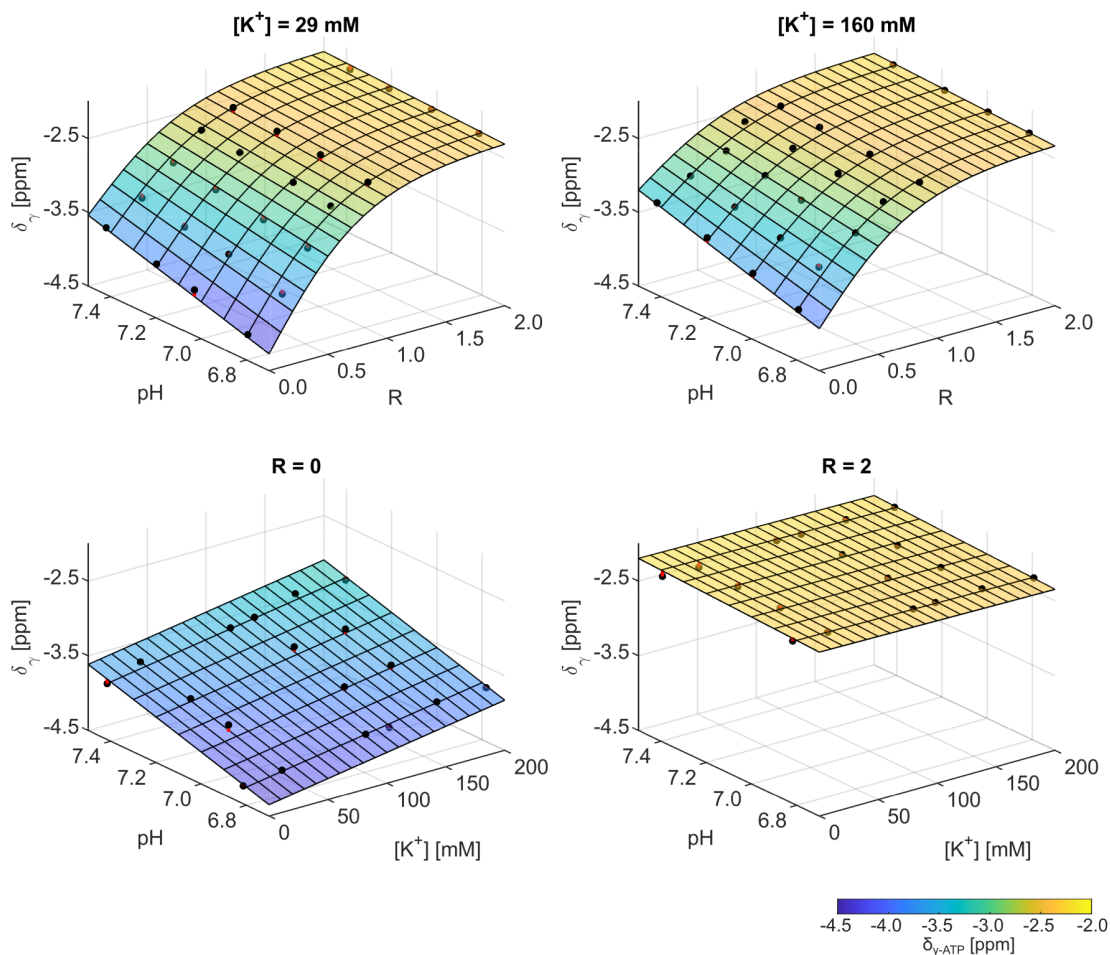


Figure 5.21: Multi-dimensional fit of the heuristically developed function $\delta_{\gamma}^{\text{Heur}}(R, pH, K)$ determined for γ -ATP. The fitted function is illustrated for the subspace $\delta(R, pH)$ with $[K^+] = 29$ and 160 mM (top row), and for the subspace $\delta(pH, K)$ with $R = 0$ and 2 (bottom row). For high magnesium ion concentration, i.e. $R = 2$, the chemical shift of γ -ATP appears to be independent on pH and $[K^+]$, whereas for no magnesium ion concentration, δ_{γ} shows a linear dependency on pH and $[K^+]$. The deviation of the fitted curve from the measured chemical shifts (black dots) is illustrated with red pins.

5.3.2 Model based on the London equation

The model function derived from the London equation yields already a two-dimensional functional dependency for δ on the magnesium ion concentration, as well as on the pH value (equation (3.6) in section 3.2). Although the herein derived function $\delta(R, pH)$ is an oversimplification, it describes the course of the data points adequately (Figure 5.22). The values for the adjusted R^2 are ≥ 0.97 for γ -, β - and α -ATP. However, for all shown subsets, i.e. $[K^+] = 29, 120, 160$ mM, the fitted curve underestimates the measured chemical shifts for $R \geq 1$, and overestimates them for $0.25 \leq R \leq 0.75$. The functions for α - and β -ATP show similar results.

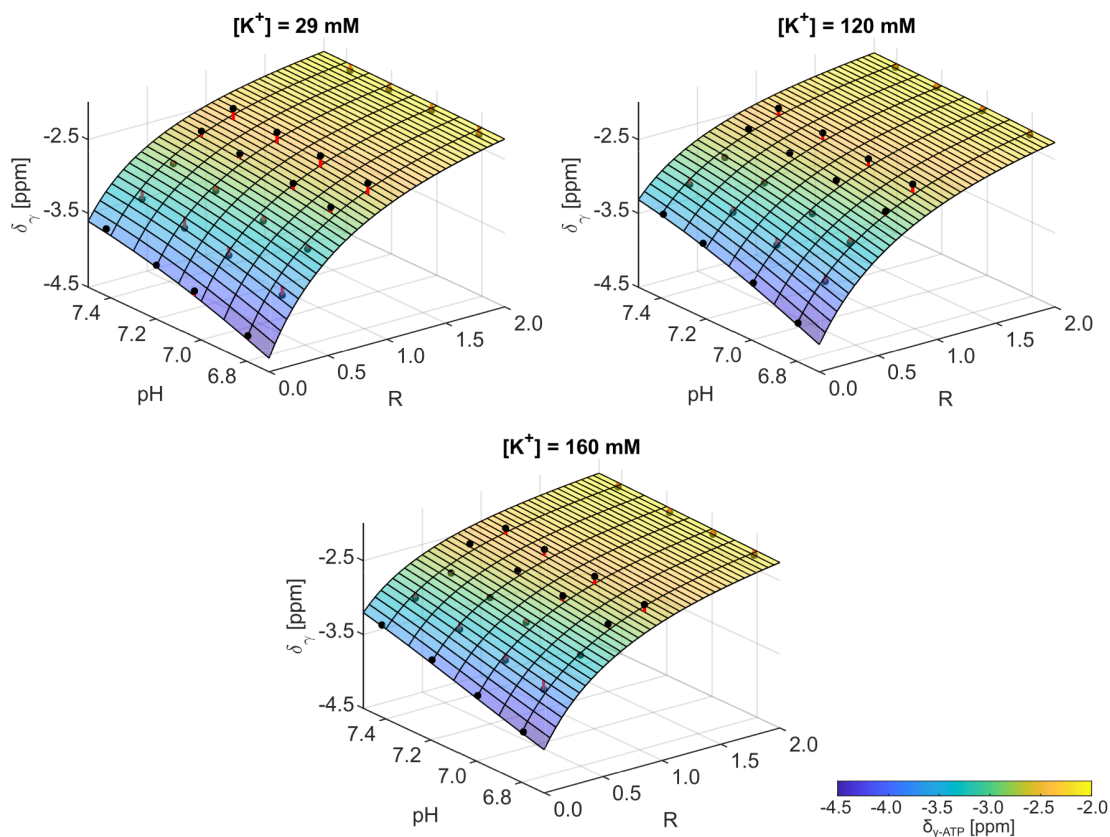


Figure 5.22: Two-dimensional function $\delta_{\gamma}^{\text{London}}(R, pH)$ fitted according to equation (3.6) (cf. section 3.2) for the subsets with $[K^+] = 29, 120, 160$ mM. The deviation of the fitted curve from the measured chemical shifts (black dots) is illustrated with red pins. The fitted curve systematically underestimates the course of the data points for $R = 1$, and overestimates it for $0.25 \leq R \leq 0.75$.

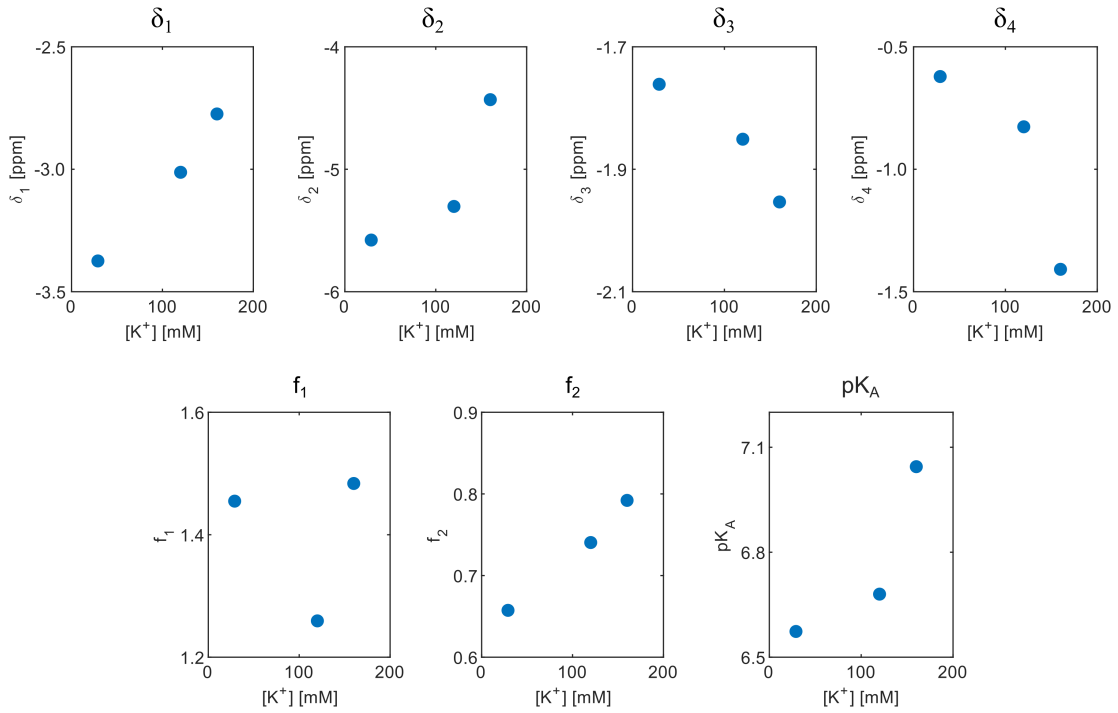


Figure 5.23: Fit parameters for the model function derived from the London equation $\delta_{\text{London}}(R, pH)$ (equation (3.6) in section 3.2) determined for γ -ATP, plotted against the potassium concentration $[K^+]$. For the limiting chemical shifts δ_i , with $i = 1, \dots, 4$, and the fraction f_2 representing the ratio of $\frac{K_D}{K_{D'}}$, a linear dependency on the potassium ion concentration can be assumed. For the ratio f_1 , no clear trend with changing $[K^+]$ is visible. The pK_A value determined from the fit increases with increasing $[K^+]$, hence for pK_A an approximately linear dependency is assumed.

When analyzing the dependency of the determined fit parameters on the potassium ion concentration of the corresponding subset (Figure 5.23), the following assumptions can be made:

- Linear dependency of the limiting chemical shifts δ_i , with $i = 1, \dots, 4$, on $[K^+]$
- Linear dependency of the fraction f_2 and the pK_A value on $[K^+]$
- No clear trend of the fraction f_1 with changing $[K^+]$ \longrightarrow modelled as constant

The fit parameters for the α - and β -ATP chemical shifts show comparable trends as described above.

5 Results

Based on the derived assumptions, the parameters in the model function (equation (3.6)) are changed as follows:

$$\delta_1 = m_1 \cdot K + b_1 \quad (5.3a)$$

$$\delta_2 = m_2 \cdot K + b_2 \quad (5.3b)$$

$$\delta_3 = m_3 \cdot K + b_3 \quad (5.3c)$$

$$\delta_4 = m_4 \cdot K + b_4 \quad (5.3d)$$

$$pK_A = m_p \cdot K + b_p \quad (5.3e)$$

$$f_2 = m_f \cdot K + b_f. \quad (5.3f)$$

With this extended version of equation (3.6) a multi-dimensional fit $\delta(R, pH, K)$ was performed for γ -, α - and β -ATP (representatively shown for γ -ATP in Figure 5.24). From the fit parameters of the multi-dimensional function (Table 5.2), the following observations can be made:

- The limiting chemical shifts δ_i with $i = 1, \dots, 4$, are dependent on $[K^+]$ in approximately the same order of magnitude (see parameters m_i). Hereby, α -ATP shows the weakest dependency on $[K^+]$.
- For the pK_A value, the strongest dependency on $[K^+]$ is observed for α -ATP, followed by β - and γ -ATP (see parameter m_p).
- The dependency of the fraction $f_2 = \frac{K_D}{K_{D'}}$ on $[K^+]$ seems to be the strongest for β -ATP, followed by α -ATP.
- The dependency of f_2 is 0 for γ -ATP, contradicting the trend in Figure 5.23.
- The fraction f_1 is approximately the same for all three ATP chemical shifts (see parameter f_1).

The values for the adjusted R^2 and the mean and maximal absolute deviations from the fit of $\delta^{\text{London}}(R, pH, K)$ are summarized at the end of the chapter (Table 5.4).

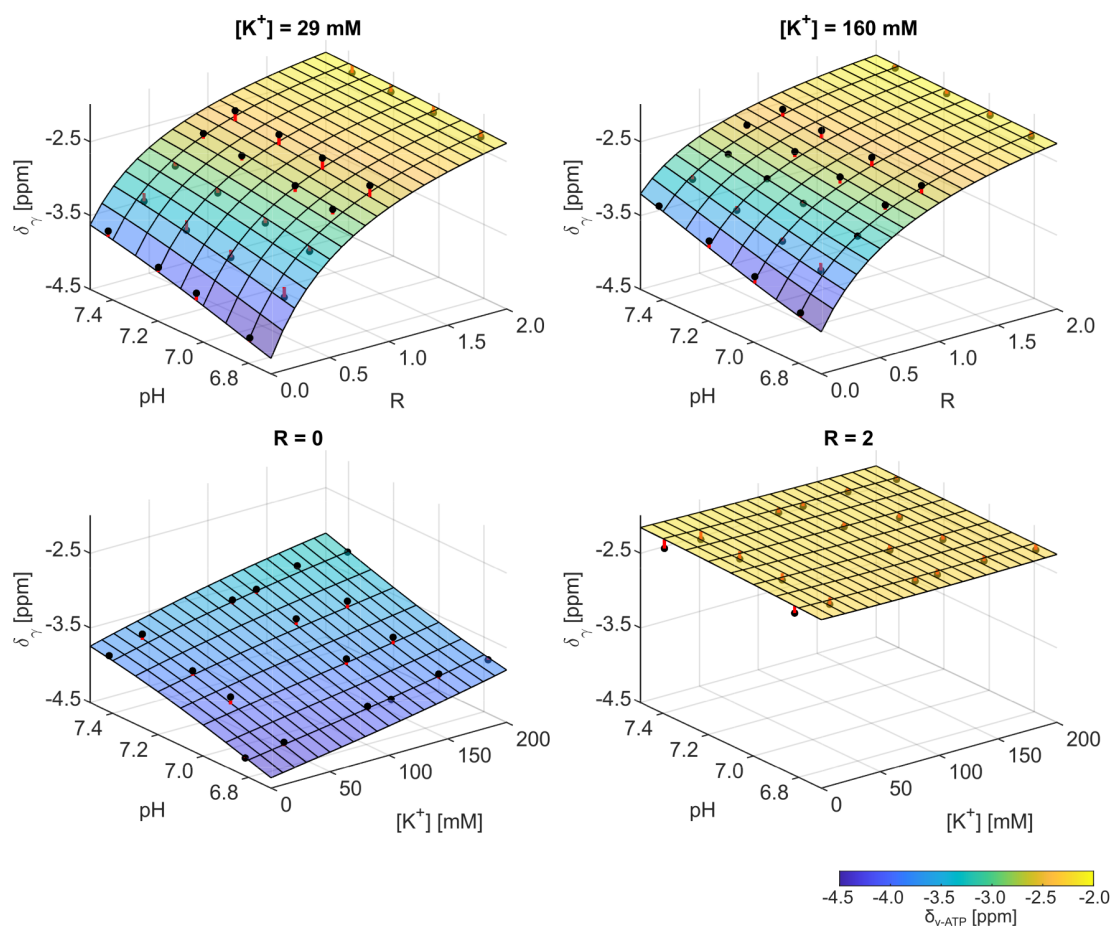


Figure 5.24: Multi-dimensional fit of the model function developed from the London equation $\delta^{\text{London}}(R, pH, K)$ for γ -ATP. The fitted function is illustrated for the subspace $\delta(R, pH)$ with $K = 29$ and 160 mM (top row), and for the subspace $\delta(pH, K)$ with $R = 0$ and 2 (bottom row). For high magnesium ion concentration, i.e. $R = 2$, the chemical shift of γ -ATP appears to be independent on pH and $[K^+]$, whereas for $R = 0$, δ_γ is monotonously increasing for pH and $[K^+]$.

Table 5.2: Fit parameters of the multi-dimensional function $\delta^{\text{London}}(R, pH, K)$ (equation (3.6) with equations (5.3a)) determined for γ -, α - and β -ATP. The parameters m_i with $i = 1, \dots, 4$ describe the dependency of the limiting chemical shifts δ_i on the potassium ion concentration, and the parameters b_i , describe the corresponding chemical shift offsets. m_f and b_f are the slope and the offset of the potassium dependency of the parameter f_2 which is the fraction $K_D/K_{D'}$. m_p describes the dependency of the pK value on $[K^+]$, and b_p is the corresponding offset. The parameter f_1 is the approximated fraction of the total magnesium ion concentration R corresponding to the ratio $[Mg^{2+}]/K_D$ (see section 3.2).

parameter	unit	γ -ATP	α -ATP	β -ATP
m_1	$10^{-3} \left[\frac{\text{ppm}}{\text{mM}} \right]$	5.9	1.1	3.3
m_2	$10^{-3} \left[\frac{\text{ppm}}{\text{mM}} \right]$	5.3	0.9	3.1
m_3	$10^{-3} \left[\frac{\text{ppm}}{\text{mM}} \right]$	-2.3	-0.7	-1.9
m_4	$10^{-3} \left[\frac{\text{ppm}}{\text{mM}} \right]$	-1.4	-1.4	-7.4
b_1	[ppm]	-3.5	-8.1	-19.2
b_2	[ppm]	-5.1	-8.1	-19.5
b_3	[ppm]	-1.7	-7.2	-14.1
b_4	[ppm]	-1.2	-7.0	-13.1
m_f	$10^{-3} \left[\frac{1}{\text{mM}} \right]$	0	3.5	4.4
b_f	-	0.8	0.3	0.1
m_p	$10^{-3} \left[\frac{1}{\text{mM}} \right]$	3.3	11	8.9
b_p	-	6.74	5.74	5.93
f_1	-	1.5	1.4	1.4

5.3.3 Model based on the Hill equation

The developed model function $\delta^{\text{Hill}}(Mg_{\text{tot}})$ (equation (3.8) in section 3.3) describes the course of the chemical shifts in dependence on the magnesium ion concentration suitably (Figure 5.25). For intermediate magnesium ion concentration, i.e. $Mg_{\text{tot}} = 5 \text{ mM}$ (respectively $R = 1$ in sections 5.3.1 and 5.3.2), the deviation of the function from the measured chemical shifts is smaller than it was the case for the previously investigated model functions. The adjusted R^2 for all shown 12 subsets is > 0.99 . For α - and β -ATP it is also > 0.99 .

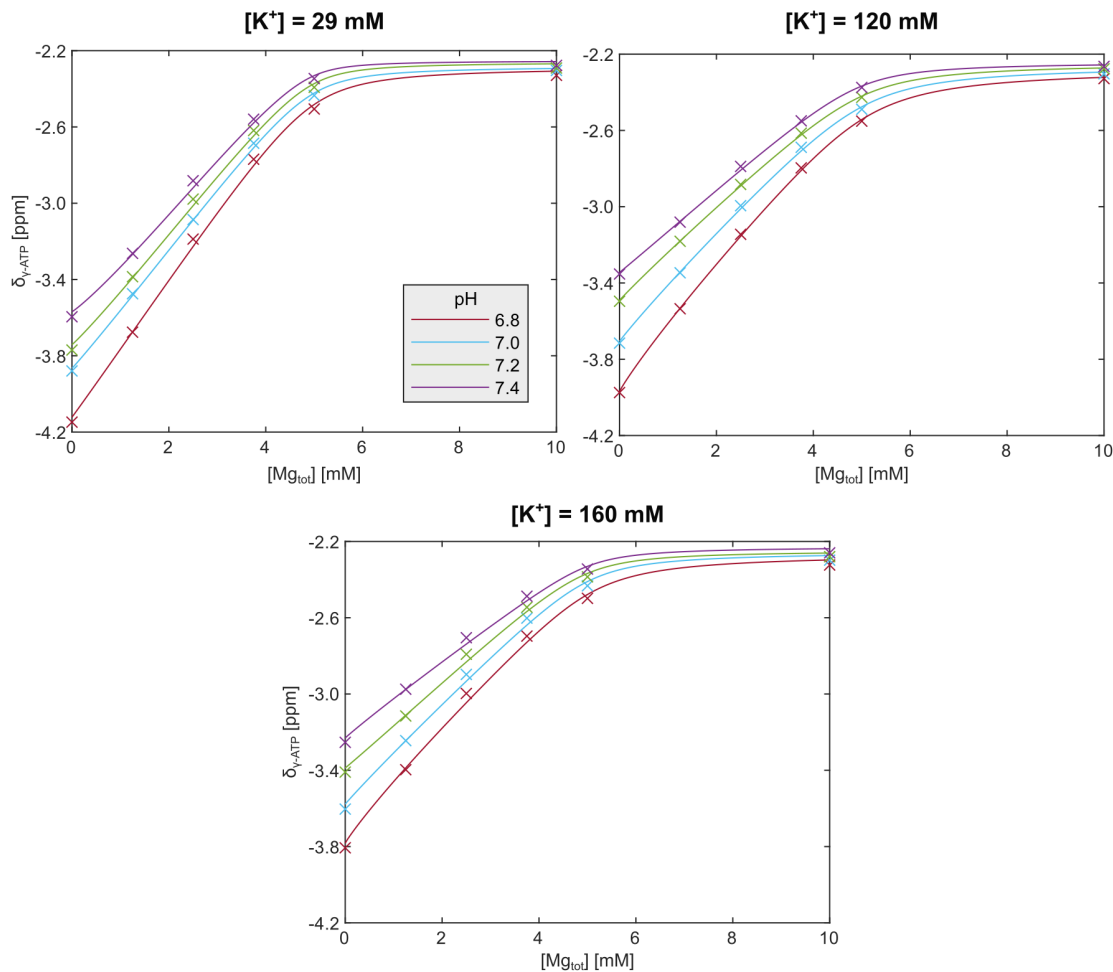


Figure 5.25: One-dimensional function $\delta_{\gamma}^{\text{Hill}}(Mg_{\text{tot}})$ fitted according to equation (3.8) (cf. section 5.3.3) for the three subsets with $[K^+] = 29, 120, 160 \text{ mM}$ and for the pH values (6.8 – 7.4) (colors). The range $[Mg_{\text{tot}}] = [0 - 10] \text{ mM}$ corresponds to $R = [0 - 2]$ used in sections 5.3.1 and 5.3.2. For intermediate magnesium ion concentration, i.e. $[Mg_{\text{tot}}] = 5 \text{ mM}$, the deviation of the fitted function from the measured chemical shifts is smaller than for the previously investigated models.

5 Results

By qualitatively investigating the pH and $[K^+]$ dependencies of the determined fit parameters (Figures 5.26 and 5.27), the following assumptions are made:

- Linear dependency of δ^{ATP} on pH and $[K^+]$
- Linear dependency of δ^{MgATP} on pH, but not on $[K^+]$ (an increase of δ^{MgATP} with increasing $[K^+]$ was not observed for all investigated subsets, i.e. for pH = 7.2)
- Linear dependency of n on $[K^+]$, but not on pH (an increase of n with increasing pH was not observed for all investigated subsets, i.e. for $[K^+] = 160$ mM)
- Linear dependency of K_D on pH, but not on $[K^+]$

Contrary to the expected linear dependency of K_D on $[K^+]$ [59], no monotonous change is observed (Figure 5.27). Due to the limited number of datapoints to further investigate whether a functional relation other than linear can be modelled, no change of K_D with varying $[K^+]$ is assumed. The parameters of equation (3.8) are changed as follows:

$$\delta^{ATP} = m_{d1} \cdot (pH - 7.1) + m_{d2} \cdot K + b_d \quad (5.4a)$$

$$\delta^{MgATP} = m_{dm} \cdot (pH - 7.1) + b_{dm} \quad (5.4b)$$

$$n = m_n \cdot K + b_n \quad (5.4c)$$

$$K_D = m_{KD} \cdot (pH - 7.1) + b_{KD} \quad (5.4d)$$

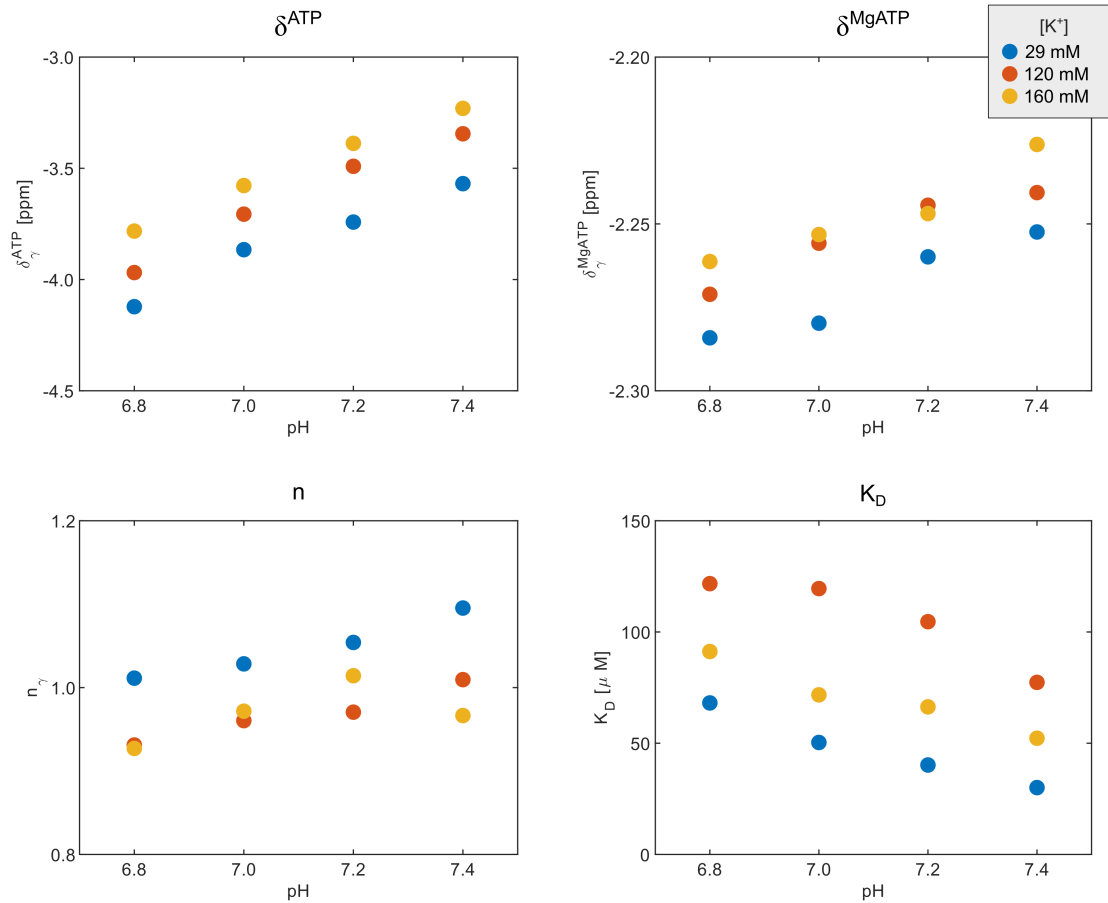


Figure 5.26: Fit parameters of the model function developed from the Hill equation $\delta_{\gamma}^{\text{Hill}}(Mg_{\text{tot}})$ (equation (3.8)) determined from the individual one-dimensional fits of the subsets for γ -ATP, plotted against the pH value and shown for the subsets with different potassium ion concentrations (colors). The following parameters were determined by the fit: the limiting chemical shifts δ^{ATP} and δ^{MgATP} , the Hill coefficient n , and the dissociation constant K_D .

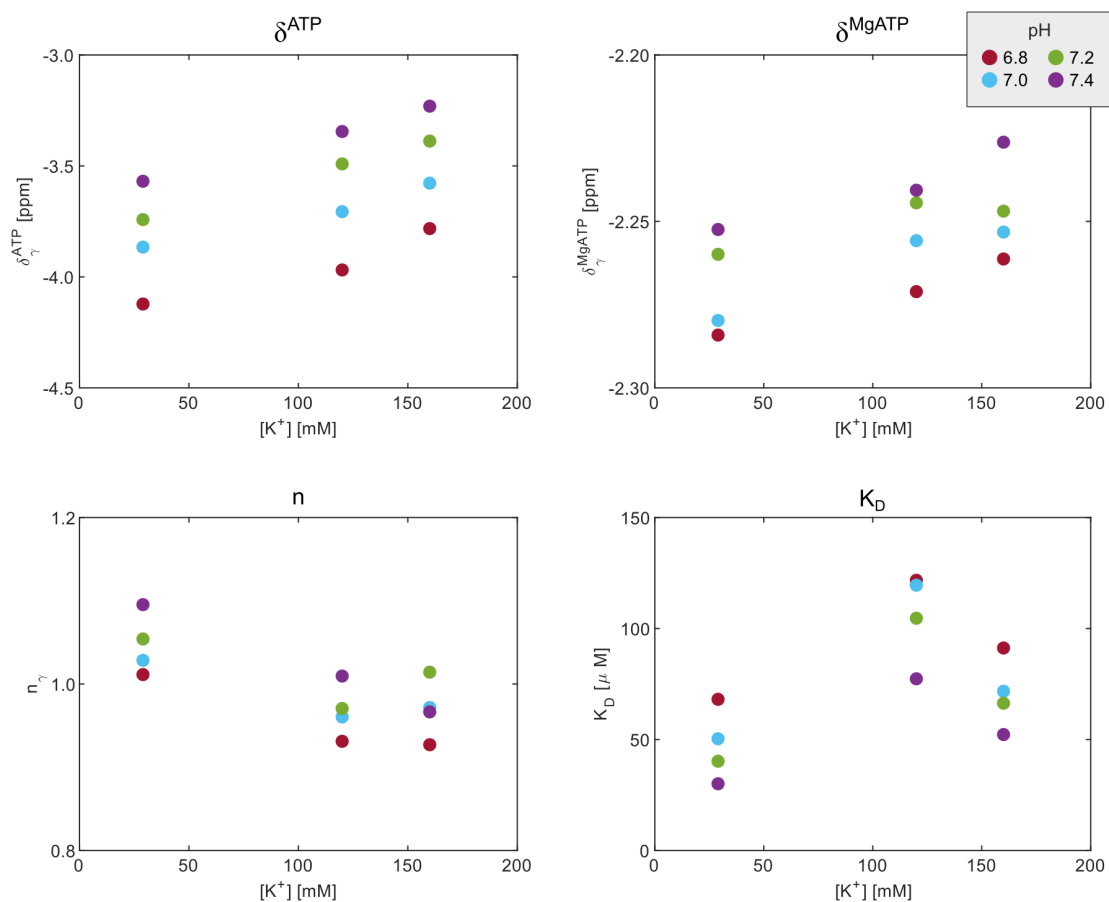


Figure 5.27: Fit parameters of the model function developed from the Hill equation $\delta_{\gamma}^{Hill}(Mg_{tot})$ (equation (3.8)) determined from the individual one-dimensional fits of the subsets for γ -ATP, plotted against the potassium ion concentration $[K^+]$ and shown for the subsets with different pH values (colors). The following parameters were determined by the fit: the limiting chemical shifts δ^{ATP} and δ^{MgATP} , the Hill coefficient n , and the dissociation constant K_D .

The extended version of equation (3.8) is then used as new function for the multi-dimensional fit $\delta^{\text{Hill}}(Mg_{\text{tot}}, pH, K)$, for which the results for γ -ATP are shown in Figure 5.28. Based on the resulting fit parameters (Table 5.3), the following conclusions can be drawn:

- The pH dependency of the limiting chemical shifts is the strongest for γ -ATP for the lower limiting shift δ^{ATP} and for β -ATP for the upper limiting chemical shift δ^{MgATP} (parameters m_{d1} and m_{dm}).
- The change of K_D with changing pH, i.e. parameter m_{KD} , is approximately the same for all three ATP chemical shifts.
- The change of the lower limiting chemical shifts δ^{ATP} with varying $[K^+]$ is the strongest for γ -ATP (parameter m_{d2}).
- The change of the Hill coefficient n is the strongest for β -ATP, and the weakest for γ -ATP (parameter m_n).

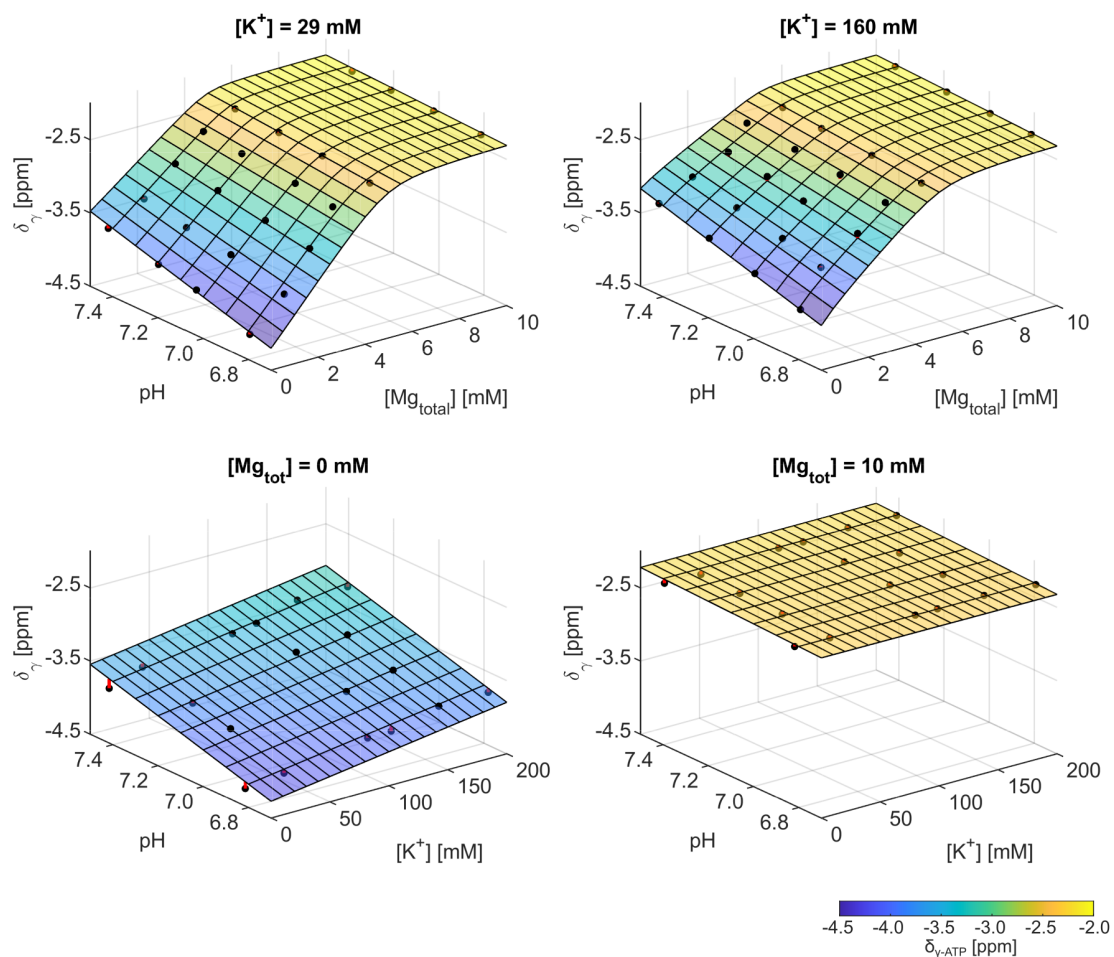


Figure 5.28: Multi-dimensional fit of the model function developed from the Hill equation $\delta^{\text{Hill}}(Mg_{tot}, pH, K)$ for γ -ATP. The fitted function is illustrated for the subspace $\delta(Mg_{tot}, pH)$ with $[K^+] = 29$ and 160 mM (top row), and for the subspace $\delta(pH, K)$ with $Mg_{tot} = 0$ and 10 mM (bottom row). The deviation of the measured chemical shifts from the fitted curve is illustrated with red pins.

Table 5.3: Fit parameters of the multi-dimensional function $\delta^{\text{Hill}}(Mg_{tot}, pH, K)$ derived from the Hill equation (combination of equations (3.8) and (5.4)) for γ -, α - and β -ATP. Parameters m_{d1} and m_{dm} describe the change of the limiting chemical shifts δ^{ATP} and δ^{MgATP} with changing pH value, and b_d and b_{dm} the corresponding offsets. m_{d2} describes the change of δ^{ATP} with the potassium concentration. The parameters m_n and m_{KD} describe the change of the Hill coefficient n and the dissociation constant K_D respectively, with changing $[K^+]$. b_n and b_{KD} are the corresponding offsets.

parameter	unit	γ -ATP	α -ATP	β -ATP
m_{d1}	$\left[\frac{\text{ppm}}{(\text{pH}-7.1)} \right]$	0.91	0.04	0.25
m_{dm}	$10^{-2} \left[\frac{\text{ppm}}{(\text{pH}-7.1)} \right]$	8.6	0.1	13.4
m_{KD}	$\left[\frac{\mu\text{M}}{(\text{pH}-7.1)} \right]$	-74	-75	-87
m_{d2}	$10^{-3} \left[\frac{\text{ppm}}{\text{mM}} \right]$	2.4	0.5	1.6
m_n	$10^{-3} \left[\frac{1}{\text{mM}} \right]$	-0.8	-1.4	-1.6
b_d	[ppm]	-3.91	-8.05	-18.98
b_{dm}	[ppm]	-2.25	-7.44	-15.72
b_n	—	1.04	1.07	1.27
b_{KD}	[μM]	58	86	102

5.3.4 Evaluation of the models

In the following, the three different developed fit models, which describe the change of the ATP chemical shifts with varying pH value, magnesium ion concentration and potassium ion concentration, will be shortly evaluated and compared.

The values for the adjusted R^2 for all three models and ATP chemical shifts are ≥ 0.97 , whereby the values for the model function based on the London equation are slightly lower than for the two other model functions (Table 5.4, compare row 2 with rows 1 and 3). The adjusted R^2 alone is not a sufficient metric to decide, which of the introduced models is the most suitable for the implementation of the look-up table. Hence, also the mean and maximal absolute deviation of the measured chemical shifts δ_{meas} from the respective chemical shifts following the model functions δ_{model} will be compared. The

Table 5.4: Fit quality measures for the different developed models describing the multi-dimensional dependency of the chemical shifts on pH, magnesium ion concentration, and potassium concentration for γ -, α - and β -ATP. Values from the model functions δ^{Heur} (white rows), δ^{Lon} (light grey rows) and δ^{Hill} (dark gray rows) are compared with each other. The adjusted R^2 , as well as the mean and maximal absolute deviation $\Delta\delta = |\delta_{\text{meas}} - \delta_{\text{model}}|$ of the chemical shift resulting from the model function δ_{model} from the measured chemical shift δ_{meas} are given. Moreover, the corresponding triple (pH, R, K) of this maximal absolute deviation is given.

Fit quality measure	γ -ATP	α -ATP	β -ATP
Adjusted R^2	0.992	0.994	0.989
	0.974	0.978	0.966
	0.993	0.994	0.993
Mean $\Delta\delta$ [ppm]	0.04	0.01	0.10
	0.07	0.02	0.18
	0.03	0.01	0.07
Max. $\Delta\delta$ [ppm]	0.13	0.05	0.27
	0.21	0.08	0.43
	0.13	0.05	0.31
(pH, R, K) at max. $\Delta\delta$	(6.8, 0.5, 120)	(7.4, 1.0, 0)	(7.4, 1.0, 0)
	(6.8, 1.0, 0)	(7.4, 1.0, 0)	(7.4, 1.0, 0)
	(7.4, 0, 0)	(7.4, 0, 0)	(7.4, 0.5, 0)

absolute deviation between measured and modelled chemical shifts is defined as:

$$\Delta\delta = |\delta_{\text{meas}} - \delta_{\text{meas}}|. \quad (5.5)$$

For all ATP chemical shifts, the values for the mean $\Delta\delta$ is smallest for the model based on the Hill equation, and the largest for the London model (Table 5.4, compare rows 4-6). Also the values for the maximal $\Delta\delta$ are the largest for the London model. For the heuristically developed model and the Hill model, the values for the maximal $\Delta\delta$ are the same for γ - and α -ATP, whereas for β -ATP, the values for the Hill model are slightly higher (compare rows 7 and 9). Interestingly, the triple (pH, R, K) corresponding to the maximal deviations are not the same for both models (compare rows 10 and 12). For the Hill model, the points of maximal deviation lie exactly at the edges of the value space, i.e. $(7.4, 0, 0)$ for γ - and α -ATP and very close to the edge of the range, i.e. $(7.4, 0.5, 0)$ for β -ATP. In contrast, the point of maximal deviation for the heuristic model and the London model, corresponds to intermediate magnesium ion concentration, i.e. $R = 1.0$, which is in line with the observations in sections 5.3.1 and 5.3.2.

To sum up, the fit model developed based on the Hill equation appears to describe the change of the ATP chemical shifts with varying pH, magnesium ion concentration, and potassium ion concentration better than the two other investigated models. First, for intermediate magnesium ion concentration, δ^{Hill} shows the lowest deviation from the measured chemical shifts δ^{meas} . Second, δ^{Hill} has the lowest overall mean absolute deviation from δ^{meas} . And third, the points of the maximal deviation lie at the edges of the investigated value range, which are the least relevant points for the application in vivo. Consequently, the interpolation of ATP chemical shifts for the implementation of the look-up table, is done based on the developed model function $\delta^{\text{Hill}}(Mg_{\text{tot}}, pH, K)$. Nevertheless, the investigation of all three models allows valuable insights for future development of the approach, which will be briefly discussed in section 6.3.

5.4 Application of the implemented approach to in vivo ^{31}P MRSI data

The implemented look-up approach, as described in detail in the methods (section 4.5), using the Hill model function for the interpolation of ATP chemical shifts, was applied to the already presented in vivo ^{31}P MRSI data from the lower leg muscles of healthy volunteers and from the human brains of patients with glioblastoma. The maps for pH, magnesium ion concentration, and potassium ion concentration, according to the implemented look-up algorithm, are compared to the conventionally calculated maps for pH and free magnesium ion concentration $[\text{Mg}_{\text{free}}^{2+}]$, which were already presented in section 5.1. It should be pointed out again that the conventional pH map pH_{Conv} is calculated based on the chemical shift of P_i applied to the modified Henderson-Hasselbalch equation (cf. section 2.5.1), and the map for $[\text{Mg}_{\text{free}}^{2+}]_{\text{Conv}}$ is calculated based on the chemical shift difference between the α - and β -resonance of ATP, i.e. $\delta_{\alpha\beta}$ following the equation from [27] (cf. section 2.5.2).

Moreover, it should be again emphasized, that the herein implemented approach yields an estimation of the total magnesium ion concentration $[\text{Mg}_{\text{tot}}]$ (cf. equation (3.8)), whereas the conventional maps show the concentration of free magnesium ions. As already mentioned before, the relative magnesium ion concentration $R = \frac{[\text{Mg}_{\text{tot}}]}{[\text{ATP}_{\text{tot}}]}$ is assumed to be a more meaningful measure when calculating magnesium maps based on ^{31}P MRS, than the use of total concentrations, i.e. $[\text{Mg}_{\text{tot}}]$ or $[\text{Mg}_{\text{free}}^{2+}]$. Hence, in the following, the magnesium maps according to the implemented look-up algorithm will be presented as relative magnesium ion maps showing the relative magnesium ion concentration $R = \frac{[\text{Mg}_{\text{tot}}]}{[\text{ATP}_{\text{tot}}]}$, which is determined by assuming $[\text{ATP}_{\text{tot}}] = 5 \text{ mM}$ in muscle [37, 57], and $[\text{ATP}_{\text{tot}}] = 3 \text{ mM}$ in brain tissue [58].

5.4.1 Preceding considerations

The implemented algorithm, as described in section 4.5, works as intended and determines triples of $(\text{pH}_{\text{Out}}, R_{\text{Out}}, K_{\text{Out}})$ for a given input triple of the chemical shifts $(\delta_\gamma, \delta_\alpha, \delta_\beta)$. The algorithm was tested on the obtained chemical shifts from all available model solution measurements (see Appendix D), resulting in good agreement between prepared $(\text{pH}_{\text{prep}}, R_{\text{prep}})$ and $(\text{pH}_{\text{Out}}, R_{\text{Out}})$ for the majority of the tested data sets. For the estimation of the potassium ion concentration, the determined value $[K^+]_{\text{Out}}$ does agree in less cases with the prepared value, which will be discussed in section 6.3. Using the data points, which have been already deployed for the model development, as test data sets for the implemented algorithm is unfavorable, but can be accepted for a first check

of functionality.

The application of the implemented approach including the chemical shifts of all three ATP resonances to the in vivo data sets resulted in maps with a high number of voxels where the assignment of $(\text{pH}_{\text{Out}}, \text{R}_{\text{Out}}, \text{K}_{\text{Out}})$ was not possible, i.e. no combination of $(\text{pH}, \text{Mg}, \text{K})$ was found in the value space of the implemented look-up table, which matches the input triple $(\delta_\gamma, \delta_\alpha, \delta_\beta)$ (representative maps shown in Appendix E). For the lower leg muscle datasets, in over 60%, and for the brain datasets in over 50% of the voxels, no solution was found. Analyses revealed, that mainly the possible solutions determined based on δ_α differed from the possible solutions based on δ_γ and δ_β . This mismatch will be further discussed in section 6.6.1. Applying a reduced version of the implemented approach only including the chemical shifts of γ - and β -ATP yields a successful assignment of the in vivo measured chemical shifts to physiological values in the majority of the input voxels. Hence, in the following, the resulting maps from the application of the reduced version of the approach only using $(\delta_\gamma, \delta_\beta)$ as input will be presented. The resulting underdetermination, i.e. the determination of three unknown parameters $(\text{pH}_{\text{Out}}, \text{R}_{\text{Out}}, \text{K}_{\text{Out}})$ with only two input values $(\delta_\gamma, \delta_\beta)$, nevertheless reduces the reliability of the determination and will also be discussed in section 6.6.1.

5.4.2 Data from the human lower leg muscle of healthy volunteers

For the 3D ^{31}P MRSI datasets of all three volunteers, an assignment of the measured chemical shifts $(\delta_\gamma, \delta_\beta)$ to the physiological values $(\text{pH}_{\text{Out}}, \text{Mg}_{\text{est}}, \text{K}_{\text{Out}})$ was successful in over 98% of the voxels in the corresponding muscle tissue, showing that the value space of the look-up table covers the in vivo conditions well. In the following, only the transversal and coronal view of the 3D maps will be shown, as they allow the most significant observations (Figures 5.29 and 5.30). The results from the ROI analyses are presented as violin plots showing the median values across the defined 3D ROIs across the muscle groups *tibialis anterior* (TA), *soleus* (Sol) and *gastrocnemius medialis* (GM) for each volunteer separately (Figure 5.31). The violin plots are shown for the values determined by the look-up approach $(\text{pH}_{\text{Out}}, \text{R}_{\text{Out}}, \text{K}_{\text{Out}})$ (orange violin plots) and for the values of the conventionally calculated maps pH_{Conv} and $[\text{Mg}_{\text{free}}^{2+}]_{\text{Conv}}$ (blue violin plots). Note the different metric for the magnesium values, i.e. $[\text{Mg}_{\text{free}}^{2+}]$ and R .

The maps for $(\text{pH}_{\text{Out}}, \text{R}_{\text{Out}}, \text{K}_{\text{Out}})$ according to the implemented look-up approach resemble the morphological features of the conventionally calculated maps, but have different absolute values (e.g. compare pH_{Conv} and pH_{Out} in Figures 5.29 and 5.30, and the ROI analyses for pH in Figure 5.31). The range of observed values in the pH_{Out} maps is clearly

5 Results

larger than for pH_{Conv} (0.3 vs. 0.1 pH units).

Most interestingly, the patterns in the pH_{Out} maps seem to resemble the morphological patterns in the $[\text{Mg}_{\text{free}}^{2+}]_{\text{Conv}}$ maps (compare rows 2 and 5 in Figure 5.29, and the ROI analyses for pH and R in Figure 5.31). In contrast, the patterns of the pH_{Conv} , show a greater similarity with the $[\text{K}^+]_{\text{Out}}$ (compare rows 1 and 3 in Figures 5.29 and 5.30, and the ROI analyses of pH_{Conv} and $[\text{K}^+]_{\text{Out}}$ in Figure 5.31). Interestingly, in the ROI analyses, the trends of low and high pH values are reversed for conventional and look-up based maps. For the conventionally calculated pH values, the lowest pH was observed in the TA, whereas for pH value according to the look-up approach, the highest values are observed in the TA.

For magnesium, comparable trends can be observed in the conventionally calculated and in the look-up based maps (compare rows 4 and 5 in Figures 5.29 and 5.30), but the difference between individual muscle groups is less pronounced in the look-up based maps (particularly seen for the difference between TA and the other two muscle groups, cf. ROI analysis for magnesium in Figure 5.31).

To sum up, (i) the observed trends are comparable for all volunteers, (ii) the contrast observed in the conventional pH maps seems to resemble the look-up based maps for potassium $[\text{K}^+]_{\text{Out}}$, whereas the contrast of the conventional $[\text{Mg}_{\text{free}}^{2+}]$ is more similar to the pH_{Out} map, and (iii) the trend of low and high pH values is partly reversed in the look-up based pH_{Out} maps compared to the conventional pH maps.

5.4 Application of the implemented approach to in vivo ^{31}P MRSI data

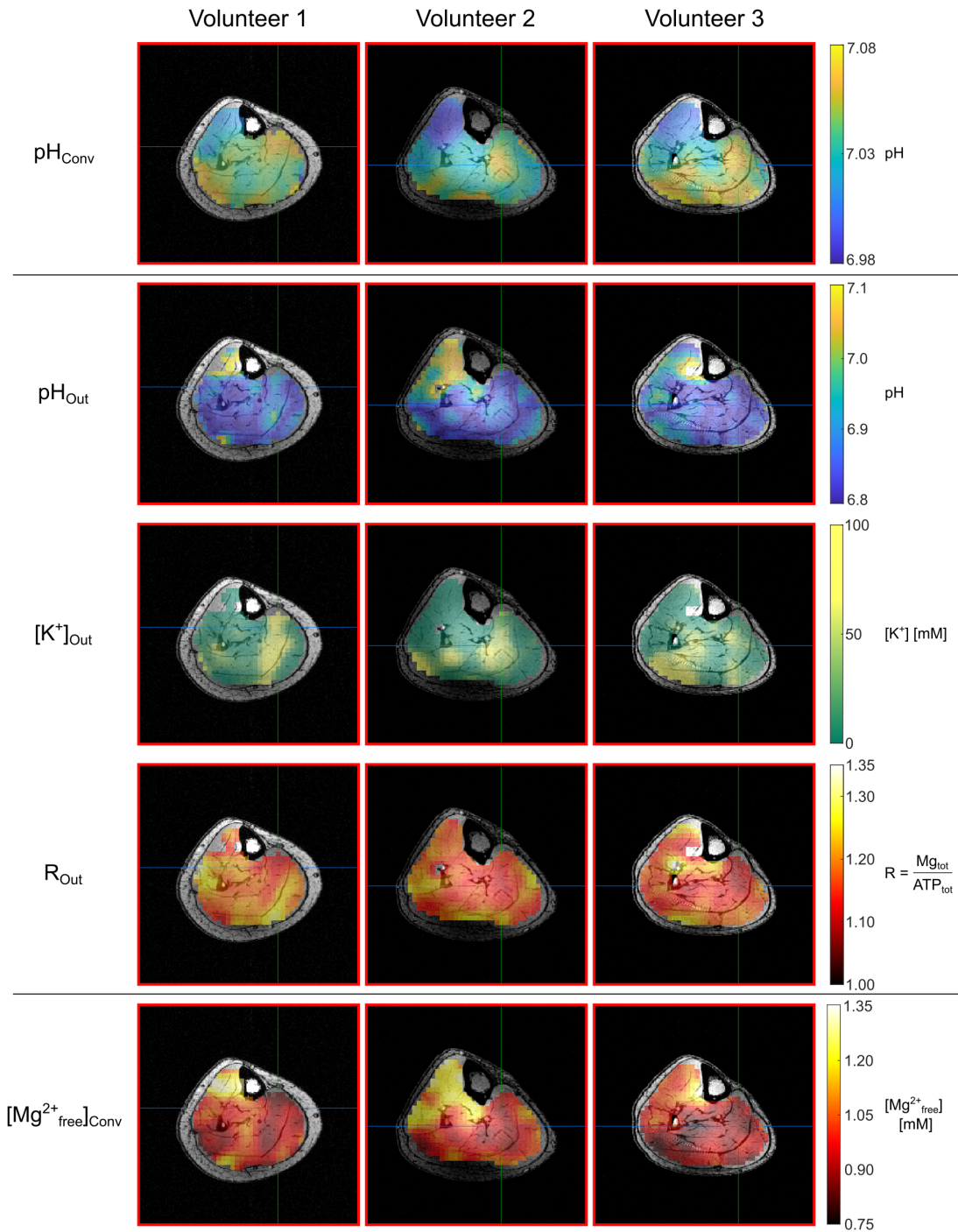


Figure 5.29: Transversal view of the 3D maps for pH_{Out} , $[\text{K}^+]_{\text{Out}}$, and $R_{\text{Out}} = \frac{[\text{Mg}_{\text{total}}]}{[\text{ATP}_{\text{total}}]}$ according to the implemented look-up approach applied to the ^{31}P MRSI data sets of the lower leg muscle of healthy volunteers. The same transversal slices are shown as in Figures 5.2 and 5.3 in section 5.1.1. For an easier comparison, the conventional maps for pH and $[\text{Mg}_{\text{free}}^{2+}]$ are also shown at the top and bottom of the figure.

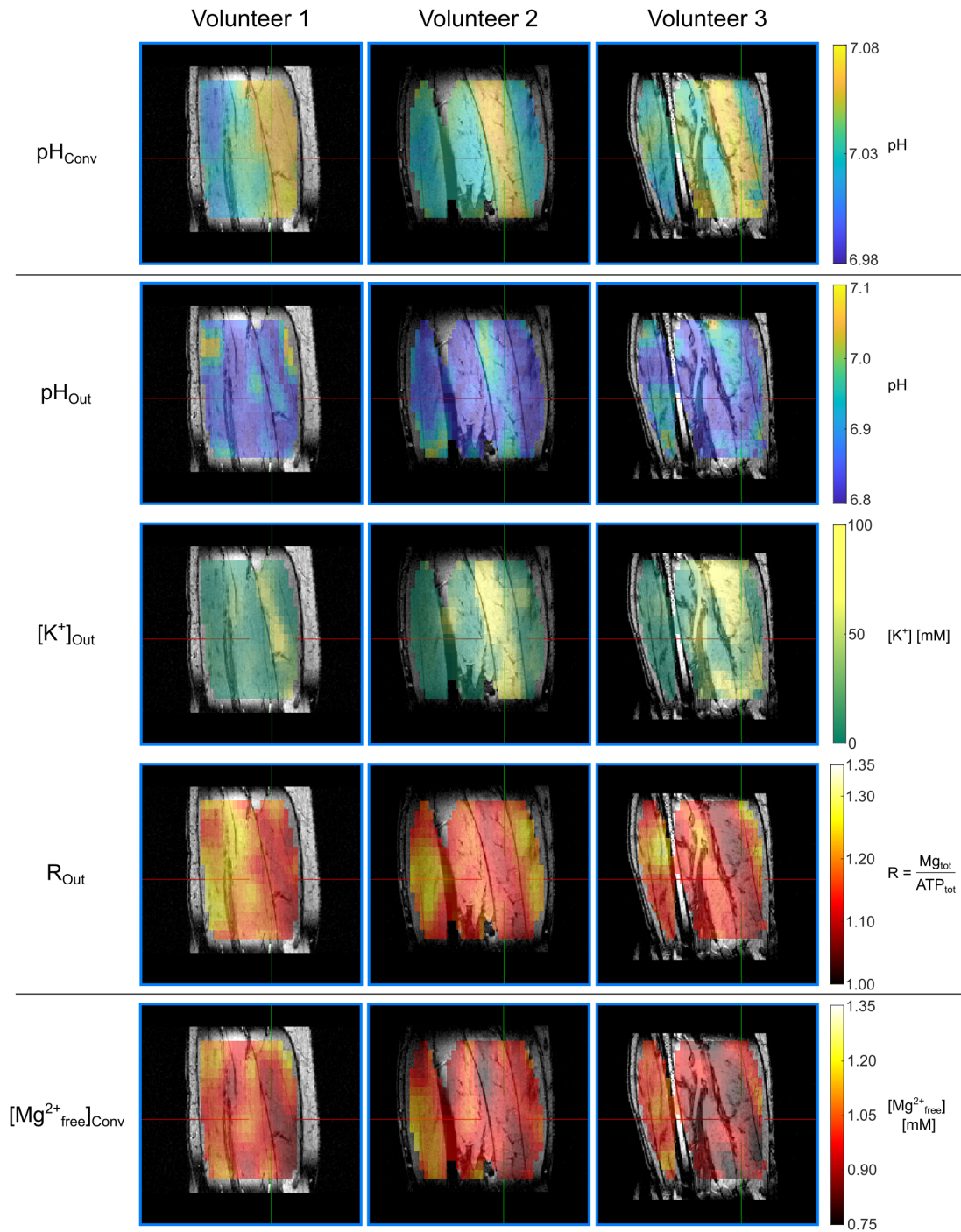


Figure 5.30: Coronal view of the 3D maps for pH_{Out} , $[\text{K}^+]_{\text{Out}}$, and $R_{\text{Out}} = \frac{[\text{Mg}_{\text{total}}]}{[\text{ATP}_{\text{total}}]}$ according to the implemented look-up approach applied to ^{31}P MRSI data sets of the lower leg muscle of healthy volunteers. The same coronal slices are shown as in Figures 5.2 and 5.3. For an easier comparison, the conventional maps for pH and $[\text{Mg}^{2+}_{\text{free}}]$ are also shown at the top and bottom of the figure.

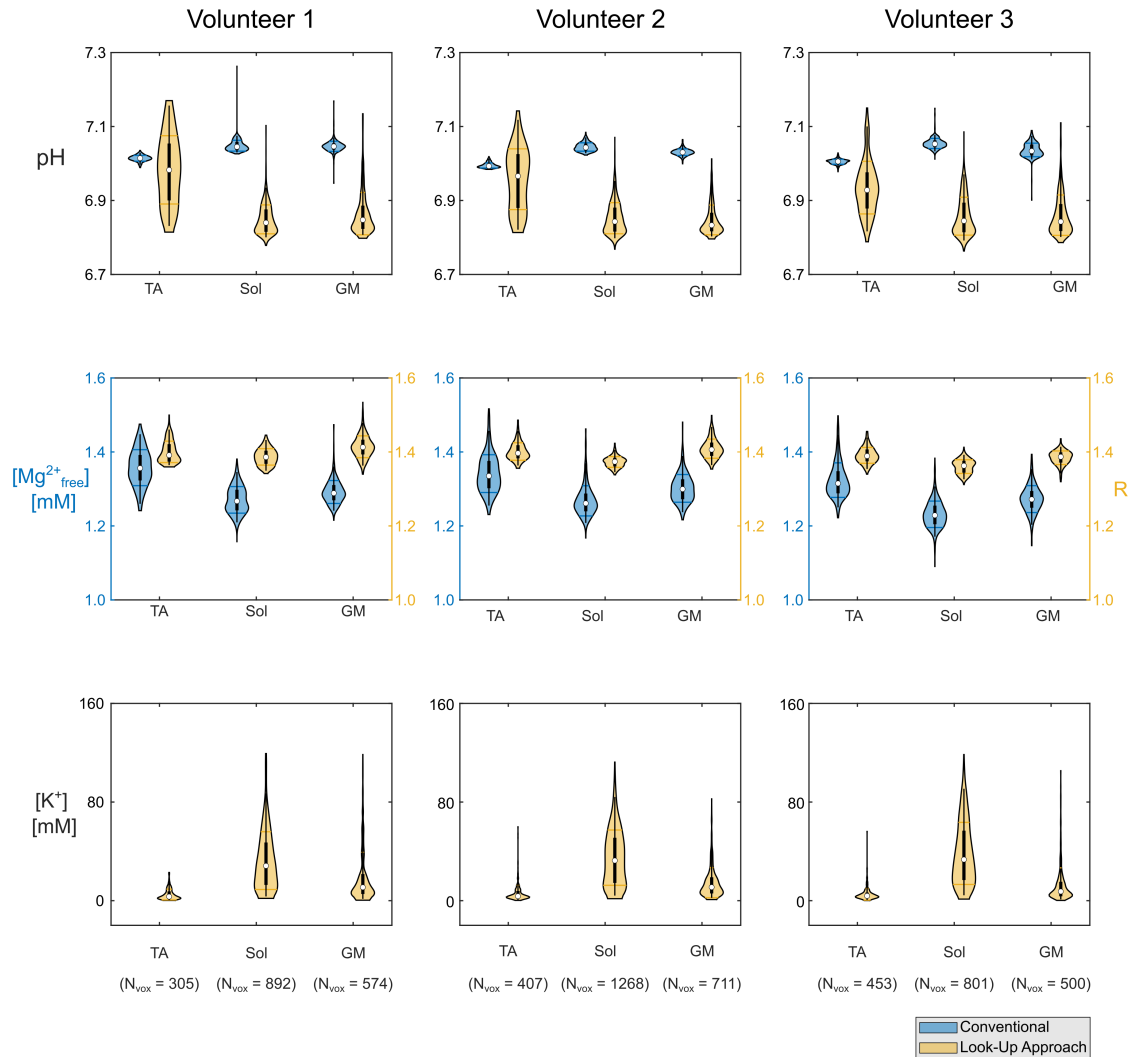


Figure 5.31: Regions-of-interest (ROIs) analyses across the muscle groups *tibialis anterior* (TA), *soleus* (Sol), and *gastrocnemius medialis* (GM), represented as violin plots for the pH value, magnesium ion concentration and potassium ion concentration for the datasets of all three volunteers. Median values across the 3D ROIs of the maps according to the look-up approach (pH_{Out} , R_{Out} , K_{Out}) (orange violin plots) are compared to the corresponding values of the conventionally calculated maps pH_{Conv} and $[\text{Mg}_{\text{free}}^{2+}]_{\text{Conv}}$ (blue violin plots). Note the different ordinate for the magnesium ion concentration. The conventionally calculated map shows $[\text{Mg}_{\text{free}}^{2+}]$, whereas the maps according to the look-up approach show values for $\text{R} = \frac{[\text{Mg}_{\text{tot}}]}{[\text{ATP}_{\text{tot}}]}$. The number of voxels included in the respective ROI analysis is indicated at the bottom of the Figure.

5.4.3 Data from patients with glioblastoma

For the 3D ^{31}P MRSI brain datasets of all three patients, an assignment of the measured chemical shifts ($\delta_\gamma, \delta_\beta$) to the physiological values ($\text{pH}_{\text{Out}}, \text{Mg}_{\text{est}}, \text{K}_{\text{Out}}$) was successful in over 90% of the brain voxels, showing that the algorithm, in principle, also works for the application to human brain data. The 3D brain maps will be shown in the transversal and in the sagittal view (Figures 5.32 and 5.33). The ROI analyses across the whole tumor region (WHT) and a contralateral region covering healthy white matter (WM) are presented as violin plots for both the conventionally calculated maps and the maps according to the look-up approach (Figure 5.34).

The maps for ($\text{pH}_{\text{Out}}, \text{R}_{\text{Out}}, \text{K}_{\text{Out}}$) (Figures 5.32 and 5.33) do not show comparable patterns for all three patients. For patient 1, the maps according to the implemented look-up approach resemble the morphological features of the conventionally calculated maps, but have different absolute values (e.g. compare pH_{Conv} and pH_{Out} in Figures 5.32 and 5.33, and in the ROI analyses for pH in Figure 5.31). The contrast observed in the pH_{Conv} map, seems to be most most similar to the look-up-based map for magnesium, i.e. R_{Out} . The maps pH_{Out} and $[\text{K}^+]_{\text{Out}}$ seem to partly resemble the pH_{Conv} map, but in a smaller region than expected from the morphological ^1H image (particularly seen in the sagittal view, Figure 5.33, column 1). The expected increase of pH in tumor tissue is seen in the sagittal view of the maps, showing values of up to 7.4 (in contrast to the values of only 7.25 in the conventionally calculated pH map). Despite these large observed pH_{Out} values, in the 3D ROI analyses across the whole tumor volume (WHT) (cf. Figure 5.34), no elevation compared to the white matter ROI can be observed. Regarding the magnesium ion maps, a clear increase of values according to the look-up approach R_{Out} in the tumor region is observed in both the maps and the ROI analyses (Figures 5.33 and 5.34, first columns), which is in line with the ROI analyses of the conventionally calculated $[\text{Mg}_{\text{free}}^{2+}]_{\text{Conv}}$ maps.

For patients 2 and 3, the maps according to the look-up approach ($\text{pH}_{\text{Out}}, \text{R}_{\text{Out}}, \text{K}_{\text{Out}}$) are more heterogeneous. It should be noted that the positions of the slices shown are different for all three patients due to the different location of the tumors. The shown transversal slices for patient 3 and especially for patient 2 are located more caudally than for patient 1. Influences of the slice location on the quality of the resulting maps, either calculated conventionally or according to the look-up algorithm, will be discussed in section 6.6.3. The expected increase of pH in tumor tissue is observed for only some parts of the tumor in the pH_{Out} maps of patients 2 and 3 (Figure 5.32). In the ROI analyses across the entire WHT ROI, this effect is averaged out, even showing a lower pH in

the WHT ROI compared to the WM ROI (Figure 5.34 last column). Here, it should be noted that this trend mainly results from the increased values in the WM ROI for patient 3. The values for $(\text{pH}_{\text{Out}}, \text{R}_{\text{Out}}, \text{K}_{\text{Out}})$ in the WHT ROI are comparable for all patients, whereas in the WM ROI the values are elevated for patient 3 compared to patients 1 and 2.

To sum up, the trends in the maps for pH, magnesium ion concentration and potassium ion concentration according to the implemented look-up based approach are not comparable for all investigated patients. For two of the three patients, the determined values for $(\text{pH}_{\text{Out}}, \text{R}_{\text{Out}}, \text{K}_{\text{Out}})$ show heterogeneous patterns. The expected increase of pH in tumor tissue was partly observed in the pH_{Out} maps for all patients showing values of up to $\text{pH} = 7.4$, but was averaged out in the ROI analyses across the whole tumor volume. For the determined magnesium ion concentration according to the look-up, for one patient, a clear increase of values in the tumor was observed in both the maps and the ROI analyses.

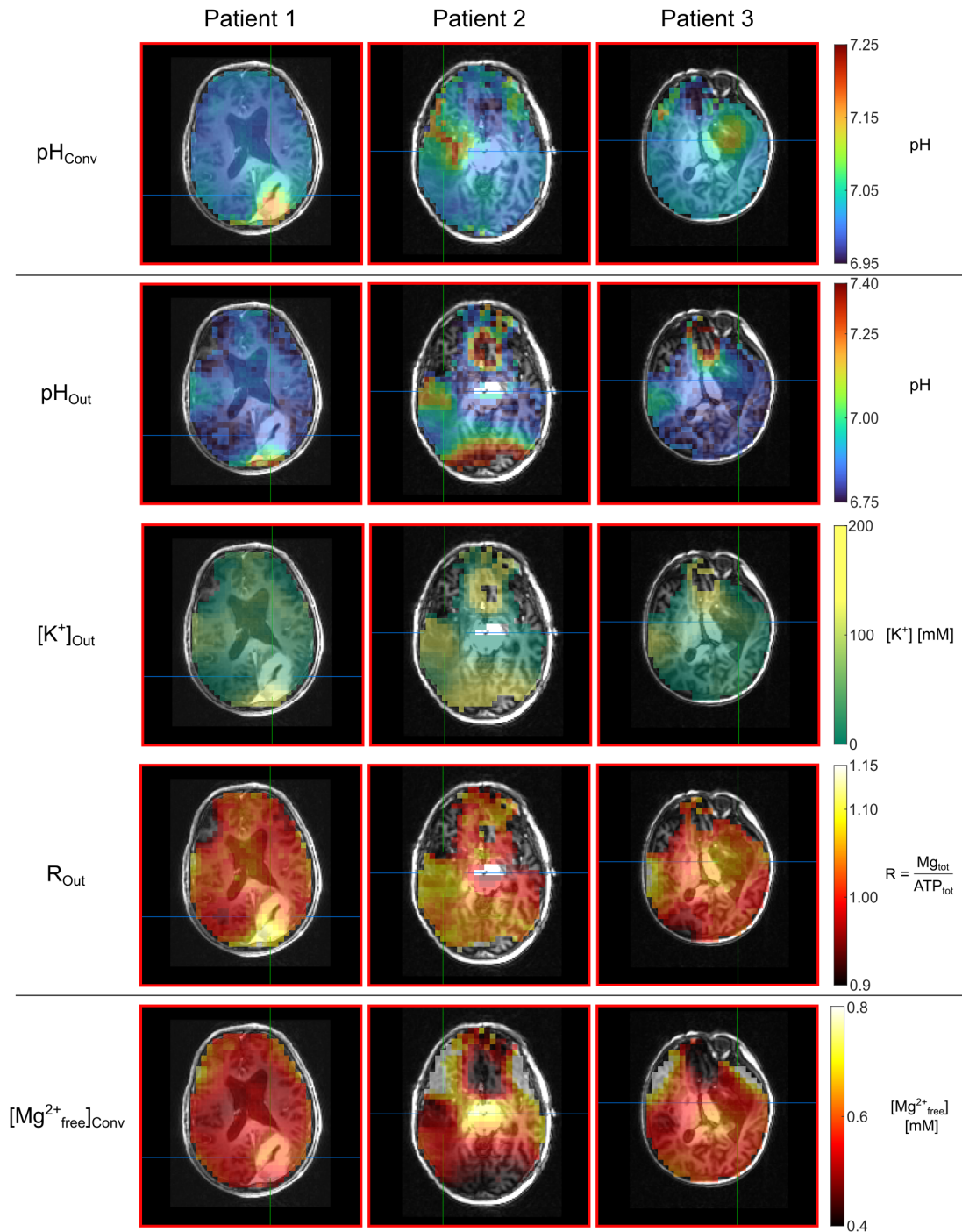


Figure 5.32: Transversal view of the 3D maps for pH_{Out} , $[\text{K}^+]_{\text{Out}}$, and $R_{\text{Out}} = \frac{[\text{Mg}_{\text{total}}]}{[\text{ATP}_{\text{total}}]}$ according to the implemented look-up approach applied to the human brain ^{31}P MRSI datasets from patients with glioblastoma. The same transversal slices are shown as in Figures 5.7 and 5.8. For an easier comparison, the conventional maps for pH and $[\text{Mg}_{\text{free}}^{2+}]$ are also shown at the top and bottom of the figure.

5.4 Application of the implemented approach to *in vivo* ^{31}P MRSI data

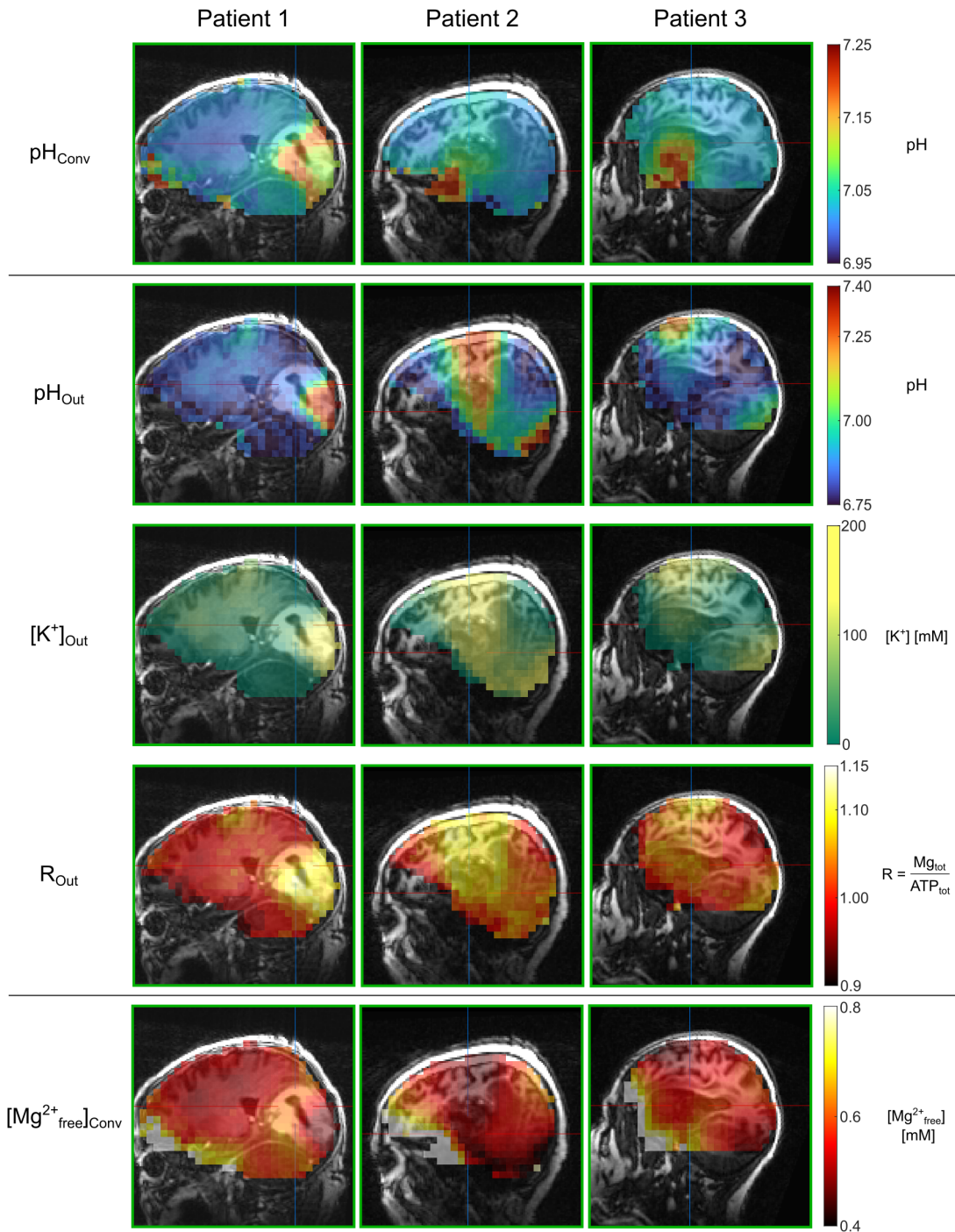


Figure 5.33: Sagittal view of the 3D maps for pH_{Out} , $[\text{K}^+]_{\text{Out}}$, and $R_{\text{Out}} = \frac{[\text{Mg}_{\text{total}}]}{[\text{ATP}_{\text{total}}]}$ according to the implemented look-up approach applied to the human brain ^{31}P MRSI datasets from patients with glioblastoma. The same sagittal slices are shown as in Figures 5.7 and 5.8. For an easier comparison, the conventional maps for pH and $[\text{Mg}_{\text{free}}^{2+}]$ are also shown at the top and bottom of the figure.

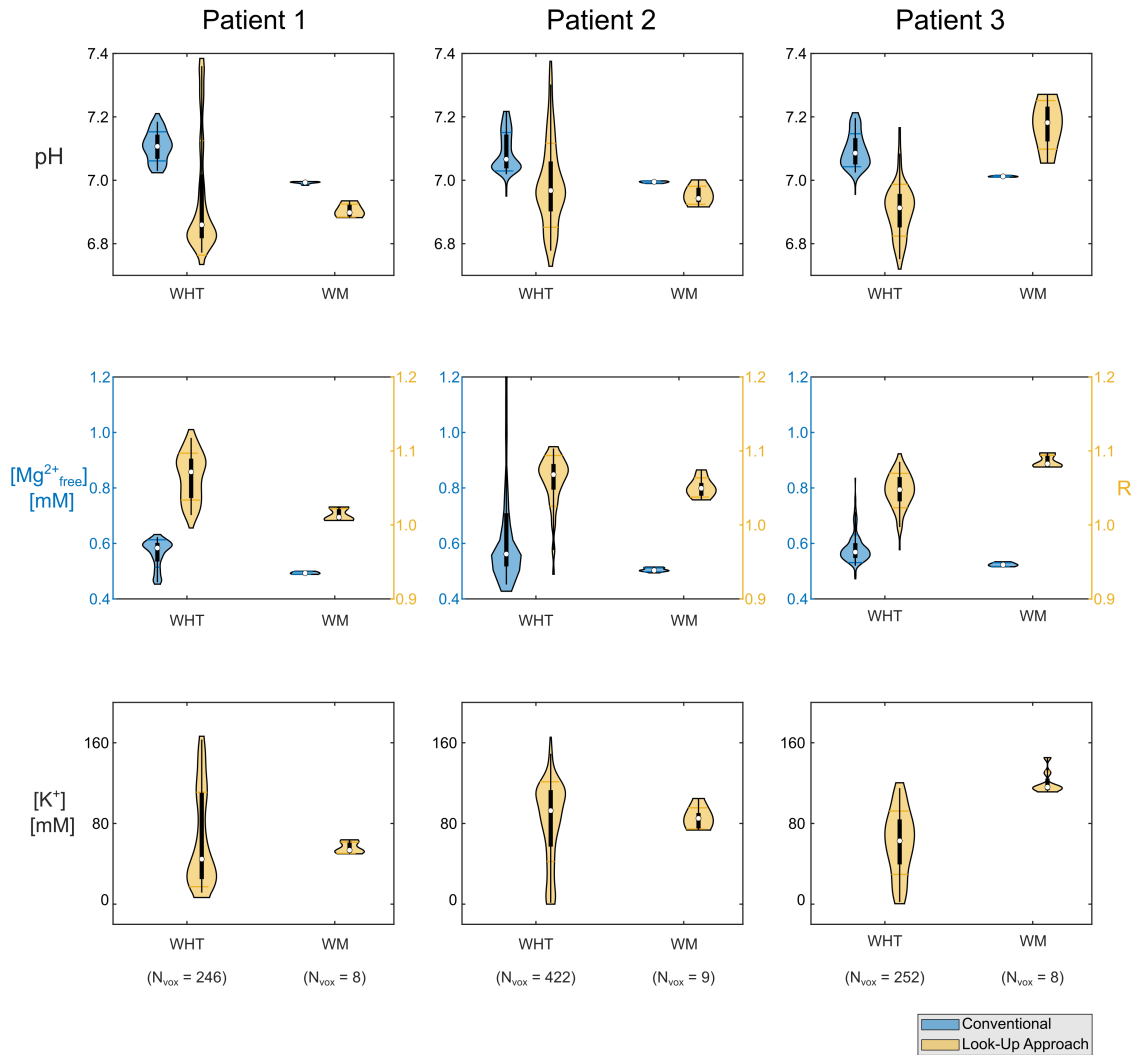


Figure 5.34: Regions-of-interest (ROIs) analyses across the whole tumor region (WHT) and a contralateral region covering healthy white matter (WM), represented as violin plots for the pH value, magnesium ion concentration and potassium ion concentration for the datasets of all three patients. Median values across the 3D ROIs of the maps according to the implemented look-up algorithm (pH_{Out} , R_{Out} , K_{Out}) (orange violin plots) are compared to the corresponding values of the conventionally calculated maps pH_{Conv} and $[\text{Mg}_{\text{free}}^{2+}]_{\text{Conv}}$ (blue violin plots). Note the different ordinate for the magnesium ion concentration. The conventionally calculated map shows $[\text{Mg}_{\text{free}}^{2+}]$, whereas the maps according to the implemented look-up algorithm show values for $R = \frac{[\text{Mg}_{\text{tot}}]}{[\text{ATP}_{\text{tot}}]}$. The number of voxels included in the respective ROI analysis is indicated at the bottom of the figure. The WM ROI was chosen small in order to prevent contribution from grey matter.

6 Discussion

6.1 Challenges of the existing methods for the determination of pH and $[Mg^{2+}]$ via ^{31}P MRS

6.1.1 Dependence on accurate calibration equations

The existing methods for the determination of pH value and magnesium ion concentration by means of ^{31}P MRS are based on the use of calibration equations, like the modified Henderson Hasselbalch equation (HHE). These calibration equations relate the measured chemical shifts of specific ^{31}P metabolites to biochemical parameters (cf. sections 2.5.1 and 2.5.2). The required parameters in these calibration curves, e.g. pK_a in the HHE (equation (2.58)), are typically determined in model solutions [22–24]. The necessity of accurate calibration equations adapted for the respective application has been highlighted in great detail [22–25]. The calibration curves $\delta(pH)$ are known to be influenced by e.g. the ionic strength, the presence of proteins, metabolite concentrations, or temperature. Nevertheless, typically, standard values or averaged values (across different experimental results) are used even for the application to pathologies. Even for the used “standard values”, there is no generally accepted consensus for every application. Table 6.1 summarizes typical values for the parameters pK_a , δ_{HA} and δ_A , of the modified HHE used in recent literature. The choice of the values influences the calculated pH value which is shown representatively for a P_i chemical shift of $\delta_{P_i-PCr} = 4.8$ ppm.

It should be noted, that for the calibration curves $\delta(Mg)$ (cf. section 2.5.2), comparable challenges arise.

6.1.2 Inorganic phosphate (P_i) as a measure for intracellular pH

The dependence of the titration curves $\delta(pH)$ (and the determined parameters pK_a , δ_{HA} , δ_A) on the exact chemical environment, is demonstrated in great detail for several ^{31}P chemical shifts in the works of Pettegrew et al. [23] and Roberts et al. [24]. Based on these works, it becomes clear, that of all investigated ^{31}P metabolites, the chemical shift of inorganic phosphate (P_i) as indirect measure for the intracellular pH value is beneficial

Table 6.1: Typical values for the parameters in the modified Henderson Hasselbalch equation (HHE) used in literature, i.e. pK_a , δ_{HA} , δ_A . The influence of the different constants on the pH value calculated via the HHE is presented representatively for a chemical shift difference of $\delta_{P_i-PCr} = 4.8$ ppm (last column).

Reference	pK_a	δ_{HA} [ppm]	δ_A [ppm]	pH _{HHE}
de Graaf ^a [31]	6.77	3.230	5.700	7.01
Meyerspeer et al. ^b [61]	6.75	3.270	5.630	7.02
Ren et al. ^c [58]	6.73	3.275	5.685	6.96
Petroff et al. ^c [22]	6.77	3.290	5.680	7.00

^a Standard text book, no specification for the application

^b Consensus paper ³¹P MRS in human skeletal muscle

^c For healthy human brain

in terms of specificity. In the physiological range, the chemical shift difference δ_{P_i-PCr} is (i) relatively sensitive to pH changes (cf. section 2.5.1), and (ii) influenced little by other chemical parameters, e.g. magnesium ion concentration or ionic strength. Nevertheless, the changes of δ_{P_i-PCr} due to other influences than pH can become highly relevant, when the chemical conditions change to a larger extent than in the normal physiological range. For an increase of the total magnesium concentration from 0 to 5 mM, an increase of the pK_a value of P_i from 6.89 to 6.77 [23], and from 6.95 to 6.7 [24], was reported. Petroff et al. also reported clear changes of the titration curves when the magnesium concentration is increased to more than 2.5 mM [22]. These results are in line with results of this work (cf. section 5.2.2), showing a change of the P_i chemical shift when the magnesium ion concentration is increased to 10 mM (Figure 5.18, first row, $R = 2$ corresponds to 10 mM). Here, it is very important to note, that the experiments in [22, 23] were performed in model solutions only containing P_i and PCr, whereas the measurements of this work were performed on model solutions also containing ATP. This is assumed to be the reason, that in this work the change of δ_{P_i-PCr} starts occurring for an increase of the Mg concentration to 10 mM, compared to (2.5 – 5.0) mM in [22, 23]. Due to the presence of ATP in the solutions, most of the added magnesium ions will be bound to ATP, reducing the amount of free magnesium ions, which influence the chemical shift of P_i [24]. Hence, a visible change in δ_{P_i-PCr} is expected only for a large increase in Mg compared to solutions without ATP.

Moreover, also changes in δ_{P_i} were observed for varying potassium concentration (Figure 5.17). Here, the concentration must also be increased strongly before clear changes in δ_{P_i} become detectable (i.e. $\Delta\delta_{P_i} \approx 0.1$ ppm for an increase from $[K^+] = 29$ mM to 160 mM). However, in pathologies such as cancer, the chemical conditions can change dramatically, which presumably leads to a clear change in the observed δ_{P_i} . Due to the fact, that the chemical conditions, e.g. the ionic strength, are not a priori known for pathologies, a simple adaption of the parameters in the HHE to the specific pathology is not a viable option. Instead, a method is required to incorporate the effects of the magnesium ion concentration and ionic strength in a different way.

Another challenge of the determination of pH via the P_i chemical shifts, is its low signal-to-noise ratio (SNR) in vivo. P_i is (i) relatively low concentrated compared to other ^{31}P metabolites, and (ii) has relatively long relaxation times. For the human brain for example, the following values were reported [58]: intracellular $[P_i] \approx 0.85$ mM compared to $[ATP] \approx 3$ mM, and $T_{1,P_i\text{intra}} \approx 3.7$ s compared to $T_{1,ATP} \approx (1.1 - 1.7)$ s. The low concentration and the long relaxation times result in a typically low SNR of P_i , translating to long measurement times and/or unreliable quantifications.

A last challenge of the pH determination via δ_{P_i} in particular for pathologies like cancer, is the question whether a clear separation of different P_i compartments is possible in tumor tissue. The opposing trend of the intra- and extracellular pH value in tumor tissue, i.e. an increase of intracellular and a decrease of extracellular pH (cf. 2.4.1), hampers the reliable quantification of the P_i resonance(s). Assuming that the resonance peak upfield of the intracellular P_i peak (cf. Figure 5.6), which is resolvable at high field strengths, is indeed resulting from P_i in the extracellular space (as suggested in [62–66]), the opposing trends of intra- and extracellular pH can lead to an overlap of the signals from P_i and eP_i . The increase in intracellular pH leads to an upfield shift of the P_i resonance, whereas the decrease of the extracellular pH would lead to a downfield shift of the eP_i resonance. This might result in an overlap of both P_i signals, posing challenges for the quantification. This overlap was observed in some of the tumor spectra acquired in the ^{31}P MRSI study on patients with glioblastoma and is discussed in [9]. The overlap of P_i and eP_i might also be the reason for the unexpected pattern in the sagittal view of the conventionally calculated pH map of patient 1 (cf. Figure 5.33 in section 5.4), showing a ring of increased pH values towards the periphery of the tumor, while in the core of the tumor the calculated pH_{conv} values are lower. The unexpected trend of lower pH values in the core of the tumor compared to the periphery might result from an overlap of P_i and eP_i signal. In contrast to P_i , ATP has the advantage that its measured MR signal is assumed

to be mainly originating from the intracellular compartment (including a mitochondrial contribution) circumventing problems due to an overlap with extracellular compartments.

All discussed challenges demonstrate the necessity of a method which is (i) applicable for various chemical conditions and (ii) might provide a reasonable alternative for the use of the P_i signal for the determination of pH. The herein proposed look-up approach using the ATP chemical shifts addresses both requirements, but relies on robust measurements in model solutions, which are influenced by several external parameters.

6.2 Influences on the ^{31}P spectra acquired in model solutions

The proposed look-up approach is dependent on the accuracy of the developed model functions δ_i^{model} with $i \in (\gamma, \alpha, \beta)$, which describe the relation between the measured ATP chemical shifts δ_i^{meas} and the underlying chemical conditions (pH, Mg, K). In order to develop a suitable model, ^{31}P spectra were acquired from model solutions prepared with different chemical conditions. The spectra resulting from these measurements are influenced by the temperature of the model solutions during the measurements, and the exact composition of the solutions.

6.2.1 Temperature of the model solutions during the ^{31}P MRS measurement

The temperature of the model solution during the titration of the pH value in the model solutions, and also the temperature during the acquisition of the ^{31}P data has an influence on the obtained chemical shifts. The pH value, as well as the apparent dissociation constant K_D of the complexation of Mg to ATP (cf. section 2.5.2) are known to be influenced by temperature [22, 25, 59, 67–69]. This poses two challenges:

1. A difference between the titrated pH value and the pH value during the measurement (influenced by the exact temperature of the model solution) might lead to an inaccurate assignment of pH to the measured chemical shifts.
2. A difference between K_D in the model solutions and in tissue (resulting from a different temperature; the temperature in muscle is reported to be around (35 – 36) °C [69]), might pose a challenge for the transferability between model and in vivo application.

6.2 Influences on the ^{31}P spectra acquired in model solutions

To address the first challenge, a temperature correction was performed (cf. section 4.4.3) prior to data evaluation and development of the model. This temperature correction assigns the acquired spectrum to a corrected pH value based on the temperature difference between titration and measurement condition (cf. equation (4.2)). The correction factor $-0.04 \frac{\text{pH}}{^\circ\text{C}}$ was experimentally determined in measurements of (pH-T) pairs in imidazole solution. Instead of performing these measurements on pure imidazole buffer solution, it should have been done on representative model solutions also containing the ^{31}P metabolites. P_i functions as buffer (cf. 2.4.2) and can therefore influence the (pH-T) dependence in the prepared solutions. The experiments for the temperature correction should be repeated as suggested above, in order to make the temperature correction more accurate. Such a correction procedure is not possible for the second case (difference in KD), as the dissociation constant cannot be as easily measured as the pH value.

In general, the accuracy of the temperature measurements during the MR measurements should be considered due to two reasons: (i) the accuracy of the temperature tracking system at the 9.4 T small animal scanner (cf. section 4.1.2), and (ii) the fact, that the temperature of the water in the outer vial was measured, and not the temperature of the actual ^{31}P model solution (cf. Figure 4.7 in section 4.4.3). Because the temperature was assumed to have a significant effect on the pH value and consequently on the measured chemical shifts, an additional experiment was performed on two different MR systems. A set of 6 model solutions with different pH values¹ was measured twice on the same day: (i) on a 9.4-T Bruker NMR spectrometer only suitable for measurements of small NMR tubes having the advantage of an accurate temperature tracking, and (ii) on the 9.4-T small animal system used for all model solution measurements. The temperature of the model solutions during the measurements on the spectrometer was 36.9°C in all cases, and the mean temperature across all solutions for the measurements on the small animal system was $(37.0 \pm 0.1)^\circ\text{C}$. A good agreement was observed between both measurements (Figure 6.1). The deviations between both measurements were maximally 0.02 ppm for most of the model solutions. For the measurement of the model solution with $\text{pH} = 6.0$, the deviation was 0.05 ppm which corresponds to a difference in pH of 0.04 pH units (calculated with the HHE with parameters from [31], for 4.80 ppm and 4.85 ppm). The good agreement between measurements at different MR systems suggests an overestimation of the discussed concerns about the accuracy of the temperature measurements. Systematic errors of the prepared pH value due to temperature influences are hence assumed to be neglectable.

¹The model solutions contained 5 mM P_i and PCr respectively, 1.36 mM MgCl and 155 mM KCl, and were prepared by Antoine Feignier in the framework of his Bachelor thesis [70].

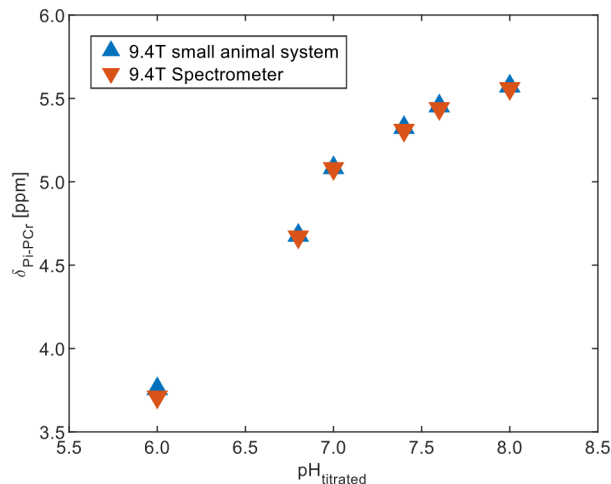


Figure 6.1: Comparison of the measured chemical shift δ_{PiPCr} in a set of 6 model solutions acquired at the 9.4 T small animal system (blue) and the 9.4 T spectrometer (red). A good agreement can be observed between both measurements. The largest deviation is observed for the measurements of the model solution with $\text{pH} = 6.0$. This deviation is ≈ 0.05 ppm, which corresponds to a pH difference of ≈ 0.04 pH units (calculated with the HHE for 4.80 ppm and 4.85 ppm respectively).

The influence of the temperature on the dissociation constants in general, which is particularly of relevance for the change of the ATP chemical shifts in dependence of varying magnesium and potassium ion concentration, was not assessed in more detail within this work. However, the dependence of K_D^{MgATP} of the dissociation of Mg^{2+} to ATP (cf. equation (2.65)) was reported to be $\Delta \log K_D = 750 \cdot \Delta T$ [71]. Based on these assumption, a temperature change from 37°C to 35°C , would result e.g. in a change of the dissociation constant $K_D = 90\mu\text{M}$ to $K_D \approx 93\mu\text{M}$. By assuming the same influence on the three other dissociation constants in equation (2.73), this would result in a change of the determined free magnesium ion concentration from $[\text{Mg}^{2+}] = 0.97\text{mM}$ at $T = 37^\circ\text{C}$ to $[\text{Mg}^{2+}] = 1.00\text{mM}$ at $T = 35^\circ\text{C}$ for $\delta_{\alpha\beta} = 8.45\text{ppm}$ with an assumed $\text{pH} = 7.0$.

6.2.2 Chemical composition of the prepared model solutions

As already discussed in section 6.1.1, the calibration equations used for the translation of measured chemical shifts to the physiological values pH and $[\text{Mg}^{2+}]$, are typically determined in experiments on model solutions. Although the proposed method in this work is also based on measurements on model solutions, it has the advantage of not being dependent on only one specific calibration equation, but incorporates various chemical conditions. Nevertheless, the composition of the used model solutions, as well as ex-

perimental influences during the preparation, have an influence on the accuracy of the determined absolute values by the implemented approach.

When comparing the chemical shifts for P_i measured in model solutions with the measured δ_{P_i} in vivo (Figure 5.18 in section 5.2.2), it was observed that only δ_{P_i} of model solutions prepared with $\text{pH} = 6.8$ were overlapping with the in vivo range of $\delta_{P_i} = [4.7 - 4.98]$ ppm.² When assuming, that the modified HHE with the parameters from [31] translate the measured δ_{P_i} to the correct pH value in vivo, the following comparison can be made:

Following the HHE, the measured $\delta_{P_i} = 4.8$ ppm would correspond to a pH value of 7.01. In contrast to that, based on the model solution measurements in this work, $\delta_{P_i} = 4.8$ ppm can only be translated to a pH value of 6.8. This mismatch can be interpreted as a systematic error in the composition of the model solutions in this work, not properly representing the conditions in vivo. Potential reasons for a significant influence of the model solution composition could be (i) the use of imidazol buffer, (ii) other influences e.g. proteins, and (iii) missing presence of other ions, i.e. calcium, chlorine.

The use of imidazole buffer (i) might have a significant effect on the measured chemical shifts of ^{31}P metabolites, and was partly investigated by Antoine Feignier in his Bachelors thesis [70]. A difference in measured chemical shifts was observed when different buffer solutions were used, whereby the largest difference was observed for the P_i resonance. The chemical shifts of ATP were less affected by the type of used buffer, e.g. $\Delta\delta_{P_i} = 0.15$ ppm and $\Delta\delta_{\gamma\text{-ATP}} = 0.06$ ppm (for the difference of imidazole and PBS buffer at $\text{pH} = 6.8$). Although, the difference between model solutions with and without imidazole buffer solution was not addressed in [70], there is reason to presume, that the presence of imidazole might have an effect on the measured chemical shifts, which might explain the mismatch mentioned before.

The influence of proteins (ii) was also investigated in [70], and found to be smaller than the measurement uncertainties, i.e. $\Delta\delta_{\text{ATP}} = [0.001 - 0.004]$ ppm and $\Delta\delta_{P_i} = 0.006$ ppm (for solutions with and without Bovine Serum Albumin (BSA), respectively). Nevertheless, differences in the order of 0.05 ppm were observed when comparing model solutions containing different proteins, i.e. BSA and protamine. This suggests, that the influence on the ^{31}P chemical shifts is different for different proteins. However, the effect of proteins on ^{31}P chemical shifts was investigated before and assumed to be neglectable [24]

²The corresponding plots for the subsets with $\text{pH} = 7.0$ and $\text{pH} = 7.2$ are not shown in section 5.2.2, but for $\text{pH} = 7.0$ only the δ_{P_i} from the subset with $[\text{K}^+] = 29$ mM overlap with the in vivo range. However, $[\text{K}^+]$ is assumed to be around 155 mM in vivo (cf. Table 2.1 in section 2.4.3).

(but also only for BSA).

The influence of other ions (iii) will be shortly addressed in section 6.7.1.

In order to find the reason for the mismatch between measured δ_{P_i} in this work and the titration curves from literature, an attempt was made to reproduce the titration curves determined by Petroff et al.[22]. Although the exact composition of model solutions as described in [22] was reproduced, a systematic shift of the measured titration curves $\delta_{P_i}(pH)$ was observed [70], which corresponds to a shift of the pK_a value of 0.17. Of course, a perfect reproduction of model solutions cannot be guaranteed, but this experiment illustrates the sensitivity of the measurements. The accuracy and reliability of the used titration curves should be reconsidered and assessed in more detail.

The mentioned external influences on the ^{31}P spectra measured in model solutions, in particular the influences of the model solution composition, might systematically affect the developed model functions. These model functions are of central importance for the reliability of the determined values by the implemented look-up algorithm. A systematic error in the developed model function $\delta^{\text{model}}(pH, Mg, K)$, would result in a systematic error in the determination of the values (pH, Mg, K) .

6.3 Assessment of the proposed approach

Within this work, three different models for the interpolation of the ATP chemical shifts in dependence on pH, magnesium and potassium ion concentration were investigated. The model based on the Hill equation was determined to be the most suitable to describe the multi-dimensional dependence $\delta(pH, Mg, K)$. Nevertheless, also the other two models might be of interest, when the investigated value range is extended, as proposed in sections 6.5 and 6.7.

It is important to point out, that there are other approaches for the simultaneous determination of pH and magnesium ion concentration based on ^{31}P chemical shifts [28–30]. Particularly the approach by Williams et al. [30] is comparable to the approach proposed in this work, which will be shortly discussed in the following.

Besides some minor differences, such as the use of different reference chemical shifts (i.e. $\delta_\gamma, \delta_\alpha, \delta_\beta$ relative to PCr here, instead of the use of the differences $\delta_{\gamma\alpha}, \delta_{\alpha\beta}$ and $\delta_{\gamma\beta}$ in [30]), or the different covered ranges for pH values and magnesium ion concentrations, three major differences should be pointed out:

1. The starting point for the model functions defining the look-up table in [30] was the dependency of the chemical shifts on the pH value (the modified HHE with $n \neq 1$ is used; cf. equation (3.8)). The dependence on the magnesium ion concentration was then incorporated by “fitting to the best exponential equation or cubic spline fit” [30]. In contrast to that, in this work, the dependence of δ on the magnesium ion concentration was the starting point for the model development. The dependence on the pH value (as well as the potassium concentration) was incorporated by linearization of the determined parameters in $\delta(R)$.
2. The influence of the ionic strength was assessed in detail in [30], but was assumed to be neglectable and hence not included in the look-up table. In contrast, in the herein proposed approach the influence of the ionic strength, i.e. of the potassium concentration as surrogate, was incorporated directly into the model $\delta(pH, Mg, K)$, as it was found to have a clear influence on the measured chemical shifts.
3. The influence of measurement uncertainties of the chemical shifts was not included in [30] (contrary to the herein proposed approach including directly a specific error margin on the measured chemical shifts). In [30], an estimation of the uncertainty of the determined magnesium ion concentration due to an error margin of δ was assessed separately.

As described in point 2, in the herein proposed approach, the influence of the ionic strength was incorporated, because it was found to be of relevance (cf. section 5.2.2). However, the potassium concentration could not be successfully determined via the implemented look-up algorithm in all test datasets (cf. Appendix D, Figure D.15), which might raise the question, whether the ansatz of [30] of neglecting the influence of ionic strength, was sufficient. Nevertheless, the influence of varying potassium concentration on the ATP chemical shifts is found to be of relevance (cf. Figure 5.17). The inaccurate determination of K via the herein proposed approach might be due to an insufficient model describing the dependency on K not correctly, or due to an underdetermination hampering a correct assignment of K . An extension of the approach by including more parameters like the linewidths and J-coupling constants (discussed in section 6.7.2), or the incorporation of sodium concentration (see section 6.7.1), might improve the performance for the determination of K .

6.4 Considerations concerning the implemented look-up algorithm

The manner in which the look-up algorithm is implemented can influence the reliability and accuracy of the (pH, Mg, K) determination. Some major points considering the details of the implementation will be discussed in the following.

Spacing of the sampling grid

The spacing of the sampling grid was deliberately chosen so that the change with varying pH value and with varying magnesium ion concentration is “sampled” in the finest steps, i.e. with step size of 0.01 pH units and 0.1 mM respectively. For the potassium concentration, the step size is 10mM, due the relatively smaller changes with changing K (compared to pH and Mg). These changes are assumed to be sufficient based on comparisons with the assumed measurement uncertainty on the chemical shifts of ± 0.01 ppm:

- A change of 0.01 pH units would correspond to a change of approximately 0.01 ppm for γ -ATP (for the case of $R = 0$ and $[K^+] = 29$ mM, cf. Figure 5.16 in section 5.2.2).
- In the range of $[Mg^{2+}] = [5 - 10]$ mM, a change of 0.1 mM would correspond to a change of 0.002 ppm for γ -ATP (for pH = 7.4, cf. Figure 5.18 in section 5.2.2). This change is clearly smaller than the assumed measurement uncertainty of 0.01 ppm.
- A change of 10mM in the potassium concentration corresponds to a change of 0.026 ppm for γ -ATP and pH = 6.8 (cf. Figure 5.17), which is larger than the measurement uncertainty. A spacing of 5 mM for potassium would have been a better choice.

Besides these considerations, the influence of the spacings was also tested by comparing the output values of the implemented algorithm for different sampling spacings for all three parameters (pH, Mg, K) . It could be confirmed, that a finer spacing for potassium only has a minor effect on the determined output values.

Assumed error margin for the measured chemical shifts

The chosen error margin of 0.01 ppm for δ_i^{meas} , $i \in (\gamma, \alpha, \beta)$ was taken as a best-case estimate, and is based on the maximal, technically possible spectral resolution of the acquired in vivo ^{31}P spectra (≈ 0.015 ppm). Typically, the uncertainties of the measured chemical shifts are larger, in particular for the resonance of β -ATP, which is typically

broad in vivo. The assumed error margin has an effect on the output values, because it shifts the weighted mean values due to the non-linearity of the model. Hence, in future work, the generally assumed error margin of 0.01 ppm should be reconsidered and the algorithm should be extended in a way that incorporates more realistic error margins, in particular for β -ATP.

Order of the value determination

The order of the value determination (pH, Mg, K) is assumed to not influence the final output values. The resulting possible solution triples (pH_k, Mg_k, K_k) should be the same, whether the look-up algorithm determines the most probable pH value pH_k for each point (Mg_k, K_k), or the most probable Mg value Mg_k for each point (pH_k, K_k). The assignment $\delta_{\text{meas}} \rightarrow (pH_k, Mg_k, K_k)$ is assumed to be uninfluenced by the order. Nevertheless this should be analyzed in future work.

6.5 Large variation of δ_α measured in vivo

In the datasets from in vivo measurements, a surprisingly large range of α -ATP chemical shifts was observed (cf. Figure 5.11 in section 5.1.3). Although the chemical shift of α -ATP is assumed to be the least sensitive to influences of the chemical environment (due to its position in the ATP molecule, cf. Figure 2.8 in section 2.4.2), its variation observed in vivo is surprisingly large. This fact raises the question, where these strong changes in δ_α observed in vivo result from.

The measurements on model solutions also showed, that the change of the δ_α with varying pH, magnesium and potassium ion concentration is relatively small compared to δ_γ and δ_β (cf. Figures 5.16, 5.17, 5.18 in section 5.2.2). This finding was confirmed by the results of the multi-dimensional modelling of $\delta_i^{\text{Hill}}(pH, Mg, K)$ (cf. Table 5.3). The influence of pH on the limiting chemical shifts of α -ATP seems to be small compared to γ - and α -ATP (parameters m_{d1}, m_{dm}, m_{d2}). However, for the change of K_D with varying pH, and the change of the Hill coefficient n with varying $[K^+]$, (parameters m_{kd}, m_n), the degree of change was comparable for all three ATP chemical shifts. This demonstrates, that α -ATP is influenced by some parameters to a comparable extent as the chemical shifts of γ - and β -ATP.

Nevertheless, it was already seen in Figure 5.18 that the measured chemical shifts in model solutions do not represent the entire range of α -ATP chemical shifts, which were

obtained in vivo. In model solutions, only δ_α values of up to approximately -7.46 ppm were measured, whereas in vivo also δ_α values up to -7.38 ppm were obtained. The fact, that for δ_γ and δ_β the entire range observed in vivo is covered by the measurements in model solutions, but not for δ_α , is very surprising. The reason for this might be a parameter influencing particularly δ_α , which is not considered yet in the model.

Also with the extrapolation of δ_α for magnesium ion concentrations up to 25 mM using the model function $\delta_\alpha^{\text{Hill}}(pH, Mg, K)$, values not larger than -7.45 ppm can be modelled (calculated for $pH = 7.4$, $[Mg^{2+}] = 25$ mM, $[K^+] = 200$ mM). Of course, the extrapolation to such a large range outside of the experimentally covered range (up to 10 mM), might not yield accurate results. However, the extrapolation is assumed to be reasonable, because the change of δ_α is decreasing with increasing R , and seems to plateau around $R = 2$. It seems unlikely that values around -7.38 ppm can be reached with further increase of R , but should however be experimentally confirmed by measuring model solutions with magnesium concentrations of up to 30 mM.

The question whether there is an effect not considered yet, which could explain the mismatch between δ_α measured in vivo and in model solutions, needs to be investigated in future work. This open question, already leads to the next very important point: the missing compatibility of the look-up values for α -ATP with the values for γ - and β -ATP, when applied to in vivo data.

6.6 Applicability to in vivo ^{31}P MRSI data

6.6.1 Missing compatibility of the look-up values for α -ATP with the look-up values for γ - and β -ATP

As already explained in section 5.4.1, the application of the implemented approach including all three ATP chemical shifts to the investigated in vivo data, does not yield output values for $(pH_{\text{Out}}, Mg_{\text{Out}}, K_{\text{Out}})$ in most of the voxels (cf. Appendix E). The reason for this is assumed to be the missing overlap of assigned solution triples based on δ_α with the assigned solution triples from δ_γ and δ_β . This hypothesis was investigated, by analyzing the output maps from a look-up version only using δ_α , i.e. $P_{\text{joint}} = P_\alpha$ (cf. Figure 4.10 in section 4.5.3). In these output maps (not shown), two observations were made:

1. For the muscle datasets, in only $\approx 58\%$ ³ of all muscle voxels an output triple

³60% for volunteer 1, 50% for volunteer 2, 62% for volunteer 3

$(pH_{\text{Out}}, Mg_{\text{Out}}, K_{\text{Out}})_{\alpha}$ could be determined; for the glioblastoma datasets, in $\approx 89\%$.⁴

2. In the voxels where a solution triple $(pH_{\text{Out}}, Mg_{\text{Out}}, K_{\text{Out}})_{\alpha}$ was successfully assigned, the determined values represented in almost all cases approximately the mean values of the defined sampling ranges for pH and K , i.e. $pH_{\text{Out}} \approx 7.04$ and $K_{\text{Out}} \approx 100 \text{ mM}$ (cf. section 4.5.4). For the determined magnesium ion concentration, in both cases $R \approx 1$.

For the muscle datasets, observation 1 is assumed to be mainly resulting from the mismatch of δ_{α} measured in model solutions (which defines $\delta_{\alpha}^{\text{model}}$ for the look-up table) with the chemical shifts measured in vivo $\delta_{\alpha}^{\text{meas}}$ (cf. section 6.5). If the measured $\delta_{\alpha}^{\text{meas}}$ is not represented in the look-up table defined by the model, it cannot be assigned to any solution triple. Interestingly, for the brain datasets, the mismatch between $\delta_{\alpha}^{\text{model}}$ and $\delta_{\alpha}^{\text{meas}}$ seems to be not the reason for the missing compatibility of the α -ATP outputs, because in more than 90% of the brain voxels an assignment to possible solution triples was possible based on $\delta_{\alpha}^{\text{meas}}$.

The missing compatibility between the outputs $(pH_{\text{Out}}, Mg_{\text{Out}}, K_{\text{Out}})_{\alpha}$ and $(pH_{\text{Out}}, Mg_{\text{Out}}, K_{\text{Out}})_{\gamma\beta}$ must be driven by observation 2, which is assumed to be resulting from the relatively small change of δ_{α} with changing chemical environment and the incorporation of the measurement uncertainty of 0.01 ppm on $\delta_{\alpha}^{\text{meas}}$. The assumed probability distribution $P(\delta_{\alpha}^{\text{meas}} \pm 5\sigma)$ (cf. Figure 4.8 in section 4.5.2) results in a broad probability distribution for the pH value $P(pH)$. The output values calculated as the weighted mean values across all possible solutions, is consequently expected to be strongly weighted by the global mean values of the sampling grids for (pH, Mg, K) , as observed in the maps for $(pH_{\text{Out}}, Mg_{\text{Out}}, K_{\text{Out}})_{\alpha}$. However, this alone cannot explain the missing overlap with the assigned values from δ_{γ} and δ_{β} . The broad distribution $P_{\alpha}(pH, Mg, K)$, makes it very likely that an overlap with $P_{\gamma}(pH, Mg, K)$ and $P_{\beta}(pH, Mg, K)$ exists. But if the probability distributions $P_{\gamma}(pH, Mg, K)$ and $P_{\beta}(pH, Mg, K)$ are very narrow, it might happen that still no overlap of all three exists. This brings us back to the point of reconsidering the relatively small error margin of 0.01 ppm for δ_{γ} and δ_{β} (cf. section 6.4). Maybe the assumption of a larger error margin for δ_{γ} and δ_{β} (which is anyhow more realistic) would enable an overlap of $(pH_{\text{Out}}, Mg_{\text{Out}}, K_{\text{Out}})_{\alpha}$ with $(pH_{\text{Out}}, Mg_{\text{Out}}, K_{\text{Out}})_{\gamma\beta}$ in more voxels.

As already mentioned, the final presented maps show the output of a reduced version of the algorithm only using δ_{γ} and δ_{β} . This works in principle, but is underdetermined (determination of three unknown parameters based on only two measured parameters).

⁴94% for patient 1, 78% for patient 2, 94% for patient 3

Hence, the mismatch of the look-up values of α -ATP with the look-up values for γ - and β -ATP, should be addressed in detail in future work, in order to improve the reliability of the method.

6.6.2 Comparison with conventional methods

When comparing the output maps of the implemented look-up approach with the conventionally calculated pH and magnesium maps, i.e. pH_{Conv} and $[\text{Mg}_{\text{free}}^{2+}]_{\text{Conv}}$, large differences were observed. These differences raise the question, whether the implemented approach actually yields a reasonable determination of physiological values in vivo. Here, it is very important to point out, that the maps referred to as the conventionally calculated maps are the only reasonable comparison available, but do not represent the “ground truth”. The challenges of the conventional methods possibly hampering the accurate determination of pH and magnesium values in vivo are intensively discussed in section 6.1. In particular for the application in pathologies, i.e. the datasets from patients with glioblastoma, the conventionally calculated maps need to be interpreted with caution.

The potential overlap of the resonances from intra- and extracellular P_i in tumor tissue, might impede a robust quantification of the pH value, which could potentially explain the unexpected patterns in the tumor region of patient 1, and the relatively small increase in calculated pH in tumor tissue of patients 2 and 3 (cf. section 6.1.2).

Moreover, a potential (and expected) change of the $\text{p}K_a$ value in tumor tissue also hampers a correct determination of the pH value, when the modified HHE with constant parameters is used. The resemblance of the patterns in the look-up maps for the potassium ion concentration K_{Out} with the patterns in the pH_{Conv} maps might hint towards the fact that the contrast in the pH_{Conv} maps might result from changes in the $\text{p}K_a$ value, and are not pure changes of the pH.⁵

The potential change of equilibrium constants also has an influence on the calculation of $[\text{Mg}_{\text{free}}^{2+}]_{\text{Conv}}$, as here standard values for the parameters in equation (2.73) are also used for the application in pathologies. Furthermore, the calculated pH values (potentially not accurately determined) are included into the calculation of $[\text{Mg}_{\text{free}}^{2+}]_{\text{Conv}}$, additionally increasing the uncertainty of the calculated values.

However, the conventional methods have been applied in numerous in vivo studies so far, and are assumed to yield reasonable results for different applications. Hence, the large

⁵The $\text{p}K_a$ value is reported to decrease with increasing ionic strength [24, 60].

differences between the output maps of the herein proposed approach with conventional maps should be investigated further.

6.6.3 Different patterns in the glioblastoma datasets

Whereas the trends in the three datasets from the lower leg muscles of healthy volunteers are comparable between all three subjects, the trends in the maps from the glioblastoma datasets partly differ quite strongly between the different subjects.

First of all, it has to be pointed out, that the physiological situation in the human brain of patients with glioblastoma is more complicated than in the human lower leg muscle of healthy volunteers. The human brain maps analyzed in this work are acquired in three different patients, meaning that for each patient (i) the location of the tumor is different, and (ii) the pathophysiology in the diseased tissue might be different. Consequently, general statements applicable to all three patients are difficult to make. The partly different trends in the three patient datasets were already seen in the conventionally calculated pH and $[\text{Mg}_{\text{free}}^{2+}]$ maps (Figures 5.7 and 5.8 in section 5.1.2), in particular in the magnesium maps.

Second, the influence of the tumor location on the general data quality needs to be shortly discussed. Compared to patient 1, the tumors of patients 2 and 3 are located more caudally i.e. further towards the neck, where more contamination from muscle tissue and more B_0 inhomogeneities due to the location at the edge of the field of view, are expected. The lower data quality in the tumor slices of patients 2 and 3 might hamper a reliable quantification of the chemical shifts, which might explain the unexpected heterogeneous patterns in the $[\text{Mg}_{\text{free}}^{2+}]_{\text{Conv}}$ and look-up output maps $(\text{pH}_{\text{Out}}, \text{Mg}_{\text{Out}}, \text{K}_{\text{Out}})_{\alpha}$.

6.7 Future steps

6.7.1 Further investigating the influences on the α -ATP chemical shift

The first step in future work should be the investigation of the mismatch of δ_{α} measured in the model solutions and in vivo. To this end, as already mentioned, experiments on model solutions with higher magnesium concentration of up to 30 mM should be performed to investigate whether the range of δ_{α} obtained in vivo can be reproduced with a higher magnesium ion concentration.

Moreover, also the sodium concentration should be investigated further. In initial experiments it could be observed, that the degree of change of measured ATP chemical shifts per $[K^+]$ unit is different than the change per $[Na^{2+}]$ unit, i.e. $\frac{\Delta\delta_\alpha}{\Delta[K^+]} \approx \frac{0.03 \text{ ppm}}{50 \text{ mM}}$, and $\frac{\Delta\delta_\alpha}{\Delta[Na^{2+}]} \approx \frac{0.05 \text{ ppm}}{50 \text{ mM}}$ for pH = 6.8. Therefore, experiments with varying sodium concentration should be extended.

Although the influence of $[Mg^{2+}]$ is presumably the most relevant, influences of other ions should also be investigated. For example, Cu^{2+} is reported to interact solely with the α - and β phosphate of ATP [72], whereas Mg^{2+} , Ca^{2+} and Zn^{2+} are assumed to only interact with γ - and β -phosphate [73]. Maybe ions binding specifically to the α -phosphate might have a significant influence on δ_α and should be investigated further.

6.7.2 Incorporating the linewidths and J-coupling constants of ATP

A very important and central next step should be the incorporation of the ATP linewidths and J-coupling constants into the proposed look-up approach. To this end, the changes of linewidths and J-coupling constants with changing chemical environment were also investigated within this work. As already seen in the qualitative analysis of the spectral changes (section 5.2.1, Figure 5.14), the ATP linewidths, particularly of γ - and β -ATP change with varying magnesium ion concentration (both to a different extent). After an initial increase with increasing magnesium ion concentration, the linewidths become narrower again, when the magnesium ion concentration is increased further. This dependence can be nicely seen when plotting the quantified linewidths against the magnesium ion concentration (Figure B.3 in Appendix B). For the J-coupling constants, a decrease is observed for increasing magnesium ion concentration (Figure B.4 in Appendix B). The observed decrease of J-coupling constant with increasing magnesium concentration is in line with findings in [68, 73, 74].

To incorporate these observed dependencies into the look-up approach, the following models should be developed:

1. A model describing the dependency of the γ - and β -ATP linewidths on the magnesium ion concentration R , which is based on the Bloch-McConnell equations.
2. A model describing the decrease of the J-coupling constants $J_{\gamma\beta}$ and $J_{\alpha\beta}$ with increasing magnesium ion concentration.

The mentioned Bloch-McConnell equations which can be used for modelling of case 1, describe the effect of chemical exchange on the transverse magnetization (cf. section 2.2.3). With these Bloch-McConnell equations the effect of the chemical exchange between free ATP and its complexed form $[\text{Mg}(\text{ATP})]^{4-}$ on the ATP linewidth can be simulated, and a model derived, which describes the dependence of the γ - and β -ATP linewidths on the magnesium ion concentration, i.e. $LW_{\gamma}(R)$, $LW_{\beta}(R)$.

For the second case, in first approximation a simple exponential decay would be modelled yielding the two functional dependencies $J_{\gamma\beta}(R)$ and $J_{\alpha\beta}(R)$.

Finally, the models for $LW_{\gamma}(R)$, $LW_{\beta}(R)$, as well as for $J_{\gamma\beta}(R)$ and $J_{\alpha\beta}(R)$ could be incorporated into the look-up approach. The look-up could then use 7 parameters, i.e. $(\delta_{\gamma}, \delta_{\alpha}, \delta_{\beta}, LW_{\gamma}, LW_{\beta}, J_{\gamma\beta}, J_{\alpha\beta})$ to estimate the underlying chemical conditions of the acquired ^{31}P spectrum.

6.7.3 Combining the proposed approach with other methods besides ^{31}P MRS

The herein proposed approach for the determination of physiological parameters, like the pH value and the magnesium ion concentration, should not only be compared to the conventional approaches by means of ^{31}P MRS (discussed in section 6.6.2), but moreover also with other methods. Hereby, it should be differentiated between methods potentially usable as validation of the proposed approach, and alternative approaches potentially allowing for complementary insights.

As validation method, the comparison of the herein generated maps with ^{39}K and ^{23}Na MR images would be of great interest. ^{39}K and ^{23}Na are both spin $\frac{3}{2}$ nuclei, and can be used for MR imaging. Direct measurements of the magnesium concentration would also be of great value. This is in principle also possible by MRI, as magnesium has a spin of $\frac{5}{2}$. Moreover, there are also methods based on Mg^{2+} binding fluorescent indicators, e.g. *furaptra*, which are described in [75].

One alternative method for the determination of intracellular pH potentially providing complementary insights, is based on Chemical Exchange Saturation Transfer (CEST) imaging and was recently proposed for example by Boyd et al. [76, 77]. The high spatial resolution of CEST imaging might provide novel insights into potential pH heterogeneity in healthy or diseased tissue.

Another emerging technique is hyperpolarized (HP) ^{13}C MRI, which allows for in vivo

6 Discussion

pH imaging by using zymonic acid as pH sensor [78]. Although this technique also depends on calibration curves acquired in model solutions, the method is described to be “independent of concentration, temperature, ionic strength and protein concentration” [78]. However, HP ^{13}C MRI depends on the injection of an exogenous substance, in this case zymonic acid.

A comparison of these three pH imaging methods (i.e. ^{31}P MRS, CEST, and ^{13}C HP MRI) would be of great value, because (i) all three methods have their advantages and drawbacks, and (ii) it could open complementary insights into the underlying metabolism in healthy and diseased tissue.

7 Summary and Conclusion

Phosphorus (^{31}P) magnetic resonance spectroscopic imaging (MRSI) enables the non-invasive imaging of physiological parameters, like the pH value and the magnesium ion concentration, in living tissue. Typically, the measured chemical shifts of inorganic phosphate (P_i) and adenosine-5'-triphosphate (ATP) are translated to pH and magnesium ion concentration, $[\text{Mg}^{2+}]$, via calibration curves, like the modified Henderson Hasselbalch equation in the case of pH. However, the required parameters in these calibration equations, e.g. the $\text{p}K_a$ value, are defined only for normal physiological conditions. The use of constant parameters in the calibration curves poses a challenge, in particular for the application to pathologic conditions, e.g. in tumor tissue, where the chemical environment might change significantly.

In this work, a novel approach for the determination of pH and $[\text{Mg}^{2+}]$ applicable for various chemical conditions, was proposed. The basic idea of this proposed approach is to use multiple quantities of an acquired ^{31}P MR spectrum to determine the underlying physiological parameters in form of a look-up table. Compared to earlier approaches, the herein proposed look-up algorithm has the advantages of (i) being applicable to various chemical conditions, as it is not dependent on a single calibration curve, (ii) reducing the complexity of the look-up by focusing solely on conditions, which are relevant in vivo, and (iii) incorporating measurement uncertainties in form of Gaussian error distributions, making the determination of the output values more robust.

As first proof-of-principle, a look-up algorithm was implemented, which determines the three parameters pH, $[\text{Mg}^{2+}]$, and ionic strength, based on the measured chemical shifts of the three resonances of ATP, $(\delta_\gamma, \delta_\alpha, \delta_\beta)$. The use of the ATP chemical shifts for the determination of pH is beneficial with regard to the measurement time, due to the typically higher signal-to-noise-ratio compared to the resonance of P_i used in the the conventional modified Henderson Hasselbalch equation. A potential reduction in measurement time is of particular importance for the prospective application in vivo. In order to implement this proof-of-principle version of the look-up-based approach, the following three steps have been carried out:

7 Summary and Conclusion

1. The ranges of ^{31}P chemical shifts, which are typically measured in vivo, and their corresponding value ranges for pH and $[\text{Mg}^{2+}]$ (according to calculations using the conventional calibration equations), were identified. To this end, high-quality in vivo ^{31}P MRSI datasets acquired at $B_0 = 7\text{ T}$ were analyzed. To cover a large range of conditions, different tissue types were used, i.e. muscle tissue from the lower leg of healthy volunteers, and brain tissue from patients with glioblastoma. These analyses revealed a large variability of the measured chemical shifts, whereby particularly δ_α showed an unexpectedly large range of $[-7.70; -7.38]$ ppm. Following the conventional calibration equations, the identified chemical shift ranges for P_i and ATP correspond to pH values of approximately (6.9 – 7.3) and to concentrations of free $[\text{Mg}^{2+}]$ of approximately (0.2 – 1.4) mM.
2. The spectral changes due to varying chemical conditions were investigated in measurements of suitable model solutions. Based on prior knowledge about the variation of ATP chemical shifts obtained in vivo, and their corresponding pH and $[\text{Mg}^{2+}]$ values (cf. point 1), 114 model solutions were prepared with different pH, $[\text{Mg}^{2+}]$ and ionic strengths, and measured at $B_0 = 9.4\text{ T}$. Significant changes of the chemical shifts, linewidths and J-coupling constants with changing pH, $[\text{Mg}^{2+}]$ and $[\text{K}^+]$ (used as surrogate for the ionic strength in general) were observed. Over the investigated ranges, δ_γ showed the largest sensitivity to changes of pH and $[\text{K}^+]$, i.e. $\frac{\Delta\delta_\gamma}{\Delta\text{pH}} \approx \frac{0.55\text{ ppm}}{0.6\text{ pH}}$ and $\frac{\Delta\delta_\gamma}{\Delta[\text{K}^+]} \approx \frac{0.34\text{ ppm}}{131\text{ mM}}$. With regard to the varying magnesium ion concentration, δ_β showed the largest change, i.e. $\frac{\Delta\delta_\beta}{\Delta[\text{Mg}^{2+}]} \approx \frac{3.15\text{ ppm}}{10\text{ mM}}$. The measured chemical shift of α -ATP was the least sensitive to changes of pH, $[\text{Mg}^{2+}]$ and $[\text{K}^+]$ (maximal observed change $\frac{\Delta\delta_\alpha}{\Delta[\text{Mg}^{2+}]} \approx \frac{0.6\text{ ppm}}{10\text{ mM}}$). A further important observation was the mismatch between the chemical shifts of α -ATP measured in model solutions and the range of δ_α observed in vivo. While for δ_γ and δ_β , the entire ranges obtained in vivo could be represented by the measurements in model solutions, this was not the case for δ_α , despite the large range of $[\text{Mg}^{2+}]$ and $[\text{K}^+]$ covered.
3. In order to implement a look-up table with sufficient entries, allowing for an accurate assignment of physiological values, an interpolation between the 114 measured datapoints was performed. For this interpolation, a suitable model describing the dependencies of the measured ATP chemical shifts on pH, $[\text{Mg}^{2+}]$, and $[\text{K}^+]$, i.e. $\delta_i(\text{pH}, \text{Mg}, \text{K})$, was required. To this end, three different approaches were pursued, whereby for all, the starting point was the non-linear dependence of the chemical shifts on the magnesium ion concentration. The dependence of $(\delta_\gamma, \delta_\alpha, \delta_\beta)$ on

pH and $[K^+]$ was incorporated by a linearization of the determined parameters of the model functions $\delta_\gamma(Mg)$, $\delta_\alpha(Mg)$, $\delta_\beta(Mg)$, finally yielding multi-dimensional model functions $\delta_i(pH, Mg, K)$, $i \in (\gamma, \alpha, \beta)$. The developed model based on the Hill equation $\delta_i^{\text{Hill}}(pH, Mg, K)$ was determined to be most suitable for the application in vivo, and hence used for the implementation of the look-up table.

Finally, the implemented approach was applied to the in vivo ^{31}P MRSI datasets analyzed before. It was found, that with the implemented look-up table utilizing all three ATP chemical shifts, no output values for (pH, Mg, K) could be assigned in over 50% of the muscle voxels, and over 60% of the brain voxels. Analyses revealed, that the reason for the unsuccessful assignments is a mismatch between the possible solutions determined for the input δ_α and the possible solutions determined for the input δ_γ and δ_β . Together with the observed large variation of measured δ_α in vivo, which could not be entirely represented in model solution measurements, this mismatch hints towards influences on the chemical shifts, which were not considered so far.

An adapted version of the implemented look-up algorithm only using the chemical shifts $(\delta_\gamma, \delta_\beta)$ resulted in a successful assignment of solution triples (pH, Mg, K) in over 98% of the muscle voxels, and over 90% of the brain voxels. The comparison of the resulting output maps according to the adapted look-up algorithm with the conventionally calculated maps for pH and free $[\text{Mg}^{2+}]$ revealed several differences. For example, generally lower pH values were determined by the look-up approach compared to the conventional calculation via the Henderson Hasselbalch equation. The expected increase of intracellular pH in tumor tissue was observed in several parts of the tumor regions for all patients, showing values of up to $\text{pH}_{\text{Out}} = 7.4$, but was averaged out in the regions-of-interest (ROIs) analyses across the entire tumor region. For the relative magnesium ion concentration determined by the look-up algorithm, for all patients, a clear increase was observed in tumor tissue, in both the maps and the ROI analyses. This trend of increased magnesium ion concentration in the tumor was not observed that clearly in the conventional $[\text{Mg}^{2+}]_{\text{Conv}}$ maps. The observed differences between the maps according to the look-up approach and the conventionally calculated maps suggest that the mentioned challenges of the conventional calibration equations might hamper a reliable determination of pH and magnesium ion concentration, particularly for the application to pathophysiological conditions.

To conclude, the novel approach proposed in this work, allows for the determination of pH values and magnesium ion concentration under various chemical conditions by utilizing multiple quantities obtained in a measured ^{31}P spectrum in form of a look-up table.

7 Summary and Conclusion

The proposed method reduces the complexity of the assignment by focusing solely on conditions which are relevant *in vivo*, and improves its robustness by including measurement uncertainties. As proof-of-principle, the approach was implemented for the determination of pH and $[\text{Mg}^{2+}]$ for different ionic strengths, by using the chemical shifts of γ - and β -ATP. A decisive strength of this novel approach is its expandability by inclusion of other quantities, like the linewidths and J-coupling constants, whose clear dependencies on the chemical environment can be potentially exploited for a more robust determination of physiological parameters. The proposed approach is an important step towards a method allowing for a detailed characterization of different tissue types under various chemical conditions, which is particularly of importance for the application to pathologies.

Appendices

A Derivation of a modified form of the Hill equation for NMR

In the work from Pettegrew et al. [23], where numerous titration curves $\delta(pH)$ for several ^{31}P metabolites were determined, the following expression for the observed chemical shift δ_{obs} in dependence on the pH value ($\text{pH} = -\log[\text{H}^+]$) is used:

$$\delta_{\text{obs}} = \frac{\delta_{\text{HA}} \cdot [\text{H}^+]^n + \delta_{\text{A}} \cdot (K_{\text{A}})^n}{[\text{H}^+]^n + (K_{\text{A}})^n}. \quad (1)$$

This expression is based on considerations from Markley [79], using a modified form of the Hill equation. The derivation of equation (1) from the general form of the Hill equation, will be shortly explained in the following.

For the binding of n molecules of ligand (L) to a receptor (R):



the Hill equation gives the following relation [80]:

$$\frac{[\text{Bound}]}{[\text{Total}]} = \frac{[\text{RL}_n]}{[\text{R}] + [\text{RL}_n]} = \frac{[\text{L}]^n}{K_{\text{D}} + [\text{L}]^n}, \quad (3)$$

where n is the so-called Hill coefficient, which is a measure of the cooperativity of the binding. The dissociation constant in equation (3) can be replaced by $K_{\text{D}} = (K_{\text{A}})^n$, where K_{A} is the concentration $[\text{L}]$, at which half of the receptors are bound. Transferred to the acid-base reaction $\text{A}^- + \text{H}^+ \rightleftharpoons \text{HA}$ (see section 2.4.1), this yields

$$\frac{[\text{Bound}]}{[\text{Total}]} = \frac{[\text{H}^+]^n}{K_{\text{A}}^n + [\text{H}^+]^n}. \quad (4)$$

The ratio of bound to total concentration of the “receptor” can be expressed in terms of NMR by a ratio of observed chemical shift differences (compare Figure 2.9 in section

Appendices

2.5.1):

$$\frac{[\text{Bound}]}{[\text{Total}]} = 1 - \frac{[\text{Free}]}{[\text{Total}]} = \frac{\delta_{\text{HA}} - \delta_{\text{obs}}}{\delta_{\text{HA}} - \delta_{\text{A}}}. \quad (5)$$

Combining equations (4) and (5) yields equation (1).

For the case of $n = 1$, equation (1) can be rearranged to the well-known modified Henderson-Hasselbalch equation (equation (2.64)) by using the expressions for pH and pK_a in section 2.4.1 (eqs. (2.50) and (2.53)).

B Quantified linewidths and J-coupling constants in dependence on the chemical environment

Besides the chemical shifts, also the linewidths and J-coupling constants for ATP were determined for all acquired ^{31}P spectra. In the following, the quantified linewidths and J-coupling constants will be presented in dependence on the pH value, the magnesium ion content, and the potassium ion concentration.

Linewidths

The linewidths are given relative to the quantified linewidth for phosphocreatine (PCr), in order to compensate for B_0 inhomogeneities, which have a significant effect on the observed linewidth of MR resonances. The error margins shown are calculated following Gaussian error propagation.

The relative linewidths of P_i and α -ATP seem to have no dependence on pH, magnesium content R , and potassium concentration $[\text{K}^+]$, whereas for γ - and β -ATP, a clear dependence on the magnesium ion content is observed (Figures B.1, B.2, and B.3). The trend of first increasing linewidths with increasing R , which become lower again for high magnesium content was already observed in the qualitative analysis of the spectral changes in section 5.2.1 (cf. Figure 5.14).

J-coupling constants

The quantified J-coupling constants $J_{\gamma\beta}$ and $J_{\alpha\beta}$ are shown in dependence on the pH value, potassium concentration $[\text{K}^+]$, and magnesium ion content $R = \frac{\text{Mg}_{\text{tot}}}{\text{ATP}_{\text{tot}}}$ in Figure B.4. Both $J_{\gamma\beta}$ and $J_{\alpha\beta}$ seem to be independent on pH and $[\text{K}^+]$, whereas for the magnesium ion content, a clear trend can be observed. Both $J_{\gamma\beta}$ and $J_{\alpha\beta}$ decrease with increasing R .

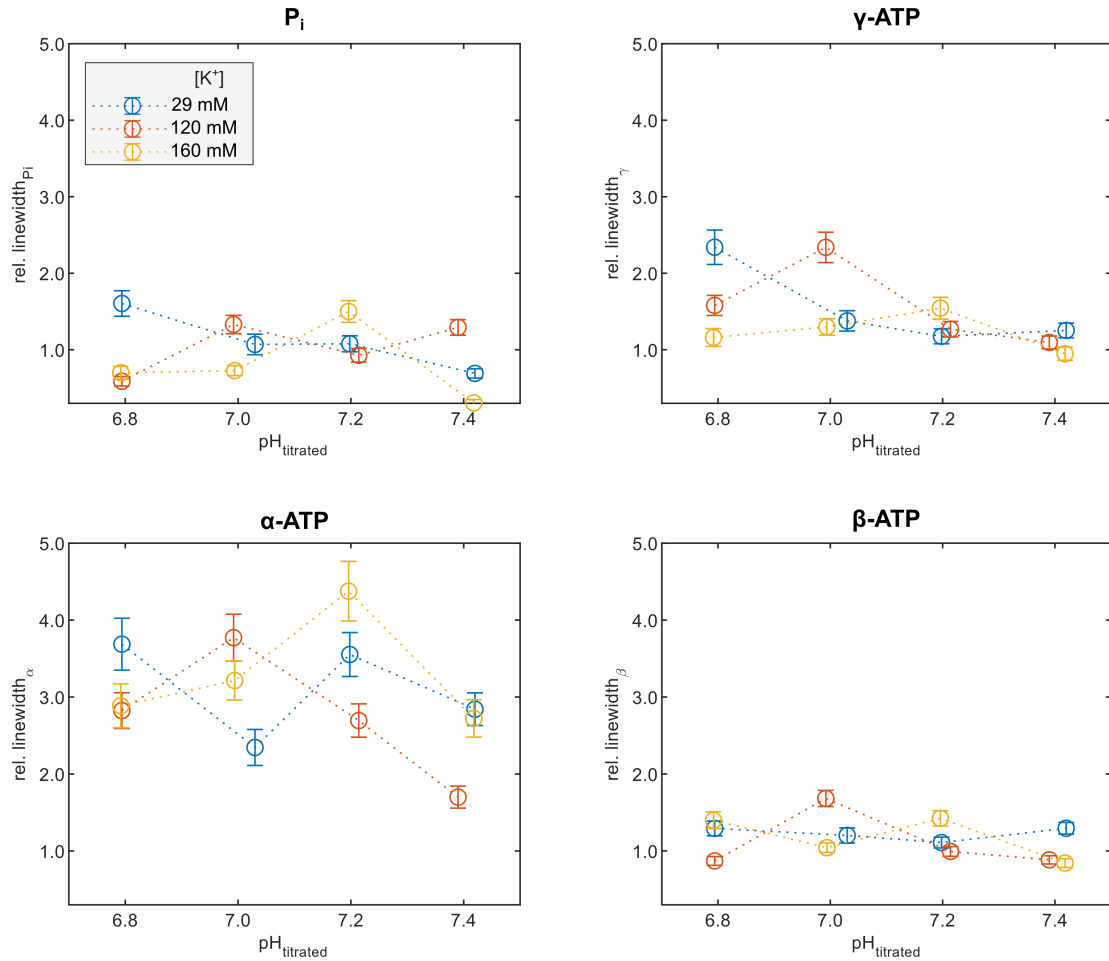


Figure B.1: Quantified relative linewidths from the subset with $R = 0$ and $[\text{Na}^{2+}] = 29 \text{ mM}$, in dependence on the titrated pH value of the model solution. The relative linewidths of P_i and the three resonances of ATP are shown for the different subsets with $[\text{K}^+] = 29 \text{ mM}$ (blue), 120 mM (red), and 160 mM (yellow). For all shown metabolites, the relative linewidths seems to be independent of the pH value.

B Quantified linewidths and J -coupling constants in dependence on the chemical environment

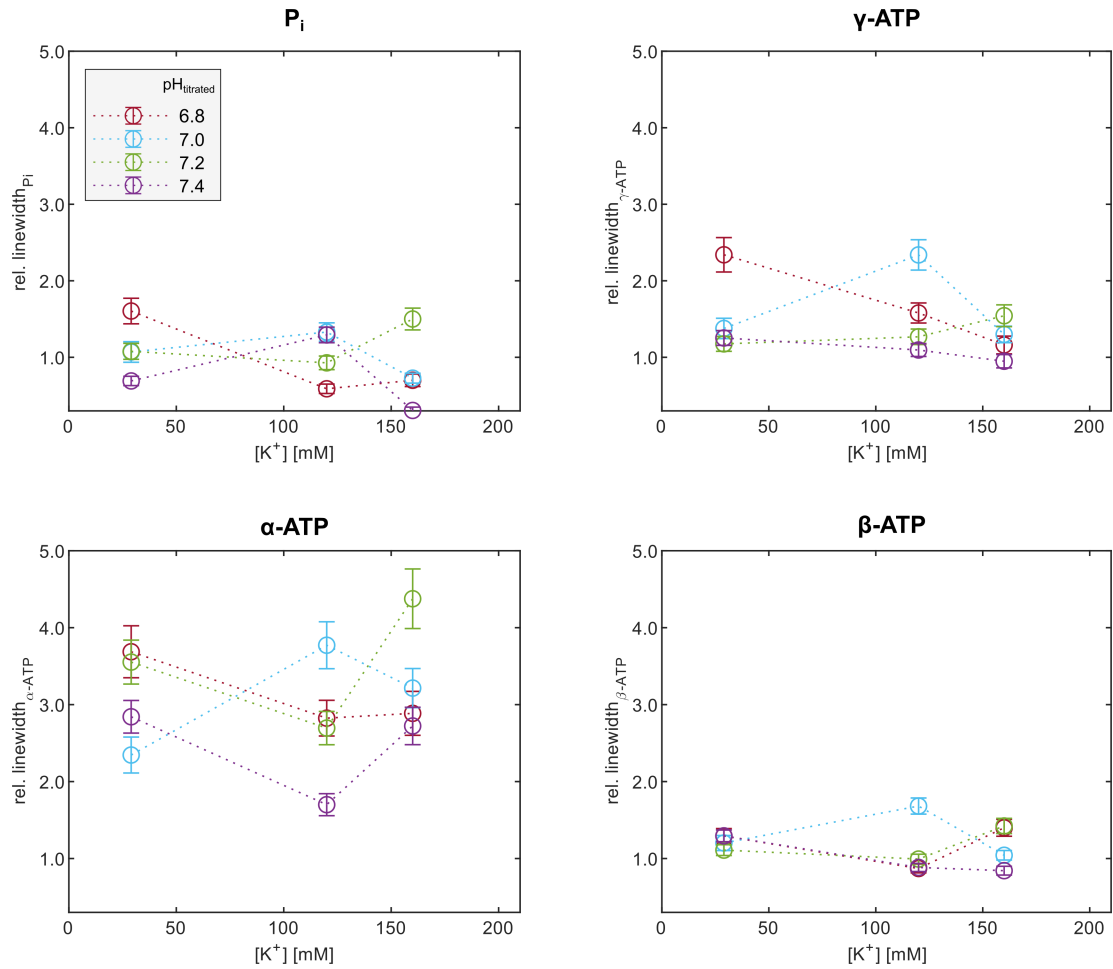


Figure B.2: Quantified relative linewidths from the subset with $R = 0$ and $[Na^{2+}] = 29$ mM, in dependence on the potassium ion concentration of the model solution. The relative linewidths of P_i and the three resonances of ATP are shown for the different subsets with pH = 6.8 (red), 7.0 (blue), 7.2 (green) and 7.4 (purple). For all shown metabolites, the relative linewidths seems to be independent on the potassium ion concentration.

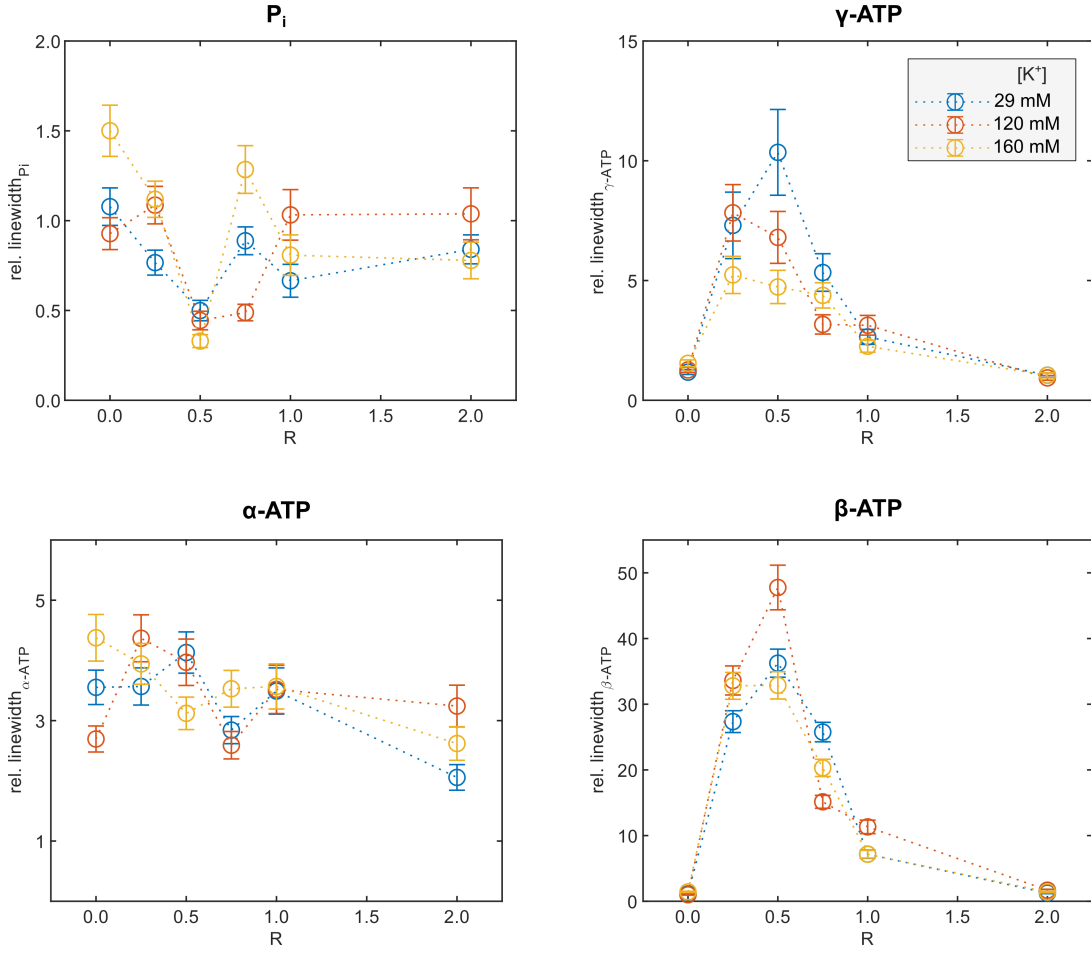


Figure B.3: Quantified relative linewidths from the subset with $\text{pH} = 7.2$ and $[\text{Na}^{2+}] = 29 \text{ mM}$, in dependence on the magnesium ion content ($R = \frac{\text{Mg}_{\text{tot}}}{\text{ATP}_{\text{tot}}}$) of the model solution. The relative linewidths of P_i and the three resonances of ATP are shown for the different subsets with $[\text{K}^+] = 29 \text{ mM}$ (blue), 120 mM (red), and 160 mM (yellow). Whereas the relative linewidth of P_i seems to be independent on the magnesium ion content, the resonances of ATP has a strong dependence on the magnesium ion content. Hereby, β -ATP shows the strongest change, followed by γ -ATP. The relative linewidth of α -ATP shows a comparable trend as for γ - and β -ATP, only for the subset with $[\text{K}^+] = 120 \text{ mM}$ (red data points).

B Quantified linewidths and J-coupling constants in dependence on the chemical environment

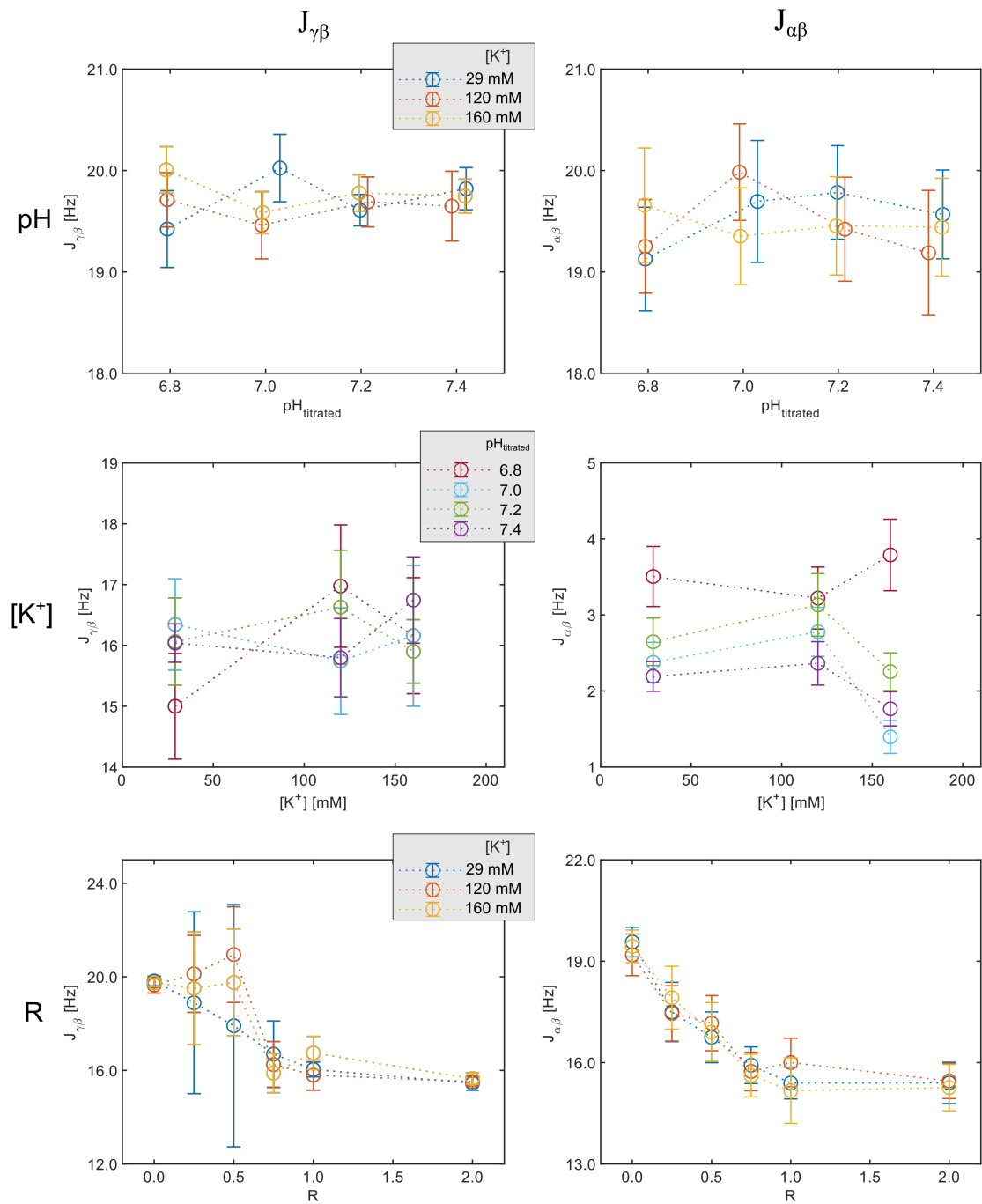


Figure B.4: Quantified J-coupling constants $J_{\gamma\beta}$ (left column) and $J_{\alpha\beta}$ (right column) in dependence on pH (first row), potassium concentration $[\text{K}^+]$, and magnesium ion content $R = \frac{\text{Mg}_{\text{tot}}}{\text{ATP}_{\text{tot}}}$. $J_{\gamma\beta}$ and $J_{\alpha\beta}$ seem to have no dependence on pH and $[\text{K}^+]$, but on the magnesium ion content. Both $J_{\gamma\beta}$ and $J_{\alpha\beta}$ decrease with increasing magnesium ion content.

C Modelling of the α - and β -ATP chemical shifts

The modelling of the chemical shifts was performed for all three resonances of ATP, but was only shown for γ -ATP in the main part of this work (section 5.3). The corresponding plots for α - and β -ATP for the model based on the Hill equation will be presented in the following.

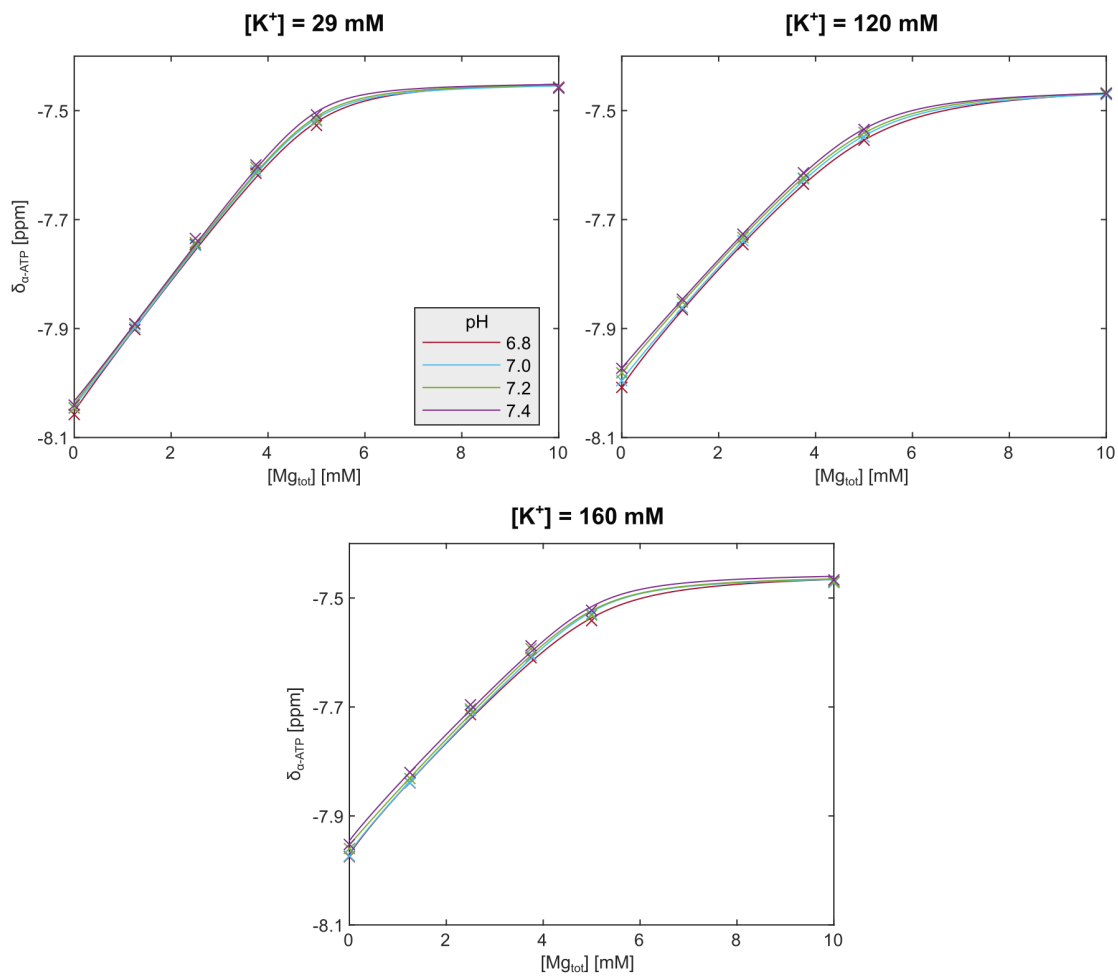


Figure C.5: One-dimensional function $\delta_{\alpha}^{\text{Hill}}(Mg_{\text{tot}})$ fitted according to equation (3.8) for the three subsets with $[\text{K}^+] = 29, 120, 160 \text{ mM}$ and for the pH values (6.8 – 7.4) (colors). The range $[\text{Mg}_{\text{tot}}] = [0 - 10] \text{ mM}$ corresponds to $R = [0 - 2]$ used in sections 5.3.1 and 5.3.2.

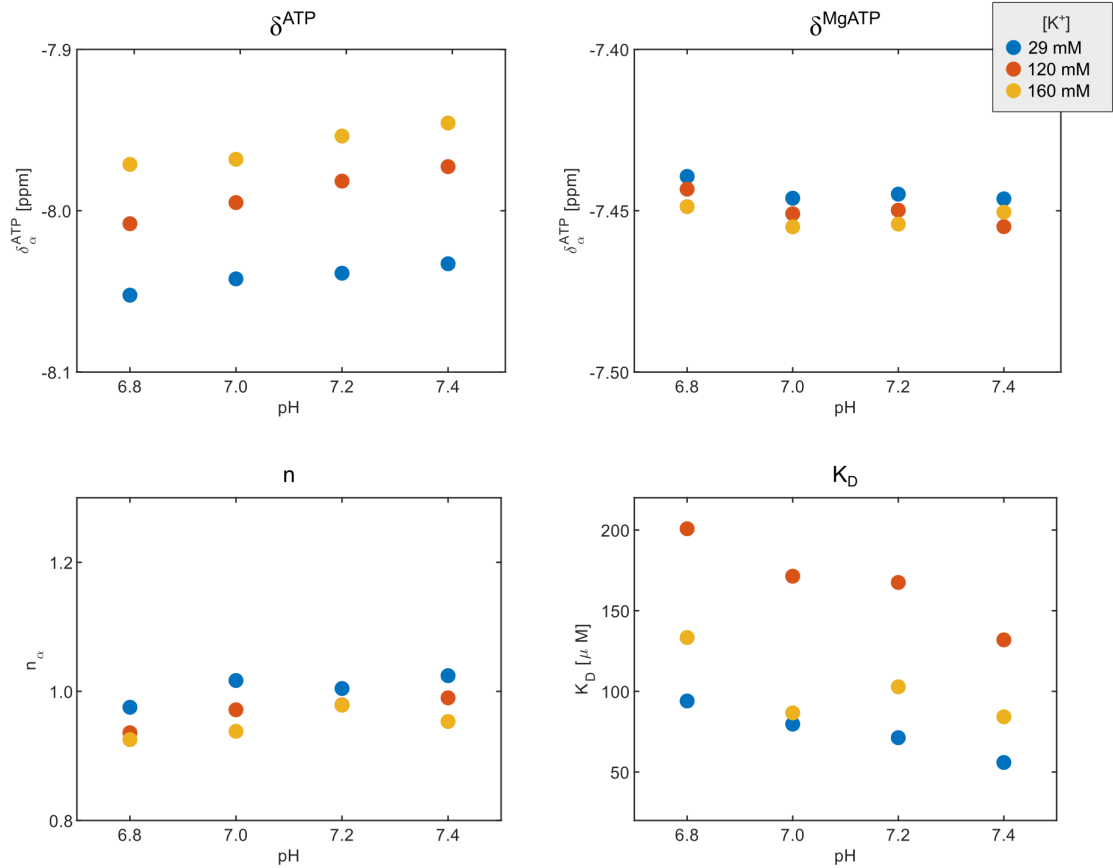


Figure C.6: Fit parameters of the model function $\delta_{\alpha}^{\text{Hill}}(Mg_{\text{tot}})$ ((3.8)) determined from the individual one-dimensional fits of the subsets for α -ATP, plotted against the pH value and shown for the subsets with different potassium concentrations (colors). The following parameters were determined by the fit: the limiting chemical shifts δ^{ATP} and δ^{MgATP} , the Hill coefficient n , and the dissociation constant K_D .

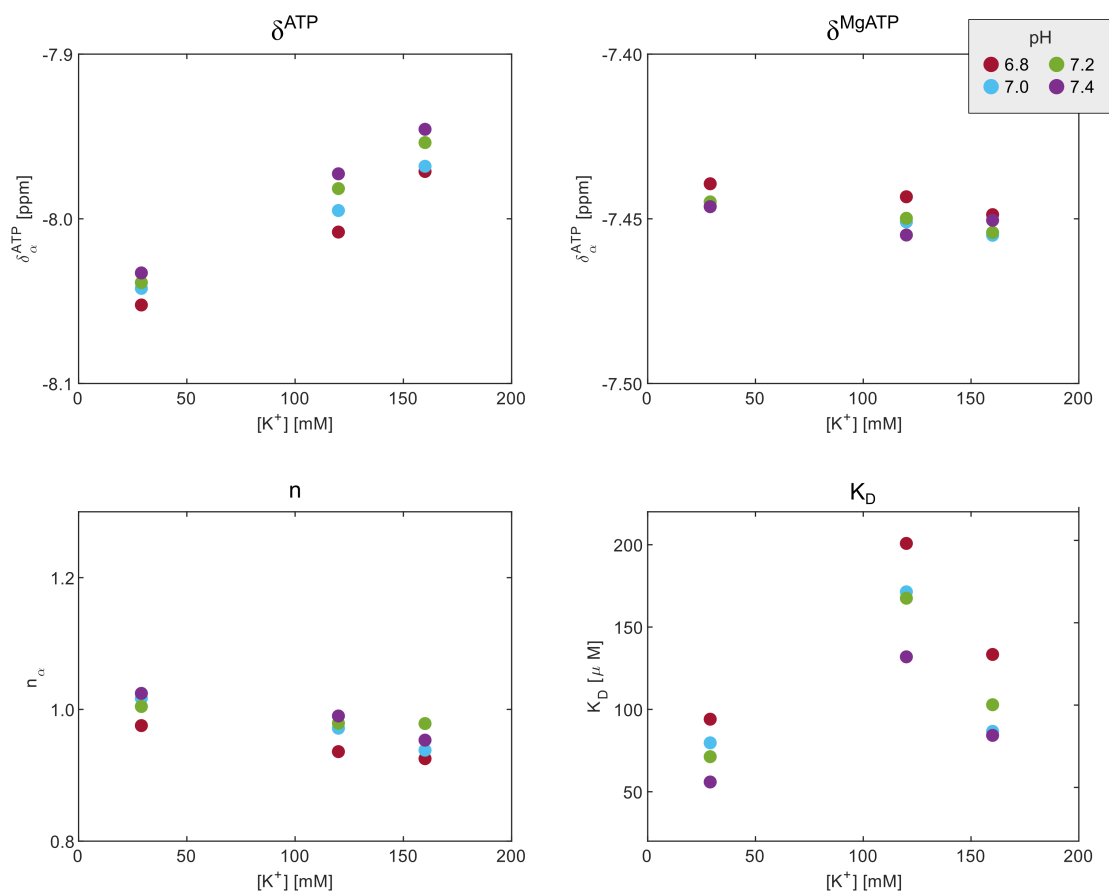


Figure C.7: Fit parameters of the model function developed from the Hill equation $\delta^{Hill}(Mg_{tot})$ ((3.8)) determined from the individual one-dimensional fits of the subsets for α -ATP, plotted against the potassium concentration $[K^+]$ and shown for the subsets with different pH values (colors). The following parameters were determined by the fit: the limiting chemical shifts δ^{ATP} and δ^{MgATP} , the Hill coefficient n , and the dissociation constant K_D .

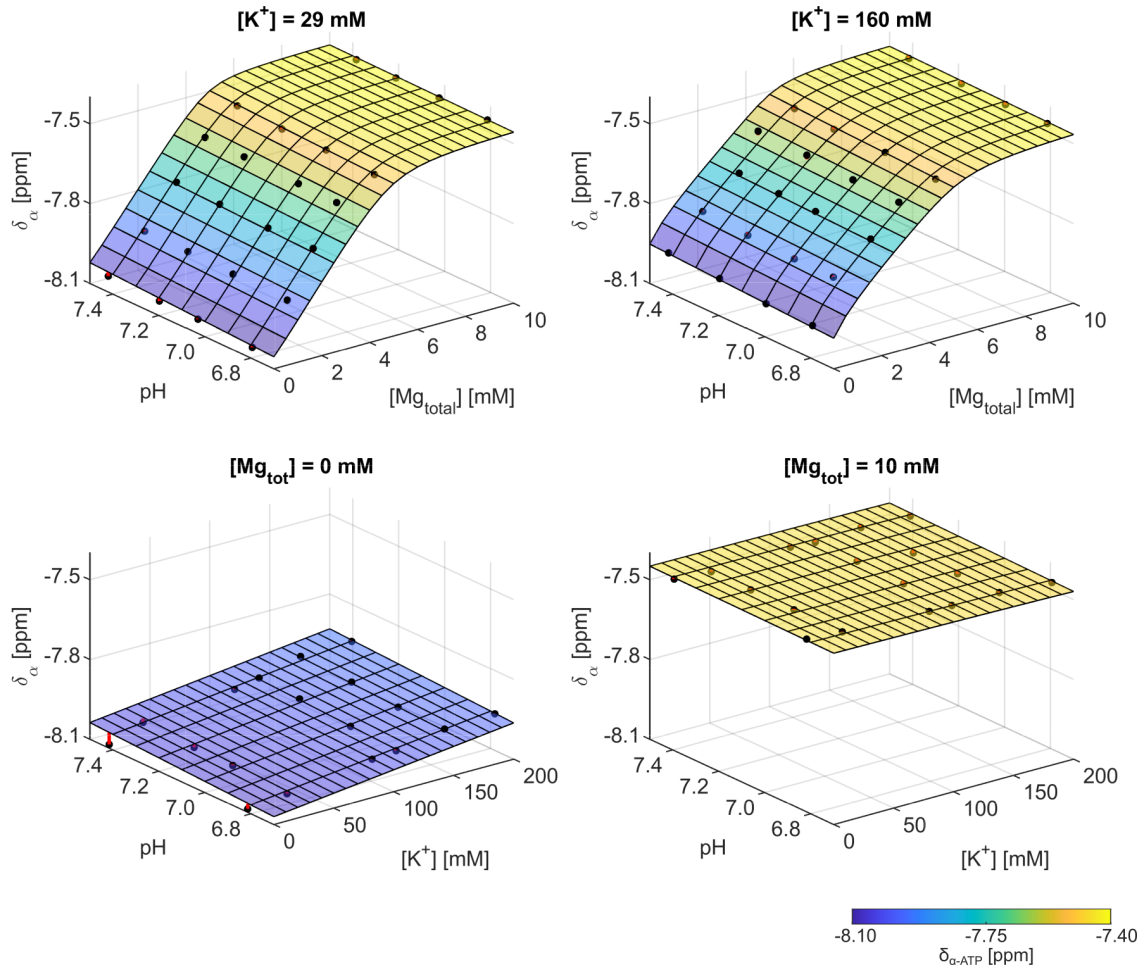


Figure C.8: Multi-dimensional fit of the model function $\delta_{\alpha}^{Hill}(Mg_{tot}, pH, K)$. The fitted function is illustrated for the subspace $\delta(Mg_{tot}, pH)$ with $[K^+] = 29$ and 160 mM (top row), and for the subspace $\delta(pH, K)$ with $Mg_{tot} = 0$ and 10mM (bottom row). The deviation of the measured chemical shifts from the fitted curve is illustrated with red pins.

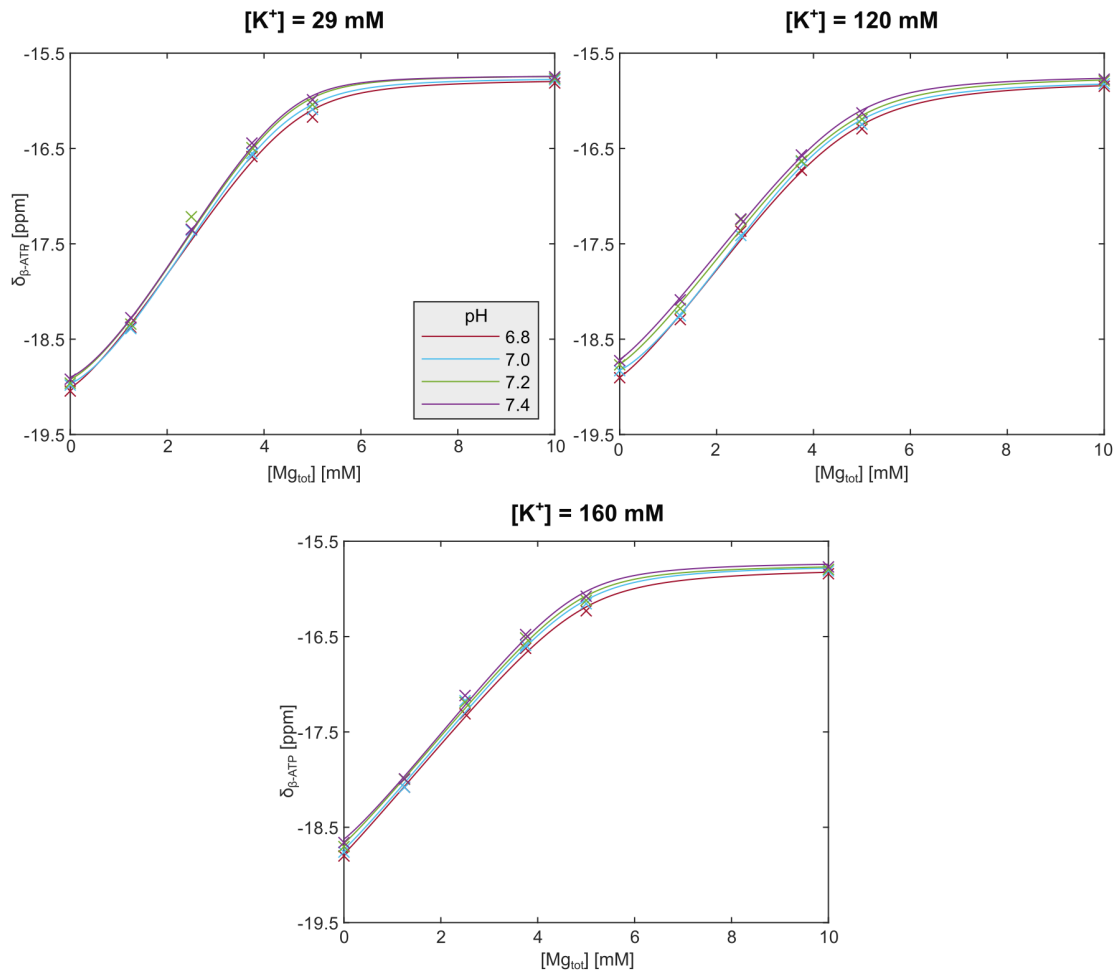


Figure C.9: One-dimensional function $\delta_{\beta}(\text{Mg}_{\text{tot}})$ fitted according to equation (3.8) for the three subsets with $[\text{K}^+] = 29, 120, 160 \text{ mM}$ and for the pH values (6.8 – 7.4) (colors). The range $[\text{Mg}_{\text{tot}}] = [0 - 10] \text{ mM}$ corresponds to $R = [0 - 2]$ used in sections 5.3.1 and 5.3.2.

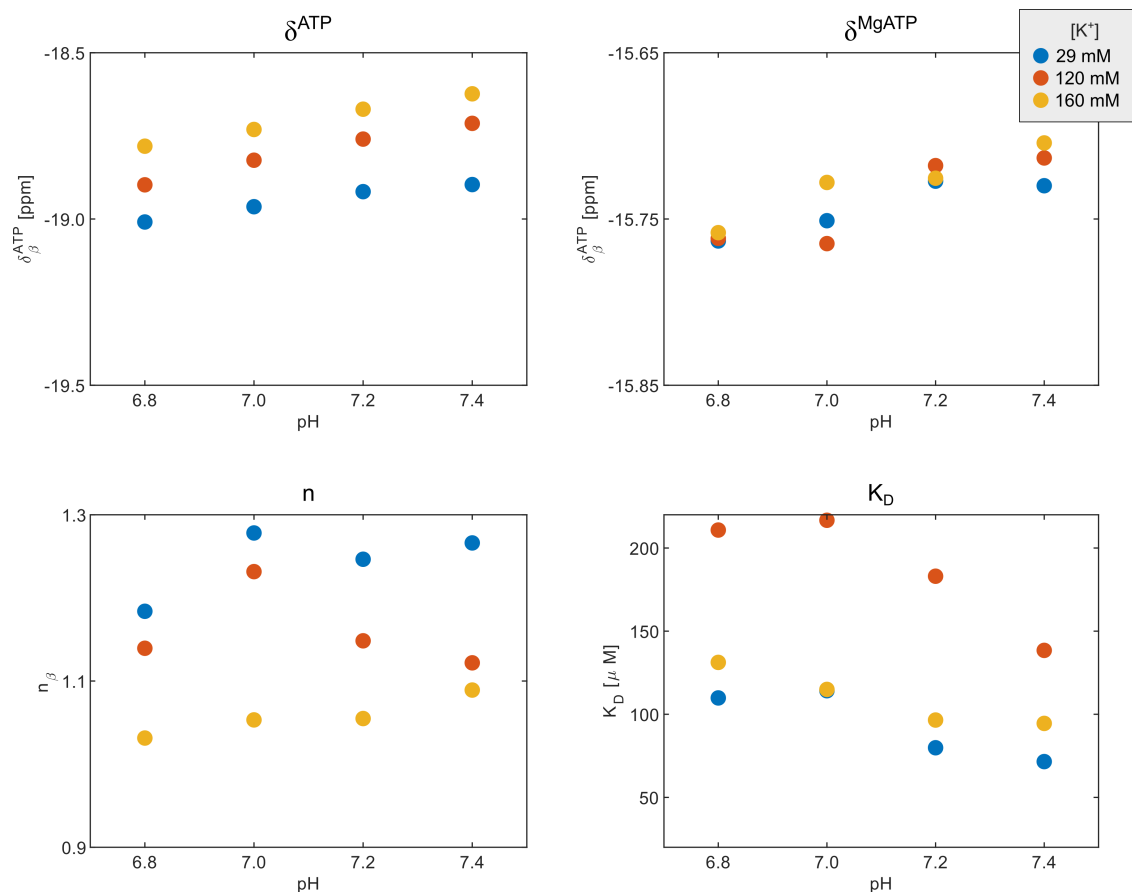


Figure C.10: Fit parameters of the model function $\delta_{\beta}^{\text{Hill}}(M_{g_{\text{tot}}})$ ((3.8)) determined from the individual one-dimensional fits of the subsets for β -ATP, plotted against the pH value and shown for the subsets with different potassium concentrations (colors). The following parameters were determined by the fit: the limiting chemical shifts δ^{ATP} and δ^{MgATP} , the Hill coefficient n , and the dissociation constant K_D .

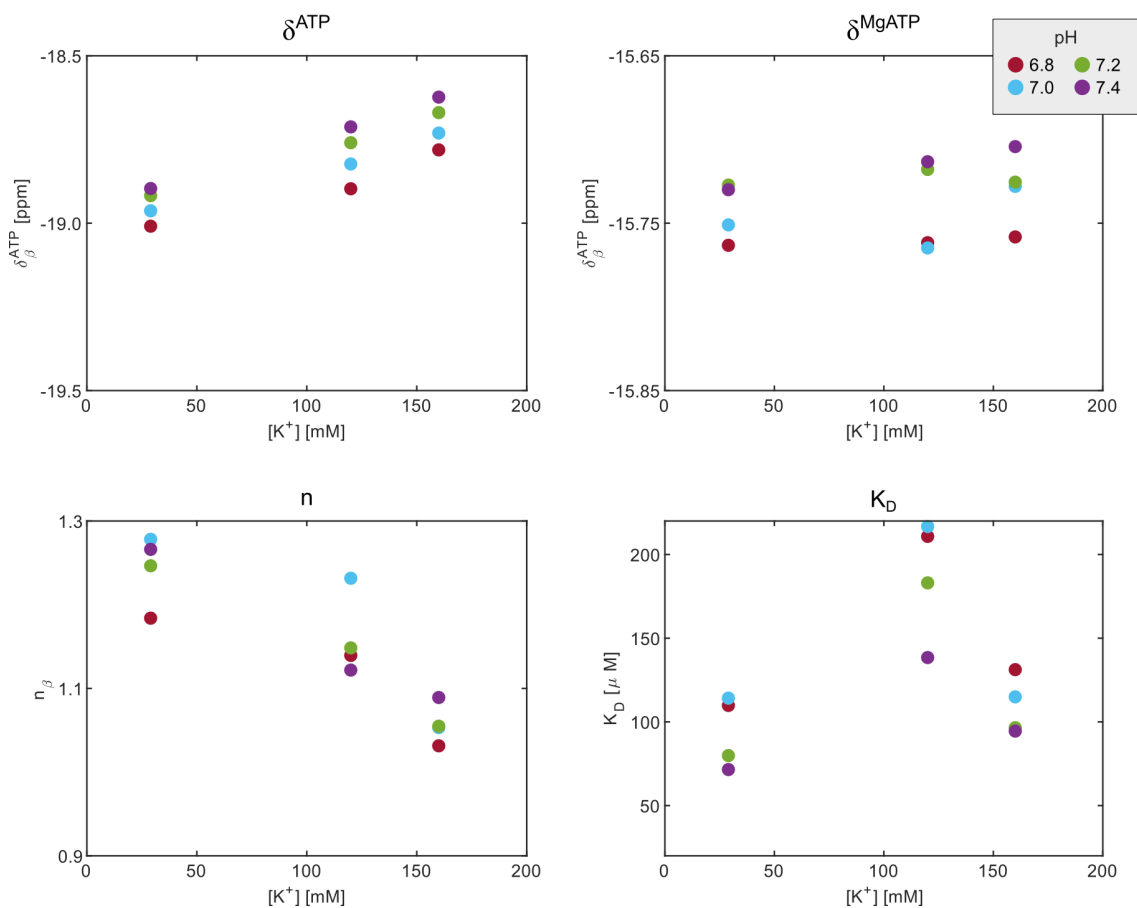


Figure C.11: Fit parameters of the model function $\delta_{\beta}^{\text{Hill}}(Mg_{\text{tot}})$ ((3.8)) determined from the individual one-dimensional fits of the subsets for β -ATP, plotted against the potassium concentration $[K^+]$ and shown for the subsets with different pH values (colors). The following parameters were determined by the fit: the limiting chemical shifts δ^{ATP} and δ^{MgATP} , the Hill coefficient n , and the dissociation constant K_D .

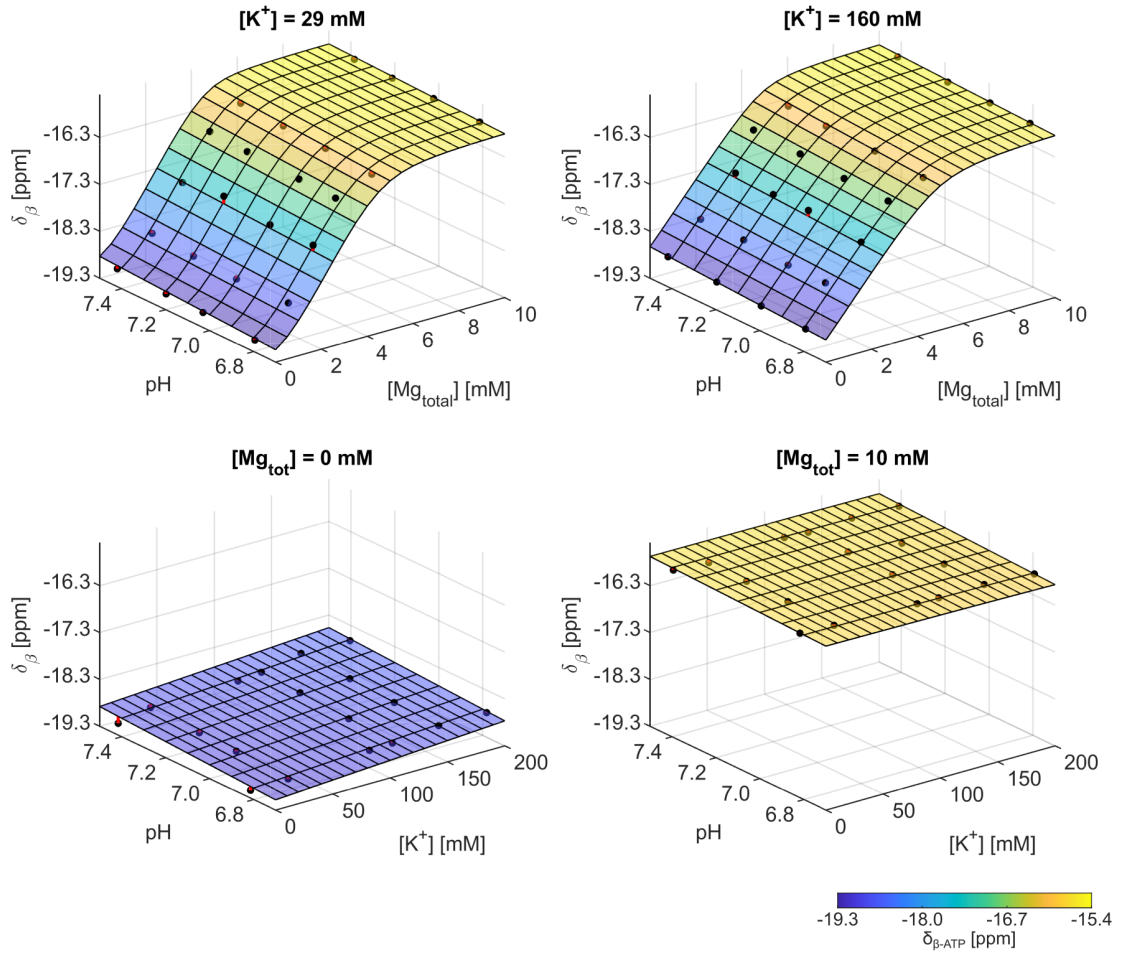


Figure C.12: Multi-dimensional fit of the model function $\delta_{\beta}^{\text{Hill}}(Mg_{tot}, pH, K)$. The fitted function is illustrated for the subspace $\delta(Mg_{tot}, pH)$ with $[K^+] = 29$ and 160 mM (top row), and for the subspace $\delta(pH, K)$ with $Mg_{tot} = 0$ and 10mM (bottom row). The deviation of the measured chemical shifts from the fitted curve is illustrated with red pins.

D Test of functionality of the implemented look-up algorithm on model solution measurements

The implemented look-up algorithm for the determination of the pH value, magnesium and potassium ion concentration based on the measured chemical shifts of γ -, α - and β -ATP (description of the algorithm can be found in section 4.5) was tested on measurements on model solutions. To this end, the measured chemical shifts ($\delta_\gamma, \delta_\alpha, \delta_\beta$) of 222 model solutions with different prepared chemical conditions were fed into the algorithm and the output values ($\text{pH}_{\text{Out}}, [\text{Mg}_{\text{tot}}]_{\text{Out}}, [\text{K}^+]_{\text{Out}}$) compared to the corresponding prepared conditions. Additionally to the model solutions used for the model development as listed in Table 4.1, also model solutions were used as test sets, which were prepared under different conditions (e.g. different sodium concentrations, imidazole buffer solution differently prepared, different temperature during pH titration). Although, the chemical conditions in 108 out of 222 test datasets is not comparable to the conditions of the model solutions used for the model development, they were all tested in order to check whether a determination of pH and magnesium is possible under slightly different chemical conditions as modelled. The error margins shown in Figures D.13, D.14 and D.15 are calculated as the respective weighted mean errors, in accordance with equations (4.4).

The determined output values ($\text{pH}_{\text{Out}}, [\text{Mg}_{\text{tot}}]_{\text{Out}}$) (Figures D.13 and D.14) are in agreement with the prepared values for most of the investigated datasets. For the estimation of the potassium concentration (Figure D.15), in most of the cases the determined values $[\text{K}^+]_{\text{Out}}$ do not agree with the prepared values. It should be kept in mind, that 108 out of the 222 tested datasets were from model solutions acquired under slightly different chemical conditions.

D Test of functionality of the implemented look-up algorithm on model solution measurements

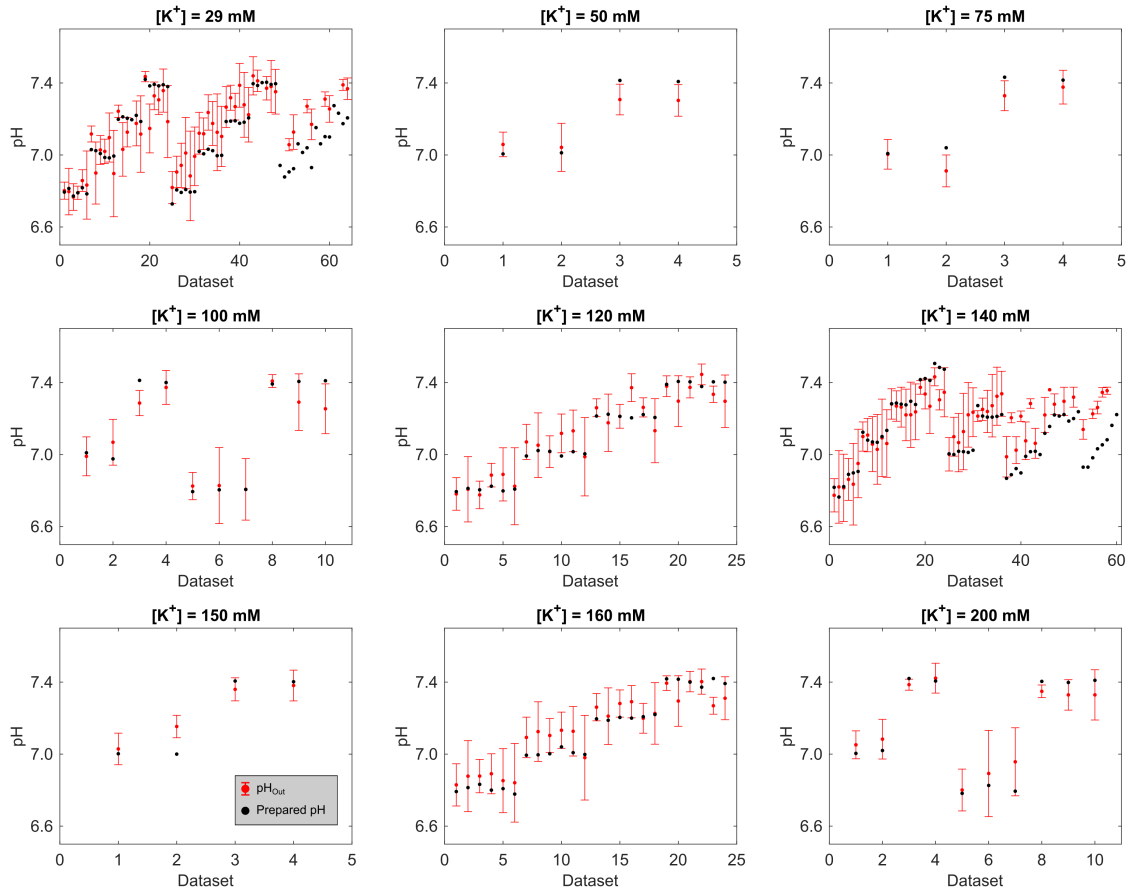


Figure D.13: Determined pH values using the implemented look-up algorithm for measurements on 222 model solutions. The determined value pH_{Dict} (red) is compared with the prepared pH value (black). For better visibility, the datasets are grouped by the potassium concentration $[K^+]$.

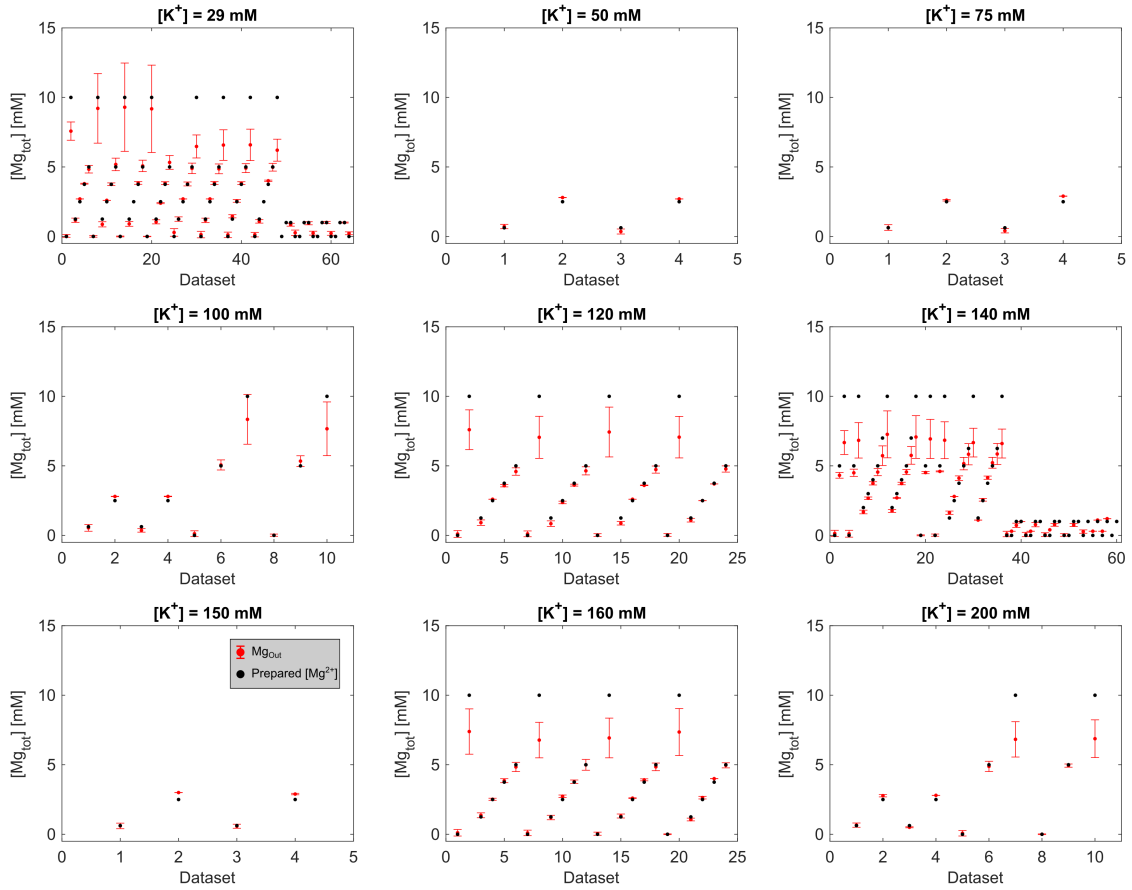


Figure D.14: Estimated values for the total magnesium ion concentration using the implemented look-up algorithm for measurements on 222 model solutions. The determined value $[Mg_{tot}]_{Dict}$ (red) is compared with the prepared $[Mg_{tot}]$ values (black). For better visibility, the datasets are grouped by the potassium concentration $[K^+]$.

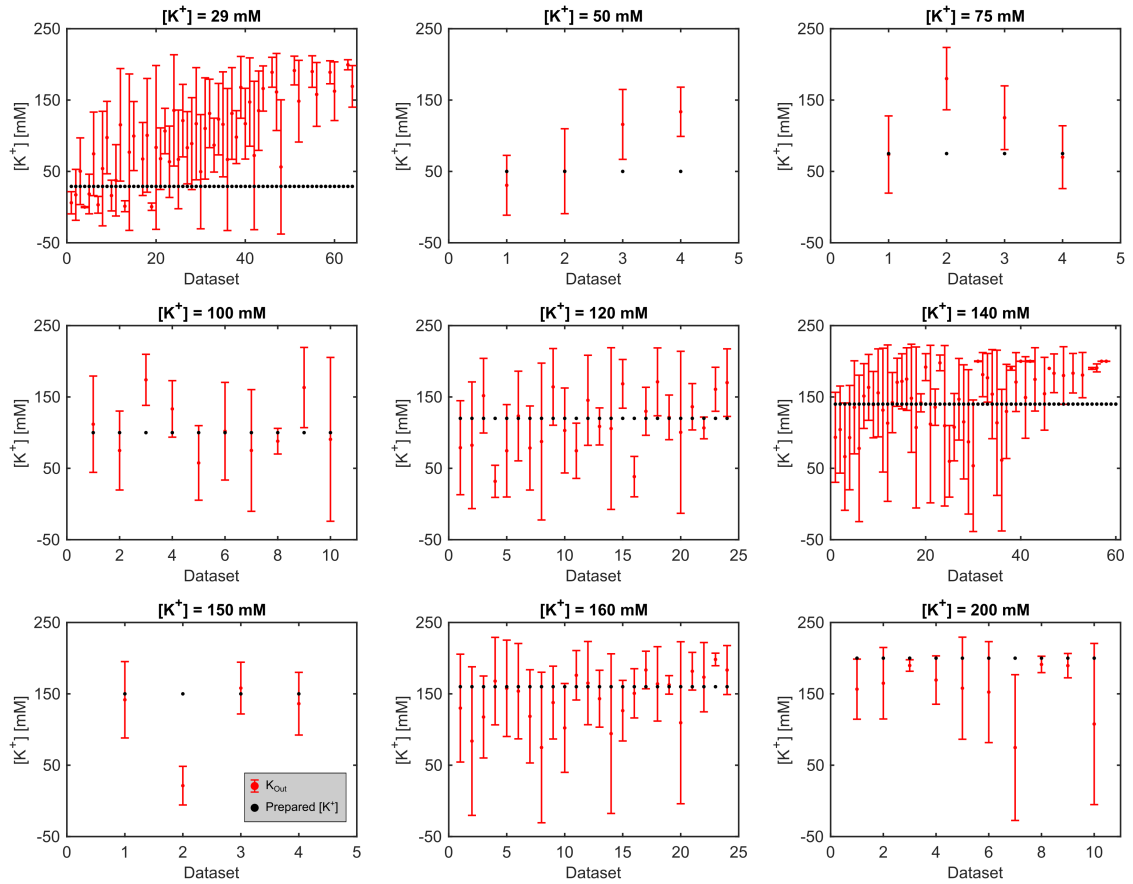


Figure D.15: Estimated values for the potassium ion concentration using the implemented look-up algorithm for measurements on 222 model solutions. The determined value $[K^+]_{\text{Dict}}$ (red) is compared with the prepared $[K^+]$ values (black). For better visibility, the datasets are grouped by the potassium concentration $[K^+]$.

E Application of the look-up algorithm to in vivo ³¹P MRSI datasets using all three ATP chemical shifts

The initial implementation of the look-up algorithm incorporated the use of the chemical shifts of all three ATP resonances, i.e. $(\delta_\gamma, \delta_\alpha, \delta_\beta)$, to determine the underlying chemical conditions (pH, Mg, K) . As described in section 5.4.1 of the results, this yielded maps with a high number of voxels, where the look-up algorithm could not find any combination of the input triple $(\delta_\gamma, \delta_\alpha, \delta_\beta)$. For the lower leg muscle datasets, in 83% (volunteer 1), 42% (volunteer 2), and 69% (volunteer 3) of the respective muscle voxels, no solution was found by the look-up algorithm. For the brain datasets, in 59% (patient 1), 61% (patient 2), and 53% (patient 3) of the brain voxels no solution was found. In Figures E.16 and E.17, the output maps of the initial version of the algorithm using all three chemical shifts $(\delta_\gamma, \delta_\alpha, \delta_\beta)$ as input are representatively shown for volunteer 2 and patient 1.

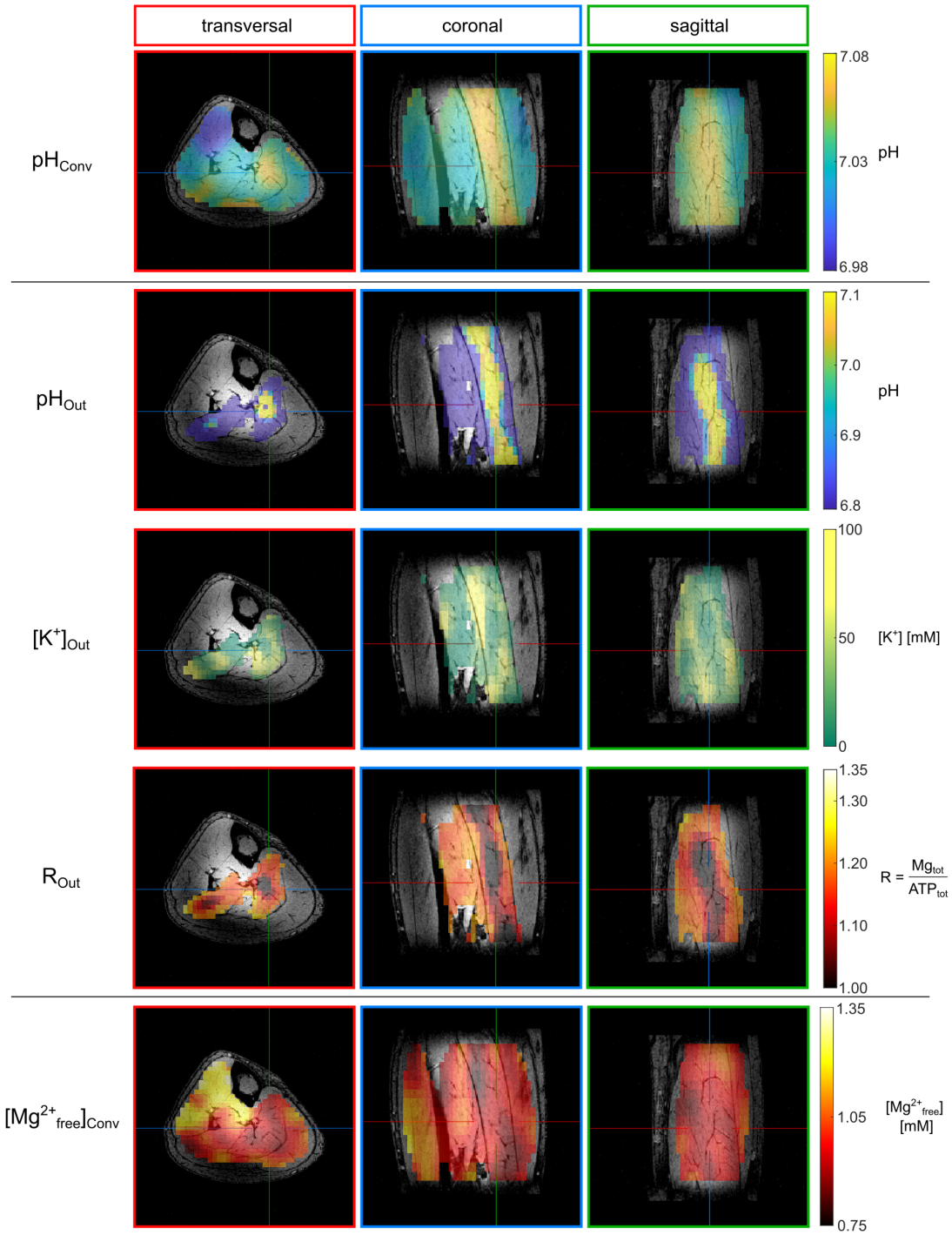


Figure E.16: Output maps of the implemented look-up algorithm using all three chemical shifts ($\delta_\gamma, \delta_\alpha, \delta_\beta$) as input for the assignment of ($\text{pH}, \text{Mg}, \text{K}$). The output maps pH_{Out} , $[\text{K}^+]_{\text{Out}}$, and $R_{\text{Out}} = \frac{[\text{Mg}_{\text{total}}]}{[\text{ATP}_{\text{total}}]}$ applied to the ^{31}P MRSI dataset of the lower leg muscles from volunteer 2 are shown. For an easier comparison, the conventionally calculated maps for pH and $[\text{Mg}^{2+}_{\text{free}}]$ are also shown at the top and bottom of the figure.

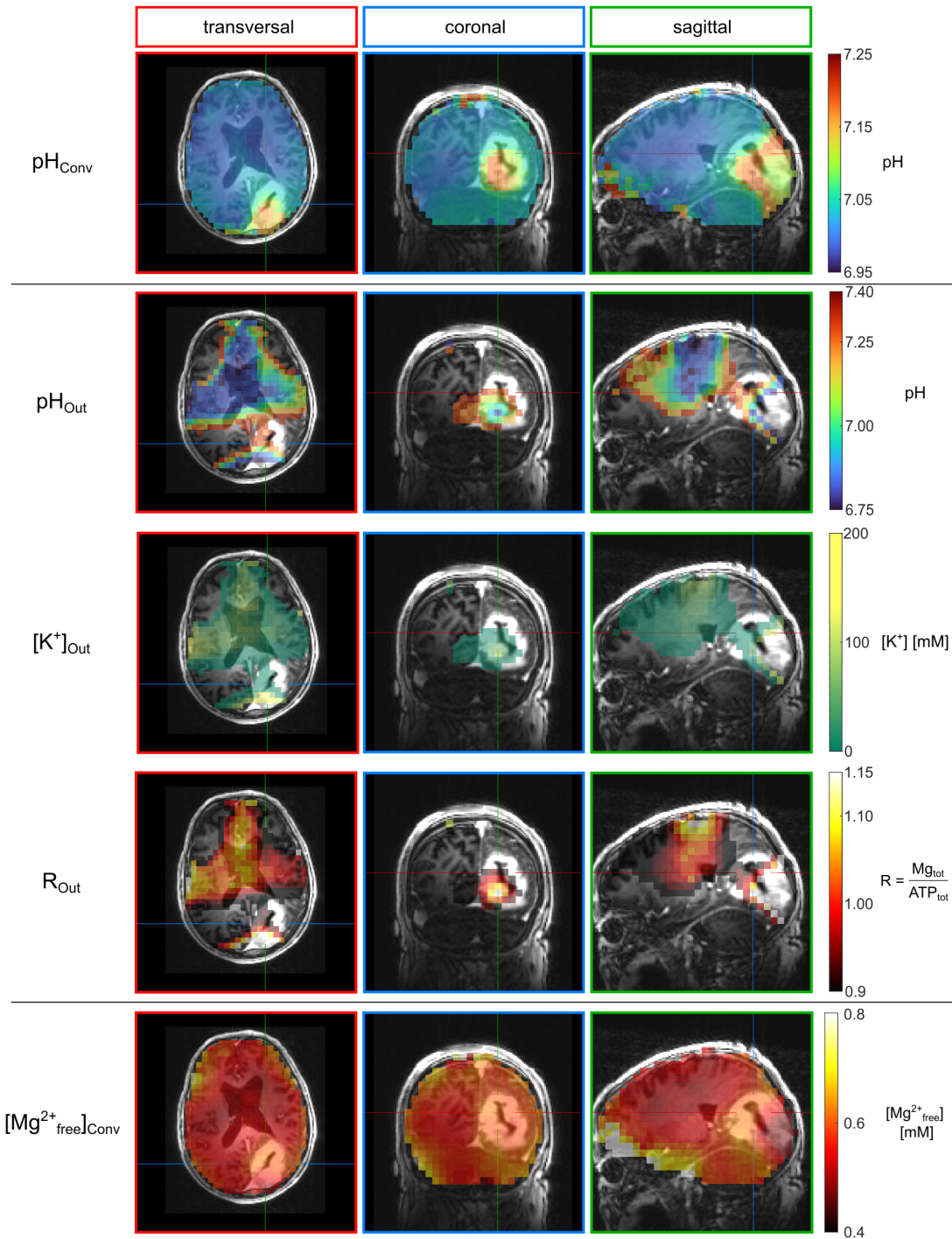


Figure E.17: Output maps of the implemented look-up algorithm using all three chemical shifts ($\delta_\gamma, \delta_\alpha, \delta_\beta$) as input for the look-up search. The output maps pH_{Out} , $[\text{K}^+]_{\text{Out}}$, and $R_{\text{Out}} = \frac{[\text{Mg}_{\text{total}}]}{[\text{ATP}_{\text{total}}]}$ applied to the ^{31}P MRSI dataset of the human brain from patient 1 are shown. For an easier comparison, the conventionally calculated maps for pH and $[\text{Mg}_{\text{free}}^{2+}]$ are also shown at the top and bottom of the figure.

List of Figures

2.1	Zeeman energy level splitting in a static magnetic field	6
2.2	Measured MR signal in time and frequency domain	11
2.3	Representative ^{31}P MR spectrum acquired in muscle tissue from a human lower leg at $B_0 = 7\text{T}$	13
2.4	Multiplet splitting of ATP	14
2.5	Schematic representation of NMR lineshapes in presence of chemical exchange	16
2.6	Chemical structures of phosphocreatine (PCr) and inorganic phosphate (P_i)	22
2.7	Schematic representation of the dissociation of phosphoric acid	23
2.8	Chemical structures of adenosine-5'-triphosphate (ATP)	24
2.9	Schematic representation of the chemical shift changes of inorganic phosphate (P_i) due to varying pH value	27
2.10	Chemical structures of the two phosphate species relevant in the physiological pH range	27
2.11	Visualization of the modified Henderson Hasselbalch equation	28
4.1	7-T MR system and used MR coils for the measurements in vivo	38
4.2	9.4-T small animal scanner and used RF coil used for the measurements in model solutions	39
4.3	Sequence diagram of a ^{31}P FID sequence	40
4.4	Sequence diagram of the used 3D ^{31}P FID-MRSI sequence	42
4.5	regions-of-interest (ROIs) definition in the lower leg muscle datasets	49
4.6	region-of-interest (ROI) definition for the brain datasets	49
4.7	Self-built phantom-mount for the measurements in model solutions	50
4.8	Schematic representation of the workflow for the calculation of the probability distributions	55
4.9	Special cases for the determination of the probability distributions	56
4.10	Schematic representation of the workflow for the determination of output values (pH, Mg, K) using the proposed look-up approach	58
5.1	Representative ^{31}P MR spectra localized in the lower leg muscles of a healthy volunteer	62

List of Figures

5.2	Conventionally calculated 3D pH maps of the lower leg muscles of healthy volunteers	63
5.3	Conventionally calculated 3D magnesium maps of the lower leg muscles of healthy volunteers	64
5.4	Distributions of the measured chemical shifts obtained from the lower leg muscle datasets	65
5.5	Distributions of the calculated pH and magnesium ion concentration obtained from the lower leg muscle datasets	66
5.6	Representative ^{31}P spectra from the human brain of a patient with glioblastoma	68
5.7	Conventionally calculated 3D pH maps of the human brain of patients with glioblastoma	69
5.8	Conventionally calculated 3D magnesium maps of the human brain of patients with glioblastoma	70
5.9	Distributions of the measured chemical shifts obtained from the human brain datasets of patients with glioblastoma	71
5.10	Distributions of calculated pH and magnesium values obtained from the human brain datasets of patients with glioblastoma	72
5.11	Chemical shift ranges obtained in vivo	73
5.12	Representative ^{31}P MR spectra acquired from two different model solutions	76
5.13	Spectral changes with changing pH value	77
5.14	Spectral changes with changing magnesium ion concentration	78
5.15	Spectral changes with changing potassium and sodium concentration . . .	79
5.16	Quantified chemical shifts in dependence on pH	80
5.17	Quantified chemical shifts in dependence on the potassium ion concentration	81
5.18	Quantified chemical shifts in dependence on the magnesium ion concentration	83
5.19	One-dimensional function $\delta_{\gamma}^{\text{Heur}}(R)$ for γ -ATP	86
5.20	Fit parameters of the heuristically developed function $\delta^{\text{Heur}}(R)$ for γ -ATP	87
5.21	Multi-dimensional fit of the heuristically developed function $\delta^{\text{Heur}}(R, pH, K)$ (equation (3.1) with equations (5.1) and (5.2)) determined for γ -ATP . . .	89
5.22	Two-dimensional function $\delta_{\gamma}^{\text{London}}(R, pH)$ for γ -ATP	90
5.23	Fit parameters for the model function δ^{London} for γ -ATP, plotted against the potassium concentration	91
5.24	Multi-dimensional fit of the model function $\delta^{\text{London}}(R, pH, K)$ for γ -ATP .	93
5.25	One-dimensional function $\delta_{\gamma}^{\text{Hill}}(\text{Mg}_{\text{tot}})$ for γ -ATP	95

5.26	Fit parameters of the model function $\delta^{\text{Hill}}(M_{g_{\text{tot}}})$ for γ -ATP, plotted against the pH value	97
5.27	Fit parameters of the model function $\delta^{\text{Hill}}(M_{g_{\text{tot}}})$ for γ -ATP, plotted against the potassium concentration	98
5.28	Multi-dimensional fit of the model function $\delta^{\text{Hill}}(M_{g_{\text{tot}}}, pH, K)$ for γ -ATP	100
5.29	Transversal view of the 3D maps according to the implemented look-up approach applied to the ^{31}P MRSI data sets of the lower leg muscle of healthy volunteers	107
5.30	Coronal view of the 3D maps according to the implemented look-up approach applied to the ^{31}P MRSI data sets of the lower leg muscle of healthy volunteers	108
5.31	Regions-of-interest (ROIs) analyses across the investigated muscle groups	109
5.32	Transversal view of the 3D maps according to the implemented look-up approach applied to the ^{31}P MRSI data from human brain of patients with glioblastoma	112
5.33	Sagittal view of the 3D maps according to the implemented look-up approach applied to the ^{31}P MRSI data from human brain of patients with glioblastoma	113
5.34	Regions-of-interest (ROIs) analyses of the human brain data of patients with glioblastoma	114
6.1	Comparison of measured chemical shift δ_{PiPCr} acquired at two different 9.4-T MR systems	120
B.1	Quantified relative linewidths in dependence on pH	IV
B.2	Quantified relative linewidths in dependence on K	V
B.3	Quantified relative linewidths in dependence on R	VI
B.4	Quantified J-coupling constants of ATP in dependence on pH , K and R . .	VII
C.5	One-dimensional function $\delta_{\alpha}^{\text{Hill}}(M_{g_{\text{tot}}})$	VIII
C.6	Fit parameters of the model function $\delta_{\alpha}^{\text{Hill}}(M_{g_{\text{tot}}})$, plotted against pH . . .	IX
C.7	Fit parameters of the model function $\delta_{\alpha}^{\text{Hill}}(M_{g_{\text{tot}}})$, plotted against K . . .	X
C.8	Multi-dimensional fit of the model function $\delta_{\alpha}^{\text{Hill}}(M_{g_{\text{tot}}}, pH, K)$	XI
C.9	One-dimensional function $\delta_{\beta}^{\text{Hill}}(M_{g_{\text{tot}}})$	XII
C.10	Fit parameters of the model function $\delta_{\beta}^{\text{Hill}}(M_{g_{\text{tot}}})$, plotted against pH . . .	XIII
C.11	Fit parameters of the model function $\delta_{\beta}^{\text{Hill}}(M_{g_{\text{tot}}})$, plotted against K . . .	XIV
C.12	Multi-dimensional fit of the model function $\delta_{\beta}^{\text{Hill}}(M_{g_{\text{tot}}}, pH, K)$	XV
D.13	Estimated pH of model solutions applying the implemented look-up approach	XVII

List of Figures

D.14 Estimated magnesium ion concentrations of model solutions applying the
implemented look-up approach XVIII

D.15 Estimated potassium ion concentrations of model solutions applying the
implemented look-up approach XIX

E.16 Output maps of the application of the look-up algorithm using $(\delta_\gamma, \delta_\alpha, \delta_\beta)$
to the muscle dataset of volunteer 2 XXI

E.17 Output maps of the application of the look-up algorithm using $(\delta_\gamma, \delta_\alpha, \delta_\beta)$
to the brain dataset of patient 1 XXII

List of Tables

2.1	Intra- and extracellular concentration of most abundant ions in vivo	25
4.1	Chemical composition of the prepared model solution sets	44
4.2	Sequence parameters of the used 3D ³¹ P MRSI sequences for the measurements in vivo	47
5.1	Fit parameters of the multi-dimensional functions $\delta^{\text{Heur}}(R, pH, K)$	88
5.2	Fit parameters of the multi-dimensional functions $\delta^{\text{London}}(R, pH, K)$	94
5.3	Fit parameters of the multi-dimensional functions $\delta^{\text{Hill}}(M_{\text{tot}}, pH, K)$. . .	101
5.4	Fit quality measures for the different developed models	102
6.1	Typical values used for the parameters in the modified Henderson Hasselbalch equation	116

List of Scientific Publications

All scientific publication that I contributed to are listed in the following. The publications containing parts of this thesis, are marked with the comment “**(Parts are used in this thesis)**”.

Journal articles

Franke VL, Breitling J; Ladd ME; Bachert P, and Korzowski A. ^{31}P MRSI at 7 T enables high-resolution volumetric mapping of the intracellular magnesium ion content in human lower leg muscles. *Magnetic Resonance in Medicine* 2022; 88: 511- 523. doi:10.1002/mrm.29231.

(Parts are used in this thesis)

Boyd PS, Breitling J, Korzowski A, Franke VL, Mueller-Decker K, Glinka A, Ladd ME, Bachert P, and Goerke S. Mapping intracellular pH in tumors using amide and guanidyl CEST-MRI at 9.4 T. *Magnetic Resonance in Medicine* 2022; 87: 2436-2452. doi:10.1002/mrm.29133

Korzowski A, Weckesser N, Franke VL, Breitling J, Goerke S, Schlemmer H, Ladd ME, Bachert P, and Paech D. Mapping an Extended Metabolic Profile of Gliomas Using High-Resolution ^{31}P MRSI at 7T. *Frontiers in Neurology* 2021. 12:735071. doi: 10.3389/fneur.2021.735071.

(Parts are used in this thesis)

Conference and workshop contributions

Franke VL, Breitling J, Bangert R, Ladd ME, Bachert P, and Korzowski A. A dictionary-based approach for the determination of pH values using ^{31}P MRS. Proceedings of the 30th Annual Meeting of the ISMRM, London, UK, 2022; Poster #1364.

(Parts are used in this thesis)

List of Scientific Publications

Platek J, Franke VL, Ladd ME, Bachert P, and Korzowski A. A simulation framework to assess the quantification reliability of 2HG in 1H MRS. Proceedings of the 30th Annual Meeting of the ISMRM, London, UK, 2022; Poster #1083.

Franke VL, Breitling J, Bangert R, Ladd ME, Bachert P, and Korzowski A. A dictionary-based approach for the determination of pH values using 31P MRS. Proceedings of the International Magnetic Resonance Spectroscopy Workshop “MRS 2022”, Lausanne, Switzerland. Poster #20.

(Parts are used in this thesis)

Platek J, Franke VL, Ladd ME, Bachert P, and Korzowski A. A simulation framework to assess the quantification reliability of 2HG in 1H MRS. Proceedings of the International Magnetic Resonance Spectroscopy Workshop “MRS 2022”, Lausanne, Switzerland. Poster #24.

Weygand J, Franke VL, Ladd ME, Bachert P, and Korzowski A. ARTT GRAPPA for Accelerating Magnetic Resonance Spectroscopic Imaging. AAMP Medical Physics 49(6): E476.

Holzwarth N, Schellenberg M, Gnirs R, Biegger P, Korzowski A, Franke VL, Dreher K, Nölke JH, Seitel A, Bachert P, Schlemmer HP, and Maier-Hein L. Tattoo image fusion: an optical pattern approach to image registration of freehand photoacoustics with other medical imaging modalities. SPIE 22 (11960-101).

Franke VL, Platek J, Boyd PS, Laier S, Müller-Decker K, Glinka A, Ladd ME, Goerke S, Bachert P, and Korzowski A. 31P MRSI in tumor-bearing mice at 9.4T. Proceedings of the 29th Annual Meeting of the ISMRM, Vancouver, Canada, 2022 (virtual); Digital Poster #0929.

Korzowski A, Weckesser N, Franke VL, Schlemmer HP, Ladd ME, Bachert P, and Paech D. 31P spectral profiles in brain tissues of volunteers and glioma patients at 7T. Proceedings of the 29th Annual Meeting of the ISMRM, Vancouver, Canada, 2021 (virtual); Digital Poster #0956.

Franke VL, Ladd ME, Bachert P, and Korzowski A. Volumetric mapping of the intracellular magnesium ion concentration in human calf muscles using 31P MRSI at 7 Tesla. Proceedings of the 28th Annual Meeting of the ISMRM, Sydney, Australia, 2020 (virtual); Digital Poster #2965.

(Parts are used in this thesis)

Korzowski A, Breitling J, Franke VL, Ladd ME, and Bachert P. Accelerating volumetric 31P MRSI of the human calf muscle at 7 Tesla: can low-rank denoising filters replace the need for signal averaging? Proceedings of the 28th Annual Meeting of the ISMRM, Sydney, Australia, 2020 (virtual); Digital Poster #2966.

Platt T, Ebersberger L, Franke VL, Nagel A, Umathum R, Schlemmer H, Bachert P, Ladd M, Korzowski A, Niesporek S, and Paech D. Mapping neuronal activity associated with finger tapping using direct measurement of 17O at 7 Tesla: proof-of-concept experiment. Proceedings of the 28th Annual Meeting of the ISMRM, Sydney, Australia, 2020 (virtual); Talk #0472.

Ebersberger L, Platt T, Franke VL, Nagel A, Umathum R, Schlemmer H, Bachert P, Ladd M, Korzowski A, Niesporek S, and Paech D. Untersuchung der regionalen Abhängigkeit des zerebralen Sauerstoffumsatzes und neuronaler Aktivität in gesunden Probanden durch dynamische 17O Magnetresonanztomografie bei 7-Tesla. RöFo 192 (S01): S2.

Franke VL, Zimmermann F, Magill AW, Ladd ME, Bachert P, and Korzowski A. Functional 31P Magnetic Resonance Spectroscopy of the Human Visual Cortex using Repeated Short-Term Stimulation at 7T. Proceedings of the 27th Annual Meeting of the ISMRM, Montreal, Canada, 2019; Digital Poster #2501.

Bibliography

- [1] Isidor Isaac Rabi et al. “A new method of measuring nuclear magnetic moment”. In: *Physical review* 53.4 (1938), p. 318.
- [2] Felix Bloch. “Nuclear induction”. In: *Physical review* 70.7-8 (1946), p. 460.
- [3] Edward M Purcell, Henry Cutler Torrey, and Robert V Pound. “Resonance absorption by nuclear magnetic moments in a solid”. In: *Physical review* 69.1-2 (1946), p. 37.
- [4] WG Proctor and FC Yu. “The dependence of a nuclear magnetic resonance frequency upon chemical compound”. In: *Physical Review* 77.5 (1950), p. 717.
- [5] WC Dickinson. “Dependence of the F 19 nuclear resonance position on chemical compound”. In: *Physical Review* 77.5 (1950), p. 736.
- [6] Paul C Lauterbur. “Image formation by induced local interactions: examples employing nuclear magnetic resonance”. In: *nature* 242.5394 (1973), pp. 190–191.
- [7] Peter Mansfield and Peter K Grannell. “NMR ‘diffraction’ in solids?” In: *Journal of Physics C: solid state physics* 6.22 (1973), p. L422.
- [8] David G Gorenstein. *Phosphorous-31 NMR: Principles and applications*. Academic Press, 1984.
- [9] Andreas Korzowski et al. “Volumetric mapping of intra-and extracellular pH in the human brain using 31P MRSI at 7T”. In: *Magnetic resonance in medicine* 84.4 (2020), pp. 1707–1723.
- [10] Andreas Korzowski et al. “Mapping an Extended Metabolic Profile of Gliomas Using High-Resolution 31P MRSI at 7T”. In: *Frontiers in neurology* 12.735071 (2021).
- [11] June S Taylor et al. “Free magnesium levels in normal human brain and brain tumors: 31P chemical-shift imaging measurements at 1.5 T.” In: *Proceedings of the National Academy of Sciences* 88.15 (1991), pp. 6810–6814.
- [12] Katharina J Wenger et al. “Intracellular pH measured by 31P-MR-spectroscopy might predict site of progression in recurrent glioblastoma under antiangiogenic therapy”. In: *Journal of Magnetic Resonance Imaging* 46.4 (2017), pp. 1200–1208.

Bibliography

- [13] Dennis WJ Klomp et al. “³¹P MRSI and ¹H MRS at 7 T: initial results in human breast cancer”. In: *NMR in Biomedicine* 24.10 (2011), pp. 1337–1342.
- [14] L. M. Resnick et al. “Intracellular and extracellular magnesium depletion in Type 2 (non-insulin-dependent) diabetes mellitus”. In: *Diabetologia* 36.8 (Aug. 1993), pp. 767–770.
- [15] Harmen Reyngoudt, Alfredo L Lopez Kolkovsky, and Pierre G Carlier. “Free intramuscular Mg²⁺ concentration calculated using both ³¹P and ¹H NMRS-based pH in the skeletal muscle of Duchenne muscular dystrophy patients”. In: *NMR in Biomedicine* 32.9 (2019), e4115.
- [16] Tadafumi Kato et al. “Decreased brain intracellular pH measured by ³¹P-MRS in bipolar disorder: a confirmation in drug-free patients and correlation with white matter hyperintensity”. In: *European archives of psychiatry and clinical neuroscience* 248.6 (1998), pp. 301–306.
- [17] Hiroshi Hamakawa et al. “Reduced intracellular pH in the basal ganglia and whole brain measured by ³¹P-MRS in bipolar disorder”. In: *Psychiatry and clinical neurosciences* 58.1 (2004), pp. 82–88.
- [18] Myriam M Chaumeil et al. “pH as a biomarker of neurodegeneration in Huntington’s disease: a translational rodent-human MRS study”. In: *Journal of cerebral blood flow & metabolism* 32.5 (2012), pp. 771–779.
- [19] Mario Barbagallo et al. “Altered ionized magnesium levels in mild-to-moderate Alzheimer’s disease”. In: *Magnesium Research* 24.3 (2011), pp. 115–121.
- [20] Richard B Moon and John H Richards. “Determination of intracellular pH by ³¹P magnetic resonance”. In: *Journal of Biological Chemistry* 248.20 (1973), pp. 7276–7278.
- [21] Raj K Gupta, Jeffrey L Benovic, and Zelda B Rose. “The determination of the free magnesium level in the human red blood cell by ³¹P NMR.” In: *Journal of Biological Chemistry* 253.17 (1978), pp. 6172–6176.
- [22] Ognen AC Petroff et al. “Cerebral intracellular pH by ³¹P nuclear magnetic resonance spectroscopy”. In: *Neurology* 35.6 (1985), pp. 781–781.
- [23] JW Pettegrew et al. “Considerations for brain pH assessment by ³¹P NMR”. In: *Magnetic resonance imaging* 6.2 (1988), pp. 135–142.

- [24] Justin KM Roberts, Norma Wade-Jardetzky, and Oleg Jardetsky. “Intracellular pH measurements by phosphorus-31 nuclear magnetic resonance. Influence of factors other than pH on phosphorus-31 chemical shifts”. In: *Biochemistry* 20.19 (1981), pp. 5389–5394.
- [25] A Madden et al. “A quantitative analysis of the accuracy of in vivo pH measurements with ^{31}P NMR spectroscopy: assessment of pH measurement methodology”. In: *NMR in Biomedicine* 4.1 (1991), pp. 1–11.
- [26] Robert E London. “Methods for measurement of intracellular magnesium: NMR and fluorescence”. In: *Annual review of physiology* 53.1 (1991), pp. 241–258.
- [27] Elke M Golding and Raymund M Golding. “Interpretation of ^{31}P MRS spectra in determining intracellular free magnesium and potassium ion concentrations”. In: *Magnetic resonance in medicine* 33.4 (1995), pp. 467–474.
- [28] James P Willcocks et al. “Simultaneous Determination of Low Free Mg^{2+} and pH in Human Sickle Cells using ^{31}P NMR Spectroscopy* 210”. In: *Journal of Biological Chemistry* 277.51 (2002), pp. 49911–49920.
- [29] S Iotti et al. “In vivo ^{31}P -MRS assessment of cytosolic $[\text{Mg}^{2+}]$ in the human skeletal muscle in different metabolic conditions”. In: *Magnetic resonance imaging* 18.5 (2000), pp. 607–614.
- [30] Gerald D Williams, Timothy J Mosher, and Michael B Smith. “Simultaneous determination of intracellular magnesium and pH from the three ^{31}P NMR chemical shifts of ATP”. In: *Analytical biochemistry* 214.2 (1993), pp. 458–467.
- [31] Robin A De Graaf. *In vivo NMR spectroscopy: principles and techniques*. John Wiley & Sons, 2013.
- [32] Jozef Kowalewski and L Mäler. *Nuclear Spin Relaxation in Liquids: Theory, Experiments, and Applications*. Taylor & Francis Group, 2006.
- [33] Malcolm H Levitt. *Spin dynamics: basics of nuclear magnetic resonance*. John Wiley & Sons, 2008.
- [34] Leif Schröder, Christian Schmitz, and Peter Bachert. “Cumulative “roof effect” in high-resolution in vivo ^{31}P NMR spectra of human calf muscle and the Clebsch–Gordan coefficients of ATP at 1.5 T”. In: *Journal of Magnetic Resonance* 174.1 (2005), pp. 68–77.
- [35] Harden M McConnell. “Reaction rates by nuclear magnetic resonance”. In: *The Journal of chemical physics* 28.3 (1958), pp. 430–431.

Bibliography

- [36] Robert W Brown et al. *Magnetic resonance imaging: physical principles and sequence design*. John Wiley & Sons, 2014.
- [37] RF Schmidt, F Lang, and M Heckmann. *Springer-Lehrbuch. Physiologie des Menschen: Mit Pathophysiologie*. 2010.
- [38] Lubert Stryer. *Biochemistry, 3rd edn. W, H.* 1988.
- [39] Leif Schröder. “Quantenmechanische Feinstruktur und molekulare Dynamik gekoppelter Spin-1/2-Systeme in der In-vivo-NMR-Spektroskopie”. Dissertation. University of Heidelberg, Germany, 2003.
- [40] Katharine A White, Bree K Grillo-Hill, and Diane L Barber. “Cancer cell behaviors mediated by dysregulated pH dynamics at a glance”. In: *Journal of cell science* 130.4 (2017), pp. 663–669.
- [41] Bradley A Webb et al. “Dysregulated pH: a perfect storm for cancer progression”. In: *Nature Reviews Cancer* 11.9 (2011), pp. 671–677.
- [42] Mehdi Damaghi, Jonathan W Wojtkowiak, and Robert J Gillies. “pH sensing and regulation in cancer”. In: *Frontiers in physiology* 4 (2013), p. 370.
- [43] Erez Persi et al. “Systems analysis of intracellular pH vulnerabilities for cancer therapy”. In: *Nature communications* 9.1 (2018), pp. 1–11.
- [44] Leo E Gerweck and Kala Seetharaman. “Cellular pH gradient in tumor versus normal tissue: potential exploitation for the treatment of cancer”. In: *Cancer research* 56.6 (1996), pp. 1194–1198.
- [45] Raffaele Lodi et al. “Deficient energy metabolism is associated with low free magnesium in the brains of patients with migraine and cluster headache”. In: *Brain research bulletin* 54.4 (2001), pp. 437–441.
- [46] Sebastian Regnery et al. “Ultra-high-field sodium MRI as biomarker for tumor extent, grade and IDH mutation status in glioma patients”. In: *NeuroImage: Clinical* 28 (2020), p. 102427.
- [47] Federica I Wolf and Achille Cittadini. “Chemistry and biochemistry of magnesium”. In: *Molecular aspects of medicine* 24.1-3 (2003), pp. 3–9.
- [48] Peter B Barker et al. “Magnesium and pH imaging of the human brain at 3.0 Tesla”. In: *Magnetic Resonance in Medicine: An Official Journal of the International Society for Magnetic Resonance in Medicine* 41.2 (1999), pp. 400–406.
- [49] DKFZ. *High-Field Whole Body MR (7 T)*. URL: <https://www.dkfz.de/en/medphysrad/workinggroups/ultrahighfieldmr/ultrahighfieldmr.html> (visited on 11/26/2022).

- [50] Leentje Vanhamme, Aad van den Boogaart, and Sabine Van Huffel. “Improved method for accurate and efficient quantification of MRS data with use of prior knowledge”. In: *Journal of magnetic resonance* 129.1 (1997), pp. 35–43.
- [51] S Cavassila et al. “Cramér–Rao bounds: an evaluation tool for quantitation”. In: *NMR in Biomedicine: An International Journal Devoted to the Development and Application of Magnetic Resonance In Vivo* 14.4 (2001), pp. 278–283.
- [52] Vanessa L Franke et al. “³¹P MRSI at 7 T enables high-resolution volumetric mapping of the intracellular magnesium ion content in human lower leg muscles”. In: *Magnetic Resonance in Medicine* 88.2 (2022), pp. 511–523.
- [53] Marco Nolden et al. “The medical imaging interaction toolkit: challenges and advances”. In: *International journal of computer assisted radiology and surgery* 8.4 (2013), pp. 607–620.
- [54] Wulf-Ingo Jung et al. “Phosphorus J-coupling constants of ATP in human brain”. In: *Magnetic resonance in medicine* 37.5 (1997), pp. 802–804.
- [55] Arend Heerschap et al. “Introduction to in vivo ³¹P magnetic resonance spectroscopy of (human) skeletal muscle”. In: *Proceedings of the Nutrition Society* 58.4 (1999), pp. 861–870.
- [56] Dinesh Kumar Deelchand et al. “Quantification of in vivo ³¹P NMR brain spectra using LCModel”. In: *NMR in Biomedicine* 28.6 (2015), pp. 633–641.
- [57] Jack V Greiner and Thomas Glonek. “Intracellular ATP Concentration and Implication for Cellular Evolution”. In: *Biology* 10.11 (2021), p. 1166.
- [58] Jimin Ren, A Dean Sherry, and Craig R Malloy. “³¹P-MRS of healthy human brain: ATP synthesis, metabolite concentrations, pH, and T1 relaxation times”. In: *NMR in Biomedicine* 28.11 (2015), pp. 1455–1462.
- [59] I Mottet et al. “Experimental ³¹P NMR study of the influence of ionic strength on the apparent dissociation constant of MgATP”. In: *Magnetic Resonance Materials in Physics, Biology and Medicine* 2.2 (1994), pp. 101–107.
- [60] Yoshiteru Seo et al. “Intracellular pH determination by a ³¹P-NMR technique. The second dissociation constant of phosphoric acid in a biological system”. In: *The Journal of Biochemistry* 94.3 (1983), pp. 729–734.
- [61] Martin Meyerspeer et al. “³¹P magnetic resonance spectroscopy in skeletal muscle: Experts’ consensus recommendations”. In: *NMR in Biomedicine* 34.5 (2021), e4246.

Bibliography

- [62] Jimin Ren et al. “Unveiling a hidden ^{31}P signal coresonating with extracellular inorganic phosphate by outer-volume-suppression and localized ^{31}P MRS in the human brain at 7T”. In: *Magnetic resonance in medicine* 80.4 (2018), pp. 1289–1297.
- [63] James H Fitzpatrick Jr et al. “NMR studies of Pi-containing extracellular and cytoplasmic compartments in brain”. In: *Journal of neurochemistry* 66.6 (1996), pp. 2612–2620.
- [64] David D Gilboe et al. “NMR-based identification of intra-and extracellular compartments of the brain pi peak”. In: *Journal of neurochemistry* 71.6 (1998), pp. 2542–2548.
- [65] Brice Tiret, Emmanuel Brouillet, and Julien Valette. “Evidence for a “metabolically inactive” inorganic phosphate pool in adenosine triphosphate synthase reaction using localized ^{31}P saturation transfer magnetic resonance spectroscopy in the rat brain at 11.7 T”. In: *Journal of Cerebral Blood Flow & Metabolism* 36.9 (2016), pp. 1513–1518.
- [66] Oliver Schmidt et al. “Unveiling extracellular inorganic phosphate signals from blood in human cardiac ^{31}P NMR spectra”. In: *Journal of Cardiovascular Magnetic Resonance* 3.4 (2001), pp. 325–329.
- [67] Timothy J Mosher et al. “Error in the calibration of the MgATP chemical-shift limit: effects on the determination of free magnesium by ^{31}P NMR spectroscopy”. In: *Magnetic resonance in medicine* 24.1 (1992), pp. 163–169.
- [68] Stefan Widmaier et al. “Magnesium-Based Temperature Dependence of the ATP Chemical-Shift Separation $\delta\alpha\beta$ and Its Relation to Intracellular Free Magnesium”. In: *Journal of Magnetic Resonance, Series B* 113.1 (1996), pp. 16–24.
- [69] Stefan Widmaier et al. “ ^{31}P NMR studies of human soleus and gastrocnemius show differences in the $J\gamma\beta$ coupling constant of ATP and in intracellular free magnesium”. In: *Magnetic Resonance Materials in Physics, Biology and Medicine* 4.1 (1996), pp. 47–53.
- [70] Antoine Feignier. “Characterization of model solutions for combined pH imaging using ^{31}P MRSI and CEST imaging”. Bachelor thesis. Hochschule Mannheim, 2022.
- [71] William J O’Sullivan and Geoffrey W Smithers. “[12] Stability constants for biologically important metal-ligand complexes”. In: *Methods in enzymology*. Vol. 63. Elsevier, 1979, pp. 294–336.

- [72] Mildred Cohn and Thomas R Hughes Jr. “Nuclear magnetic resonance spectra of adenosine di- and triphosphate: II. Effect of complexing with divalent metal ions”. In: *Journal of Biological Chemistry* 237.1 (1962), pp. 176–181.
- [73] Tran-Dinh Son, Madeleine Roux, and Michel Ellenberger. “Interaction of Mg²⁺ ions with nucleoside triphosphates by phosphorus magnetic resonance spectroscopy”. In: *Nucleic Acids Research* 2.7 (1975), pp. 1101–1110.
- [74] Fumiyuki MITSUMORI. “Phosphorus-31 nuclear magnetic resonance studies on intact erythrocytes. Determination of intracellular pH and time course changes in phosphorus metabolites”. In: *The Journal of Biochemistry* 97.6 (1985), pp. 1551–1560.
- [75] T Günther. “Concentration, compartmentation and metabolic function of intracellular free Mg²⁺”. In: *Magnesium research* 19.4 (2006), pp. 225–236.
- [76] Philip S Boyd. “Mapping intracellular pH of tumors in vivo using CEST-MRI: methodological development and preclinical investigation”. Dissertation. University of Heidelberg, Germany, 2022.
- [77] Philip S Boyd et al. “Mapping intracellular pH in tumors using amide and guanidyl CEST-MRI at 9.4 T”. In: *Magnetic Resonance in Medicine* 87.5 (2022), pp. 2436–2452.
- [78] Stephan Düwel et al. “Imaging of pH in vivo using hyperpolarized ¹³C-labelled zymonic acid”. In: *Nature communications* 8.1 (2017), pp. 1–9.
- [79] John L Markley. “Observation of histidine residues in proteins by nuclear magnetic resonance spectroscopy”. In: *Accounts of Chemical Research* 8.2 (1975), pp. 70–80.
- [80] James N Weiss. “The Hill equation revisited: uses and misuses”. In: *The FASEB Journal* 11.11 (1997), pp. 835–841.

Acknowledgments — Danksagung

In erster Linie möchte ich mich bei Herrn Prof. Peter Bachert für die Unterstützung während meiner gesamten bisherigen Zeit am DKFZ bedanken. Angefangen mit meiner Bachelor- und Masterarbeit, über die Bewerbungsphasen für mein Auslandsjahr in den USA oder für das Helmholtz-Promotionsstipendium, bis hin zur finalen Entscheidung meines Dissertationstitels, konnte ich immer auf Ihre Unterstützung zählen. Vielen Dank!

Ich danke auch Herrn Prof. Michael Hausmann dafür, dass er sich die Zeit für die Zweitbegutachtung meiner Dissertation nimmt. Ich kann mir vorstellen, was es für einen enormen zeitlichen Aufwand bedeutet, eine Doktorarbeit aus einem anderen Forschungsbereich bewerten zu müssen. Vielen Dank Ihnen dafür!

Mein größter Dank geht an Andi (aka Dr. Andreas Korzowski, um auch hier den korrekten Titel zu verwenden). Ich kann nicht in Worte fassen, wie dankbar ich dir für die ganze Unterstützung der letzten Jahren bin. Ich habe so viele Dinge von dir gelernt. Du hast mir geduldig alles erklärt was ich wissen musste (auch zum wiederholten Male), und hast mich immer wieder aufs Neue motiviert, auch wenn ich verzweifelt bin. Ich kenne kaum jemanden, der so für seine Arbeit brennt und mit einer solchen Freude sein Wissen und seine Motivation weitergibt, wie du.

Ein großer Dank gilt auch Dr. Johannes Breitling, der mir bei vielen Projekten sehr viel geholfen hat, auch nachdem er das DKFZ bereits verlassen hat. Ich weiß das wirklich sehr zu schätzen! Des Weiteren möchte ich natürlich Renate Bangert für die großartige Unterstützung bei den Experimenten an den Modelllösungen danken. Ich weiß, wie viel Arbeit die Vorbereitung aller Proben war und danke dir sehr für deine Unterstützung. Ohne dich wäre das Projekt in der kurzen Zeit nie so weit gekommen! Auch die Arbeit von Antoine Feignier war eine große Unterstützung und hat uns viele neue Erkenntnisse geliefert. Es hat sehr großen Spaß gemacht, mit dir zusammenzuarbeiten, und wir würden uns alle freuen, wenn dich dein Weg nochmal zu uns führt.

Ein besonderer Dank gebührt natürlich Dr. Philip Boyd. Auch wenn du mich mehr als einmal an den Rand des Wahnsinns getrieben hast, bist du doch der beste work spouse,

Acknowledgments

den ich mir hätte wünschen können. Ohne dich wäre meine Promotionszeit nicht einmal ansatzweise so lustig gewesen, wie sie es war. Und auch wenn ich es nicht gern zugebe, hast du mir natürlich mehr als ein Mal sehr geholfen, insbesondere jetzt als PostDoc-Boyd.

Auch möchte ich insbesondere Juystna, Marcel, Helen und Flo dafür danken, dass sie Teile meiner Arbeit korrekturgelesen habe, und viel wichtiger noch, für so viel Spaß bei der Arbeit sorgen. Darüber hinaus geht auch ein großes Dankeschön an die gesamte Arbeitsgruppe. Die Unterstützung, die jedem von uns zu Teil wird, und die tolle Stimmung, die jeden Tag bei uns herrscht, ist nicht selbstverständlich und kaum zu toppen! Ich bin sehr dankbar dafür, dass ich Teil einer so tollen Arbeitsgruppe sein darf.

Zum Schluss möchte ich mich auch bei all meinen Freunden, insbesondere Fuchsi, Clara, Melli und Alina, und meiner ganzen Familie für die dauerhafte Unterstützung bedanken! Allen voran, möchte ich meinen Eltern danken. Zum einen dafür, dass ihr mir ein so sorgenfreies Studium ermöglicht habt und zum anderen, und noch viel wichtiger, dafür, dass ihr der Anker in meinem Leben seid. Ihr gebt mir die nötige Kraft und Zuversicht, meinen Weg im Leben zu gehen. Ein großes Dankeschön geht auch an Chris. Ich danke dir dafür, dass du mich immer wieder darin ermutigt hast, an mich zu glauben und über mich hinauszuwachsen. Danke für deine Unterstützung, nicht nur in diesen letzten, extrem anstrengenden Wochen, sondern während der gesamten 3 Jahre.